Crystalline Titania Nanorods for Colloidal Liquid Crystal Based Switchable Optics

Naveed Hosseini

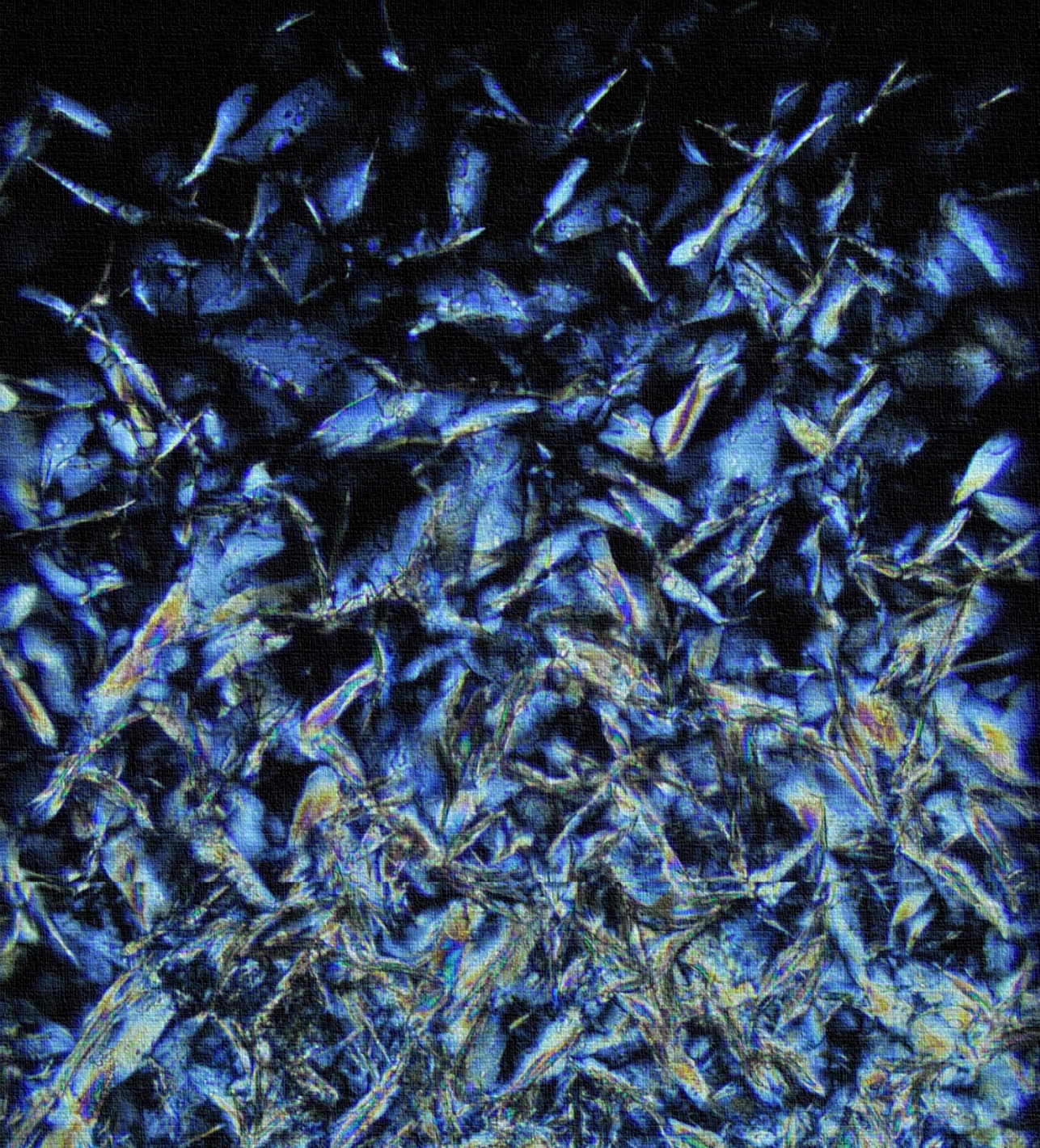

Crystalline Titania Nanorods for Colloidal Liquid Crystal Based Switchable Optics

Cover: Polarized optical microscopy images of a sedimenting sample from a dispersion of titania NRs in toluene. On the front cover, elongated nematic tactoids floating in the isotropic fluid and the coexistence of nematic domains with sharped-edge smectic LC phases are illustrated. On the back cover, the whole capillary with three distinct regions is demonstrated.

Ph.D. Thesis, Utrecht University, The Netherlands, September 2022

ISBN: 978-94-6423-982-9

A digital version of this thesis is available at https://colloid.nl/publications/theses/

Printed by: ProefschriftMaken // www.proefschriftmaken.nl

Crystalline Titania Nanorods for Colloidal Liquid Crystal Based Switchable Optics

Kristallijne Titania Nanostaafjes voor Schakelbare Optiek Gebaseerd op Colloïdale Vloeibare Kristallen

(met een samenvatting in het Nederlands)

Proefschrift

ter verkrijging van de graad van doctor aan de Universiteit Utrecht op gezag van de rector magnificus, prof.dr. H.R.B.M. Kummeling, ingevolge het besluit van het college voor promoties in het openbaar te verdedigen op maandag 19 september 2022 des middags te 2.15 uur

door

Seyed Naveed Hosseini Nohoji

geboren op 21 september 1988 te Esfahan, Iran

Promotor:
Prof. dr. A. van Blaaderen

Copromotoren:
Dr. A. Imhof
Dr. P.J. Baesjou

This research is supported by the Dutch Technology Foundation STW (Grant No. 14176), which is part of the Netherlands Organization for Scientific Research-Applied and Engineering Sciences (NWO-TTW) and partly funded by the Ministry of Economic Affairs.

1

Introduction

1

1.1 Liquid crystals

Liquid crystals (LCs) are typically associated with the development of various LC-based displays (LCDs) such as flat-panel televisions, touchscreen displays, and computer monitors used in our daily lives. Besides massive achievements in the field of LCDs over the last decades,[1] LCs have also attracted attention in a broad range of non-display applications from telecommunication technologies, photonics, sensors, and medicine to self-assembled amphiphilic soap molecules, which are on the borderline between soft condensed matter and nanotechnology.[2–4] This class of matter is of great interest mainly due to its fascinating anisotropic properties (i.e., refractive index, viscosity, elastic constant, electric conductivity, or magnetic susceptibility) that can be manipulated via responses to applied external stimuli (i.e., mechanical, electric, magnetic, or even optical stimuli) or their spontaneous self-organization.[1,5] Nowadays, many optical applications benefit from the elastic behavior of LCs (specifically commercial thermotropic LCs) which can be tuned via electric or magnetic fields. The alteration in the orientation of the mesogens in these LCs changes the orientation of the optical axis, resulting in birefringence. Several effects of the anisotropic properties of LCs with polarized light are reproduced from references[6,7] and shown in Figure 1-1.

In general, LCs are referred to as intermediate phases or mesophases formed by elongated building blocks or mesogens which can be organic, inorganic, or organometallic compounds. These mesophases are thermodynamically stable and located between the three-dimensional solid crystal and the viscous liquid, which is an isotropic disordered phase. Therefore, LCs are characterized by long-ranged orientational order, which can be combined with long-ranged positional order in one or two dimensions of their long mesogens axis, resulting in direction-dependent physical properties analogous to crystalline solids whereas the ability to flow and long-ranged diffusion is preserved similar to fluids.[8]

Although some liquid crystalline properties were observed and described by several researchers more than 100 years ago, thermotropic LCs were not realized until 1888 when Reinitzer[9] discovered this state of matter, which was followed by Lehmann[10] in 1889 who assigned the term ‘thermotropic liquid crystals’ to these mesophases (the references are in German).[11] In general, two main classes of LCs are distinguished: thermotropic

and lyotropic. Whereas the former exhibit orientational order in a certain range of temperatures, the latter form molecular aggregates as a function of the concentration in the form of micelles and columns into ordered structures such as hexagonal, cubic or lamellar phases.[12] Figure 1-2, reproduced from ref [13], shows some of the different LC phases classified based on the degree of order that are stable in diverse temperature regimes (in thermotropic LCs) or various ranges of concentrations (in lyotropic LCs). In thermotropic LCs, the frequent phase observed at temperatures below the isotropic liquid phase is called nematic, where the long axis of rod-like mesogens shows only orientational long-ranged order. The spatial and temporal average of this long axis is called the nematic director. At lower temperatures, smectic phases are formed and observed, which have both orientational order together with one or two-dimensional positional order of the mesogen centers of mass.[12] The simplest smectic phase is the smectic-A phase with one-dimensional positional order, while the director of the phase is in direction of the normal director of the smectic layer. The phase director is also an optical symmetry axis of the system which can be tilted with respect to the layer's normal director, resulting in the formation of a smectic-C phase. However, if mesogens are ordered in a hexagonal manner within the layers and at the same time stand parallel to the layer's normal director, the smectic phase is called smectic-B. If the hexagonal order inside the layers exhibits a long-range positional order, the structure will be therefore a three-dimensional crystal.[12] Likewise, the aforementioned LC phases are observed in lyotropic LCs, however, due to the nature of these mesophases, they are formed when the concentration of the anisotropic mesogens is raised to a high enough value. If anisotropic molecular mesogens form lyotropic LCs, the phase diagrams are quite complex since not only are they largely dependent on concentration they may also change at different temperatures.[13]

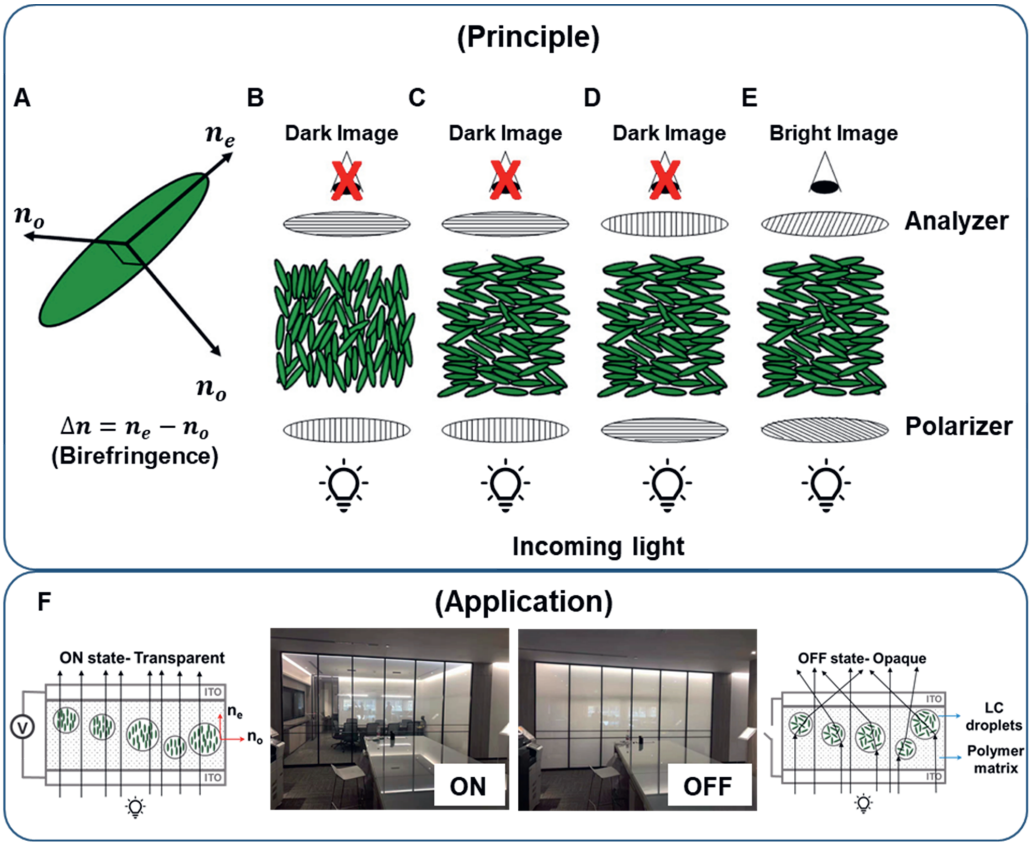

Figure 1-1. Polarized light microscopy of nematic LCs with the LCs orientations differently oriented between the cross polarizers which are called polarizer and an analyzer. (A) Schematic illustration of a nematic LC mesogen with an uniaxial ellipsoidal shape. Two distinct refractive indices are shown: a refractive index parallel to the nematic director ($\mathbf{n_e}$) and a refractive index perpendicular to the director ($\mathbf{n_o}$). The difference between these refractive indexes is known as birefringence ($\Delta\mathbf{n} = \mathbf{n_e} - \mathbf{n_o}$). (B–D) Examples of orientations of LCs while observed between crossed polarizers, displaying a dark optical state. In B, the director of the LC is aligned parallel to the direction of the propagation of the incoming light coming through the LC. In C and D, the director of the LC is oriented in the plane of the sample with an azimuthal alignment such that it is either perpendicular (C) or parallel (D) to the placed polarizers. (E) Elliptically polarized light coming through the LC layer can result in transmitted light when the director of the LC is oriented in the plane of the sample but with an azimuthal orientation lying between the polarizer and analyzer. (F) An example of LCs applications in switchable smart windows showing the principle of a polymer dispersed liquid crystal, PDLCs, changing from a clear state, when voltage is applied, to a light scattering state at zero applied voltage. Images A to E are reprinted with permission from ref [6]. Copyright 2013 American Chemical Society. The commercial image is from www.magic-film.com

1.2 Colloidal liquid crystals

Inorganic lyotropic LCs or mineral lyotropic LCs were firstly discovered in 1902 by Majorana as a new branch in lyotropic LCs when he observed in his experiments an induced optical anisotropy in sols of iron oxide colloidal particles under magnetic fields.[14] This type of lyotropic LCs, which have been called by Lekkerkerker and Vroege 'mineral colloidal LCs' or briefly 'colloidal LCs', consist of diverse shape-anisotropic particles (mostly minerals and clays) in the form of colloidal suspensions of rod and plate shaped particles that can produce LC phases above a critical concentration.[15–17] Back in the 1920s, several experimental observations were reported by Freundlich and Zocher (some of his papers are in German) on the birefringence of vanadium pentoxide dispersions which were followed in the 1930s by the observation of nematic LCs formed in suspensions of rod-like tobacco mosaic virus (TMV).[18–21] Trying to explain this experimental evidence theoretically, in 1949, Onsager showed that these intriguing self-organization into nematic LCs could be described for rod or disk-like particles through an excluded volume theory. In his theory, colloidal particles are assumed to be hard particles with no attractive interactions. Moreover, translational entropy and orientational entropy of the colloidal rods are considered as the two main factors for entropy-driven phase transitions. He showed that when rods align, they lose orientational entropy while simultaneously gaining translational entropy via decreasing their excluded volume. At sufficiently high concentrations, gaining translational entropy dominates which results in a phase transition and colloidal rods form a nematic LC phase.[22] A year later in 1950, a smectic phase was also observed in suspensions of TMV besides the expected nematic LC phase.[23] As expected, suspensions of synthetic colloidal rods generally have specific properties such as size polydispersity, limited aspect ratios, and sometimes interparticle interactions (i.e., long-range repulsions or attractions) which are different from the infinitely thin hard rods assumed in Onsager's theory. All of these parameters were further investigated by the development of several colloidal model systems such as boehmite (γ-AlO(OH)),[24] akaganeite (β-FeO(OH)),[25] and goethite (α-FeOOH)[26], together with theoretical extensions of Onsager's theory by several research groups.[27–30] Among these we specifically want to point to works of Lekkerkerker et al.[31–38] and Frenkel et al.[33,37,39–45] who contributed to both experimental, theoretical and simulations aspects. Furthermore, many important simulation and theoretical results, quite relevant

to the colloidal systems in this thesis, have been reported by Dijkstra and van Roij et al. on various colloidal LC phases.[30,45–51] For instance, as shown in Figure 1-3, various LC phases for hard spherocylinders of different aspects ratios were predicted in simulations which were confirmed by experimental observation in our group, as well.[27,41]

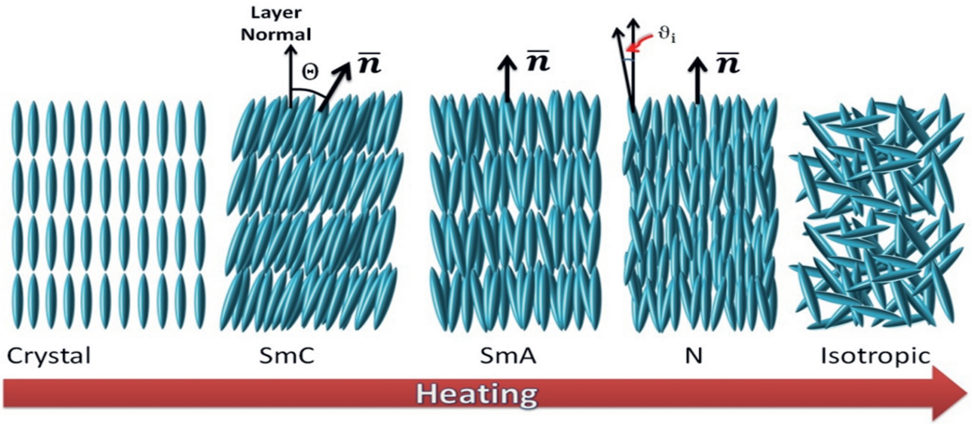

Figure 1-2. Schematic drawing of diverse LC phases observed during heating a thermotropic LC from the crystalline state. Initially, smectic phases are observed while the positional ordering is partially preserved in the form of smectic-C and smectic-A together with orientational order along the long molecular axis of elongated mesogens. In the next step, a nematic phase is detected since the positional order is lost as a result of further heating. Ultimately, all LC phases disappear at a specific temperature known as the clearing point and an isotropic liquid state is obtained. The image is reproduced from ref [13].

Over the last decades, additional solid-state chemistry emerged based on the sol-gel methods and inorganic polycondensation reactions that provide an excellent capability to manipulate the shape and size of the colloidal nanoparticles (NPs) at the nano-scale.[52–57] Among various types of NPs, colloidal nanorods (NRs), as anisotropic colloidal particles, have attracted more attention in colloid-based LC science due to their potential applications, especially in optical and optoelectronic devices.[58–60] In this regard, colloidal gold NRs are known to exhibit remarkable optical properties based on their two distinct surface plasmon resonance (SPR) absorption bands of individual gold NRs.[61–63] Analogous to gold NRs, CdSe and CdSe/CdS semiconductor NRs are known as another example of well-studied colloidal NRs which have robust synthesis procedures and amazing photoluminescence properties (i.e., strong and tunable light emission, high photoemission linearly polarized along the NRs length).[52,64–66] Other metallic or semiconductor colloidal NRs investigated in the literature can be summarized as ZnSe/CdS,[67] Au/Ag,[68] Fe_3O_4,[69] CdSe/CdTe,[70] SnO_2,[71] CdTe,[72] CdS/PbSe and PbSe/CdSe,[73] Co/TiO_2,[74] CdS/Ag_2S,[75] ZnO,[76] and TiO_2.[77] Among all of these systems, we are interested in colloidal TiO_2 NRs to exploit their high refractive

indices in optical applications. Thus, these nanomaterials are discussed further in the next section.

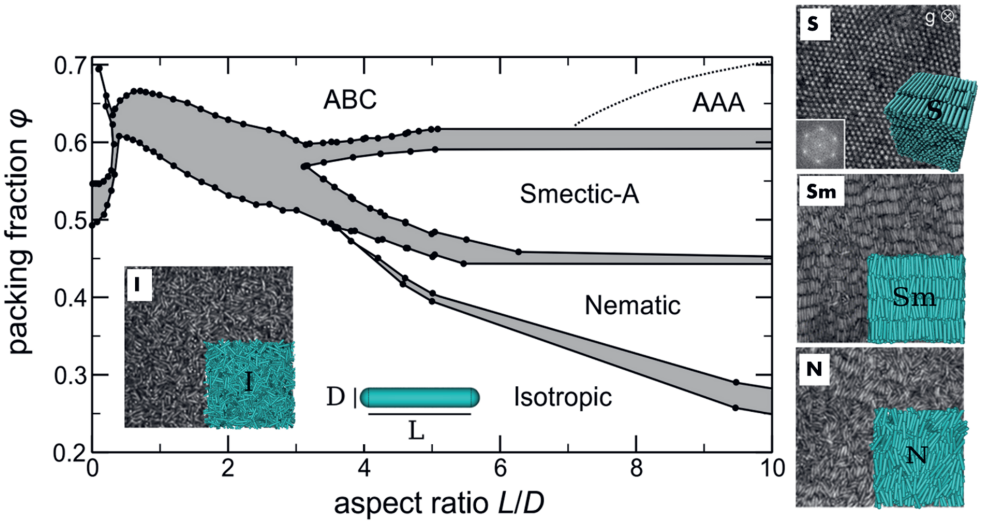

Figure 1-3. Phase diagram of hard spherocylinders, adapted with permission from computer simulation results by Bolhuis and Frenkel in ref [40]. The gray areas indicate biphasic regions. Representative snapshots from ref [30] for I, N, Sm, and S are shown on experimental results on the phase behavior of colloidal silica rods by Kuijk et al. from ref [27].

1.3 Colloidal TiO_2 NPs

Titanium dioxide or titania (TiO_2) is one of the most strongly studied metal oxides in the world. There are at least 11 reported bulk and/or nanocrystalline phases of TiO_2 including rutile, anatase, brookite, TiO_2(B), columbite (α-PbO_2)-like phase TiO_2(II), baddeleyite (ZrO_2)-like phase, hollandite-like phase TiO_2(H), ramsdellite (MnO_2 or VO_2)-like phase TiO_2(R), fluorite (CaF_2)-like cubic phase, TiO_2-OI, and cotunnite($PbCl_2$)-like phase TiO_2-OII.[78,79] The four popular phases of TiO_2 are rutile, anatase, brookite, and TiO_2(B) that are observed in natural samples and minerals. All of the four mentioned phases are categorized as stable ambient/low-pressure bulk phases.[78] Earth abundance, nontoxicity, thermal consistency, and high chemical stability of titania make it one of the most utilized components in a broad range of applications such as paints and pigments, sunscreens and cosmetics, biomedical implants, pharmaceuticals, food products, and sensors.[80] After breakthroughs in nanoscience in the last century and the emergence of

the concept of nanotechnology,[81] many scientists devoted tremendous efforts to the development of nanostructured materials, among which nanostructured TiO_2 is one of the most studied ones. Although some research evidence suggests that TiO_2 nanoparticles (NPs) may induce cellular toxicity effects which have limited their direct applicability in the cosmetics, food, and pharmaceutical industries,[82–85] many other emerging technologies have been revealed to highly benefit from these NPs, examples of which include catalysis and photocatalysis for water splitting and air/water/wastewater treatment,[86] self-cleaning and antifogging surfaces, photovoltaics, batteries, and optoelectronics.[87–90] This great interest, shown in the development of TiO_2 nanomaterial structures, originates from their inherent advantages including cost-effective fabrication, diversity in size and shapes of nanostructured TiO_2, high refractive indices, and high visible light transparency coupled with high UV light absorption due to their wide bandgaps.[91,92] Since we want to benefit from the shape and orientation-dependent collective properties of TiO_2 NPs in liquid crystalline states for optical applications, colloidal TiO_2 NRs were selected instead of differently shaped TiO_2 NPs. Rod-shaped NPs, not only can spontaneously form LC phases, but they also have other advantages over spherical TiO_2 NPs in terms of high surface-to-volume ratio, improved number of delocalized carriers, and enhanced charge transport provided by their anisotropic geometry.[93,94] Furthermore, TiO_2 NRs, with sizes significantly less than 100 nm (e.g. 10 nm), are sufficiently small not to strongly scatter light, but at the same time, they exhibit high visible light transparency combined with high refractive indices and anisotropies which can be employed for light beam manipulation. To this aim, precise control over particle size, shape, and polymorphic phases of crystalline TiO_2 NRs is required that can be achieved via various chemical routes. Among these methods, non-hydrolytic sol-gel techniques are quite popular in producing uniform TiO_2 NRs by employing structure-directing agents, known as ligand organic molecules.[92,95] In **chapters 2** and **3**, we will describe two successful procedures for synthesizing TiO_2 NRs that are based on non-hydrolytic sol-gel methods.

1.4 Outline of the thesis

This thesis covers the synthesis, characterization, and optimization of two different polymorphs of titania, namely anatase and brookite TiO_2 NRs, in the form of colloidal dispersions. In the next step, these material systems are investigated to develop switchable

colloidal LCs beneficial for adaptable optical applications. Furthermore, the possibility of charging these colloids in nonaqueous solvents are assessed in terms of electrophoretic measurements, which can be interesting in optical applications that are based on (di)electrophoresis effects.

In **chapter 2** the synthesis pathway of fairly monodisperse and colloidally stable brookite TiO_2 NRs in a scaled-up version of a literature procedure is discussed. We highlight the role of the surface ligands' density in ensuring more 'hard-rod-like' behavior for brookite NRs. Then, various self-assembled liquid crystalline structures formed at the liquid interface and in bulk are investigated by different microscopy techniques. We show nematic and smectic liquid crystalline phases, qualitatively analogous to the predicted ones for hard rod-shaped particles as well as tunable ordering within the smectic layers from hexagonal to tetragonal by tuning the brookite NRs' hard cores. In **chapter 3** another synthesis procedure but this time for anatase TiO_2 NRs is described via a single step nonhydrolytic sol-gel method. Possible mechanisms on the formation and the unusual growth path of the anatase NRs and its by-products, TiO_2(B) NPs, are discussed. Likewise, spontaneous formation of colloidal LCs in bulk and at the liquid interface is observed in anatase TiO_2 dispersions, making them a promising candidate for further assessment in electro-optical measurements.

In **chapter 4** we evaluate the isotropic dispersions of brookite and anatase TiO_2 NRs in external electric fields. We observe electric-field-induced birefringence, known as the Kerr effect or (para)nematic liquid crystalline phases, in external electric fields. We observe outstanding electro-optical responses in the dispersions of TiO_2 NRs where switching times are within $250\,\mu s$, one order of magnitude faster than commercial molecular LCs where the switching is based on the collective Freedericksz transition. Possible mechanisms contributing to the reorientation of the TiO_2 NRs are discussed. Moreover, we validate experimental observations on switching times and the refractive indices of TiO_2 colloidal dispersions, in terms of estimated birefringence, in various volume fractions by employing relevant theories.

In **chapter 5**, we investigate the possibility of charging such colloidal NRs in nonaqueous media. We employ two different nonionic surfactants in apolar and low-polar dispersions. Then, ion formation and electric charges are evaluated in terms of

electrophoretic measurements where formed reverse micelles by the added surfactants are indicated as important factors in charging these colloids. Finally, we rationalize our experimental results in the framework of acid-base charging theory for metal oxide particles in nonaqueous media.

1

2

Smectic Liquid Crystalline Titanium Dioxide Nanorods: Reducing Attractions by Optimizing Ligand Density

Crystalline titanium dioxide (TiO_2) semiconductor nanorods (NRs) feature several optical properties, such as birefringence combined with high refractive indexes and a wide bandgap precluding optical absorption in visible-light spectrum, making them attractive for many applications such as optoelectronics. Dispersing these NRs in suitable solvents creates inorganic liquid crystals (LCs) offering enhanced collective and orientation-dependent properties, which can additionally be utilized to manipulate optical behavior. Herein, a synthetic procedure from literature is scaled up and coupled with an important post-synthesis-treatment step such that self-assembled NRs dried onto a liquid interface and in bulk can be investigated. Comprehensive characterizations confirm the vital role of surface ligand density of the NRs in reducing the effects of attractions between them and thus increasing the range of volume fractions in which these dispersions can be exploited. Various symmetries (hexagonal or tetragonal) can be achieved in the smectic layers of NRs by tuning the aspect ratios of the NRs from 4.8 to 8.5. Experiments show that external fields such as shear flow or electric fields can easily either induce a reversible nematic order in isotropic dispersions or order existing LC phases over much longer regions, opening many opportunities to manipulate light for optical applications.

2.1 Introduction

Anisotropic colloidal particles have many properties different from spherical particles that can be exploited in different crystal and liquid crystalline phases that form by self-assembly (SA).[96–100] Liquid crystals (LCs) formed by inorganic anisotropic particles demonstrate tunable optical characteristics that are of great interest for optical and optoelectronic devices.[58–60] In addition to analogous properties exhibited by LCs formed by small molecules, inorganic LCs can be utilized not only as a model system to investigate molecular interactions and LC formation,[38,101–103] but can also greatly benefit from intrinsic properties of the dispersed building blocks.[104–107] For instance, nanocrystalline TiO_2 is of interest because of its high refractive indexes, ranging from n = 2.448 to n = 2.947, a wide band gap, and strong UV absorption combined with low light absorption in the visible-light spectrum.[108,109] In addition, crystalline TiO_2 nanoparticles (NPs) have been shown to be of interest as a (photo)catalyst or as catalyst support in heterogeneous catalysis.[87,109–112] Therefore, colloidal TiO_2 nanocrystals in different polymorphs have been synthesized through various chemical routes that exert precise control over particle size and shape, and nanorods (NRs) are well-studied among them.[92,109,110,113,114] In the formation of inorganic LCs from these NRs, attractions caused by van der Waals forces and/or depletion effects are to first order proportional to the particle size and can strongly affect the phase behavior. In recent works from our group, it was shown that spherical nanoparticles with van der Waals attractions that at contact have a magnitude of 0.5 kT with k Boltzmann's constant and T the absolute temperature, crystallized at the same volume fraction of 0.5 as hard spherical particles. However, stronger attractions of 2 kT already decreased the volume fraction to 0.11 and caused the systems to fall out of equilibrium.[115,116] We are interested in using the high refractive indexes of TiO_2 NRs for optical applications, for which it is advantageous if they can be used over as broad range of volume fractions as possible. This can be achieved if the (hard) particle shape dominates the phase behavior, while particle charges and interparticle attractions can be neglected.[41]

In recent years many groups working on the self-assembly of NPs have highlighted the importance of ligands on the interactions between NPs and thus on what type of colloidal (liquid) crystal phases, with different symmetries and interparticle spacings they

ultimately form.[117–129] The role of ligands on self-assembly was also recently reviewed.[117] Here we will only mention some typical examples of the role of ligands on SA as discussed in the literature and almost all of relevance to the present paper: Nanocrystals (NCs) have generally different facets with different surface tensions and thus different densities of ligands generally which has been shown to affect the SA behavior of the NPs.[117,118,122,123,130] For instance, in Ref.[122] the differences in the density of the ligands on different facets of the plate-shaped NPs was determined by density functional calculations by the Glotzer group and the differences that this caused in the interactions between the particles was found to be essential in subsequent simulations of the SA process to explain the colloidal crystal phases as observed by the Murray group. The interparticle distances and thus the interactions are also found to be influenced by the amount of solvent that is still present[124,125] or if an anti-solvent for the ligands is added.[126] The local density of ligands can even be affected by the colloidal crystal phase formed.[123] Excess ligands, even if added after completion of the SA, were also found to be able to affect interparticle spacings and the order in colloidal crystals already formed.[127] It is often the case that ligands are not bound covalently to the surface and thus can be replaced or removed by frequent washing steps[126,130–133] and conversely that the presence of excess ligands affects SA.[127,134] Additionally, addition of excess ligands above the critical micelle concentration can cause the formation of micelles which can induce depletion attractions between the NPs.[134] It is therefore also no surprise that temperature[72,77,128,135] and even pressure[129] have been shown to affect the ligand interactions and these effects have even been used to improve the order in already assembled colloidal crystals.[128] Varying the core size while keeping the ligands the same also affects the SA and interactions, [119,120,124,125] in such series sometimes the ratio between the core size and ligand length is related to a 'softness parameter'. Even in such a well-controlled series where core material and ligands are kept the same,[120] there are already many factors changing that may affect the interactions indicating how complex these interactions in general are: ligand density, which can be a function of the radius of curvature, van der Waals interactions, effective softness. In short, being able to treat the ligand layer as a thin layer that only slightly affects the hard particle size and is simply there to add steep repulsive forces is the exception in the SA of NPs, not the rule.

TiO_2 NPs are typically surface-functionalized with various commercially available alkyl-containing ligands to attain dispersibility in organic solvents.[95] Polymeric surfactants and dendritic macromolecules have also attracted significant attention due to their ability to better mask the strong van der Waals adhesion forces between the NPs and even shapes of the core particles that they are adsorbed onto.[72,136–139] Although polymer-functionalized TiO_2 NPs have been utilized as building blocks for lyotropic LCs, there are a few disadvantages to using these ligands.[76,77,140] Firstly, the synthesis of polymeric ligands adds more complicated steps as they are often not yet available commercially. Furthermore, thick surface coverage by polymeric surfactants on the order of a few nanometers considerably suppresses the effective refractive index of complete particles, which is not desirable for optical applications. Finally, the effective hard aspect ratio is reduced because the interactions between two surfaces with polymers adsorbed to them are generally (much) softer than for shorter ligands like oleylamine (OLAM) or oleic acid (OLAC) as used in this paper.

In this work, TiO_2 NRs were synthesized using a scaled-up version of a literature procedure.[110] We found that a post-synthesis-treatment step designed to fully saturate the surface with ligands reduced attractions and ensured more hard-rod-like phase behavior and thus maintained colloidal stability of the NRs at higher volume fractions in the apolar organic solvents used. The resulting crystalline NRs were mainly composed of the brookite phase of TiO_2 and ranged from almost 27.8 to 83.0 nm in length and 3.4 to 7.0 nm in thickness. Brookite NRs were monodisperse enough that smectic liquid crystal phases of as much as hundreds of layers formed easily both in bulk and onto a liquid interface in 2D. Textures of the LC phases formed in bulk were investigated by polarizing optical microscopy (POM) to identify the phases and these were consistent with what was observed by transmission electron microscopy (TEM) on the liquid interface assembled structures. Preliminary experiments showed that shear and electric fields could easily induce LC behavior in an isotropic NR dispersion and/or align existing NRs' LC phases

2.2 Results and Discussion

2.2.1 Characterization of Synthesized Brookite TiO_2 Nanorods

Figure 2-1 illustrates the formation of brookite TiO_2 NRs with tunable aspect ratios (short NRs (SNRs), medium NRs (MNRs), and long NRs (LNRs)) achieved through the seeded growth approach from anatase seeds (**for details, see Table 2-1 and Modified synthesis method and Nanorods formation mechanism in Supporting Information**).

Table 2-1 Properties of the systems of TiO_2 NRs used in this work. Here, L is the length of inorganic rods, T the thickness, σ the polydispersity, L/T the hard rod aspect ratio, and $(L/T)_{eff}$ the effective rod aspect ratios (where 3 nm was added to both L and T reflecting twice the length of the ligand molecules).

System	L [nm]	σL [%]	T [nm]	σT [%]	L/T	(L/T)eff	SA onto an interface (concentrations) [mg/ml]	Interparticle spacing [nm]	SA in bulk (volume fraction) [%]
SNR	27.4	9.6	3.4	8.7	8.1	4.8	1.0, 4.0, 8.0	as-synthesized: 1.2 ± 0.2 post-treated: 2.2 ± 0.3 with depletant: 2.7 ± 0.3	(dispersion I)a 25 % (dispersion II)b 32 %
MNR	42.2	10.3	5.1	12.0	8.3	5.6	1.0, 4.0, 8.0	as-synthesized: 1.1 ± 0.2 post-treated: 2.5 ± 0.4 with depletant: 3.6 ± 0.3	___
LNR	82.9	12.6	7.1	12.6	11.7	8.5	___	___	___

[a,b](dispersion I and II were prepared from as-synthesized and post-treated SNRs, respectively.)

The formation of the anatase seeds and brookite nanorods was confirmed by XRD analyses and high-resolution transmission electron microscopy (HRTEM) images (**Figure 2-1** and **Figures S1 to S3**). Presumably, some residual strain remained after the transformation from anatase to brookite, as it was observed in this and previous studies[110,130,141,142] that the synthesized NRs became increasingly bent as their length increased (while still maintaining a single crystalline nature as shown in **Figure S2**).

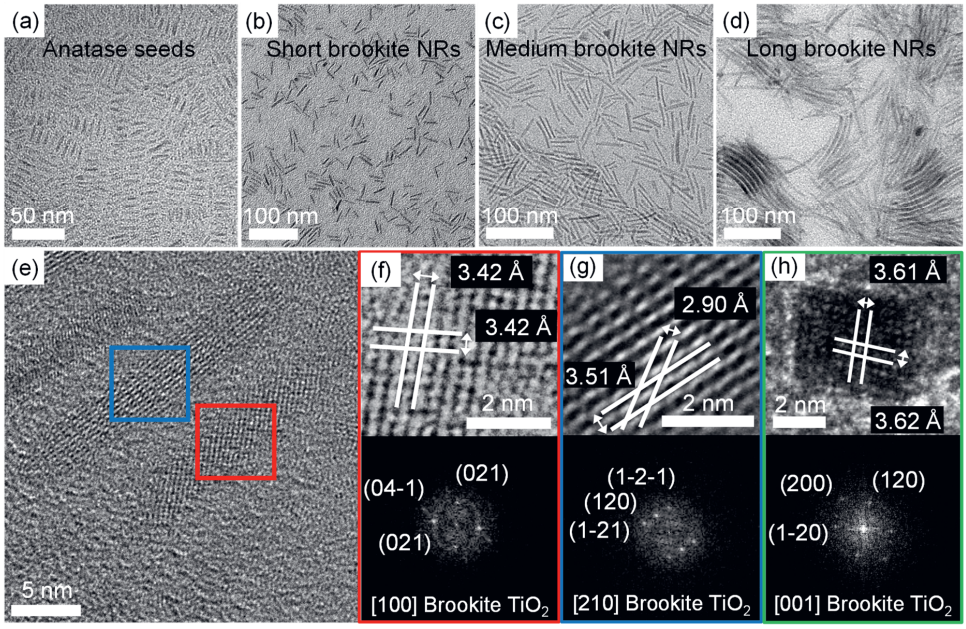

Figure 2-1.(a) Anatase seeds and (b-d) various brookite NRs with different aspect ratios (short- medium- long) synthesized by adding different amounts of titanium precursor. (e-g) High-resolution TEM micrographs of short TiO_2 NRs with the brookite crystal structure. (f and g) The red and blue insets highlight selected areas and their corresponding electron diffraction power spectra (FFT). (h) The green inset highlights a selected area containing one medium nanorod standing perpendicular to the image showing a rhomboidal cross-section and its corresponding power spectrum (FFT). In the selected areas of the micrograph, the distance between the identified planes is presented. In the power spectra, the indexed zone axes are displayed

While not mentioned in previous reports, dispersions of as-synthesized brookite NRs, even the smallest, quickly formed gel phases with a yield stress (small bubbles not rising in the dispersion) in any apolar solvent, i.e. hexane, chloroform or toluene. From these observations and the large discrepancies with expected hard rod-like phase behavior, we inferred that significant attractions between the NRs were responsible for the birefringent gelled states (**Figure S4a and b**). Similarly, a surface ligand density as high as possible was found necessary to guarantee crystallization in binary spherical nanoparticles, a process quite sensitive to the presence of attractions between the particles.[131] As it is known that both ligands used here (OLAC and OLAM) do not have extreme bonding

strengths,[126,131,132] we have put extra effort in saturating the surfaces of the NRs with additional ligands. Although density functional theory calculations have shown that OLAM plays the most important role in stabilizing {120} planes along the length of the brookite NRs,[130] we observed that OLAM by itself was insufficient. The NRs were synthesized in an excess amount of OLAM and most likely all the potential adsorption sites for OLAM are already occupied. However, those as-synthesized NRs still suffered from remaining attractions. In contrast, we found that post-treatment with excess OLAC was successful in improving the colloidal stability of the NRs. These post-treated NRs exhibited no gel formation even at high volume fractions (up to 32 vol% in toluene) for SNRs with an aspect ratio of 4.8 and dispersions were stable for months (**Figure S4**). We surmise that the main reason that OLAC is more successful than OLAM, is that while both ligands chemisorb to the surface of the nanoparticles, OLAC forms stronger monodentate carboxylate based bonding to surface sites of the transition metal oxide nanoparticles as compared to the (neutral) amine ligands.[133] This is further supported by the observation that post-treatment of the NRs with OLAM did not result in improved stability. After post-treatment Thermogravimetric analysis/mass spectrometry (TGA/MS, **Figure S5**) showed a clear increase in surface coverage of post-treated compared to as-synthesized SNRs (**Table 2-1**). From the weight loss and the average dimensions of the SNRs (L = 27.8 ± 2.6 nm and T = 3.4 ± 0.3 nm), measured from TEM images, the ligand density on the surface of as-synthesized SNRs was found to be around 2.3 molecules/nm^2 (**see ligand density calculations in Supporting Information and Figure S5**). Post-treated SNRs had a ligand density of approximately 2.7 molecules/nm^2. The difference in ligand density also translated into an almost 1.0 nm larger interparticle spacing of neighboring NRs lying parallel, as observed in TEM images (1.2 ± 0.2 nm as-synthesized SNRs to 2.2 ± 0.3 nm post-treated SNRs). Moreover, the post-treatment raised the temperature at which the ligands were completely decomposed by 47 ^{o}C. Hence, the enhanced thermal stability is attributed to a higher ligand density and, in particular, more monodentate bound carboxylates, which ensure higher dispersibility of brookite NRs.[131,133] Therefore, by coupling the post-treatment step with a scaled-up synthesis process, brookite NRs were synthesized which were better ligand capped so that van der Waals forces were better suppressed.

The presence of the vertically oriented brookite NRs imaged on the TEM grid in **Figure 2-1h** allowed us to estimate the relevant distances of closest approach for the calculation of van der Waals attractions between the inorganic cores. The cores were parallelepipeds with a square cross-section, for which theoretical expressions are available[143] (**See van der Waals interactions calculations in the supporting information and Figure S6**). **Figure 2-2** shows calculated van der Waals interactions between short and medium NRs for three different relative orientations and using the Hamaker constants of anatase and brookite (solid and dashed lines, respectively).

The results clearly show a significantly reduced attraction between the post-treated NRs. The strongest attractions occur when rods are perfectly aligned face-to-face, as expected. However, the calculated interactions are an overestimation as they assume perfectly smooth brookite cores with atomically flat interfaces. Any surface roughness would make the 'perfect' parallel approach between two rods much less efficient and reduce the actual van der Waals interactions (**Figure S2**).[144,145] Additionally, although parallel NRs experience remarkably larger van der Waals attractions, they are rare in an

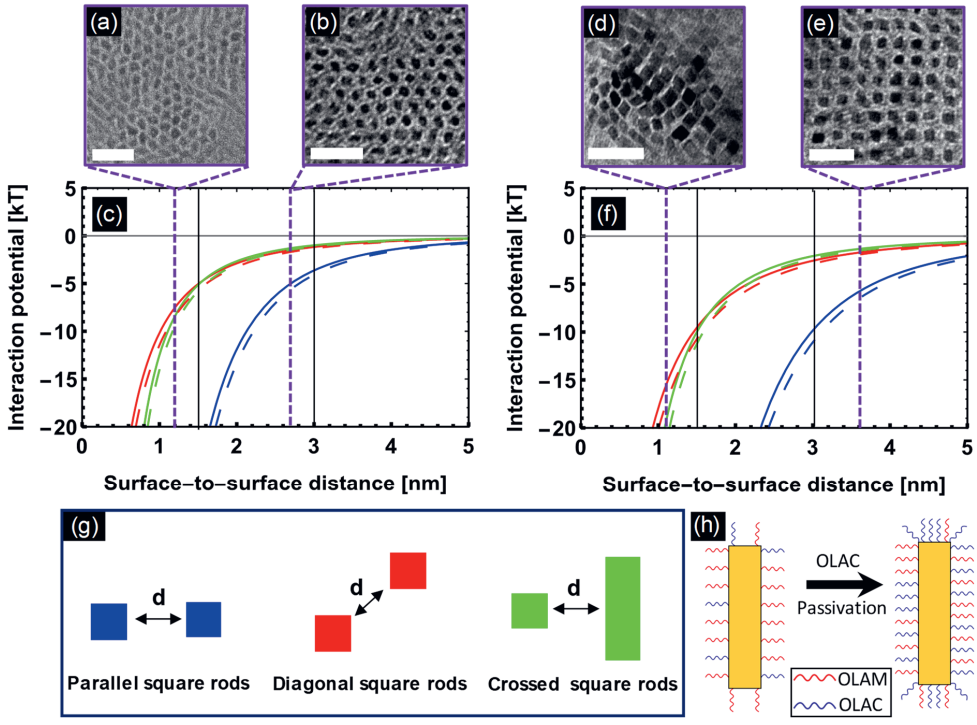

Figure 2-2. van der Waals interaction potentials between two *bare* TiO_2 NRs of anatase (solid lines) and brookite (dashed lines) phase, respectively, as well as schematic representation of a single nanorod before and after post-treatment step with OLAC molecules. In (a, b, and c) van der Waals potentials are calculated for short brookite and anatase NRs in which NRs encounter each other in parallel, diagonal, or crossed configuration shown in blue, red and green colors, respectively. Two TEM micrographs are presented which show the interparticle distances observed in this study. In (a) as-synthesized SNRs are self-assembled while in (b), post-treated SNRs are self-assembled by depletion attractions. Panels (d, e, and f) are the same as (a, b, and c) but for MNRs of brookite and anatase. Vertical black solid lines depict one and two times the effective ligand length of 1.5 nm while the vertical purple solid lines are corresponded to the interparticle spacing observed in the linked TEM images. The reduced spacing in (a and d) could possibly be linked to less ligand coverage around the as-synthesized NRs. (h) a sketch of proposed passivation of brookite NRs surface with OLAC molecules. Scale bars in (a,b,d, and e) are 20 nm.

isotropic rod dispersion since the majority of collisions will occur in more or less crossed and/or diagonal orientations resulting in less van der Waals attractions.

2.2.2 Self-assembly of Brookite TiO_2 NRs into Liquid Crystalline Phases onto a liquid interface

In order to investigate the phase behavior of the TiO_2 NRs, the toluene solvent of a dispersion of the NRs was allowed to evaporate, resulting in a self-assembled layer on top of an immiscible water phase. This technique to obtain a monolayer or multilayer assembly of colloidal crystals of NPs was made quite popular by the Murray group.[146,147] It has been shown that the static dielectric constant and surface tension of polar liquids utilized as subphases, can strongly direct the orientation of NCs superlattices formed on the liquid interface.[59,148,149] However, it should be mentioned that depending on the particular NP system, it is also possible that a 2D self-assembled layer also or instead forms on the toluene-air interface. Water, owing to its high polarity, high surface tension, and immiscibility with apolar inorganic solvents like toluene, was found to greatly enhance the formation of large horizontal liquid crystalline structures at the interface (**Figure 2-3a and d**) (for instance as compared to directly drying of the toluene droplets onto a TEM grid, results not shown). Nonhorizontal configurations of the TiO_2 NRs were formed when OLAC was added to the system, while other parameters that could affect the final morphology such as subphase, temperature, dispersing solvent, and monodispersity were kept the same (**Figure 2-3b, c, e, f**). OLAC and other ligands can form micelles above the so-called critical micelle concentration (approximately 0.08 M for OLAC in toluene) during the later stages of the drying process, which can induce depletion attractions between the colloidal NRs **Figure 2-3**.[150,151] Furthermore, these micelles could possibly be adsorbed onto the ligand layers and form 'bilayers'.[152,153]

Figure 2-3a and d show smectic LC layers for which the 1D crystalline order lies parallel to the local director of the rods in the plane of the TEM grid. For SA, 40.0 μL of NRs dispersion in toluene (4.0 mg/mL) was dropcast on to the water subphase (dispersion thickness was around 14.0 μm) and covered with a glass petri dish to slow evaporation. It is highly unlikely that the smectic layers, visible in **Figure 2-3a and d**, formed in bulk, but more likely either on the water surface and/or the toluene-air interface. For hard spherocylinders with effective aspect ratios of 4.8 (SNR) and 5.6 (MNR), the nematic to smectic transitions are at packing fractions of 0.50 and 0.47, respectively, although these

values are only an indication as they are for idealized monodisperse systems,[41] but the experimental polydispersity, reported in **Table 2-1**, modifies the phase behavior.[27,43,154–157] As indicated in **Figure 2-3d and Figure S7b and c**, defects such as edge dislocations, splay distortions, domains perpendicularly positioned with respect to the other layers, and point defects (e.g., interstitial NRs lying or standing between lamellae as transverse interlayer particle[27,45] or foreign differently shaped nanoparticles trapped as inclusions) can be observed. At lower concentrations of both SNRs and MNRs (1.0 mg/mL), only short-ranged local smectic ordered layers with the rods parallel to the grid were observed (**Figure S7d**). However, interestingly, by increasing the NR concentration up to 8.0 mg/mL, regions of vertically aligned NRs were found among horizontally aligned smectic layers. These were ordered occasionally with hexagonal symmetry or randomly packed similarly to structures observed for smectic-A phases (**Figure S7e and f**). Although we cannot presently prove this, we think it is likely that the vertically aligned layers were nucleated in bulk and were then oriented with the particles perpendicular to the TEM grids and liquid interface.

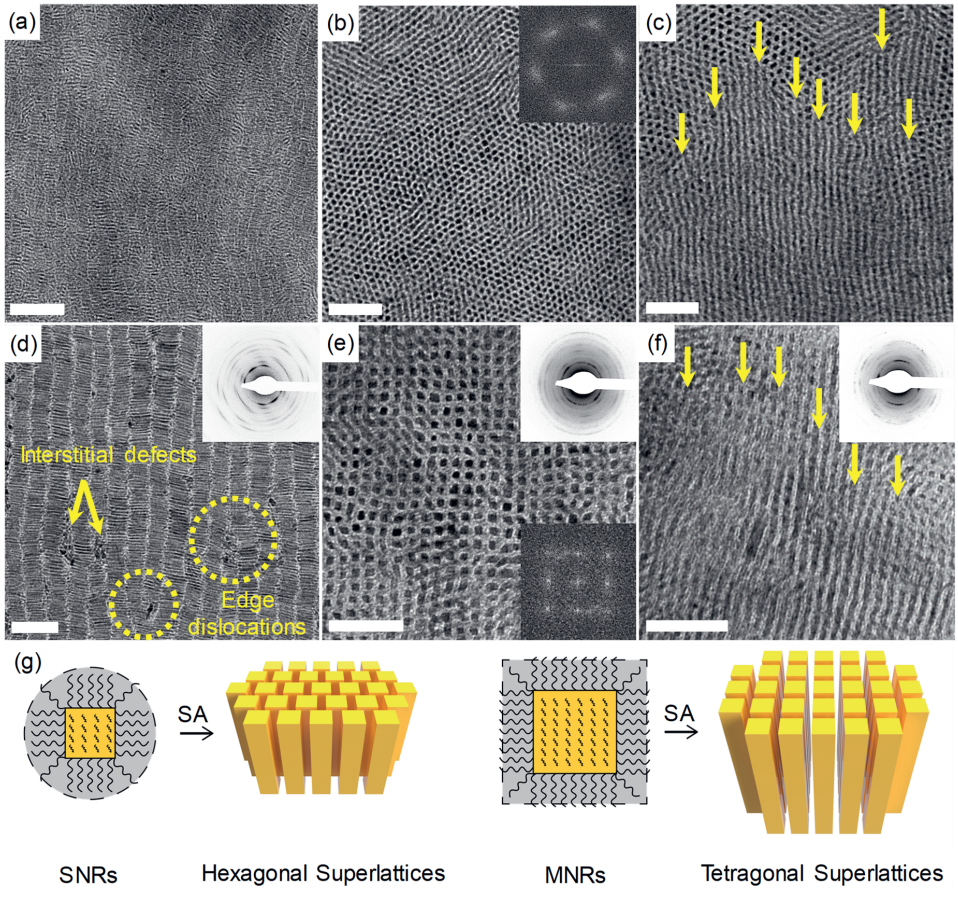

Figure 2-3. TEM micrographs of short and medium brookite NRs self-assembled at a liquid/air interface. (a) short NRs in a large smectic liquid crystalline domain formed without adding depletant. (b and c) Hexagonal superlattices of vertically aligned short NRs formed with added OLAC. Inset in (b) shows the corresponding FFT pattern. In (c) NRs have a tilted orientation, similar to rows of fallen dominoes (yellow arrows). (d) medium NRs in a large smectic liquid crystalline domain formed without adding depletant, demonstrating crystalline structural defects such as edge dislocations and interstitial defects. (e and f) medium NRs vertically aligned in tetragonal superlattices (see the corresponding FFT in e) with expanded ligand shell due to the addition of OLAC and formation of the bilayer at the NRs surface. (f) Tilted rods are observed in medium NRs similar to short NRs. (g) a sketch of proposed effective shape and aspect ratio and resulting influence on stable hexagonal superlattices for SNRs and tetragonal superlattices for MNRs. Scale bars in (a and d) are 100 nm and in (b, c, e, f) 50 nm.

Based on the shape of the inorganic core of the brookite NRs, we also investigated the role of the core shape on the ordering inside the smectic layers; examples of which can be seen in **Figure 2-1h** and **Figure S7g**. Brookite NRs are parallelepipeds growing along [001] direction while they are confined between {120} facets. Therefore, a rhomboidal shape could be recognized as the brookite core cross-section when the rods were imaged standing up on the TEM grid. The observed interparticle spacing for post-treated SNRs was around 2.2 nm, which was less than twice the length of the capping molecules (~ 3.0 nm). This spacing is a lower boundary as we assume the nanorods are standing perfectly straight and exactly parallel. If either of these conditions is not met, the projected distance becomes less than the actual local distance between the brookite surfaces. Nevertheless, the ligand shell was still relatively long in comparison with the diameter of these SNRs, giving them approximately a spherocylinder shape when the 'cloaking' effect of the softer ligand shell is taken into account and hence superlattices with hexagonal symmetry formed.[136] It is worth noting that if these had been truly hard/sharp parallelepipeds then different close-packed structures would be predicted.[158] We observed (**Figure 2-1** and **Table 2-1**) that during the size tuning step, not only do these parallelepipeds grow longitudinally, but they also become slightly thicker. Therefore, we investigated if this thicker core influences the symmetry in the smectic layers. As expected, at a higher concentration for the MNR system, small bundles of vertically aligned MNRs formed with a tetragonal symmetry, because the thickness of the MNRs cores was almost 1.5 times larger compared to the SNRs making the effective cross section of the MNRs much more square (**Figure 2-3g**). The interparticle spacing was around 2.5 nm (see **Figure S7h and Table 2-1**), but because this is a projected distance it is a lower limit of the local distances between the NRs.

In earlier SA experiments that were performed with a similar NR system on an ethylene glycol interface, it was found that SA into regularly structured smectic and smectic-like arrangements was only found to occur when an excess of OLAC was present in the NR dispersion.[159] This was attributed to a depletion-induced attraction that was necessary to induce SA. This is contrary to our finding using a water surface and is also not what is expected, as SA into smectic phases will also occur with more-or-less hard rods, except at higher volume fractions. Nevertheless, we studied the effect of OLAC micelles on the SA for our rods and observed large self-assembled structures with

maximum packing density and hexagonal and tetragonal symmetries for SNR and MNR systems, respectively (**Figure 2-3b and e**). However, there were noticeable increases in the interparticle spacings: 2.7 nm and 3.6 nm for the SNR and MNR systems, respectively, where the values for post-treated NRs without excess OLAC ligands were 2.2 nm and 2.5 nm, respectively. The excess OLAC ligand molecules clearly expanded the ligand shell around the NRs. Thus, the softness of these NRs increased. Nevertheless, the hard core for the MNR system was still found to determine a tetragonal symmetry in the smectic layers standing perpendicular to the TEM grids. This fact was also observed in simulations for hard parallelepipeds.[153] Under the same experimental circumstances where vertically oriented self-assembled NRs were found, some large domains of slightly tilted structures were always observed, similar to rows of dominoes fallen into a certain direction, which were also found in the literature before (**Figure 2-3e and f**).[134,150,159] Also, several other structures of interest were sometimes spotted such as overlapping bilayers of upstanding NRs with unique patterns, different vortexes, and linear 'rail-track' structures which are commonly observed in inorganic LCs and can be observed with their details in **Figure S7**.[59,160]

2.2.3 Liquid Crystalline Phase Behavior in Bulk

To examine the formation of various liquid crystalline phases in bulk, two dispersions were investigated (see **Table 2-1**): 1) **Dispersion I** from as-synthesized SNRs (ca. 25 vol.%) and 2) **Dispersion II** from post-treated SNRs (ca. 32 vol.%). Both dispersions were prepared from SNRs with an effective aspect ratio of 4.8 in which the effective ligand length of 1.5 nm was taken into account.

For **dispersion I**, the gel formation became evident from ca. 4.5 vol.% upward due to insufficient surface passivation of the NRs. A gentle shaking of this sample still could induce a transient birefringence, seen with the sample between crossed polarizers (**Figure S4b**), indicating that shear induced alignment and relaxation to an isotropic state were still possible. Although at low volume fractions **dispersion I** exhibited flow birefringence with relatively fast relaxation times up to a few seconds, at higher volume fractions (nearly 25 vol.%) the dispersion was highly viscous and relaxation became very slow (on the

order of a few days). In literature, it has been observed that heating may increase the stabilizing effect of ligand layers also for rod-like systems.[72,77,135] We similarly found that by increasing the temperature to around 65 °C **dispersion I** underwent the isotropic to nematic transition. **Figure 2-4a-c** shows POM images of **dispersion I** sheared between two glass slides.

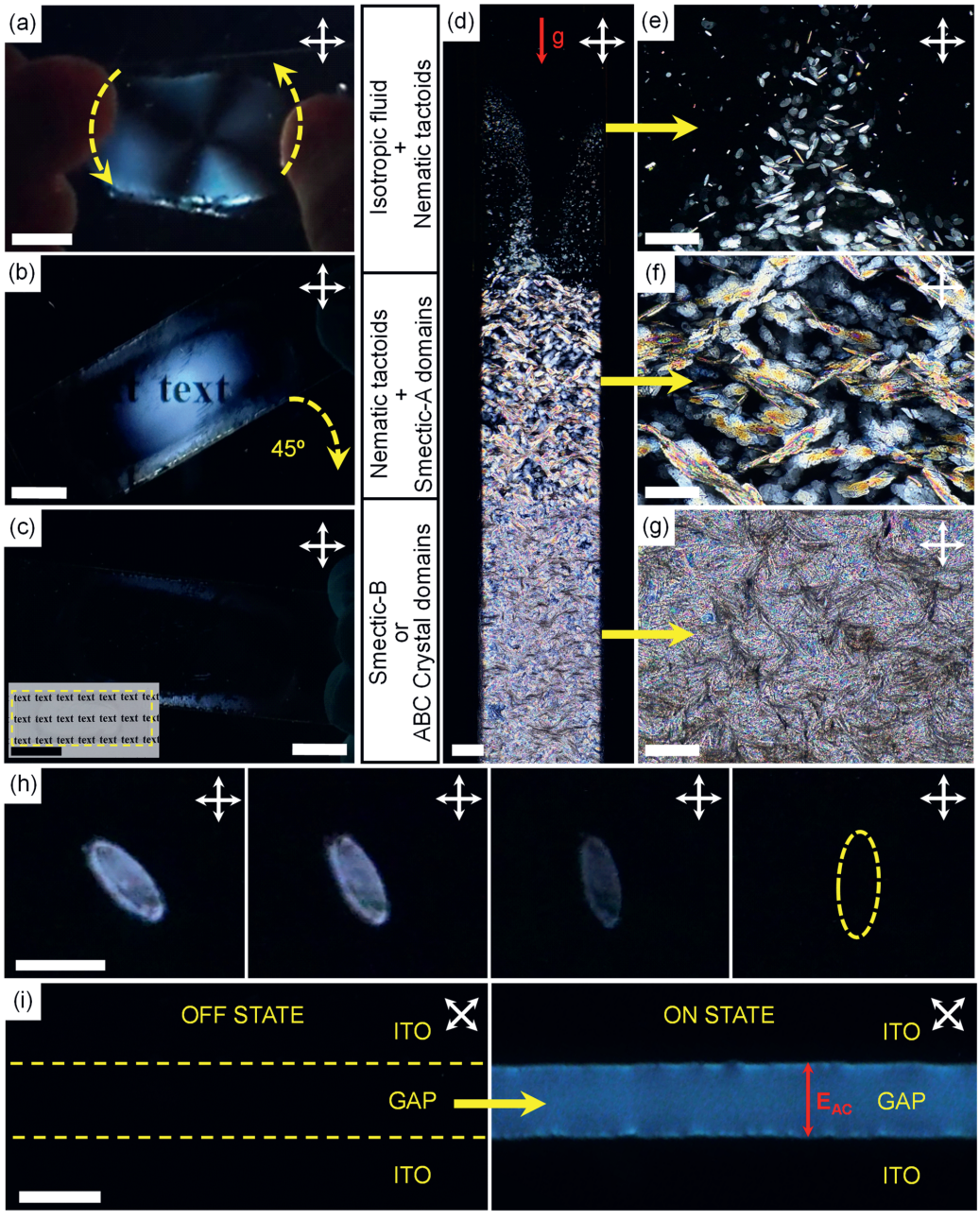
(a)
(b)
(c)
(d)
(e)
(f)
(g)
(h)
(i)
Isotropic fluid + Nematic tactoids
Nematic tactoids + Smectic-A domains
Smectic-B or ABC Crystal domains
g
45°
OFF STATE
ON STATE
ITO
GAP
E_{AC}

Figure 2-4. Crossed polarized images of **dispersion I** and **II** distinguish between isotropic (dark) and birefringent liquid crystalline phases. (a-c) large bright birefringent domains with typical nematic Schlieren texture from a few droplets of **dispersion I** placed between two glass slides and viewed between an LCD monitor and a polarizing sheet. The orientation of domains is simply manipulated by applying rotational shear forces (yellow arrows in a); and (b and c) A large nematic domain completely transmits or blocks light when it is oriented at 45° or 0° with respect to the polarizer axis, respectively. (d) a sedimenting sample of dispersion II in a capillary with three distinct regions. From top to bottom: (e) homogeneous nematic tactoids floating in isotropic fluid; (f) coexistence of nematic tactoids and smectic-A LC phase showing sharped-edge focal-conic Schlieren patterns; (g) a striated liquid crystalline texture with the highest packing density belonging to smectic-B and/or crystal phase. (h) a typical homogeneous tactoid formed in a sedimenting sample of **dispersion II** exhibiting a uniform change from the highest brightness to a perfect extinction when it is rotated from 45° to 0° relative to either of the polarizers (in the picture from left to right). (i) A large induced nematic-like domain formed from the isotropic **dispersion II** after an alternating current (2.5 V/μm, 1kHz) was applied across a gap in the indium tin oxide (ITO) substrate. Inset in h shows that the sample is transparent in unpolarized light. The scale bar in (a,b,c) is 1 cm, in (c-inset) is 2.5 cm, in (d) is 500 μm, in (e, f, g) is 50 μm, in (h) is 10 μm, and in (i) is 150 μm

Large brightly birefringent domains with typical nematic Schlieren textures are clearly observed. Transmitted light is completely blocked when the sample is oriented at 45° with respect to the polarizer axis (**Figure 2-4a-c**). The orientation, size and direction of domains with a locally similar orientation could simply be manipulated by applying rotational or uniaxial shear forces with shear rates applied on the order of half a second. As a result of rotational shear forces, a large disclination defect with strength +1, seen by 4 dark radial brushes (**Figure 2-4a**), annealed out the strain caused by the shear stress via bending the nematic director around.[160] As presented in **Figure 2-4i**, we also performed preliminary measurements using an external electric field (2.5 V/μm, 1 kHz). Such a field could induce a nematic LC phase reversibly in an isotropic liquid dispersion of the SNRs in **dispersion II** at 32 vol.%, thus creating a para nematic phase (**see movie in Supplementary Information**). It was also possible to affect the direction of the LC director in **dispersion I** (25 vol.%) where the gelled rest state was already a nematic. A full study of the phase behavior of this titania based LC forming model system will be presented in an upcoming paper with a focus on optical applications of this tunability.

In **dispersion II** with an initial concentration of 32 vol.% we observed equilibrium phase behavior reminiscent of that of hard rods as a result of post treatment of the rods (**Figure 2-4d-h**). **Dispersion II** was initially in an isotropic fluid state and was optically transparent as is expected for hard spherocylinders with an aspect ratio of 4.8 (**Figure S4c and d**). **Figure 2-4d** shows a POM image of the capillary after resting vertically for 15 days and demonstrates how the formation of a sedimentation equilibrium affected the phase behavior.[161] When the increased diffusional flux upwards created by the osmotic pressure increase balances the settling flux, an equilibrium concentration profile has formed in the gravitational field.[27,49,161] Although the unequivocal assignment of the various LC phases visible requires more detailed characterization techniques such as small-angle X-ray scattering (SAXS), here different types of LC phases were identified based upon comparing their LC textures to the predictions of computer simulations on the phase behavior of hard rods.[28,62,71,73,74] As shown in **Figure 2-4e**, nematic droplets, also known as tactoids, were seen to nucleate and freely float in the isotropic phase in the upper part of the capillary.[162] Owing to their anisotropic surface tension these tactoids were initially quite elongated with a fairly large aspect ratio of around 4.0 and thus almost needle-like with lengths less than 5 μm. Most of these gradually changed into prolate **Figure 2-4h**, a typical tactoid exhibited a uniform change from bright to perfect extinction when rotated from 45° to 0° relative to either of the polarizers, indicating that the tactoid was homogeneous with a uniform director field.[162] Further down, the volume fraction was higher and coalescence of the tactoids and formation of a biphasic region can be seen (**Figure 2-4f**). These elongated domains, nearly similar to chains of multiple tactoids, primarily showed nematic-like textures. During the tactoids' growth by coalescence, the elongated domains altered their morphologies resulting in sharp edges and birefringence induced interference colors due to variations in the thicknesses inside the domains. These sharped-edge focal-conic-like patterns are the characteristic texture of smectic.[27,49,163] Eventually, a striated LC texture was distinguished at the lowest part of the capillary belonging to the highest volume fraction which was quite distinctive from the texture of a smectic-A phase (**Figure 2-4f**). Based on the observed liquid crystalline structures with hexagonal ordering, two-phase coexistence of smectic-B and crystal at the bottom of the capillary might be still possible (**Figure 2-4g**). We surmise that although we have a

polydispersity of ca. 10% in length of the TiO_2 NRs, length fractionation and sedimentation-induced macroscopic separation still could provide a possibility to form a crystal phase as well.[27,157] Nevertheless, more detailed X-ray diffraction studies are required to further investigate the intriguing phase behavior.

2.3 Conclusions and outlook

In summary, brookite TiO_2 NRs were synthesized in a scaled-up version of a literature method[110] to such an extent that the liquid crystalline phase behavior of the resulting NRs dispersions could be investigated. These NRs are small enough not to strongly scatter light, but their high refractive indexes and anisotropies can be utilized to manipulate (polarized) light. We investigated various self-assembled liquid crystalline structures formed onto a liquid interface and in bulk by TEM and POM techniques. The NRs were highly crystalline, mainly composed of the brookite phase with tunable aspect ratios between 4.8 to 8.5. Longer brookite NRs were found to become slightly bend (roughly above a length of 50.0 nm and an aspect ratio of 6.0). We found that saturating the brookite NRs interface with OLAC ligand in a post-treatment step was crucial to minimize the detrimental effects of destabilizing attractions between the NRs, which is quite important for use of these systems in applications. Self-assembled structures of the brookite NRs were qualitatively similar to the nematic and smectic liquid crystalline phases predicted for hard rod-shaped particles as the attractions were minimized. Additionally, we could observe that the ordering within the smectic layers could be tuned from hexagonal to tetragonal (which reflects the shape of the brookite cores) by playing with the masking effects of the softer ligand outer layer with respect to the harder core dimensions. Finally, in preliminary experiments on the use of shear or an external electric field we showed that when attractions between the rods were minimized (para) nematic ordering could be reversibly induced in isotropic dispersions, while in dispersions that were already in an LC phase could be also easily oriented and switched. In follow up work we intend to use the possibilities that this nice model system provides in optical applications where the changes in the effective refractive index of the dispersion will be manipulated by external electric fields (e.g. by changing the orientation of the rods and/or the local concentration by (di)electrophoresis).[164] Additionally, we intend to structure these NR LC phases into droplets as well (as we already did earlier with much larger silica

rod-based systems also using external electric fields),[165] which would even significantly enlarge the possibilities to arrive at switchable optical devices such as lenses and diffusers.[166]

2.4 Experimental

2.4.1 Materials and modified synthesis method

Monodisperse brookite titanium dioxide (TiO_2) NRs were synthesized following a slightly modified and scaled-up version of the synthesis as described by Murray et al.[109,110] (**for details, see Modified synthesis method in Supporting Information**).

2.4.2 Post-treatment of brookite NRs

As-synthesized brookite NRs dispersed in toluene were mixed with OLAC in a 1:5 volume ratio, heated at 75 °C under vacuum, degassed for 15 minutes, and stirred under nitrogen overnight similar to the literature reported for iron oxide nanoparticles.[131] The resulting NRs were collected by precipitation with the antisolvent ethanol, centrifugation at 8000 rcf for 5 minutes and re-dispersion in toluene. This post-treatment procedure was repeated twice and ultimately the highly sterically stabilized brookite NRs were re-dispersed in toluene in dilute dispersions. Dispersions with the desired concentration were prepared by careful solvent evaporation. In the case of SNRs, concentrated dispersions of as-synthesized SNRs and post-treated SNRs were referred to **dispersion I** and **dispersion II**, respectively. (see **Table 2-1**)

2.4.3 Self-assembly

The liquid interfacial assembly of two-dimensional superlattices was performed by following the procedure as previously described in the literature.[146] In a typical process, brookite NRs from **dispersion II** in toluene (40.0 μL with concentration of 4.0 mg/mL) was dropped onto the surface of the water subphase in the glass petri dishes (30.0 mm in diameter and was half-filled with water) and slowly dried by placing a bigger glass petri dish over it. In the case of depletion mediated superlattices, OLAC (5.0 μL) was mixed with brookite NRs dispersion (5.0 μL with concentration of 5.0 mg/mL) in a vial of

toluene (400.0 μL). The mixture was sonicated for 5 minutes and 40.0 μL of the dispersion was dropcast on the water subphase. Once the NRs dispersion on the interface was fully dried to form the self-assembled layers, resulting films were transferred to carbon-coated 300 mesh copper TEM grids (Agar Scientific). The TEM grids were further dried in a vacuum chamber to remove residuals and used for microscopy analysis. To investigate liquid crystalline textures of self-assembled domains in bulk, a sedimentation experiment was performed as previously reported by Kuijk et al.[27] Briefly, a glass capillary (0.2 × 2.0 × 60.0 mm^3, Vitrocom) was filled with SNRs from **dispersion II** with an initial volume fraction of 32 %, effective length L = 30.8 nm, diameter D = 6.4 nm, and an aspect ratio of 4.8, in which the ligand length of 1.5 nm was taken into account. Then, the capillary was sealed using a two-component epoxy glue (Bison Kombi rapid) and left vertically to sediment. For **dispersion I,** at high concentrations (volume fraction of 25 %) a highly viscous mixture was observed due to the vdW attractions. Thus, the waxy state was suppressed by heating the sample on a hotplate and dropping the melted mixture between two microscope glass slides to investigate the LC effect by polarizing microscopy.

2.4.4 Characterization

X-ray diffraction analysis (XRD) was performed using a Bruker-AXS D2 Phaser X-ray diffractometer with Co Kα radiation (λ = 1.79026 Å) operated at 30 kV and 10 mA. Thermogravimetric analysis–mass spectrometry (TGA-MS) was performed using a PerkinElmer Pyris1 TGA. This technique was utilized to determine the pure inorganic (naked brookite SNRs) loadings and to verify the presence of organic ligands, which contributed to a mass loss at 350–500 °C and specific MS peaks. Two samples (5–10 mg) were prepared from the same batch of SNRs with aspect ratio 4.8, one of had been post-treated. For TGA measurements, samples were initially held at 150 °C to dry out the remaining water for 30 minutes which was followed by heating to 800 °C in an air or argon flow at a rate of 10 °C/min. TGA measurements were performed in duplicate. Transmission electron microscopy and selected area electron diffraction (SAED) of the brookite NRs were performed on an FEI Tecnai 20 electron microscope operating at 200 kV. The crystalline structures of the brookite NRs were measured by a high-resolution transmission electron microscope (FEI-Talos F200X electron microscope). Typically, at least 100 particles were counted to calculate the brookite NRs size distribution and

polydispersity index. Polarized optical microscopy (POM) was performed with a Leica DM2700P microscope equipped with crossed polarizers and images were recorded with a Nikon Z6 camera.

2.5 Acknowledgments

I would like to thank Dennie Wezendonk for the TGA/MS measurements, Peter Helfferich and Chris Schneijdenberg for technical assistance, Winnie Kong and Anna Nikolaenkova for their help with electric field experiments, Albert Grau-Carbonell for carrying out numerical calculations for van der Waals interaction potentials, Xiaobin Xie and Xiaodan Chen for HRTEM measurements, Dr. Matteo Cargnello for very useful advice on synthesizing long brookite nanorods, and Prof. Henk Lekkerkerker for fruitful discussions.

2.6 Supporting information

2.6.1 Materials

Titanium(IV) chloride (TiCl4, 99%), oleylamine (OLAM, 70%), oleic acid (OLAC, 90%), 1-octadecene (1-ODE, 90%), isopropanol, acetone, toluene were purchased from Sigma Aldrich and used as received. Ultra-pure water (Millipore systems) was used as a subphase for the self-assembly experiments at a liquid-liquid interface. All synthesis procedures were carried out either in an inert atmosphere using a standard Schlenk line setup or in a glove box.

2.6.2 Modified synthesis methods

In a typical synthesis of brookite NRs, OLAC (5.0 mL), OLAM (100 mL), and 1-ODE (100 mL) were mixed in a three-neck round-bottom flask and heated at 120 °C for 1 hour. Afterward, the flask was cooled down under vacuum to 60 °C, followed by switching to nitrogen and the swift addition of a stock solution of TiCl4 (15.0 mL), which was prepared in the glove box and consisted of $TiCl_4$ (0.2 M) and OLAC (1.0 M) in 1-ODE. Then, the solution was heated to 290 °C (heating ramp of ~20 °C min^{-1}) and held for 30 minutes to form anatase seeds. After seed formation, based on the desired length of the final brookite NRs, various amounts of stock solution were added to the solution by employing a KDS syringe pump system at a rate of 0.25 mL min–1. Here, to obtain short brookite NRs (inorganic size of 27.4 nm in length and 3.4 nm in thickness) and medium-sized brookite NRs (inorganic size of 42.2 nm in length and 5.1 nm in thickness), 10.0 mL and 50.0 mL of the stock solution were injected, respectively. In the case of long brookite NRs, the concentration of the main batch, stock solution, and also the injection rate were changed. Initially, the main batch (a mixture of OLAC (1.9 mL), OLAM (51.0 mL), and 1-ODE (12.0 mL)) was degassed at 120 °C for an hour. Then, it was cooled down under vacuum to 60 °C, and switched to nitrogen. In this step, (1.5 ml) from a new stock solution (consisted of $TiCl_4$ (0.5 M) and OLAC (1.0 M) in 1-ODE) was quickly added to the main batch and then (15.0 mL) of the same stock solution was injected dropwise by using a KDS syringe pump system over the course of 150 minutes at 290 °C. The heating mantle was then removed and the flask was allowed to cool to room temperature. Excess ligand and unreacted precursors were removed from the crude reaction product initially

by centrifugation at 6000 rcf for 10 min and then by redispersion and precipitation of the NRs using toluene and ethanol as a solvent/antisolvent pair. We chose toluene as a solvent in purification steps since it has a high refractive index which reduces the van der Waals attractions between the rods and also is a good solvent for OLAC. It has been shown that hexane has higher miscibility with oleic acid than toluene and can strip ligands off in the presence of antisolvent, while in toluene ligands prefer to remain at the surface of the NPs.[126] In the case of MNRs and LNRs, a size-selective precipitation process was needed to improve the length monodispersity. Therefore, the NRs were dissolved in toluene and acetone was added gently to the dispersion until the mixture became turbid. The mixture was then centrifuged at 3400 rcf for 5 min to isolate the nanocrystals as a precipitate. The supernatant was discarded and the length polydispersity improved for MNRs and LNRs up to 10.3% and 12.6%, respectively. Finally, the precipitates were redispersed in toluene at the desired concentration and will be referred to as-synthesized brookite NRs.

2.6.3 Nanorods formation mechanism

TiO_2 seeds were initially formed as a result of injecting the stock solution of $TiCl_4$ into the mixture of degassed solvents and surfactants. In the first step, OLAC reacted quickly with $TiCl_4$ which generates yellow titanium carboxylate complexes and hydrochloric acid.[167] Within the first time interval at 290 °C, aminolysis of titanium carboxylates occurred progressively in presence of surfactants leading to active monomers by hydroxylating of titanium (Cl_3Ti-OH), with concomitant release of oleyl amide as a byproduct.[109,141,168] Afterward, the monomers accumulated gradually to form the oxide network, forming the seeds, which follows classical nucleation theory.[169] Although in the original protocol anatase seeds were formed within 10 minutes at 290 °C, we found it necessary to hold the reaction at this temperature for 30 minutes to obtain monodisperse nanorods in larger quantities in the end. Therefore, seed nanocrystals were grown more uniformly to almost 15 nm in length (Figure S1) before they were grown to the size of interest in the size tuning step. As argued in the literature, initially formed anatase seeds trigger heterogeneous nucleation of brookite and promote subsequent growth of the nanorods in the brookite phase via a self-regulated phase-switching seed-catalyzed mechanism.[141] At the synthesis temperature, bulk rutile has been reported to be thermodynamically favorable compare to bulk anatase with a small Gibbs free energy

difference (2.01 kJ/mol at 563 °K).[170] Although already thermodynamic measurements have been performed on nano-sized phases of TiO_2,[171,172] the Gibbs free energies and the surface tensions for NPs as a function of shape with different crystal facets and carrying a surfactant are not known. Moreover, it is also not known if the shapes that are grown are local equilibrium structures or are (partially) also determined by kinetic factors and thus out-of-(local)equilibrium. We refer here to 'local' thermodynamic quantities knowing that all these NPs are certainly out-of-equilibrium with respect to one bulk phase of the same material. Nevertheless, Zhang and Banfield have shown that the transformation sequence among anatase, brookite, and rutile is size-dependent since the energies of the three polymorphs are sufficiently close that they can be reversed by small differences in surface energy. Their experimental evidence confirmed a crossover from anatase to brookite nanoparticles around 14 nm which is in a qualitative agreement with results presented in our work (Figure S1 and Figure S2).[141,171,173,174] Therefore, in addition to the thermodynamic arguments, we believe that differences in surface energy and kinetic factors such as surfactants contents could potentially change the relative stability of TiO_2 polymorphs within the reaction.

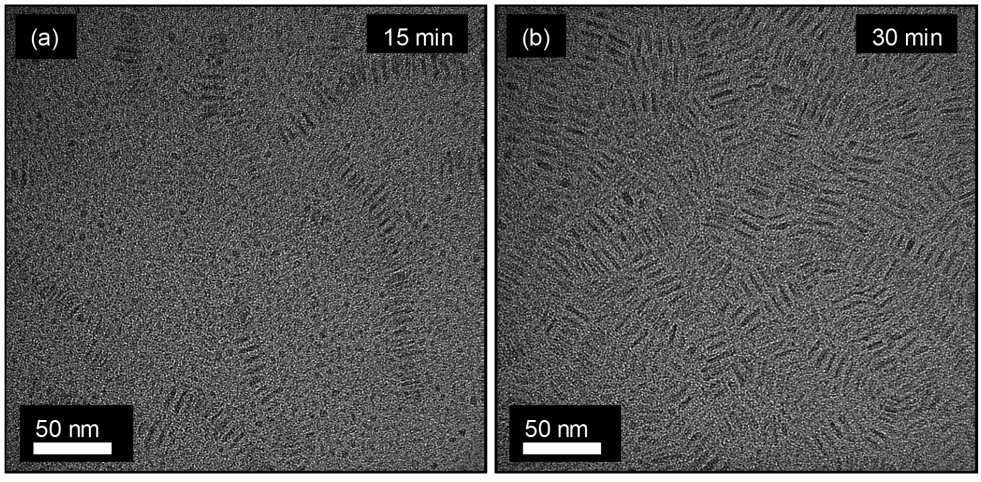

Figure S1. TEM micrographs of anatase seeds formation in different time intervals

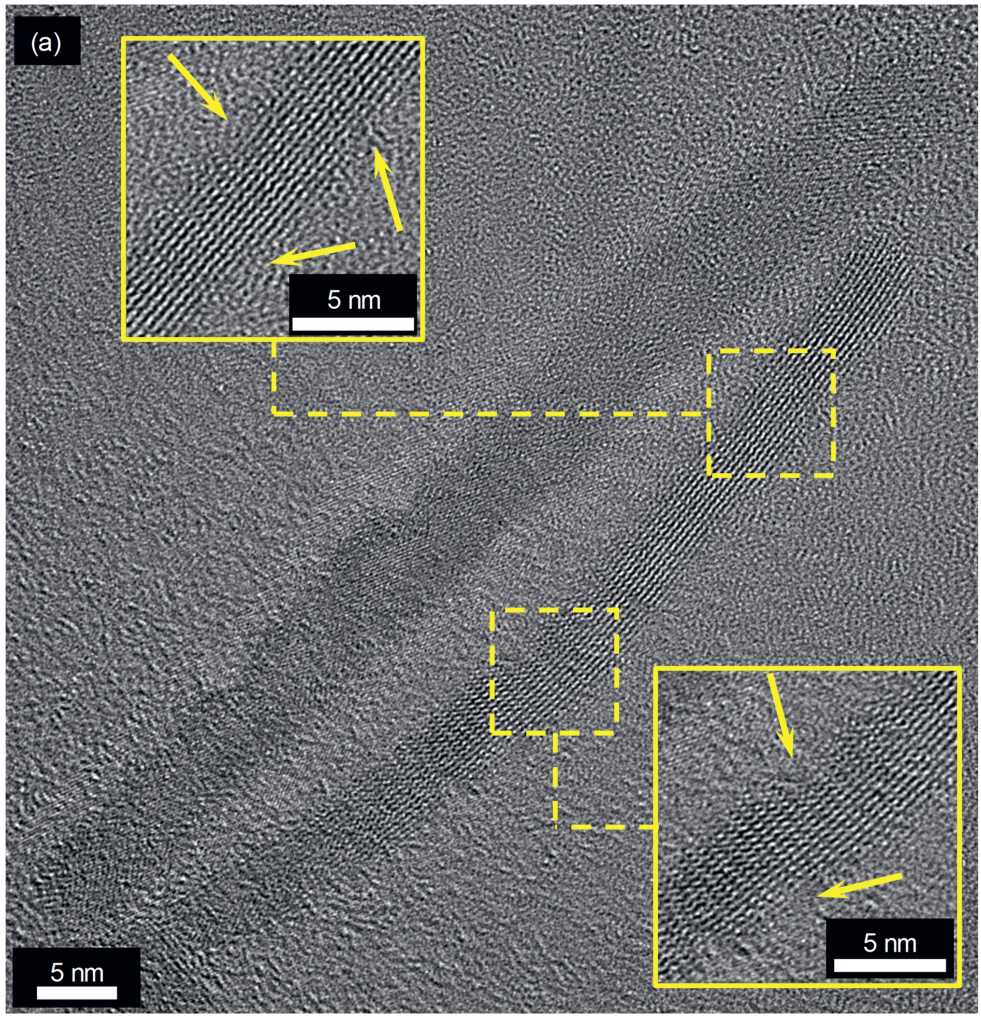
(a)
5 nm
5 nm
5 nm

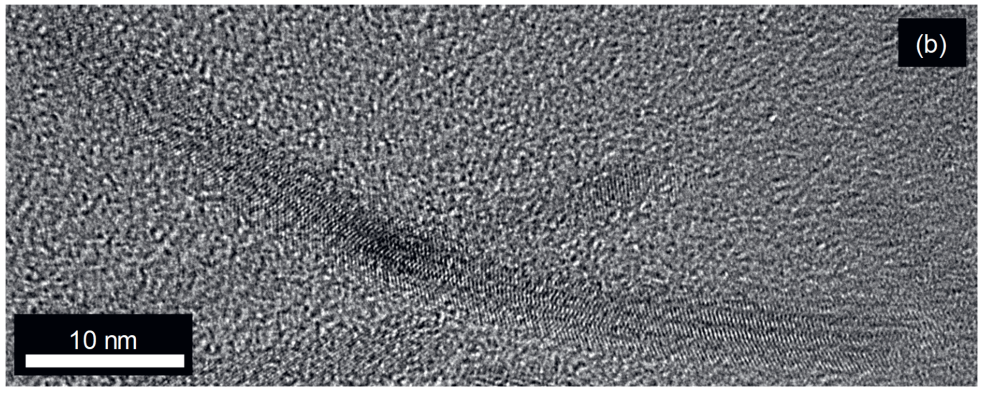
(b)
10 nm

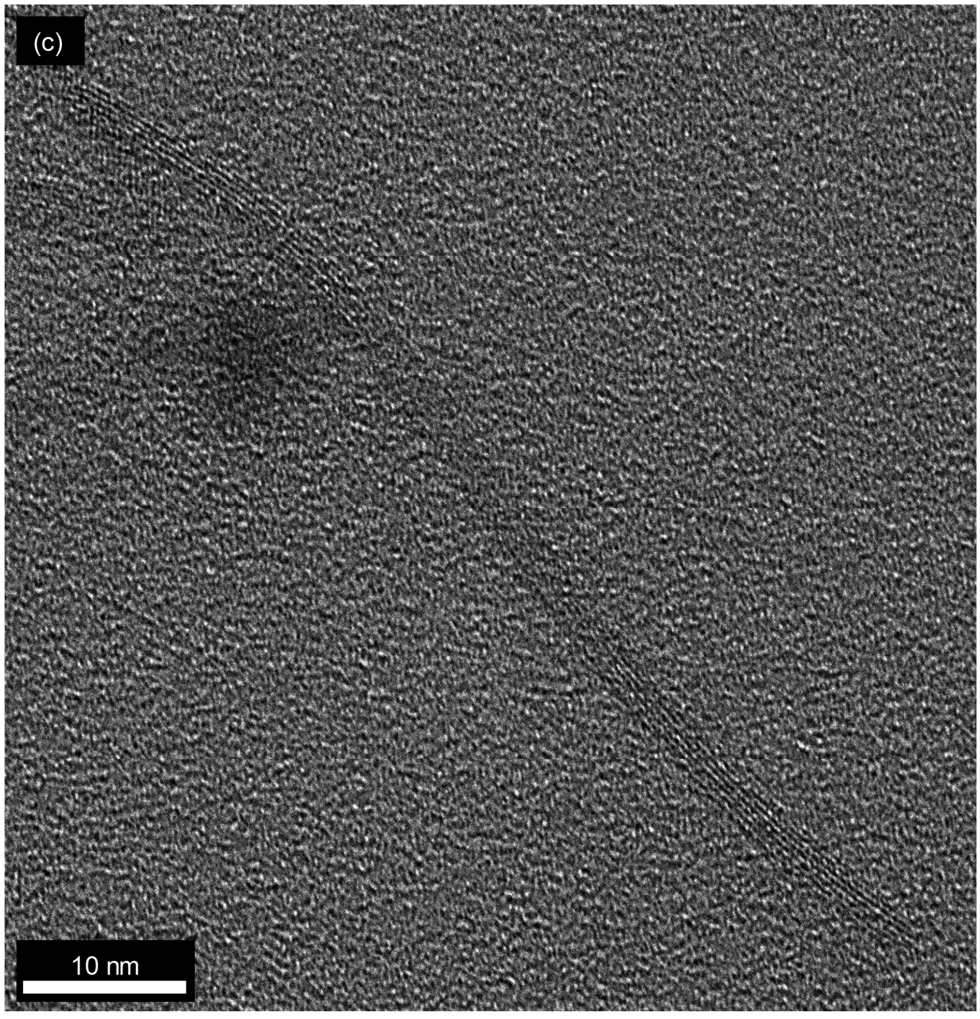

Figure S2. (a) HRTEM micrograph of MNRs showing a brookite core that does not have atomically flat interfaces. Surface roughness and some defects have been magnified for clarity and depicted with yellow arrows. Also, the MNRs in (a and b) become increasingly curved while still maintaining a single crystalline nature, and the longer the NRs were grown, the higher the curvature that was observed. In the case of LNRs (c), we could also observe some NRs with opposite curvatures in both sides due to some residual strain remained after the solid state phase transformation from anatase to brookite.

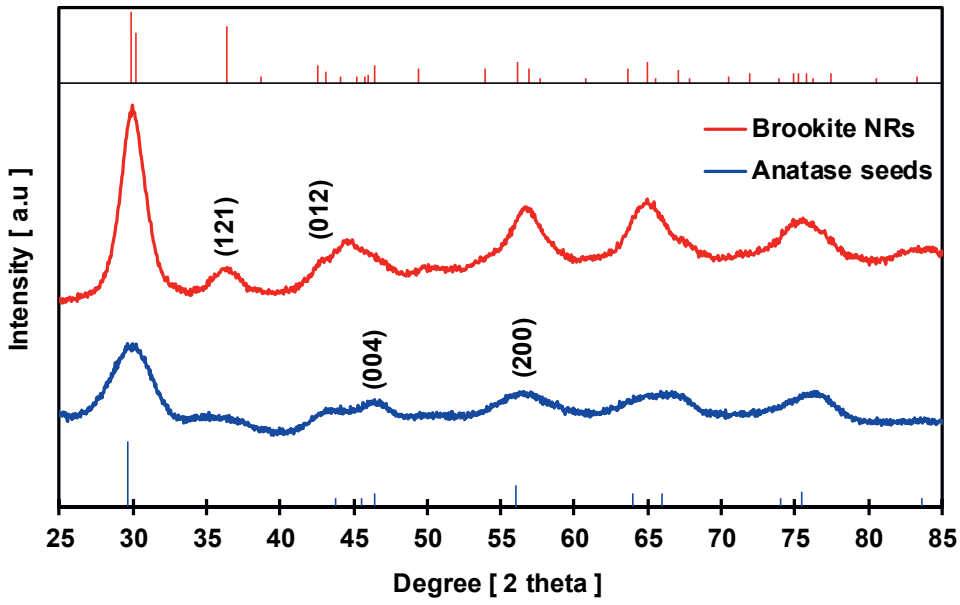

Figure S3. XRD patterns of synthesized anatase seeds and brookite NRs. Bragg peaks at 29.5°, 46.4°, 56.0°, 64.6°, 66.1°, and 75.6° indicate the existence of the anatase phase of TiO_2 (tetragonal, space group I41/amd, JCPDS No.01-086-1155). Due to low shape anisotropy in anatase seeds along the [001] direction, the intensity of the (004) peak is still slightly lower in comparison with that of the (200) peak which could increase by more anisotropic growth of anatase rods in their length.[141,168,175] XRD analyses clearly show the occurrence of new Bragg peaks at 35.9°, 42.3°, 43.5°, 49.7°, 56.8°, 64.9°, and 75.5° which are characteristic for the brookite structure (orthorhombic, space group Pbca, JCPDS No.029-1360). Furthermore, due to phase transformation from tetragonal to orthorhombic, a shift is observed of the anatase Bragg peak at 46.4° to 42.3°, which is matched with {201} planes in brookite and is in a nice agreement with HRTEM images (Figure S2 and Figure 1).

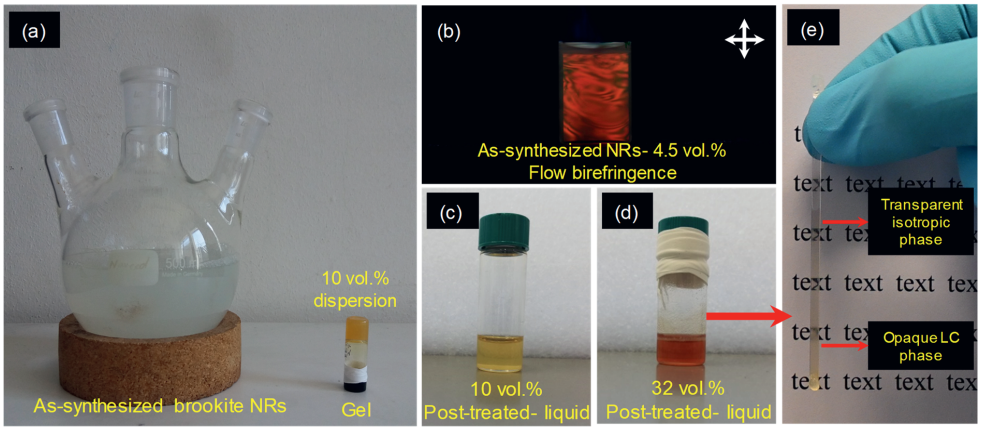

Figure S4. Dispersions of SNRs with an effective length L = 30.8 nm (σ_L = 9.6 %), diameter D = 6.4 nm (σ_T = 8.7 %), and aspect ratio of 4.8, in which the ligand length of 1.5 nm was taken into account. (a) as-synthesized SNRs and a 10.0 vol.% dispersion of them after purification step in toluene formed as a gel. (b) the same sample as (a) but at 4.5 vol.% volume fraction showing flow birefringence between cross polarizers. (c and d) post-treated SNRs at two different volume fractions of 10.0 vol.% and 32.0 vol.%, respectively. (e) a sedimenting sample of the same sample as (d) known as **dispersion II** in a capillary which was left standing vertically for 15 days to observe how the liquid crystalline phases formed in the sedimentation equilibrium. A transparent isotropic phase is observed near the top of the capillary, while the decreasing transparency down the height of the capillary indicates that denser liquid crystalline domains are formed. The capillary was sealed using a two-component epoxy glue on the both sides.

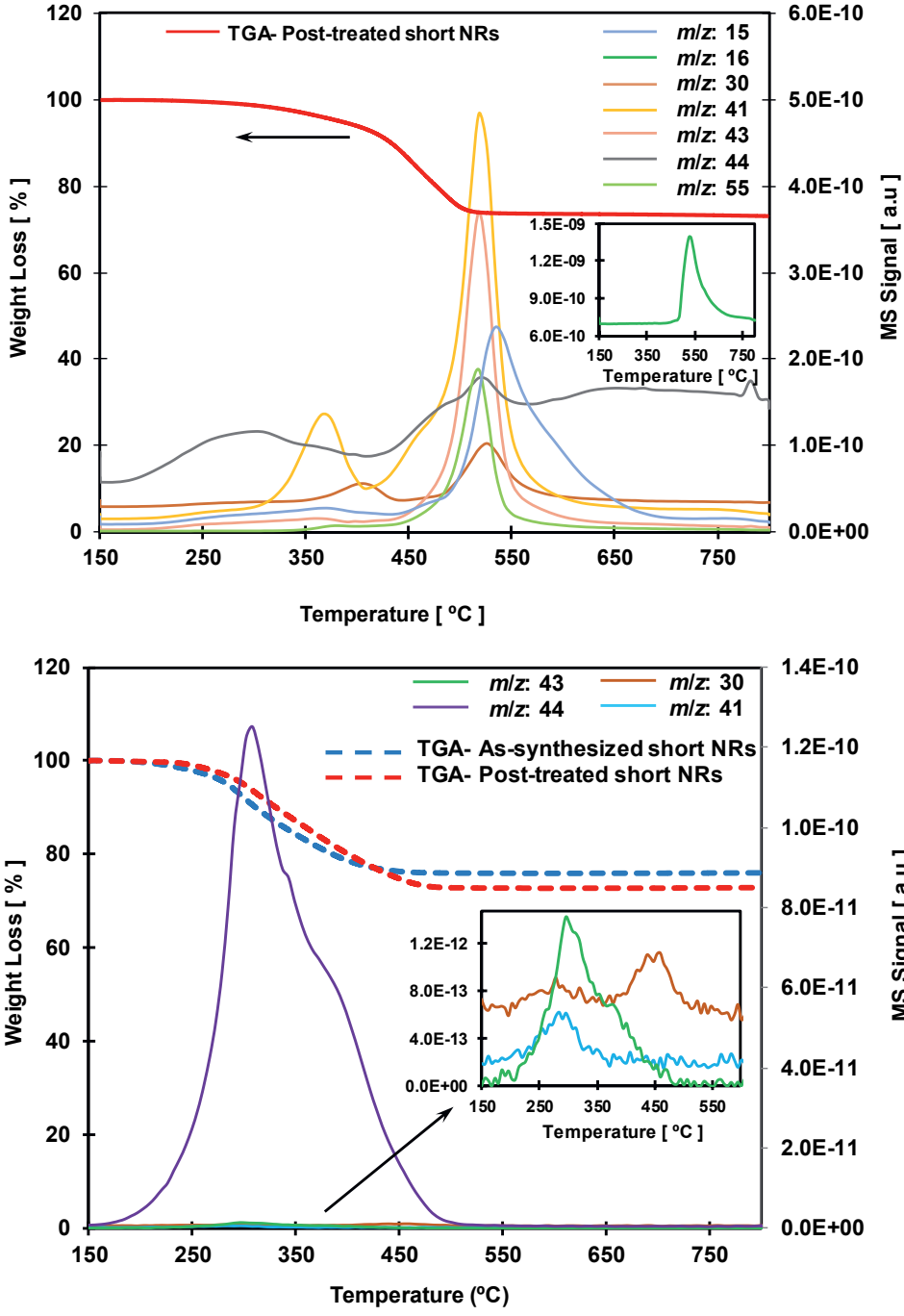

Figure S5. TGA/MS plots of as-synthesized and post-treated SNRs. (a) The decomposition of organic ligands occurred in an Argon atmosphere. The MS signals are

correlated to the decomposition of OLAM and OLAC to various hydrocarbon ions. The origin of the strongest signal with m/z value of 16 could be NH_2 and CH_4 from the decomposition of OLAM and OLAC.[176] Moreover, three other fragments were detected, including CH_4N, C_2H_3N, and C_2H_5N with m/z values of 30, 41, and 43, respectively, indicating the degradation of OLAM into fragments of various sizes.[177,178] In addition to CH_4N, the peak at m/z value of 30 could also attribute to oxidized carbon species such as CH_2O.[179] Other fragments such as C_2H_4O, CH_4N_2, $CONH_2$ may correspond to peak at m/z value of 44 and C_4H_7 to peak at m/z value of 55.[176,179] Thus, based on the TGA curve and MS signals, we could clearly see that OLAC and OLAM were both strongly attached to the surface of TiO_2 NRs and almost 0.39 mg of ligand has bound per 1.0 mg TiO_2 NRs. (b) The decomposition of organic ligands occurred under an airflow showing the CO_2 as the main fragment detected with an m/z value of 44. The weight losses of 24.0% and 27.2% are observed for as-synthesized and post-treated short brookite NRs, respectively.

2.6.4 Ligand density calculations

In order to do these calculations for short brookite NRs based on the TGA results, the following circumstances are considered:

- Short brookite NRs are considered as parallelepipeds with two equal short edges ($a = b$) and one long edge (c):

$$V_{single\ NR} = a^2 \times c = 323.68 \times 10^{-27} m^3$$

$$S_{single\ NR} = 2(a^2 + ac + ac) = 403.92 \times 10^{-18} m^2$$

Where $a = b = 3.4\ nm$, $c = 28.0\ nm$

- For as-synthesized short NRs, 5.524 mg of naked brookite NRs is left after TGA measurements. Considering $\rho_{brookite} = 4.13\ g/cm^3$, thus:

$$Number\ of\ short\ brookite\ NRs = \frac{V_{total}}{V_{single\ NR}} = 4.134 \times 10^{15}$$

$$S_{total\ for\ as-synthesized\ short\ NRs} = 1.669\ m^2$$

$$Amount\ of\ ligand\ burnt\ in\ TGA = OLAC + OLAM = 1.741\ mg$$

By considering the equal distribution of two types of ligands on the surface of the NRs ($50\%\ OLAC + 50\%\ OLAM$) and $M_{w,OLAC} = 282.46\ g$, $M_{w,OLAM} = 267.49\ g$, and $N_A = 6.02 \times 10^{23}$:

$$\rho_{\left(\frac{ligand\ molecules}{nm^2}\right)} = \frac{3.815 \times 10^{18}\ molecules}{1.669 \times 10^{18}\ nm^2} = 2.3\ \frac{molecules}{nm^2}$$

- For post-treated short NRs, 4.732 mg of naked brookite NRs is left after TGA measurements. Thus:

$$Number\ of\ short\ brookite\ NRs = \frac{V_{total}}{V_{single\ NR}} = 3.541 \times 10^{15}$$

$$S_{total\ for\ post-treated\ short\ NRs} = 1.430\ m^2$$

$$Amount\ of\ ligand\ burnt\ in\ TGA = OLAC + OLAM = 1.763\ mg$$

By considering the equal distribution of two types of ligands on the surface of the NRs ($50\%\ OLAC + 50\%\ OLAM$) and $M_{w,OLAC} = 282.46\ g$, $M_{w,OLAM} = 267.49\ g$, and $N_A = 6.02 \times 10^{23}$:

$$\rho_{\left(\frac{ligand\ molecules}{nm^2}\right)} = \frac{3.864 \times 10^{18}\ molecules}{1.43 \times 10^{18}\ nm^2} = 2.7\ \frac{molecules}{nm^2}$$

2.6.5 van der Waals potentials calculations for square rods

The van der Waals interactions between titanium dioxide nanorods with parallelepiped cross-sections were approximated by calculating the well-established van der Waals interactions between square cross-section rods (with perfectly flat faces) for three different configurations.[143] In the parallel square rods configuration (**Equation 1**), two rods are parallel with their length, flat faces toward each other. In the diagonal square rods configuration (**Equation 2**), the two rods are parallel with their length and edges facing each other. The angle between the flat faces and the vector between both particle edges is 45 degrees. In the crossed square rods configuration (**Equation 3**), the flat faces of the rods face each other but the long sides of the rods are at 90 degrees one to the

other. The schematic of the three configurations can be seen in Figure 2g in the main text.

$$V = -\frac{Al}{12}\left\{\frac{(w^2+d^2)^{\frac{3}{2}}}{w^2d^2} + \frac{(w^2+(d+2t)^2)^{\frac{3}{2}}}{w^2(d+2t)^2} - \frac{2(w^2+(d+t)^2)^{\frac{3}{2}}}{w^2(d+t)^2}\right\} + \frac{\pi q^2 \lambda l}{8}\left[\frac{1}{d^2} + \frac{1}{d+2t} - \frac{2}{d+t}\right] \quad (1)$$

$$V = -\frac{Al}{24}\left\{\frac{1}{dcos^2\theta sin^2\theta} + \frac{4[(q+t)^2+(p+w)^2]^{\frac{3}{2}}}{(q+t)^2(p+w)^2} + \frac{[(q+2t)^2+p^2]^{\frac{3}{2}}}{(q+2t)^2p^2} + \frac{[(p+2w)^2+(q)^2]^{\frac{3}{2}}}{(p+2w)^2(q)^2} + \frac{[(p+2w)^2+(q+2t)^2]^{\frac{3}{2}}}{(p+2w)^2(q+2t)^2} - \frac{2[(q+t)^2+(p+2w)^2]^{\frac{3}{2}}}{(q+t)^2(p+2w)^2} - \frac{2[(p+w)^2+(q+2t)^2]^{\frac{3}{2}}}{(p+w)^2(q+2t)^2} - \frac{2[(p+w)^2+q^2]^{\frac{3}{2}}}{(p+w)^2q^2} - \frac{2[(q+t)^2+p^2]}{(q+t)^2p^2}\right\} \quad (2)$$

$$V = -\frac{Aw^2}{12}\left[\frac{1}{d^2} + \frac{1}{(d+2t)^2} - \frac{2}{(d+t)^2}\right] \quad (3)$$

Where d is the closest distance between the surfaces of the particles, w and t are the dimensions of the rod's sides at the cross-section (in our case, w equals t and can be found as thickness 'T' in Table 1 in the main text), l is the length of the particles, A is the Hamaker constant, p is $dsin\theta$, q is $dcos\theta$. θ is defined as the angle between the flat faces and the vector between both particle edges.

The Hamaker constants of brookite and anatase titania where 50.11 k_BT and 44.56 k_BT, respectively. The Hamaker constants were approximated via their refractive indexes and the expression for the symmetric case of two identical phases (Phase 1) interacting across a different medium (Phase 2) given by **Equation 4** (in units of k_BT):[145]

$$A = \frac{3}{4}\left(\frac{n_1^2 - n_3^2}{n_1^2 + n_3^2}\right)^2 + \frac{3h\nu_e}{16\sqrt{2}k_B T}\frac{(n_1^2 - n_3^2)^2}{(n_1^2 + n_3^2)^{\frac{3}{2}}} \quad (4)$$

Where n_1 and n_3 are the refractive indexes of the two different phases, T is the absolute temperature, k_B is the Boltzmann constant, ν_e is the plasma frequency of the free electron gas (often is taken to be equal to 3×10^{15} s^{-1}) and h is the Plank constant.

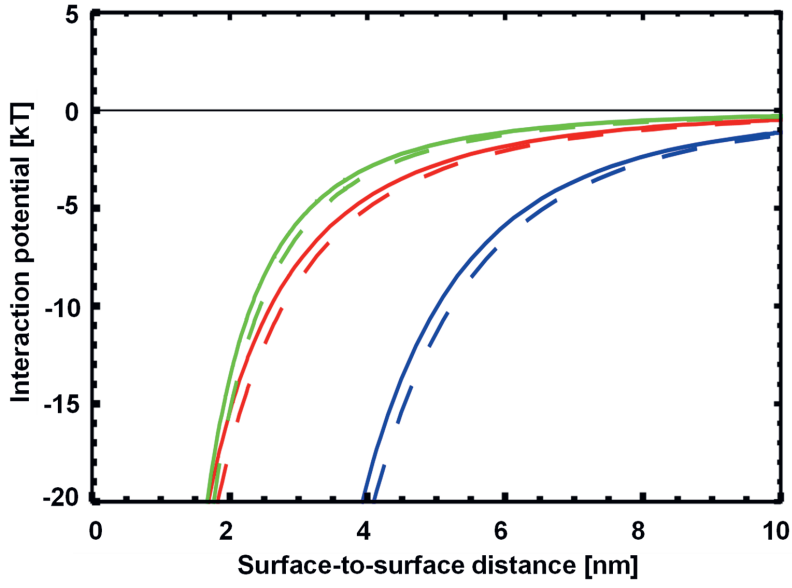

Figure S6. van der Waals interaction potentials between two bare long TiO_2 NRs are plotted such that solid and dashed lines are associated with anatase and brookite phase, respectively (see Table 2-1 for more information about LNRs). The potentials are calculated for both long brookite and anatase NRs where NRs encounter each other in parallel, diagonal, or crossed configurations shown in blue, red, and green colors, respectively.

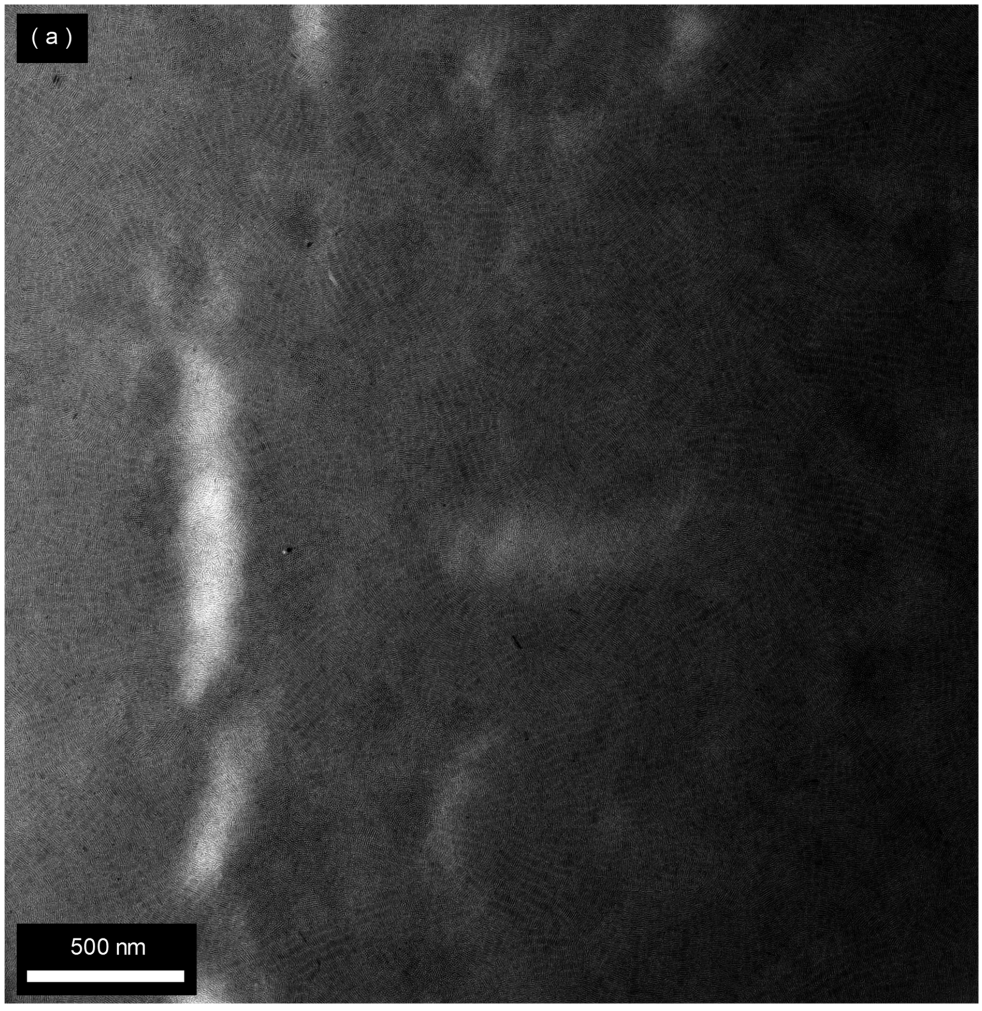
(a)
500 nm

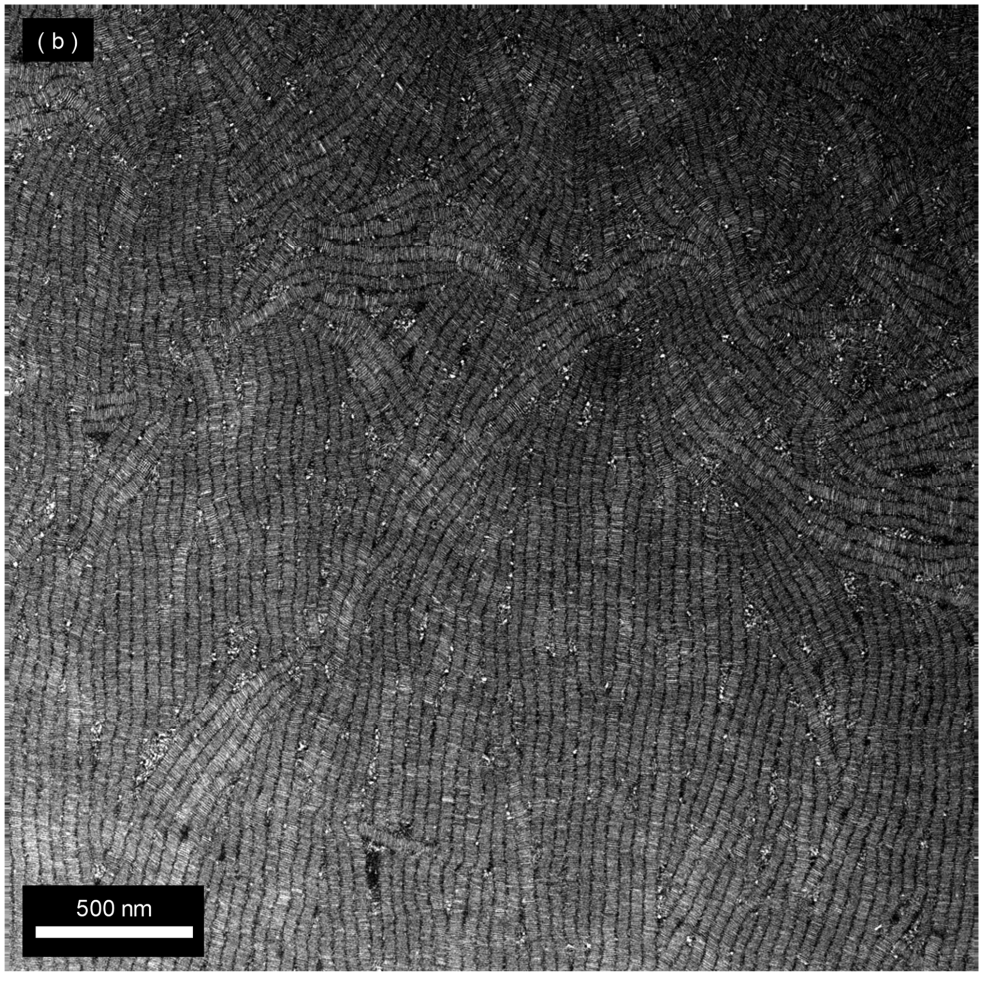
(b)
500 nm

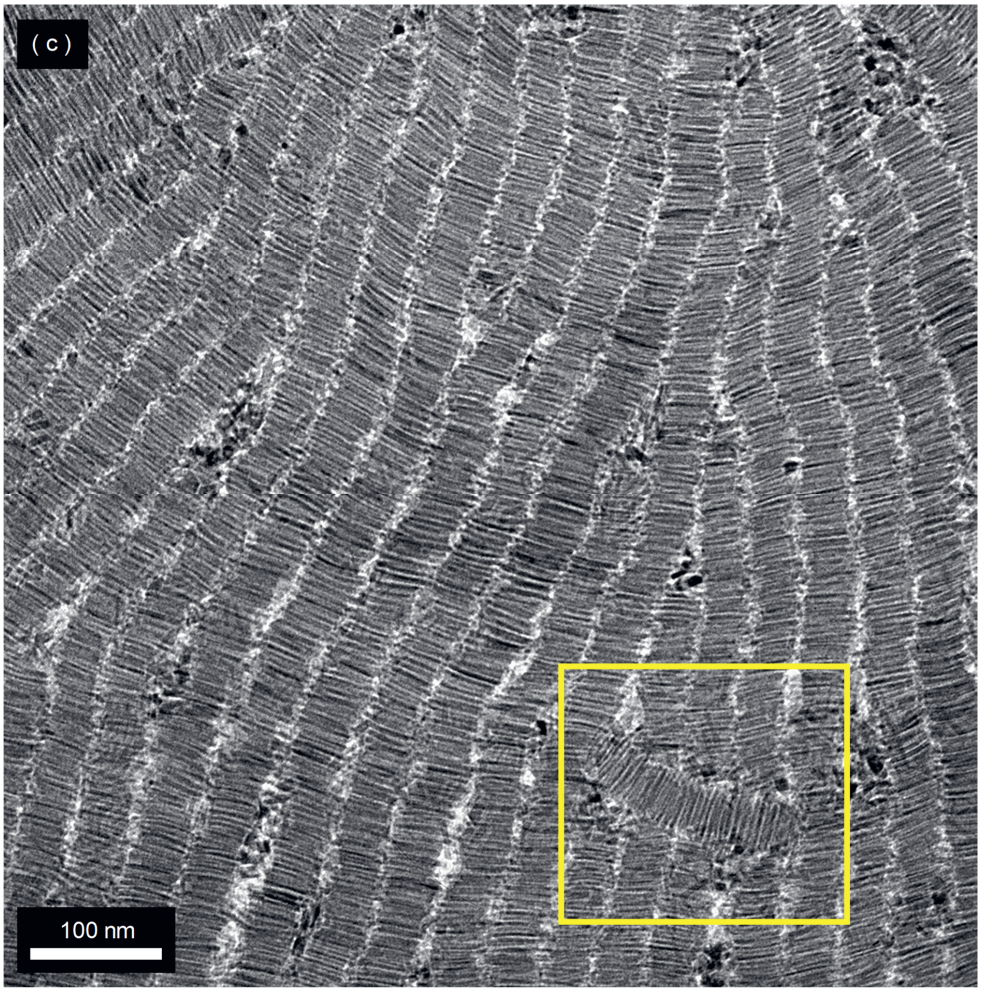
(c)
100 nm

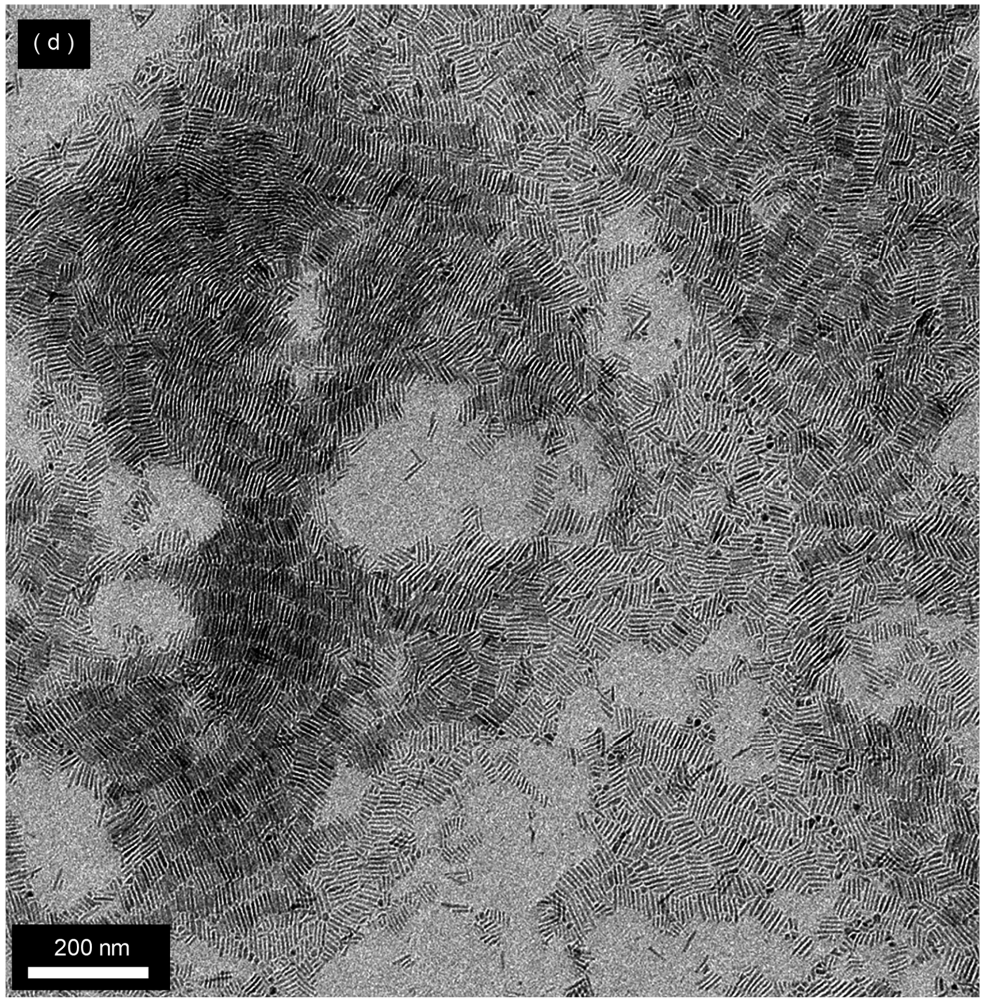
(d)
200 nm

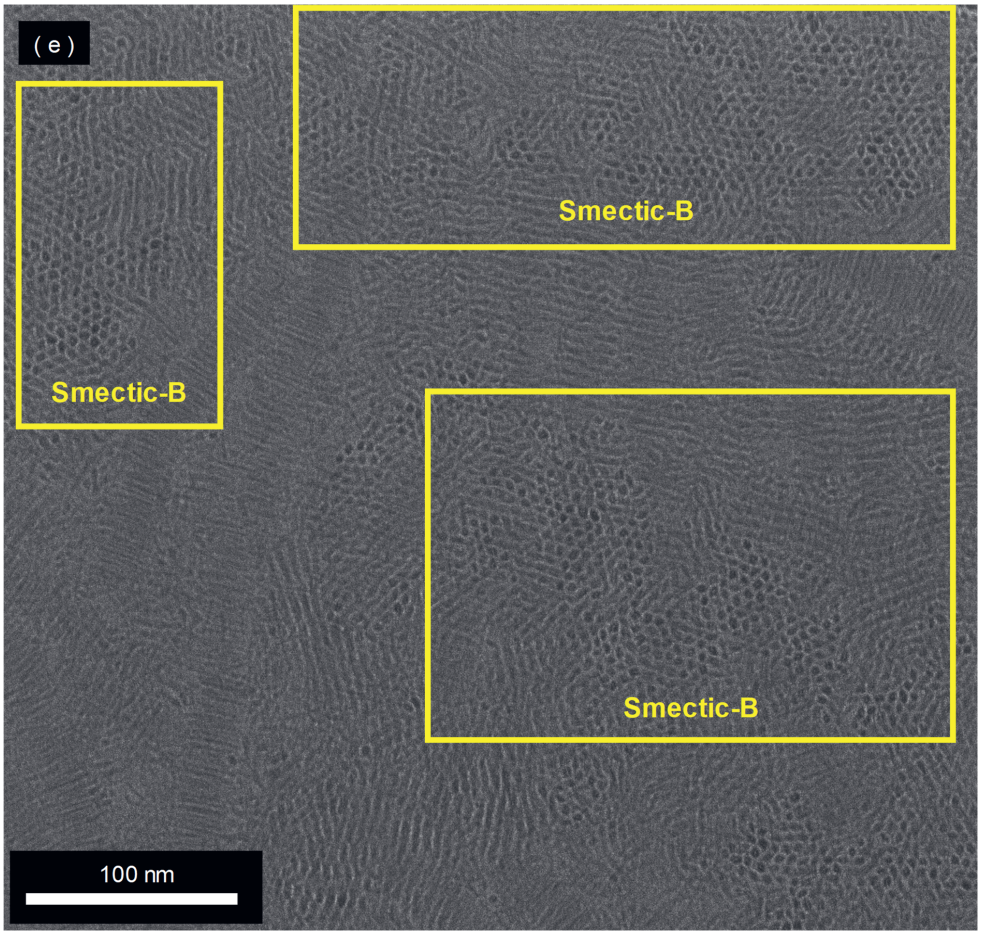
(e)
Smectic-B
Smectic-B
Smectic-B
100 nm

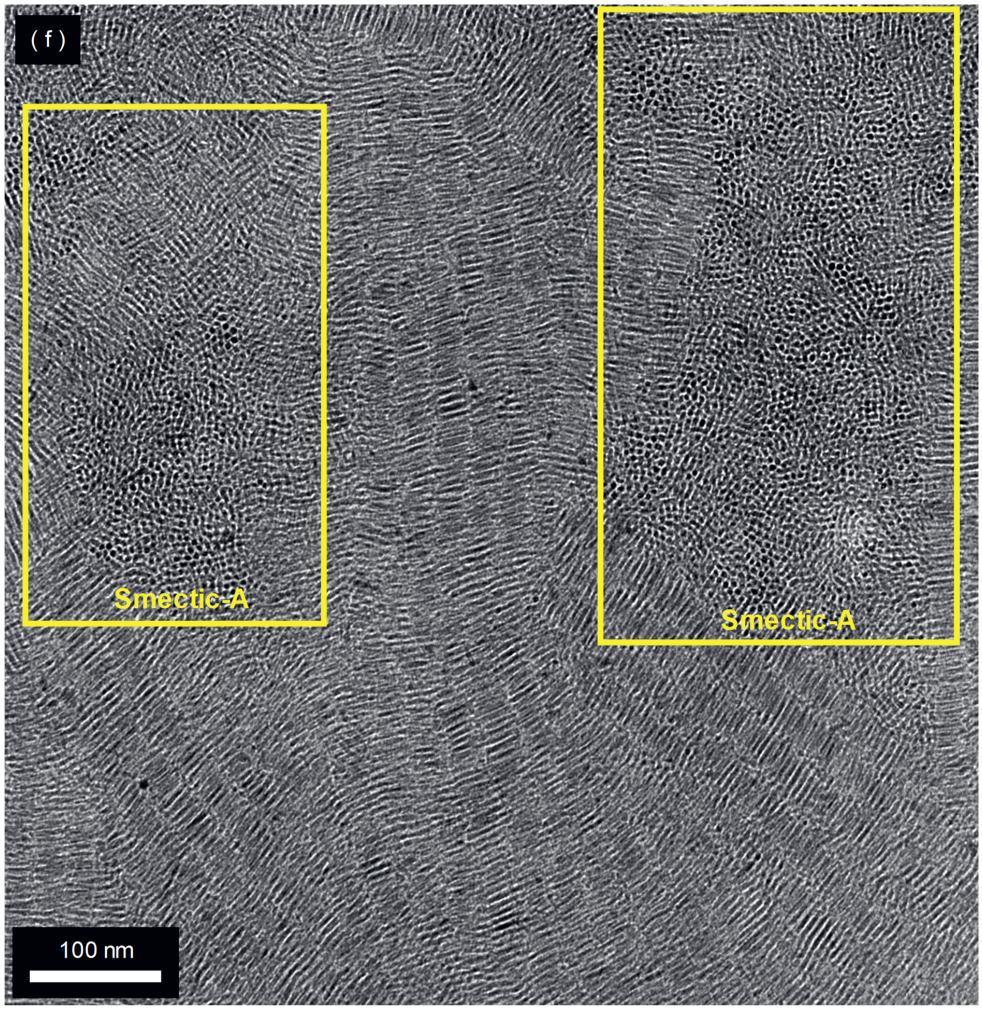
(f)
Smectic-A
Smectic-A
100 nm

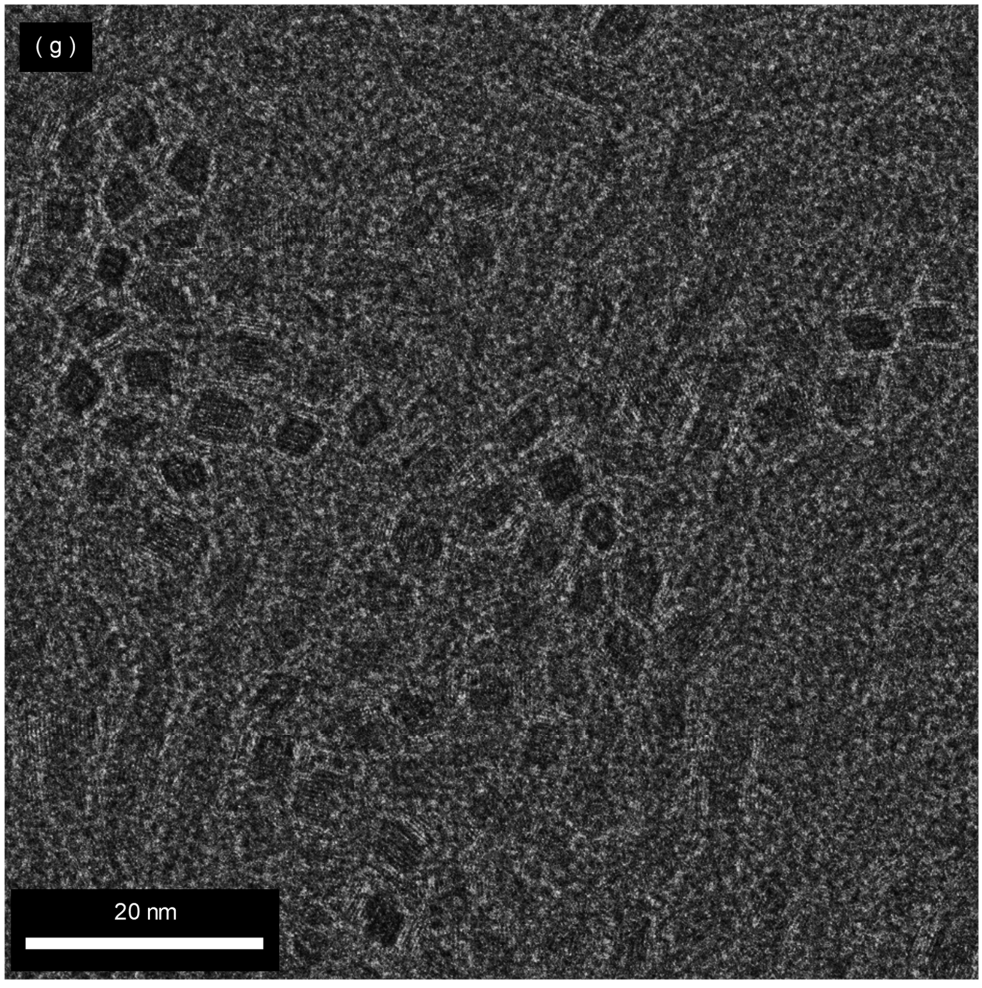
(g)
20 nm

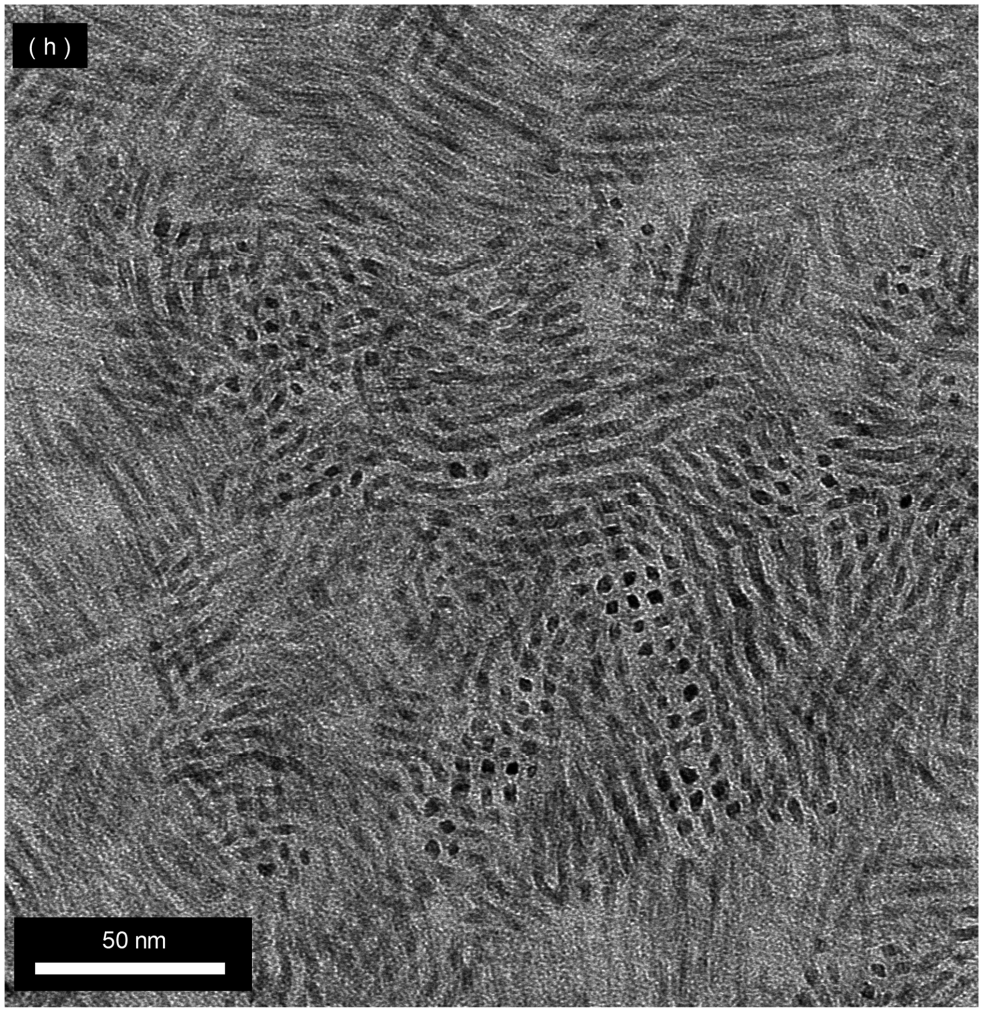
(h)
50 nm

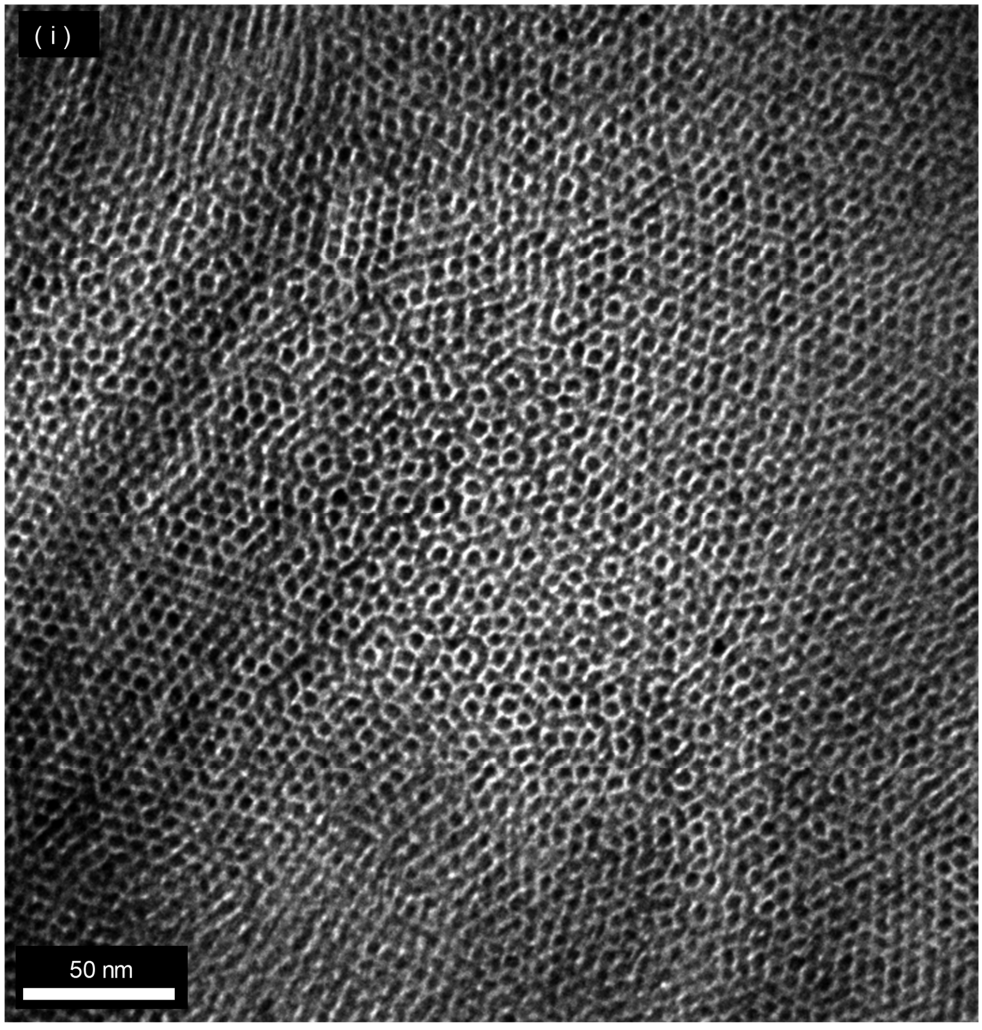
(i)
50 nm

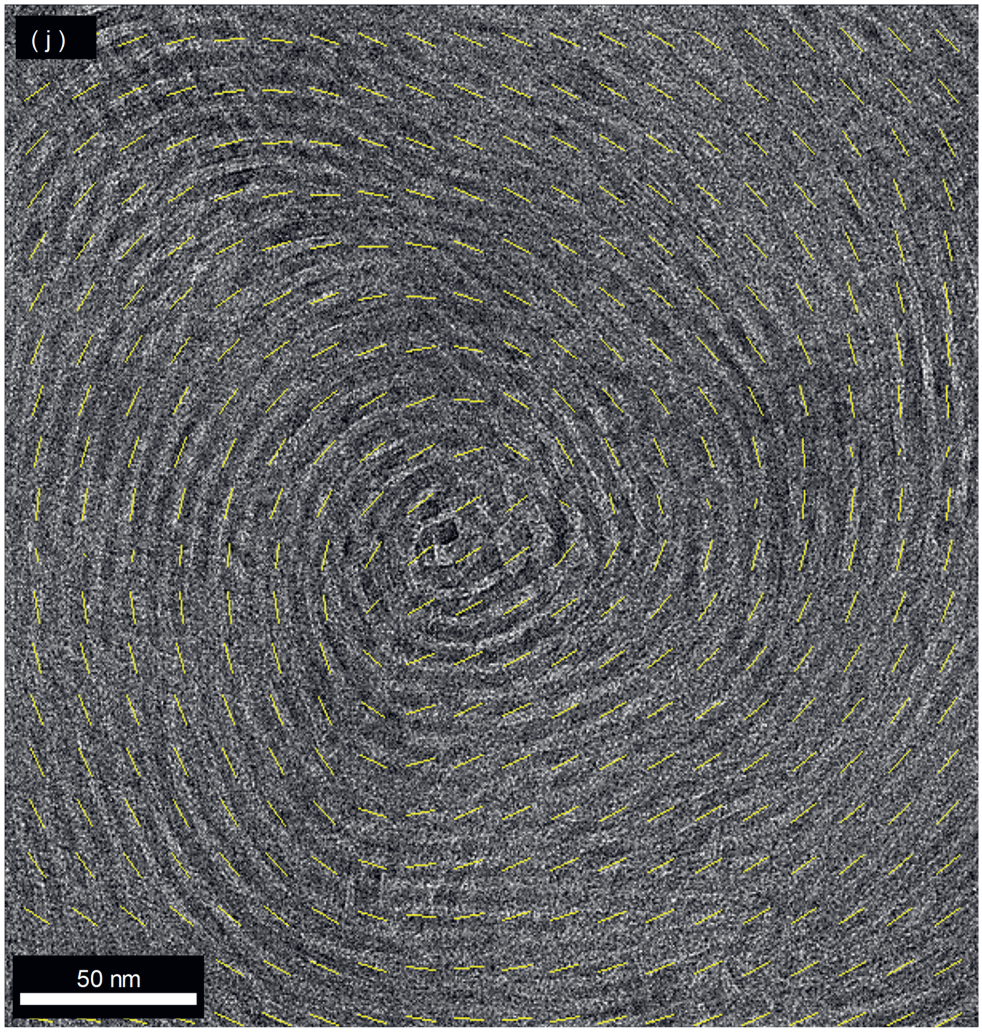
(j)
50 nm

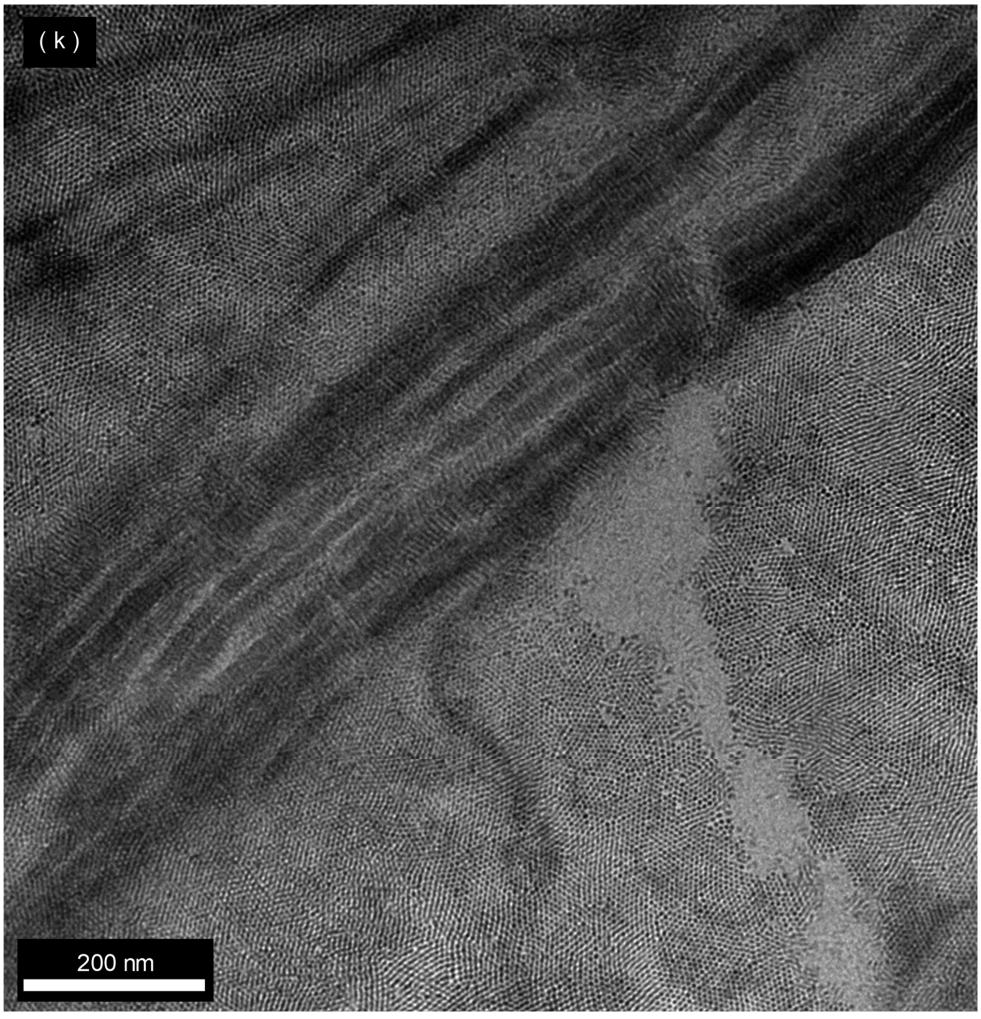
(k)
200 nm

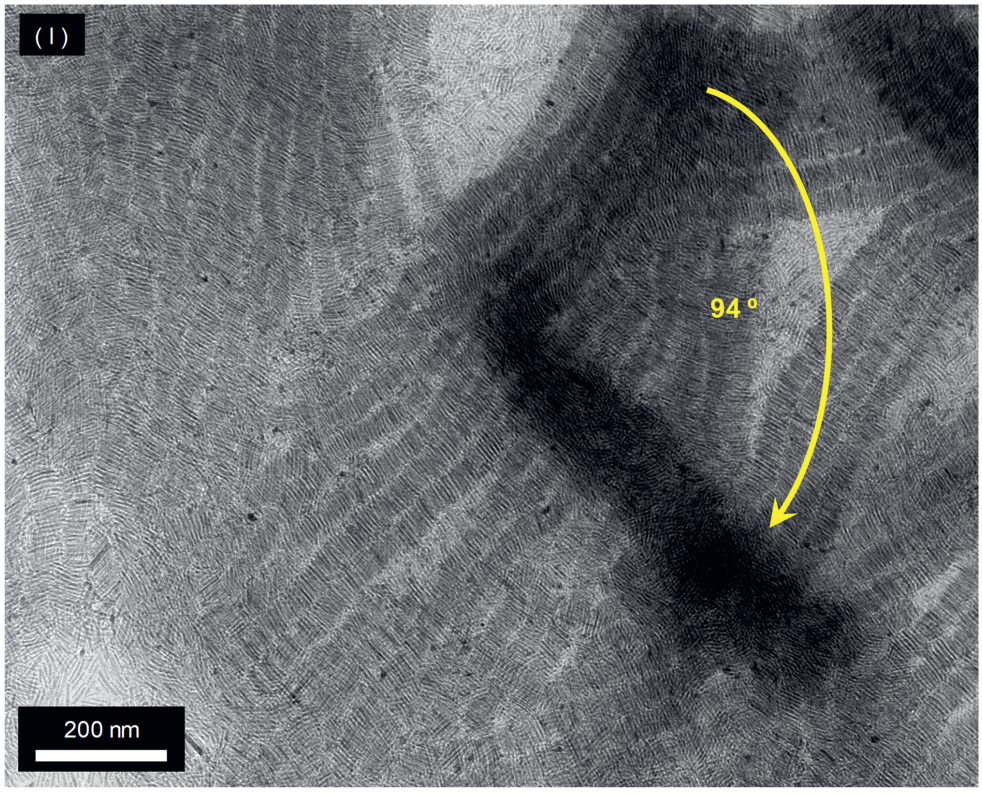

Figure S7. TEM micrographs of (a and b) large domains of post-treated SNRs and MNRs, respectively, formed in the smectic liquid crystalline structure onto a liquid interface. The samples' concentration for SA was 4.0 mg/ml (see **Table 1**). (c) perpendicularly positioned domains with respect to other layers as crystalline structural defects magnified from the sample in (b) and depicted with a yellow box. Moreover, interstitial NRs lying or standing between lamellae as transverse interlayer particles or differently shaped nanoparticles trapped as inclusions can be seen. (d) short smectic tracks formed at lower volume fractions (initial SA concentration 1.0 mg/ml) of post-treated SNRs (e and f) vertically ordered domains of post-treated SNRs occasionally with hexagonal symmetry or randomly packed similarly to structures observed for smectic-A phases trapped between lying smectic domains with an initial SA concentration of 8.0 mg/ml. (g and h) post-treated SNRs and MNRs in small bundles showing a rhomboidal shape for the inorganic core of brookite NRs imaged standing up on the TEM grid, respectively. (i) overlapping bilayers of hexagonally close-packed monolayers of

upstanding post-treated SNRs self-assembled by depletion attractions are shown which are shifted slightly with respect to each other and are observed simultaneously in transmission mode. (j) a vortex structure centered on one locally homeotropically ordered NR similar to a disclination of strength +1 that can be observed in nematic LCs.[160,180] (k) linear 'rail-track' self-assembled structures of post-treated SNRs occurred frequently when SA was induced by depletion attractions. These tracks were of different lengths, mostly on top of or near close-packed upstanding self-assembled structures. (l) linear rail tracks formed under the same conditions as (k) but for MNRs. Interestingly, these tracks could bend at relatively high angles (94 ° degrees) without breaking, suggesting that an attractive force is at work and also that they might have been distorted by drying forces.[181]

Supporting movie:

Our preliminary measurements using an external electric field (2.5 V μm^{-1}, 1 kHz). Such a field could induce a nematic LC phase reversibly in an isotropic liquid dispersion of the SNRs in dispersion II at 32 vol% and created a para nematic phase.

https://drive.google.com/file/d/1OVcMvwRjP1ATj2Zc5KEht4Gjw63Jt0Zu/view?usp=sharing

3

Synthesis and Characterization of Anatase TiO_2 Nanorods: Insights from Nanorods' Formation and Self-Assembly

Highly crystalline, organic-solvent-dispersible titanium dioxide (TiO_2) nanorods (NRs) present promising chemicophysical properties in many diverse applications. In this paper, based on a modified procedure from literature, TiO_2 NRs were synthesized via a ligand-assisted nonhydrolytic sol-gel route using oleic acid as the solvent, reagent, and ligand and titanium (IV) isopropoxide as the titanium precursor. This procedure produced monodisperse TiO_2 NRs, as well as some semi-spherical titania nanocrystals (NCs) that could be removed by size-selective precipitation. X-ray diffraction and selected area electron diffraction results showed that the nanorods were anatase, while the semipheres also contained the TiO_2(B) phase. By taking samples during the particle growth, it was found that the average length of the initially grown NRs decreased during the synthesis. Possible reasons for this unusual growth path, partially based on high-resolution transmission electron microscopy (HRTEM) observations during the growth, were discussed. The dispersion of anatase TiO_2 nanorods was capable of spontaneous formation of lyotropic liquid crystals on the TEM grid and in bulk. Considering high colloidal stability together with the large optical birefringence displayed by these high refractive index liquid crystalline domains, we believe these TiO_2 NRs dispersions are promising candidates for application in transparent and switchable optics..

3.1 Introduction

Nanocrystalline TiO_2 has been receiving increasing attention in many applications such as optoelectronics [182], catalysis and photocatalysis (such as water splitting, air, and water purification) [78,86,87,109–112], solar energy conversion [57], gas sensing [91], and nanostructured coatings for biomedical implants due to its modified material properties and chemical reactivity at the nanoscale [183]. The literature on producing nanocrystalline titania is quite extensive, leading to TiO_2 nanoparticles (NPs) in various sizes, morphologies, and crystalline phases in different yield scales [86,184]. Therefore, choosing an appropriate method to synthesize titania NPs consistent with the desired characteristics for the final application is of great importance. Among titania polymorphs that are commonly recognized, rutile is known to be thermodynamically the most stable phase for bulk material at standard pressure (1 bar) within the range 300–1000° K [185]. However, anatase and the less common brookite and titanium dioxide bronze phase (TiO_2(B)), are also formed commonly at the nanoscale [171,174]. Though brookite and TiO_2(B) are rarely observed in nature, their importance in photocatalysis, photovoltaics, and lithium-ion insertion has been recently recognized [186]. The transformation sequence among anatase, brookite, and rutile is size-dependent and their transformation into each other can be reversed even by slight differences in the surface energies [78]. In the case of TiO_2(B), it can be nucleated directly from the solution as a metastable phase and tends to transform into anatase titania at temperatures above 800° K [187].

We are interested in the unique intrinsic properties of crystalline titania NPs, such as high refractive indexes, wide bandgap, and strong UV absorption with no light absorption in the visible part of the spectrum. Additionally, we want to benefit from the shape and orientation-dependent collective properties of these inorganic NPs in liquid crystalline states for optical applications, as such nanorod (NR) liquid crystal phases can be switched at lower field strengths than molecular counterparts [58,188]. Thus, we focused on titania NRs as colloidal anisotropic building blocks to not only benefit from their spontaneous liquid crystal (LC) formation but also to gain other advantages over spherical titania counterparts in terms of high surface-to-volume ratio, improved number of delocalized carriers, and enhanced charge transport provided by their anisotropic geometry for relevant research in optoelectronics and photocatalysis [93,94]. To achieve

crystalline titania NRs, solution-phase methods, and in particular non-hydrolytic sol-gel techniques, are well known to give precise control over particle size, shape, and polymorphic phases by employing structure-directing agents, i.e., ligand organic molecules. Furthermore, these ligand molecules offer general dispersibility in diverse organic solvents [92]. Therefore, preparation of concentrated dispersions of titania NRs is achievable, which is important for lyotropic liquid crystal formation [14,16]. Many reports by different research groups such as Colvin et al. [189], Moritz et al. [190], Alivisatos et al. [191], Niederberger et al. [192], Vioux et al. [193,194], Han et al. [168], Cozzoli et al. [93,141,195], Murray et al. [92,109,110], and Hyeon et al. [175,196] have been devoted to the optimizing and understanding of titania NRs synthesis via non-hydrolytic sol-gel methods. In all of those experiments, the TiO_2 NRs are formed via hydrolysis and condensation reactions. In these reactions, the oxygen for the oxide NPs formation is provided by the solvent (ethers, alcohols, ketones, or aldehydes) or by the organic constituent of the precursor (alkoxides or acetylacetonates) [194,197]. Along with that, several key condensation reactions are proposed depending on the precursor and solvent in the reaction system such as alkyl halide elimination by a titanium alkoxide and a titanium halide reaction [191,193,196], ester elimination between titanium carboxylates and titanium alkoxides reaction [175,194], and ether elimination by two titanium alkoxides reaction [198].

Herein we report a synthesis route, based on a modified procedure from the literature [175], to produce titanium dioxide NRs from ultrathin NRs via a ligand-assisted nonhydrolytic sol-gel pathway in which the ligands (oleic acid, OLAC) also acted as the solvent and reagent. The used synthetic procedure also produced semispherical nanocrystals (NCs), but these could be removed from the NRs by size-selective precipitation. A possible formation mechanism for the ultrathin NRs, morphological evolution, and accompanying NCs is discussed as it was observed that the initial nanorod length was seen to decrease after the first 10 min of synthesis. Moreover, we showed that the anatase NRs we obtained were monodisperse enough to spontaneously self-organize into inorganic smectic liquid crystal phases on the TEM grid and in bulk, making them a promising candidate for LC-based optoelectronic applications.

3.2 Results and Discussion

3.2.1 Growth Mechanism of TiO_2 Nanocrystals

Titanium dioxide nanocrystals (NCs) were synthesized following a slightly modified synthesis method as described by Joo et al. [175] where oleic acid (OLAC) was used as the solvent, reagent, and ligand [55]. Our modifications were mainly related to the reduced precursor amounts and lowering the reaction temperature from 270 °C to 250 °C to control the reaction temperature fluctuations and foam expansions. Figure 3-1 shows the as-synthesized TiO_2 NCs characterized by TEM and high-resolution TEM (HRTEM) images. As can be seen in Figure 3-1a, as-synthesized TiO_2 NCs mostly consisted of nanorods (NRs) with various lengths as well as some semispherical NCs. To effectively separate the TiO_2 NRs specifically in terms of their length to obtain the desired polydispersity index (standard deviation divided by mean length), size-selective precipitation, or more correctly aggregation, was performed on the TiO_2 mixture. This well-known purification technique is mainly based on the magnitude of the van der Waals attraction forces between particles which increase with particle size [199]. In the case of NRs, the van der Waals attraction forces induced the aggregation between NRs with larger lengths [145]. We found that to achieve a higher yield of monodisperse NRs (yield of ~50% or almost 1 g of NRs), it was crucial to separate first the larger NCs (here TiO_2 NRs) from the reaction mixture *just through centrifugation* prior to the addition of antisolvent in the size-selective precipitation process. After centrifugation of the reaction mixture, separation of the TiO_2 NRs by length was highly efficient by the dropwise addition of acetone as an antisolvent to the dispersion of the NRs in toluene. Due to the hydrophobicity of the ligand layer around TiO_2 NRs, the dispersion of the NRs was destabilized by the addition of the polar acetone which resulted in the aggregation and fast sedimentation of the NRs leaving many of the synthetic by-products and shorter rods in solution. Finally, both the TiO_2 NRs as main products and the semispherical NCs left in the supernatant were redispersible in a variety of nonpolar solvents such as toluene as shown in Figure 3-1(d and e) and resulted in the isolation of relatively monodisperse TiO_2 NRs (σ_L = 14%). The dimension of the NRs was on average 3.6 ± 0.4 nm (thickness) and 24.6 ± 3.4 nm (length), while the semispherical NCs had an average diameter of 5.7 nm.

Figure 3-1b shows the selected area electron diffraction (SAED) pattern of these NRs revealing the highly crystalline anatase phase. The reflected rings were clearly indexed to (101), (103), (004), (200), and (105) planes of anatase indicating the high crystallinity of these particles which is consistent with the HRTEM images and X-ray diffraction (XRD) results in Figure 3-4. In Figure 3-1c where a [010] zone axis is perpendicular to the imaging plane, a single nanorod can be seen to have grown along its *c* axis in the [001] direction. The reason is that {001} surfaces in the anatase phase have a higher surface energy in comparison to {101} surfaces [190,200]. Thus, the typical fast growth in anisotropic anatase NRs is observed with a preferential growth in the [001] direction as was also the case in our synthesis. The lattice fringes of approximately 0.35 nm are depicted with yellow parallel lines corresponding to the (101) planes of the anatase phase.

In the following, we will discuss the mechanism of the titania NRs formation in our experiment based on the literature on the nonhydrolytic sol-gel routes to synthesize titanium oxide NPs [56,168,175,191,201–203] and on what we observed by following our synthesis in time by taking samples of reaction mixtures at 10-min intervals.

In general, nonhydrolytic sol-gel processes can be divided into two main categories: ligand-assisted and solvent-controlled routes. In the case of the ligand-assisted process, ligands, mainly in the form of hot ligand solutions (e.g., trioctylphosphine oxide, oleic acid, and oleylamine), are present in the reaction mixture, either as a solvent or as a coordinating ligand providing control over the growth, size, and shape of the metal oxide NPs [202]. However, in solvent-controlled approaches, the initial reaction mixture mainly consists of two components, metal oxide precursors and common organic solvents. Thus the role of solvents may include acting as a reactant, oxygen donor, structure-directing agent, or reducing factor [192,204]. One should also keep in mind that these nonhydrolytic sol-gel routes, also known as nonaqueous reactions, are not necessarily totally water-free. In fact, even though the initial components of the reaction mixture have been dried and degassed, specific organic reactions are able to produce water in situ (e.g., aldol condensation and esterification reactions), rendering the system in principle hydrolytic. Therefore, even in the (virtual) absence of water, it is possible to have hydroxylation reactions [197].

In our experiment, titania NRs were synthesized via a ligand-assisted nonhydrolytic sol-gel method in which the rapid thermal decomposition of a titanium precursor (titanium (IV) isopropoxide or TTIP) occurred in a hot solvent solution (OLAC), at a relatively high temperature (around 250 °C). It is well-known that titanium alkoxides are relatively reactive (e.g., as compared to silicon alkoxides) and almost instantly react with carboxylic acids (e.g., oleic acid, decanoic acid, linoleic acid, etc.,) even under mild conditions producing mixed alkoxy carboxylates and hydroxyalkoxides [55,93,205]. For instance, it was shown that titanium (IV) butoxide ($Ti(OBu)_4$ where Bu refers to $-C_4H_9$) can readily react with linoleic acid ($C_{17}H_{31}CO_2H$) yielding a titanium butoxide-carboxylate complex $Ti(OBu)_{4-x}(C_{17}H_{31}CO_2)_x$ with the release of *x*BuOH. This BuOH formed, may react with unreacted linoleic acid left in the mixture leading to the formation of water by an esterification reaction [202,205]. Analogous to the literature, we believe that in our experiment, upon the addition of TTIP ($Ti(O^iPr)_4$ where Pr refers to $-C_3H_7$) to the degassed OLAC ($C_{17}H_{33}COOH$) solution at room temperature and as indicated by a color change of the mixture to pale yellow, a titanium carboxylate complex ($(C_{17}H_{33}COO)_x–Ti(O^iPr)_{4-x}$) formed with the release of *x*PrOH. Since the OLAC molecules were present in an excess amount acting as both ligand and solvent, therefore *x*PrOH could react with OLAC molecules and release water molecules via an esterification reaction. The water produced could then react with the titanium carboxylate complex to generate Ti–OH and subsequently through a hydrolysis–condensation process, Ti–O–Ti bonds were formed [206]. It has been shown that in synthetic routes where the ligand and solvent are the same, the desorption rate of ligand bound at the surface of the NCs is low giving them higher colloidal stability [203].

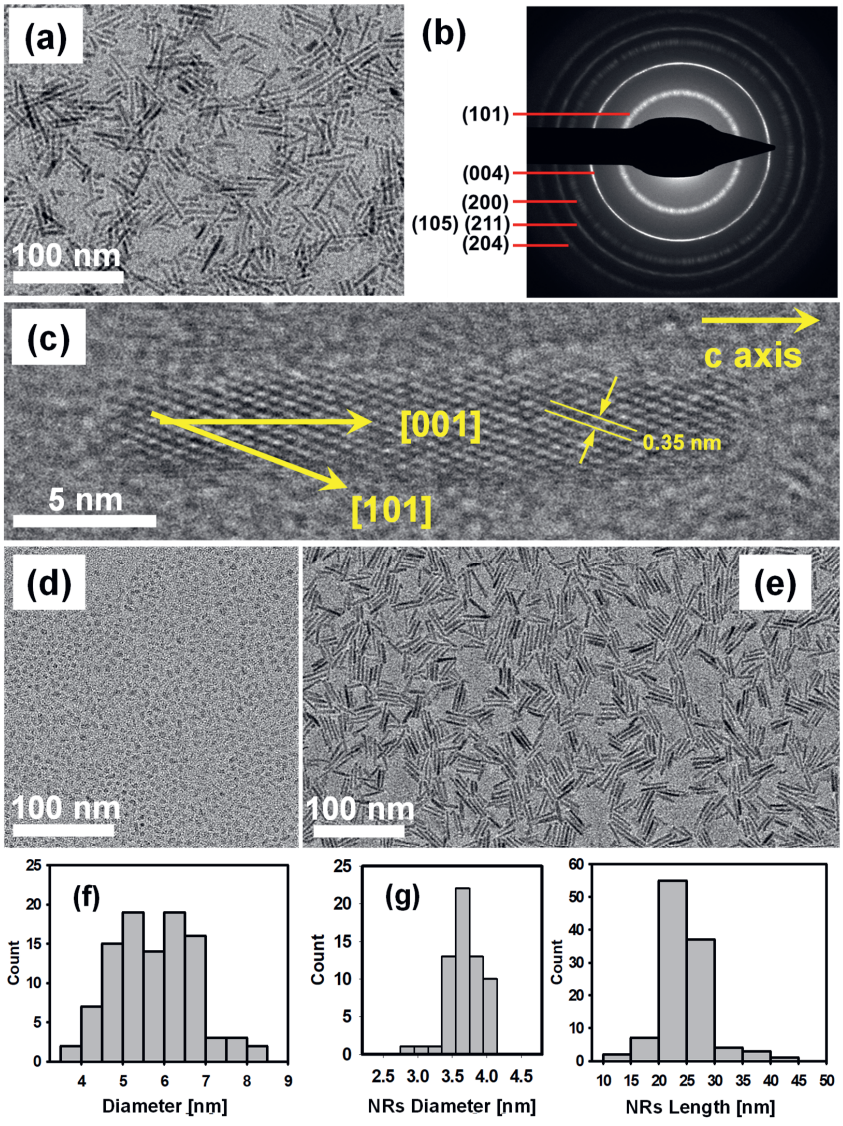

Figure 3-1. (**a**) As-synthesized TiO_2 NCs including NRs of different aspect ratios and semispherical NCs; (**b**) SAED pattern of anatase NRs presenting reflected rings clearly indexed to typical planes of anatase; (**c**) an individual anatase NR that has a [010] zone axis growing along the [001] direction. (**d**–**g**) TiO_2 NCs after the size-selective process in two main categories, NRs and semispherical NCs, and their corresponding size distributions from a statistical analysis of TEM images

It has also been demonstrated that the in situ water generated during the esterification reaction favors the formation of anatase and TiO_2(B) which is in agreement with our results in Figure 3-4, as well [207]. The abovementioned reaction route is described in (Eq. 3-1) to (Eq. 3-3):

$$Ti(O^iPr)_4 + xC_{17}H_{33}COOH \rightarrow (C_{17}H_{33}COO)_x - Ti(O^iPr)_{4-x} + xPrOH \quad \text{(Eq. 3-1)}$$

$$PrOH + C_{17}H_{33}COOH \rightarrow C_{17}H_{33}COOPr + H_2O \quad \text{(Eq. 3-2)}$$

$$(C_{17}H_{33}COO)_x - Ti(O^iPr)_{4-x} + H_2O \rightarrow (C_{17}H_{33}COO)_x(O^iPr)_{3-x}TiOH + xPrOH$$

$$(C_{17}H_{33}COO)_x(O^iPr)_{3-x}TiOH + (C_{17}H_{33}COO)_x(O^iPr)_{3-x}TiOH \rightarrow (C_{17}H_{33}COO)_x(O^iPr)_{3-x}\mathbf{Ti–O–Ti}(C_{17}H_{33}COO)_x(O^iPr)_{3-x} + H_2O \quad \text{(Eq. 3-3)}$$

3

Although we think that the hydrolysis followed by condensation is the main route of oxide formation, the possibility of a nonhydrolytic condensation of titanium carboxylate complex to form Ti–O–Ti bonds cannot be ruled out, either.[93] It is known that an oxo bridge can be formed by a condensation reaction between two functional groups bonded to two metal centers (M) along with eliminating an organic ester molecule as it is shown in (Eq. 3-4).[202]

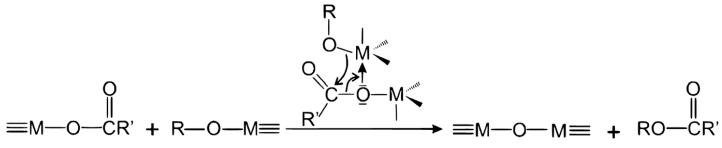

(Eq. 3-4)

Thus, after the formation of the titanium carboxylate complex, also a transesterification can occur between the complex and TTIP precursor to generate the

Ti–O–Ti bonds and eliminate an ester. These reaction steps are shown in (Eq. 3-5) and (Eq. 3-6).

$$Ti(O^iPr)_4 + (C_{17}H_{33}COO)_x - Ti(O^iPr)_{4-x} \rightarrow (C_{17}H_{33}COO)_{x-1}(O^iPr)_{4-x}\mathbf{Ti–O–Ti}\ (O^iPr)_3 + (C_{17}H_{33}COOPr) \quad \text{(Eq. 3-5)}$$

$$n(C_{17}H_{33}COO)_x - Ti(O^iPr)_{4-x} \rightarrow {}^{n}/_{2}\ [(O^iPr)_{3-x}\mathbf{Ti–O–Ti}(C_{17}H_{33}COOPr)_{x-1}] + {}^{n}/_{2}\ (C_{17}H_{33}COOPr) \quad \text{(Eq. 3-6)}$$

Cozzoli et al. suggested that these molecular species were enclosing a compact Ti–O–Ti framework of hexa-coordinated Ti atoms and could be regarded as titania monomers protected by carboxylate ligands. In these monomers, OLAC molecules have a tendency to bridge titanium centers [93]. Therefore, we surmise that titania NCs synthesized in our experiment might have been formed via both hydrolytic–condensation and nonhydrolytic–condensation routes, but it is not clear to what extent each path contributed.

In Figure 3-2, we monitored the progressive evolution of TiO_2 NCs by extracting aliquots of the hot reaction mixture at scheduled time intervals. These hot extractions were swiftly cooled down to room temperature via quenching in toluene to stop further crystal growth. Interestingly, ultrathin TiO_2 NRs (1.8 ± 0.3 nm (thickness) and 36.4 ± 10.1 nm (length)) were produced in the early stages of the reaction (first 10 min). These ultrathin NRs were of the anatase polymorph. This relatively fast formation of the titania NRs was also reported in the literature for the case of $Ti(OBu)_4$ decomposed in a pure OLAC medium leading to anatase NRs in less than 15 min [203]. In each panel of Figure 3-2, the length distribution of TiO_2 is shown as a histogram. In addition to the length distributions, we can observe that the ultrathin TiO_2 NRs became thicker over time from 1.8 ± 0.3 nm to 3.6 ± 0.4 nm. Moreover, in the first 10 min of the experiment, ultrathin NRs had a broad length distribution of 36.4 ± 10.1 nm. After 10 more minutes, shorter but thicker NRs of 21.8 ± 2.8 nm were mostly detected in the reaction mixture, which then increased in both thickness and length, finally resulting in nanorods with a broad

length distribution of 27.6 ± 6.9 nm and a collection of semispherical NCs. We also noticed that during the growth steps, some NRs became unequally thicker such that the thickness was somewhat larger in either one tip of the NRs (matchstick-like NR shown in Figure 3-2b-inset) or in both tips (dumbbell-like NR shown in Figure 3-2d-inset).

For titania NRs, a process of shape evolution after initial crystallization has been described in several previous reports, as well [190,191,200,205,208,209]. In some cases, anatase NCs that were formed in acidic conditions nucleated almost exclusively as truncated tetragonal bipyramidal NCs with {101}, {001}, and {010} facets [92,210]. Then, these primary NCs were kinetically promoted to grow via the oriented attachment mechanism [211,212]. We note that oriented attachment in one, two, three dimensions as well as mesocrystal formation have been reported frequently for surface-functionalized titania NPs synthesized in both hydrolytic and nonhydrolytic media [190,211,213]. Elaborate investigations by Dalmaschio and Leite [203] on anatase NRs, synthesized by thermal decomposition of titanium(IV) butoxide in an OLAC mixture revealed that the oriented attachment of these truncated tetragonal bipyramidal NCs occurs via sharing the (001) plane with a preferential growth in the [001] direction. In our results, we also observe typical morphological evolution as a function of time, for instance, an increase in the thickness of the NRs while the length reduced in the NRs and the emergence of relatively smaller NRs and NCs. Dalmaschio and Leite attributed these shape alterations to the fragmentation of the titania NRs into smaller NCs induced by a Rayleigh instability-like phenomenon [197,203]. Furthermore, they stated that the mass transportation to the tips of the NRs via a surface diffusion process could kinetically advance the detachment process. In the Rayleigh instability phenomenon, an unstable liquid cylinder breaks into droplets driven by surface tension fluctuations coupled with a lowering of the total energy. It has been proposed that under certain circumstances, this concept can be extended to solid NPs and therefore NRs could also be vulnerable to fragmentation into smaller NPs [214–217].

Although we cannot rule out the occurrence of directed attachment during the growth steps, we believe that due to the existence of ligands in the solution, the growth

mechanism in Figure 3-2 is mainly attributed to the fast out-of-equilibrium growth of the NRs from the solution.

In Figure 3-3, HRTEM images of several synthesized anatase NRs have been presented. As can be observed, the structural features depicted by yellow arrows and lines on the surface of the NRs such as steps, corrugated sides, zigzag patterns, and sharp edges give indications of the critical pinch points formed during the surface diffusion step that are vulnerable to the detachment. Considering TEM images of ultrathin NRs formed in the early stages of the reaction (Figure 3-2) and HRTEM images of final NRs in Figure 3-3, the Rayleigh instability-like detachment phenomena could also be the reason in our experiment that led to shorter titania NRs and pinched off semispherical titania NCs. However, further in-depth investigations are needed to precisely confirm the exact

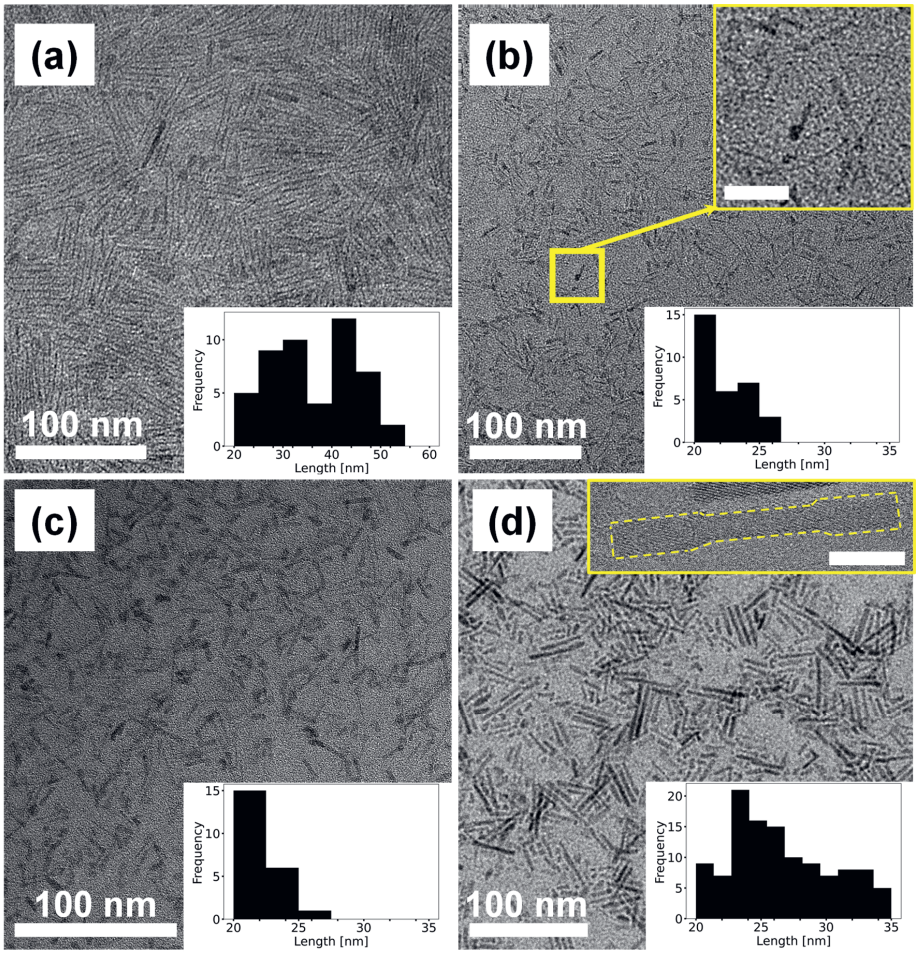

Figure 3-2. (**a**–**d**) TEM micrographs of TiO_2 NCs depicting progressive evolution of NCs at different time intervals (10 min, 20 min, 60 min, and 120 min, respectively) from ultrathin NRs to the final mixture of NRs of various lengths and semispherical NCs. The length distributions of TiO_2 are shown in histograms as insets with black columns. The average thickness of the NRs are 1.8 ± 0.3 nm in (**a**), 2.6 ± 0.5 nm in (**b**), 2.9 ± 0.7 nm in (**c**), and 3.6 ± 0.4 nm in (**d**). Inset in (**b**) shows the occurrence of irregularities at the tip of the NRs. Inset in (**d**) shows an HRTEM image of a single NR exhibiting a dumbbell shape at higher resolutions. Scale bar in b-inset is 25 nm and in d-inset is 5 nm.

mechanism behind these TiO_2 NRs growth and their shape evolution during this experiment.

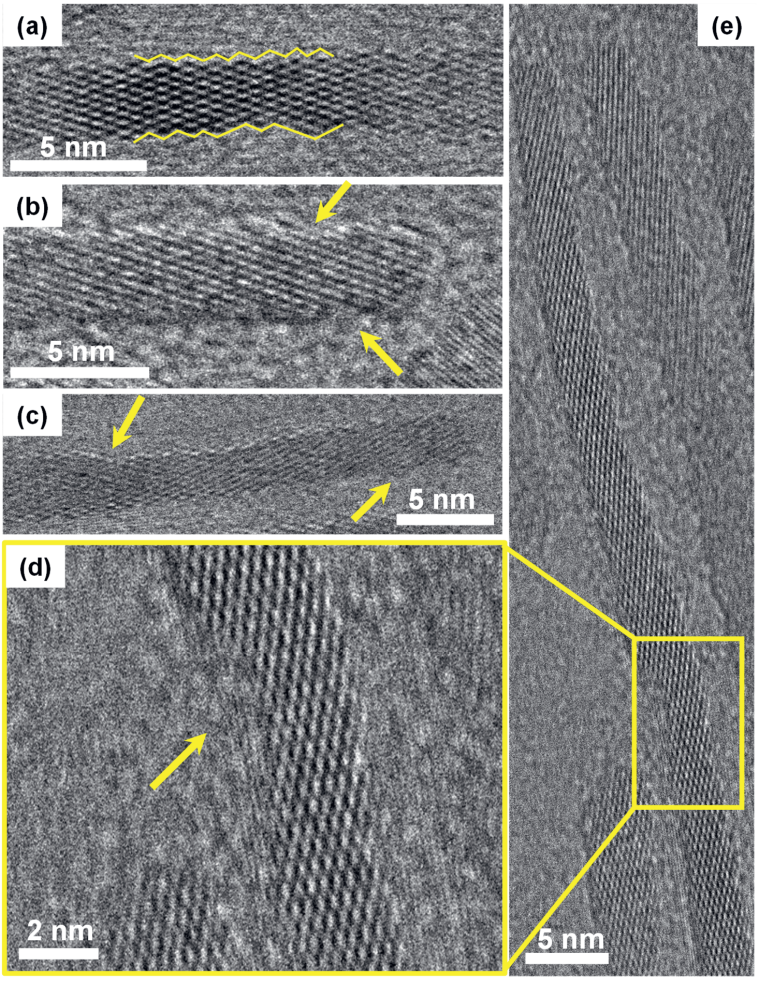

Figure 3-3. HRTEM micrographs of anatase NRs. (**a**–**e**) Surface features labeled by yellow arrows and lines on the surface of the NRs such as steps, corrugated sides, zigzag patterns, and sharp edges demonstrating give indications of the critical pinch points vulnerable to the detachment.

3.2.2 Characterization of Synthesized TiO_2 Nanocrystals

The crystallinity of the synthesized NCs was analyzed by the XRD technique (next to HRTEM observations and selected area electron diffraction results). Contrary to the results presented in the paper from which we follow the synthesis protocol (Joo et al. [175]) our XRD patterns (Figure 3-4) confirmed the existence of two titanium oxide polymorphs in the resulting NCs. Both the anatase phase and the titanium dioxide bronze

phase (TiO_2(B)) could be recognized in our data. The XRD data, together with reference data of anatase TiO_2 (JCPDS-01-086-1155) and TiO_2(B) (JCPDS-00-046-1238), respectively, are shown in Figure 3-4, as well. In the case of anatase NRs, the relative intensity of the diffraction peak for (004) planes has been reported to become more pronounced as compared to the intensity of (200) planes [113,168]. This is a well-known phenomenon for anatase crystals if their anisotropic growth occurs along the *c* axis of the anatase lattice: the (004) diffraction peaks become stronger and sharper in comparison to (200) diffraction peaks and this is consistent with our TEM observations and the NRs SAED pattern in Figure 3-1b [175,190,205,218]. Furthermore, the bandgap of the anatase NRs was found to be ca. 3.28 eV by using their light absorption spectrum. The measured bandgap value was indeed analogous to reported optical bandgaps for nanocrystalline anatase NPs [109,175,219] (See Figure S1). To confirm that the peak broadening arose from NCs' size and shape effects, the average crystallite sizes of the anatase NCs were calculated by using the Scherrer formula [220] (See Table S1). Scherrer analysis from the (101), (200), and (004) diffraction peaks yields approximately 3.8, 3.5, and 19.9 nm, respectively, for the dimensions of the anatase NRs which are in agreement with the measured width and length from the TEM micrographs. Furthermore, the optical properties of the anatase NRs were characterized using their light absorption spectrum. Even though several diffraction peaks could be matched with the anatase reference signal, some other peaks at 34.4°, 35.4°, 36.2°, and 52.3° were pointing at the existence of another phase. Dickerson et al. suggested that these peaks could correspond to crystalline OLAC aggregated present among the TiO_2 NRs due to the fact that these NRs were formed in an excess amount of OLAC [221]. However, in our experiment, TiO_2 NRs were purified via a size-selective aggregation process after the synthesis step, therefore the presence of aggregated OLAC seems less likely to us. Moreover, a possible explanation of these signals could be the formation of brookite titania as an impurity, as it has been reported before during the synthesis of the other polymorphs [189,218,222]. Although the diffraction peak located at 36.2° could be assigned to the (121) plane of the brookite phase, the other three diffraction peaks at 34.4°, 35.4°, and 52.3° are not compatible with the brookite, anatase, or rutile polymorphs [223]. After careful examination, we concluded that the last four measured reflections could be a fit for the TiO_2(B) phase of titania, which is given in the reference card (JCPDS-00-046-1238). The (001), (–111), (003) reflections

are typical of TiO_2(B) titania which were detected in the XRD patterns of both the NRs and the semispherical NCs [187,224]. These peaks are relatively more prevalent in the semispherical NCs rather than NRs. The reason could be the existence of semispherical NCs left after the size-selective process among anatase NRs since the full separation of the small NCs from bigger NRs is practically difficult. Furthermore, it has been shown that surface hydroxylation during TiO_2(B) NCs formation will introduce surface relaxation and thereby the TiO_2(B) NCs may exhibit an ellipsoidal shape in the c direction [187,224]. Therefore, not only the semispherical NCs, found mostly in the supernatant, but also some of the shorter NRs left among anatase NRs after the purification step could be elongated TiO_2(B) NCs.

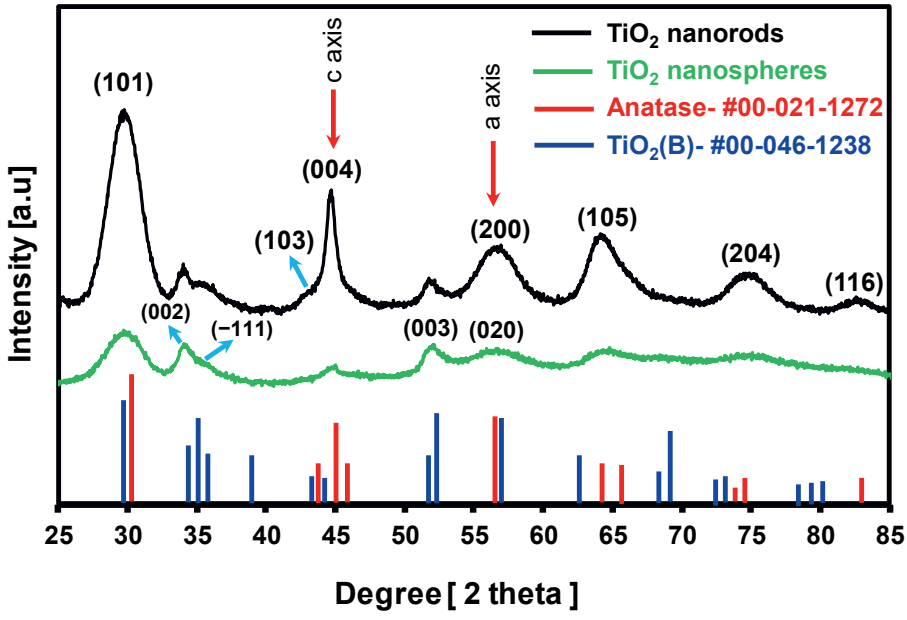

Figure 3-4. XRD patterns of synthesized TiO_2 NRs and semispherical NCs. Bragg peaks at 30.5°, 45.4°, 57.0°, 64.6°, 66.1°, and 74.6° indicate the existence of the anatase phase of TiO_2 (JCPDS No.01-086-1155) for NRs. XRD analyses clearly show the occurrence of other Bragg peaks at 34.6°, 35.9°, 52.7°, and 57.9° mainly due to semispherical NCs that are fit with the TiO_2(B) phase of titania with the reference card (JCPDS-00-046-1238). The (002), (–111), (003), and (020) reflections are typical of TiO_2(B) titania

3.2.3 Liquid Crystalline Phases of TiO_2 NRs

In the next step, we investigate liquid crystal phases formed by the self-assembly of the anatase NRs made. As we showed in our early work elsewhere [188] that we are interested in the collective properties of TiO_2 NRs specifically for optical applications. We already showed that brookite TiO_2 NRs exhibit an intriguing LC phase behavior in bulk as well as promising switchability in external fields. Here, to compare anatase TiO_2 NRs with their brookite counterparts, we represent several self-assembled domains achieved on a carbon-coated copper TEM grid in the dry state as well as LC domains along with the sedimentation profile in a capillary in bulk (Figure 3-5). Similar to brookite TiO_2 NRs, anatase TiO_2 NRs can be fairly well approximated as spherocylinders with an effective aspect ratio (L/T) defined by the total length (L) divided by thickness (T). To obtain the relevant aspect ratio (AR) for self-assembly we also added 3.0 nm to both L and T, reflecting twice the effective length of the ligand molecules based on interparticle spacings measured from TEM images. The phase diagram for hard anisotropic shapes has been determined by Frenkel and Bolhuis using computer simulations [41]. However, colloidal rods are never all the same due to polydispersity in their length and diameter. Initially, Onsager predicted that length polydispersity in the system of hard rods broadens the biphasic region where longer rods preferentially enter the nematic phase [22]. Later, many papers investigated the effects of polydispersity for continuous distributions of rigid rods where they also found that increase in polydispersity shifts the isotropic boundary to lower concentrations while the nematic boundary moves to notably higher ones leading to a broadened biphasic region [27,154–157,225]. In our system, based on the average dimensions of the examined anatase NRs (L = 24.6 ± 3.4 nm and T = 3.6 ± 0.3 nm measured by TEM images), an effective aspect ratio of 4.2 was calculated which for monodisperse hard rods is close to the AR where next to nematic, also smectic LC phases can be formed and ABC-stacked crystals at high volume fractions [27,49,50]. Figure 3-5a depicts short smectic tracks of NRs aligned side-by-side in several domains. For rods with hard interactions, it has been shown that smectic phases of hard rods nucleate first in 2D smectic layers which are most likely related to why such tracks form on top of a flat wall, but it should also be remembered that the drying forces are large compared to the average kinetic energy kT, where k is the Boltzmann's constant and T the absolute temperature. Therefore, it is also possible that these tracks are formed at the liquid–air interface, as it

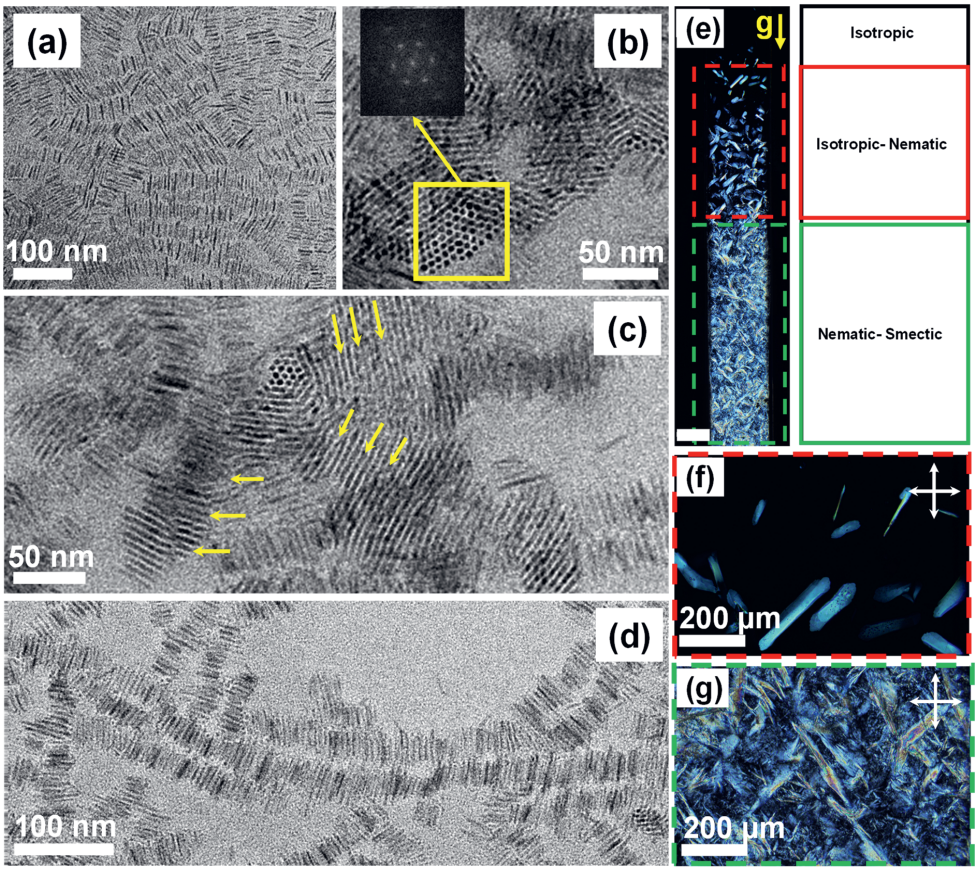

Figure 3-5. TEM micrographs of anatase NRs self-assembled on a TEM grid (**a**–**d**) and optical micrographs of a dispersion in toluene between crossed polarizers (**e**–**g**). (**a**) Anatase NRs in small smectic liquid crystal-like domains. (**b**,**c**) Hexagonal superlattices of vertically aligned anatase NRs. Inset in (**b**) shows the corresponding FFT pattern illustrating a close-packed hexagonal order. In (**c**), NRs have a tilted orientation, similar to rows of fallen dominoes (yellow arrows) around a vortex structure centered on a small cluster of locally homeotropically oriented NRs. In (**d**), a linear "rail-track" pattern was observed from the side-by-side assembly of the NRs into the rail-tracks of various lengths. (**e**) A sedimenting sample from a dispersion of anatase NRs in toluene (~29 vol%) in a capillary with three distinct regions. From top to bottom: isotropic fluid at the top, (**f**) elongated nematic tactoids floating in the isotropic fluid, and (**g**) coexistence of nematic domains and sharped-edge smectic LC phases. Scale bar in (**e**) is 500 µm.

is known that being attached to the interface induces lateral forces between the rods because of the deformation of the interface [226].

Although the self-assembled arrays in Figure 3-5a seem to be a single layer, we presented some self-assembled domains in Figure 3-5b,c where part of the titania NRs were imaged standing normal to the TEM grid evidencing more extended 2D smectic layer formation. The vertically aligned NR layers were seen to form with close-packed hexagonal order within the smectic layers (Figure 3-5b inset) [27]. Additionally, in some parts of the 2D smectic layers with the rods standing perpendicular most likely the drying forces made parts of the rods end up in a tilted orientation. Some of the rods fell over like dominoes in a certain direction; similar observations were made with different systems of NRs such as TiO_2 [134,150,159,188], CdS [227], CdSe [160], and CoO [228]. By considering the electron diffraction data, we conclude that these structures are otherwise the same as the vertically aligned arrays with a precise orientational and positional order and also the same interparticle separation as observed for the vertical superlattices. In Figure 3-5b,c we could also observe part of a vortex structure centered on one or a small cluster of locally homeotropically ordered rods. Since the orientation of the individual nanorods changed continuously around the vortex defect, it is similar to a disclination of strength +1 that can be observed in nematic liquid crystal phases [160,180]. The presence of this structure can be linked to twist or bend distortions of the nematic, and possibly also smectic liquid crystal domains produced by microflows during drying [59,181,229].

In Figure 3-5e–g, polarized optical microscopy (POM) images of the LC domains of anatase NRs are displayed. The initial volume fraction of these NRs was approximately 29 vol% and they were in an isotropic state showing no optical activity between cross polarizers. Analogous to our remarks in the previous report on brookite NRs lyotropic LCs [188], the dispersion of anatase NRs exhibited an equilibrium phase behavior along the concentration gradient that occurred in the capillary. Since these NRs were too small to sediment under gravity, this gradient was most likely formed by phase separation as a result of sufficiently high initial volume fraction and weak long-ranged van der Waals attractions. Along the capillary, three main regions were observed: the isotropic region on the top of the capillary, a biphasic region consisting of nematic tactoids nucleating and floating in the isotropic liquid, and a biphasic region of sharp-edged smectic domains in coexistence with a nematic at the bottom of the capillary that was quite identical to that of smectic-A LC phases of brookite NRs [188]. No striated LC texture indicative of a pure

smectic phase was detected at the bottom of the capillary in the case of anatase NRs in comparison to brookite LCs. This could be attributed to the higher level of polydispersity in the length of the anatase NRs or the initial volume fraction could be too low to form such a phase. We also note that similar to the dispersion of brookite NRs reported elsewhere [188], a dispersion of anatase NRs in an isotropic state responded to an external electric field. An induced nematic LC phase was reversibly achieved known as a para nematic phase (results are not shown here). In our follow-up work in the near future, we intend to study these behaviors and dynamics in external electric fields.

As can be seen in Figure 3-5f,g, needle-like nematic tactoids nucleated in the isotropic liquid, and resulted in a biphasic region of sharp-edged smectic domains in coexistence with nematic domains. One should consider that tactoids are generally known to adopt a spindle shape depending on mesogen orientation, interfacial tensions, and elastic constants of the nematic phase [162,230]. Besides that, it has been shown that the existence of attractions among these colloidal mesogens in lyotropic LCs enhances this anisotropy toward needle-like tactoids [231–233]. In this regard, Green et al. [233] showed the phase behavior of rodlike particles with solvent-mediated attractions and repulsions. They showed that rods in the nematic tactoids are separated by average distances much smaller than their counterparts in the isotropic phase. Therefore, these rods in the nematic tactoid would spend considerably more time in the attractive well, which existed as a result of short-range electrostatic repulsive forces in combination with van der Waals attraction forces. Due to these attraction forces, the LC tactoids became needle-like and even in the case of highly attractive single-walled carbon nanotubes in superacids, they were referred to as "spaghetti" LC domains [233].

To roughly estimate the van der Waals attraction forces between the anatase cores and compare them with brookite counterparts, we calculate the van der Waals interactions between anatase NRs and brookite NRs of the same size (solid and dashed lines, respectively in Figure 3-6) for three different relative orientations by using the Hamaker constants of anatase and brookite in toluene. The details of van der Waals interactions calculations have been described in detail in our earlier work [188]. As expected, the strongest attractions occur when rods are perfectly aligned face-to-face. However, the calculated interactions are an overestimation as they assume perfectly smooth inorganic

cores with atomically flat interfaces. Any surface roughness and irregularities, as shown in HRTEM images in Figure 3-3, also would make the "perfect" parallel approach between the two rods much less efficient and reduce the actual van der Waals interactions [145,188]. The difference between anatase and brookite is seen to be very small. The vertical line at 3.0 nm shows the distance of the closest approach based on twice the ligand length. Therefore, both anatase and brookite NRs are expected to experience van der Waals attractions of a few *kT*, which may be sufficiently large to induce parallel alignment at high volume fractions, caused by their high refractive indexes. Nevertheless, employing apolar solvents with high refractive indexes in combination with the existence of atomic irregularities at the surface of NRs and sufficient steric repulsion between NRs by adsorbing ligand molecules could still efficiently reduce van der Waals attractions, making both of these material systems promising candidates for LC-based optical applications.

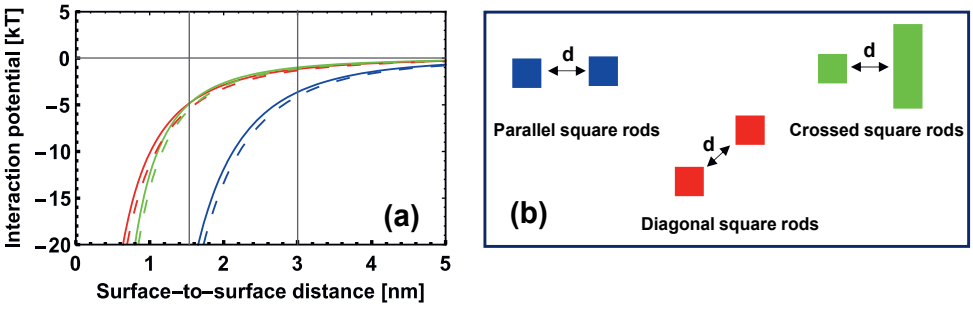

Figure 3-6. van der Waals interaction potentials between two bare TiO_2 NRs of anatase (solid lines) and brookite (dashed lines) phase of the same size in toluene. Vertical gray solid lines represent one and two times the effective ligand length of 1.5 nm corresponding to the interparticle spacing observed in the TEM images. (**b**) Schematic representation of NRs encounter each other in parallel, diagonal, or crossed configuration shown in blue, red, and green colors, respectively. Nanorods are assumed as parallelepipeds of length 27.4 nm and thickness 3.4 nm.

3.3 Conclusions and Outlook

In this work, we successfully synthesized highly crystalline organic-solvent-dispersible TiO_2 NRs based on a modified procedure from literature via a ligand-assisted nonhydrolytic sol-gel route. X-ray diffraction and selected area electron diffraction results showed the coexistence of anatase and TiO_2(B) phases of titania in the particles made. This synthesis yielded relatively concentrated dispersions of the anatase NRs (~500 mg/mL), after careful size-selective precipitation steps (yield of nearly 50%) to remove the largest rods as well as semispherical particles, which is twice the amount reported for the same size brookite NRs in ref. [188]. Possible reaction and formation mechanisms for the NRs were discussed based on the unusual observation that relatively early in the synthesis (after 10 min) rods were already present that subsequently reduced in length and increased in thickness during further growth, while semispherical particles were formed as well. Furthermore, we showed that anatase NRs were monodisperse enough to spontaneously self-assemble into smectic liquid crystalline phases on the TEM grid and in bulk. Because of their high refractive indexes and at the same time minimal light scattering due to their size, both anatase and brookite TiO_2 dispersions are promising candidates for application in electro-optical devices based on inorganic liquid crystals

3.4 Acknowledgments

The authors would like to thank Dennie Wezendonk for the X-ray measurements, Peter Helfferich for his help during POM measurements, Chris Schneijdenberg for technical assistance in electron microscopy analysis, Albert Grau-Carbonell for carrying out numerical calculations for van der Waals interaction potentials, and Dagney Mackaaij for her contributions on titania synthesis experiments.

3.5 Experimental

3.5.1 Materials

Titanium (IV) isopropoxide or TTIP ($Ti(OCH(CH_3)_2)_4$, 97.0%), oleic acid (OLAC, 90%), acetone, and toluene were purchased from Sigma Aldrich (Amsterdam, the Netherlands) and used as received. All experimental procedures were carried out either in an inert atmosphere using a standard Schlenk line setup or in a glove box.

3.5.2 The Modified Synthesis of TiO_2 NRs;

Anatase titanium dioxide NRs were synthesized following a slightly modified version of the synthesis described in the literature by Joo et al. [175] Our modifications were mainly related to the following factors: (I) we reduced the precursor amounts by half, (II) lowered the reaction temperature from 270 °C to 250 °C, and (III) performed a careful size-selective washing step, as discussed below. In a typical synthesis, OLAC (100.0 mmol, 31.6 mL) was degassed in a 250 mL three-neck round bottom flask at 120 °C for an hour under vacuum and vigorous stirring. Then the flask was cooled down under vacuum to 40 °C, followed by switching to nitrogen and the swift addition of TTIP (34.0 mmol, 10 mL) which was prepared in the glove box in advance. The mixture was then heated up to 250 °C in 20 min and kept at this temperature for 2 h. Caution should be taken as the reaction is rather violent with the concomitant release of gases and foam formation expanding in the flask and should be controlled by nitrogen overflow/pressure. After thermal fluctuations at high temperatures, the yellow solution gradually turned into a white-gray foam and finally a gray solution. The heating mantle was then removed after 2 h and the flask was allowed to cool to room temperature. To effectively separate TiO_2 NRs specifically in terms of their length with the desired polydispersity index (standard deviation divided by mean length), a size-selective precipitation process was performed on as-synthesized TiO_2 NCs. We observed that to achieve a higher yield of NRs, it was crucial to separate larger NCs (here TiO_2 NRs) from the reaction mixture *just through centrifugation prior to the addition of antisolvent in the size-selective precipitation process*. Therefore, at first, we centrifuged the crude reaction mixture at 6000 rcf for 10 min and extracted the supernatant. In the next step, we separated the TiO_2 NRs that were

redispersed in toluene by the addition of acetone dropwise as an antisolvent to the NRs dispersion. The milky solution was centrifuged at 3400 rcf for 5 min and then NRs precipitations were redispersed in toluene. The washing step was repeated at least two times to achieve optically clear dispersions of titania NRs. The titania NRs were relatively monodisperse in their length (σ_L = 14%). The dimension of the NRs was on average 3.6 ± 0.3 nm (diameter) and 24.6 ± 3.4 nm (length) while the semispherical NCs had an average diameter of 5.7 nm. The NCs were redispersible in a variety of nonpolar solvents such as toluene or hexane. However, we chose toluene as a solvent in purification steps since it has a high refractive index which reduces the van der Waals attractions between the rods and is also a good solvent for OLAC. It has been shown that hexane has a higher solubility for oleic acid than toluene and can strip off ligands in the presence of antisolvent, while in toluene ligands remain at the surface of the NPs [126]. To monitor the evolution of the TiO_2 NCs, we extracted aliquots of the hot reaction mixture at scheduled time intervals using long capillary soda-lime glass Pasteur pipettes. These hot extractions were swiftly cooled down to room temperature via quenching in a toluene medium to stop further crystal growth and investigated by the transmission electron microscopy technique.

3.5.3 Self-Assembly of TiO_2 NRs

Typically, a droplet (~5 μL) of ligand-capped titania NRs dispersion with a low concentration (roughly 4 mg/mL) was dropcast on a carbon-coated 300 mesh copper TEM grids (Agar Scientific). The TEM grids were further dried in a vacuum chamber to remove residuals and used for microscopy analysis. To examine liquid crystalline structures of self-assembled domains in bulk, a sedimentation experiment was performed as previously reported elsewhere [27,188]. Briefly, a glass capillary (0.1 × 1.0 × 60.0 mm^3, Vitrocom) was filled with ligand-capped titania NRs dispersion with an initial volume fraction of 29.8 vol.%, effective length L = 27.6 nm, diameter D = 6.6 nm, and an aspect ratio of 4.18, in which the ligand length of 1.5 nm was taken into account. Then, the capillary was sealed using a two-component epoxy glue (Bison Kombi rapid), left vertically to sediment for 10 days, and was further investigated by polarizing optical microscopy (POM) technique.

3.5.4 Characterization of TiO_2 NCs

The X-ray diffraction analysis (XRD) was performed using a Bruker-AXS D2 Phaser X-ray diffractometer with Co Kα radiation (λ = 1.79026 Å) operated at 30 kV and 10 mA. Transmission electron microscopy and selected area electron diffraction (SAED) of the brookite NRs were performed on an FEI Tecnai 20 electron microscope operating at 200 kV. The crystalline structures of the TiO_2 NRs were measured by a high-resolution transmission electron microscope (FEI-Talos F200X electron microscope). Typically, at least 100 particles were counted to calculate the anatase NRs size distribution and polydispersity index. The bandgap of the NRs was studied at room temperature (20 °C) with a diffuse reflectance UV-Vis spectrometer (HP 8452a model). Typically, the NRs dispersion was diluted in toluene and added to a quartz cuvette (optical path: 10 mm) sealed with a Teflon stopper. The absorption spectrum was measured while the wavelength was varied from 250 nm to 700 nm. For POM images, a Leica DM2700P microscope equipped with crossed polarizers a Nikon Z6 camera was utilized.

3.6 Supporting information

TableS1. Calculated parameters used in Scherrer equation ($L = K\lambda/\beta Cos\theta_\beta$) where ($\beta \cong 0.041b$), L is the average size, λ is the X-ray wavelength, β is the full-width at half maximum value calculated in radians by fitting peaks with a 4-parameter Gaussian profile, b is a coefficient in the 4-parameter Gaussian fit profile, θ_β is the Bragg angle for the measured peak, and K is a constant equal to 0.94.

plane index	2T	T	cos(T)	b	β	βcos(T)	L
{101}	29.8	14.9	0.966	1.117	0.0459	0.0443	3.78
{004}	44.6	22.3	0.925	0.221	0.0090	0.0084	19.97
{200}	56.6	28.3	0.881	1.324	0.0544	0.0479	3.506

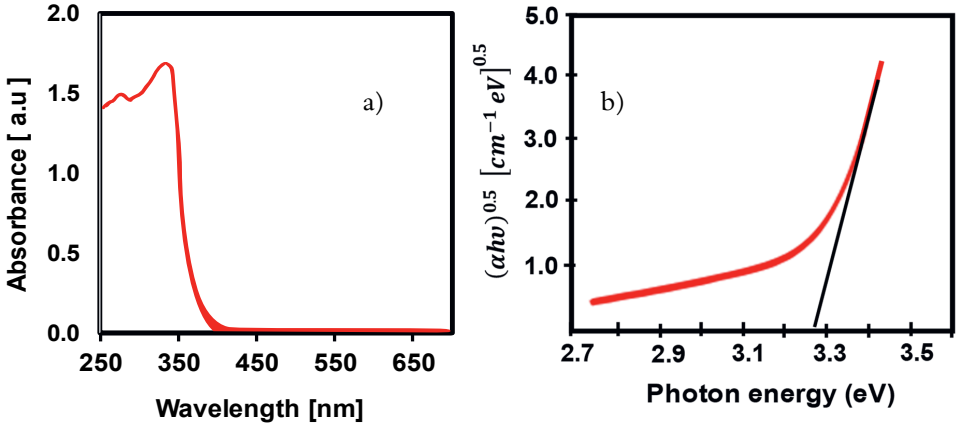

Figure S1. (a) A typical UV-Vis absorption spectrum of dilute dispersion of TiO_2 NRs in toluene. The spectrum shows a sharp absorption edge at 380 nm corresponding to band-to-band transitions. (b) Energy dependence of $(\alpha hv)^{0.5}$ versus Photon energy (hv) for the determination of the band gap derived from diffused UV-Vis absorption spectrum of TiO_2 NRs based on indirect transitions (n=0.5) for anatase NRs. The bandgap of the anatase NRs was estimated based on ($\alpha = K(h\nu - E_g)^{0.5}/h\nu$) where E_g is the bandgap, α is the absorption coefficient, K is the absorption constant for indirect transitions, and hv is the incident photon energy. The bandgap of the anatase NRs is equal to 3.28 eV which is calculated from the extrapolation of the absorption edge onto the energy axis where $\alpha = 0$.

Extra HRTEM images on anatase NRs

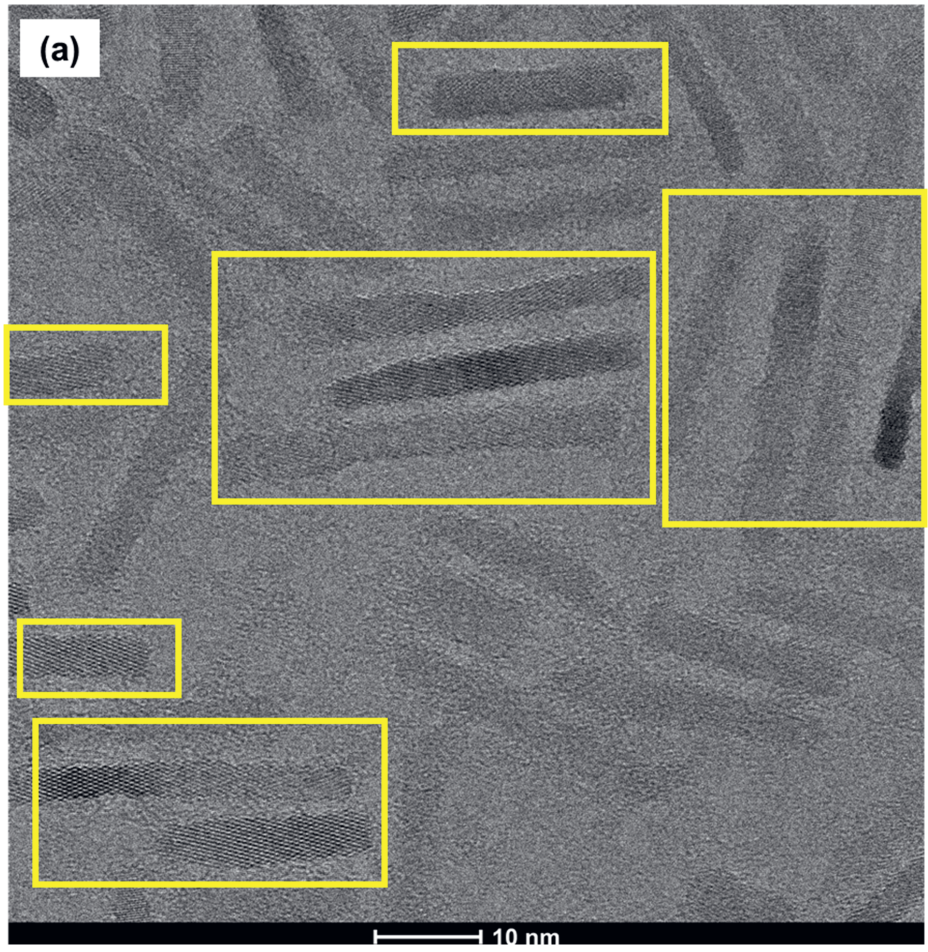

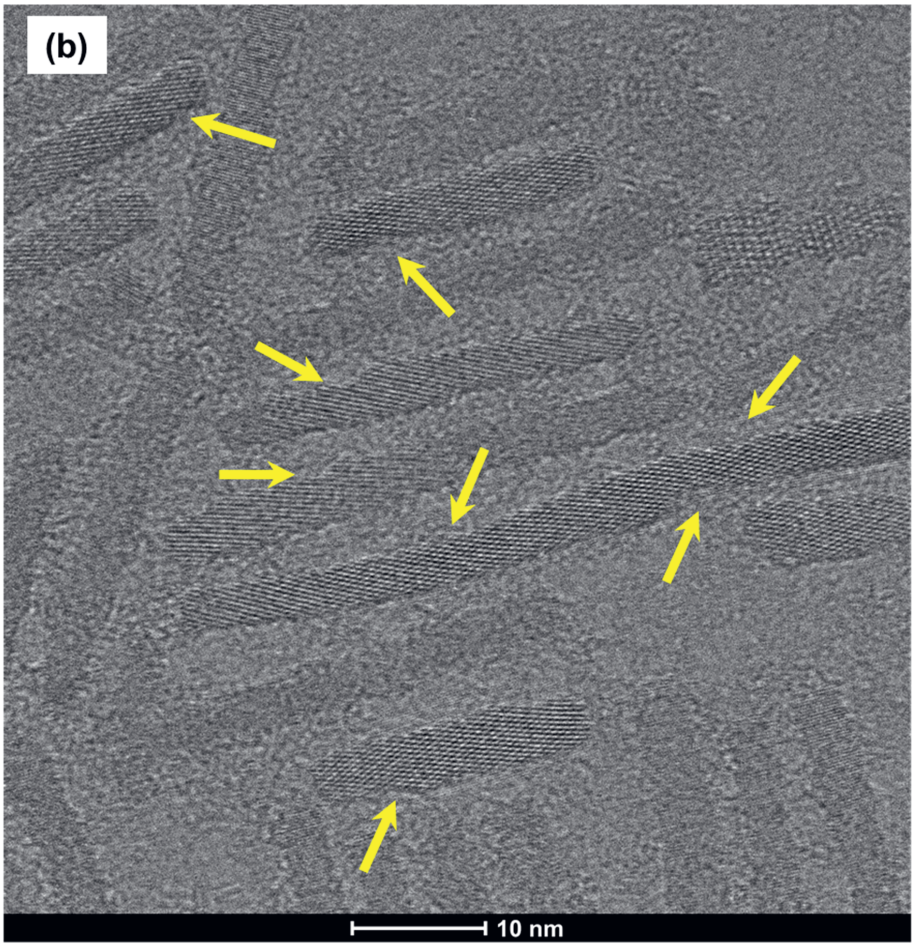

Figure S1. Extra HRTEM micrographs of anatase NRs. Surface features of the NRs are labelled by yellow arrows and lines on the surface of the NRs such as steps, corrugated sides, zigzag patterns, and sharp edges.

Extra TEM images on self-assembled anatase NRs

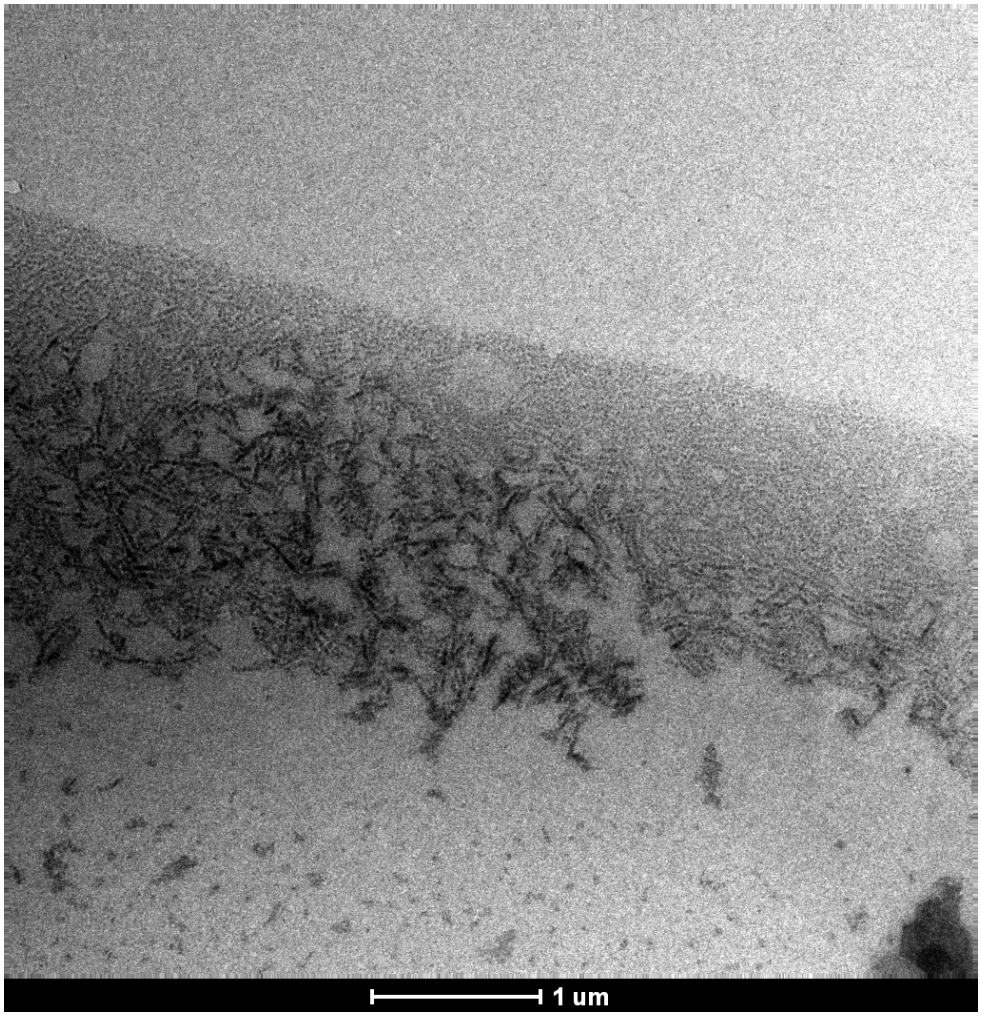

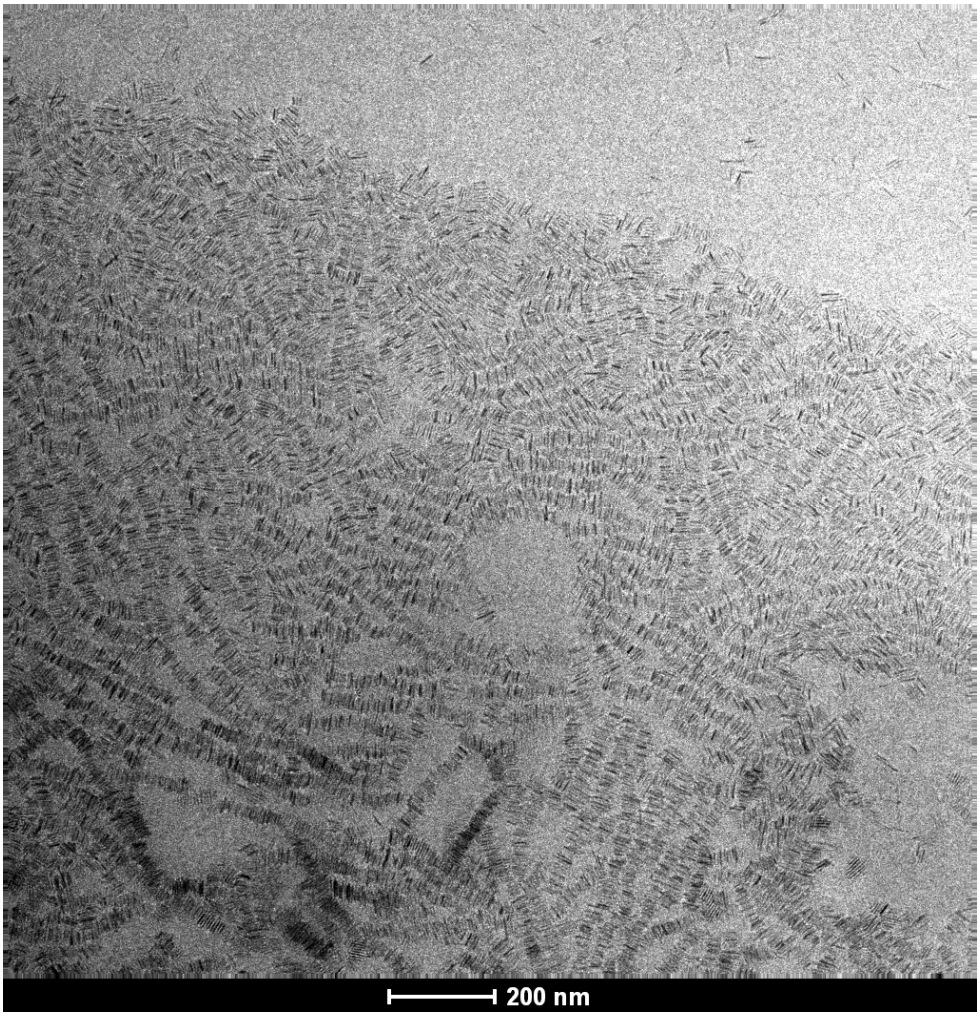
200 nm

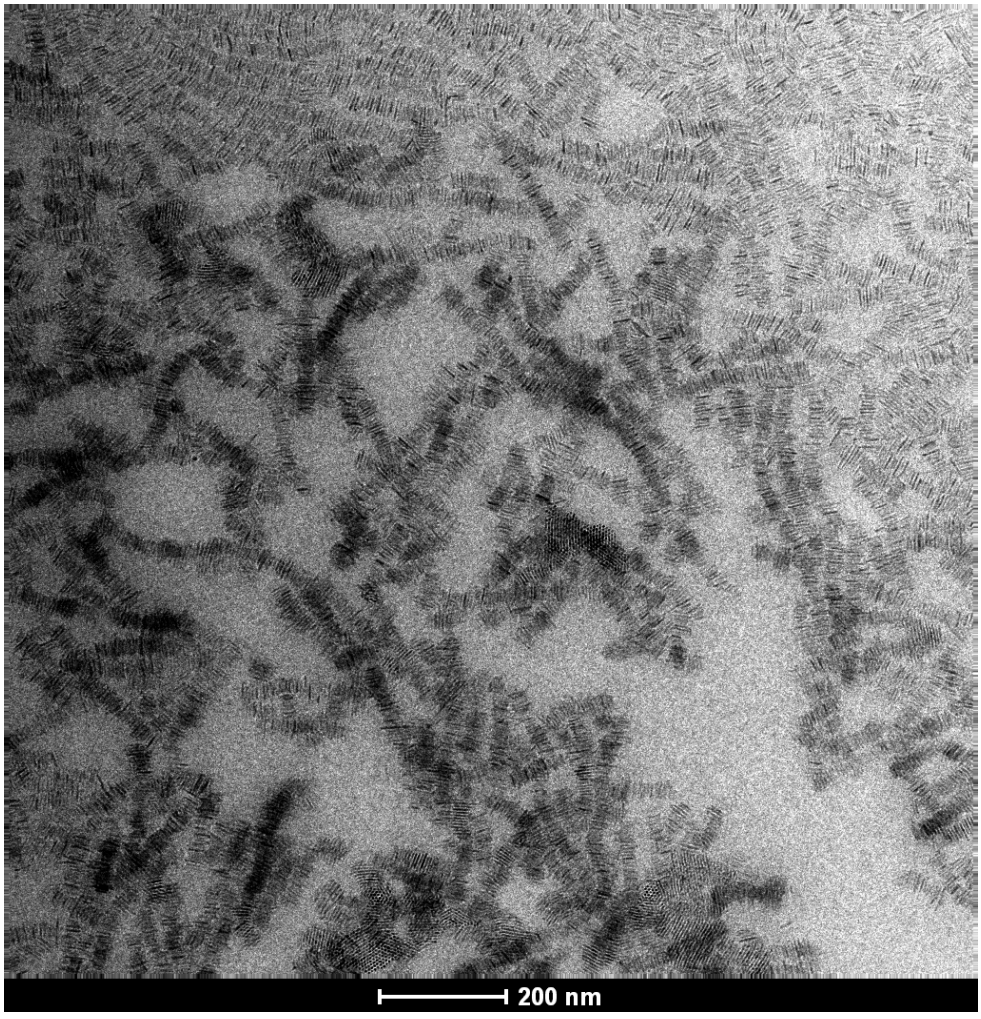

Figure S2. TEM images of anatase NRs self-assembled on a TEM grid at different magnifications. In the zoom out image, a region similar to the so-called coffee-ring region can be observed where the fluid flow transported NR rail-tracks radially outward and accumulated at the perimeter resulted in laterally packed tracks and random smectic domains. In the inner part of the coffee-strain ring, we could either examine vertically ordered NRs in closed-pack regions or shorter rail-tracks randomly arranged even on top of each other like criss-crossed.

4

TiO_2 nanorod liquid crystals in external electric fields

Brookite and anatase titanium dioxide (TiO_2) nanorods (NRs) dispersed in apolar solvents form highly stable colloidal dispersions and can self-assemble into various colloid-based liquid crystal phases. Here, we illustrate the electric-field-induced birefringence, known as the Kerr effect and the induction of (para)nematic liquid crystal phases from isotropic dispersions of TiO_2 NRs by external electric fields. The electro-optical responses of these two NRs dispersions are probed by utilizing in-plane pulsed d.c. electric fields. In our preliminary results, we observed that the NRs could be aligned into the direction of the applied electric field within ca. 250 μs switching times at various field strengths, one order of magnitude faster than commercial molecular liquid crystals undergoing a Freedericksz transition by an external electric field. Possible mechanisms contributing to the reorientation of the TiO_2 NRs studied are discussed. Induced dipole moments are calculated based on electric polarizabilities of titania NRs in various electric fields ranging from ca. 12 Debye in $3\,V/\mu m$ for anatase NRs in toluene to ca. 92 Debye in $10\,V/\mu m$ for brookite NRs in butylbenzene. Nevertheless, since the TiO_2 NRs studied were charged particles in the solvents studied, in d.c. electric fields, the polarization of their electrical double layer via the Maxwell–Wagner–O'Konski mechanism is hypothesised to contribute also significantly to the mechanisms describing the alignment dynamics of the NRs. By validating our experimental observations with theories, we find that rise times in anatase dispersion $(\varphi_{\mathrm{ana,disp}} = 0.298)$and brookite dispersion $(\varphi_{\mathrm{bro,disp}} = 0.229)$ are on the order of 16 to 27 μs for $E = 10\,V/\mu m$, whereas the relaxation times are approximated to be between ca. 120 to 240 μs in these semi-dilute NRs dispersions. Moreover, to estimate the refractive index of TiO_2 dispersions and possible birefringence observed in the electric field, we measured refractive indexes of anatase and brookite colloidal dispersions at various volume fractions and compared it with effective medium models such as Maxwell-Garnett and Bruggeman theories. The estimated intrinsic birefringence at a volume fraction of about 10.0% for the studied anatase and brookite NRs dispersions (which come to 28.0 vol.%, including the ligand layers) based on the NRs' birefringence, were approximated to be 0.043 and 0.075, respectively. We believe that the high-speed switching times of these non-aqueous transparent colloidal dispersions coupled with high degrees of Kerr induced birefringence allow us to utilize them in fast switchable optics applications.

4.1 Introduction

One of the first experimental observations on the existence of inorganic liquid crystals (LCs) goes back to 1902 when Majorana studied the induced optical anisotropy in dispersions of anisotropic magnetic particles applying magnetic fields which was so-called after him the Majorana effect.[14] Afterward, Diesselhorst and Freundlich in 1915 and Zocher 1925 reported on the birefringence of vanadium pentoxide dispersions subjected to flow or to external electric fields.[11,16–20] In 1949, in the pioneering work of Onsager, the spontaneous formation of lyotropic LC phases was theoretically predicted through an excluded volume theory for hard rods with the 'infinite' (large) aspect ratios. In this statistical physics model, the onset of nematic order in dispersions of thin hard rod-shaped particles in a first-order phase transition is explained.[22,38] Subsequently, in the last several decades, numerical simulations of LC mesogens combined with many experimental observations provided a more comprehensive framework to understand the phase behavior of such hard rod-shaped dispersions.[28,41,44]

Several reasons for the interest in these colloid-based lyotropic LCs can be summarized as follows: 1)To extend properties in the more conventional molecular thermotropic LCs such as threshold voltage, response times, birefringence (dielectric anisotropy), viscosity. 2)To add certain functionalities to the LC phases more easily such as ferromagnetism and fluorescence. 3)To combine colloid-based LCs with molecular LCs. 4)To use colloid-based LCs as model systems to learn more about LC phases and phase transitions as the interactions between colloids can be manipulated relatively easily and they can be studied quantitatively in real space on a single particle level.[69,101,234–236] Organic mesogens are already often used in thermotropic LC-based devices such as displays, spatial light modulators, switches, and filters, but they have an important downside which can be improved by using colloid-based LC phase: their response times for fast switchable electro-optical applications is relatively slow. This is intrinsically linked to the fact that individual anisotropic molecules have small polarizabilities as compared to colloidal particles as this property scales with the volume, which prevents them from coupling to external electric fields strongly unless they are already condensed into a LC phase. The Fréedericksz transition is a phase transition in LCs produced when a sufficiently strong electric or magnetic field is applied to a LC in an undistorted state. Below a certain field threshold the director, which is a vector that is pointing locally in

the average same direction as the rod-like particles are pointing in, remains undistorted.[237] As the field value is gradually increased from this threshold, the director begins to twist until it has aligned with the field. However, for molecular LCs, the Freedericksz transition is slowed down because of the relatively large viscosity of molecular LC phases which causes a strong hydrodynamic coupling leading to a slow relaxation time, typically in the order of milliseconds where the cell gap in the LC cell (d), the elastic constant (K), and η the viscosity of the LC mesogens are the main controlling factors ($\tau_{off} \approx \eta d^2/K$).[238]

A lot of studies have been devoted to improving the switching dynamics employing different routes such as hybrid LC composites,[239,240] novel device designs[241], or as we are pursuing in the present paper: colloid-based LCs.[238,242,243] In this regard, several inspiring reports were published by Fontana et al. on switchable gold nanorods (NRs) colloidal dispersions that were proposed as a novel substitution for conventional molecular LCs.[238,244–246] They confirmed that gold NRs can have faster switching times, namely microseconds ($\eta l^3/k_bT \approx \mu s$, where l is the length of the NRs, η is the viscosity, k_b is the Boltzmann constant, and T is the temperature), in comparison to typical organic molecular LCs. They attributed the much faster switching times to the large electric susceptibility of the gold NRs. In the strong fields out of the Kerr regime, the required time to align the LC mesogens along the applied electric field (on-time) scales proportionally to the square of the applied field, $\tau_{on} \approx \eta/\varepsilon E^2$, where ε is the dielectric permittivity, and E is the electric field strength.[245] We note that in the Kerr regime, the Kerr constant of the dielectric liquid is the same in the whole applied electric field range. However, the relaxation time of aligned particles (τ_{off}) is due to the thermal rotational diffusion of the LCs and is characteristically the limiting parameter to control the overall switching time. As mentioned, in the case of gold NRs dispersions, switching dynamics enhanced to microsecond timescales, three orders of magnitude faster than switching of conventional typical molecular LCs based on the Freedericksz transition.[244] In follow-up work by Fontana and coworkers, they showed that by employing sophisticated fiber optics components, switching times could be further reduced to submicrosecond switching times because of the larger electric fields (up to ca. 32 V/μm) that could be used.[245] In this work we wanted to see how fast semiconductor colloidal rods could be switched and how this compared to the metallic nanorods.

We investigate the electro-optical response of isotropic TiO_2 NRs dispersions in terms of field-induced birefringence via the Kerr effect. Additionally, using measured RIs and volume fractions of anatase and brookite NRs in effective medium models, estimated RIs for the TiO_2 NRs colloidal dispersions were obtained and compared with the experimentally measured values. The dynamics of TiO_2 NRs in dilute and semi-dilute dispersions were studied theoretically and compared with the relaxation times observed experimentally. Possible mechanisms contributing to the reorientation of TiO_2 NRs are discussed. In preliminary experiments, we show that our NRs, anatase dispersion $(\varphi_{ana,disp} = 0.298)$ and brookite dispersion $(\varphi_{bro,disp} = 0.229)$, could be aligned into the direction of the applied electric fields within ca. 250 μs. These switching times are at least 10 times faster than conventional LCs mesogens. The high-speed switching times of these optically clear and highly stable colloidal dispersions can be potentially utilized to modulate optical signals in optical shutters, filters, and spatial light modulators.

4.2 Theory

4.2.1 Refractive index of molecular and colloidal NRs based LCs

In general, it is the anisotropic optical properties of LCs that make them of interest to many optical applications.[5,247] For instance, the RI and birefringence are two essential features in designing various LC-based technologies. In uniaxial LCs, the incoming light wave after entering the anisotropic LC medium splits into an ordinary ray polarized parallel to the nematic director and an extraordinary ray polarized perpendicular to the director. When the two rays recombine as they exit the LC medium, the retardation or phase shift results in a different polarization state of the transmitted light.[248] Therefore, LC phases generally have two major RIs: n_e is the extraordinary RI observed for the extraordinary ray of a light with the electric vector parallel to the director field. In contrast, the ordinary RI, n_o, is observed when the electric vector of the linearly polarized light wave is perpendicular to the director of the LC. Birefringence is then defined by the difference between the two RIs ($\Delta n = n_e - n_o$), which is mostly positive ($\Delta n > 0$) for the conventional molecular LCs.[3] In general, birefringence is an intrinsic property of many materials with anisotropic optical properties such as calcite, quartz, and crystalline TiO_2 which is caused by asymmetries in their crystal structures and is thus direction-dependent.

Nevertheless, it can also stem from other reasons, such as structural ordering, physical stress-strain, and/or flow. Structural birefringence is a property of a wide range of anisotropic soft matter structures including biological macromolecular assemblies, synthetic fibers, long-chain polymers, and liquid crystalline structures. Structural birefringence can be sensitive to RI fluctuations or gradients in the surrounding medium caused by external forces and/or deformations.[6,249]

In thermotropic LCs, the structure of the mesogens together with the operating wavelength and temperature are the key parameters in determining the LC RIs. In these LCs, when the temperature increases, n_e will decrease monotonously whereas n_o may decrease or increase depending on the transition temperature of the LC used.[250] Therefore, it is quite important to know the wavelength-dependent RIs as well as the thermal effects in advance to optimize for applications of these materials.[248] Organic rod-like molecular LCs are stiff extended molecules often with extended π-conjugated double bonds. Because of this various models such as the Lorentz-Lorenz equation and Cauchy equation, which are common for isotropic liquids, need to be modified before they can be used for organic LCs to evaluate the RI dependencies as a function of wavelength and temperature.[251] For instance, Vuks in 1966 proposed a semiempirical model analogous to the classical Clausius-Mossotti equation correlating the microscopic LC molecular polarizabilities to the macroscopic RIs.[252] Afterward, based on this model several phenomenological models such as the single-band model, the three-band model, and extended Cauchy equations were established to approximate the LC RI dependencies in various wavelengths and temperature ranges.[251–253]

The lyotropic LCs studied in this chapter are as mentioned dispersions of anisotropic particles in an isotropic liquid. When these particles collectively form LC mesostructures in the isotropic medium, they affect the light wave passing through this composite medium. Hence, several mixture models such as the Maxwell–Garnett equation (M-G),[254] the Bruggeman equation,[255] the Heller empirical correction equation,[256] the Lichtenker rule,[257] and the Jaysundere–Smith equation[258] have been proposed for predicting the effects of second phases on various electrical properties of composite media including dielectric permittivities and RIs. To follow these models, several points should be taken into account: 1) The particles may have an intrinsic birefringence due to asymmetry in their crystallographic structures. 2) In the models as

used in this paper it is assumed that both the particles and matrix components should not have a dielectric loss in frequency regions of interest. 3) Most of these models were developed for spherical particles and therefore need to be modified for anisotropic systems. To consider shape anisotropy, a depolarization factor can be introduced in some models which is related to this deviation from sphericity and isotropy. 4) How the particles are dispersed or structured within the dispersion medium, e.g. non-touching or in the other extreme as a percolating network, affect the dielectric properties and RIs. 5) Several of the models make certain assumptions on to the volume fractions of the dispersed particles and only are valid in specific volume fractions limits.[259,260]

Most of the TiO_2 dispersions studied in this chapter, when no field is applied, have NRs loading up to nearly 30.0 vol.%, which for the aspect ratios of the particles studied is close to but below the volume fraction at which they would form LC phases, they are then uniformly dispersed in the solvent with isotropic properties. Therefore, based on these conditions as well as other experimental results reported for similar systems,[260–264] we compared our experimentally observed RI of the dispersions with the M-G equation,[263,265] a modified M-G equation for anisotropic particles,[259] and Bruggeman's equation.[265]

4.2.1.1 Maxwell-Garnett equation

The M-G theory is an effective medium model that approximates the physical properties of a composite material using averaging functions depending on the properties of the components and their proportions. Following reference[265], we consider an isotropic medium of dielectric permittivity ε_m filled with spherical particles of dielectric permittivity ε_p. The volume fractions of the filler particles and the medium are denoted by φ_p and $\varphi_m = 1 - \varphi_p$. By considering a small volume fraction approximation ($\varphi_p \ll 1$) and no dielectric loss in frequency regions of the interest, the effective average electric field in the composite mixture $\vec{E}_{eff}$ can be written as a function of the electric fields inside the filler particles $\vec{E}_p$ and the host medium $\vec{E}_m$ as:

$$\vec{E}_{eff} = \varphi_p \vec{E}_p + (1 - \varphi_p)\vec{E}_m. \qquad \text{Eq. 4-1}$$

In the same way, the average dielectric displacement can be considered as follows:

$$\vec{D}_{eff} = \varepsilon_0 \varepsilon_{eff} \vec{E}_{eff} = \varphi_p \varepsilon_0 \varepsilon_p \vec{E}_p + (1 - \varphi_p) \varepsilon_0 \varepsilon_m \vec{E}_m. \quad \text{Eq. 4-2}$$

where ε_0 is the vacuum permittivity and ε_{eff} is the effective dielectric permittivity. When the size of the particles, d, is relatively small compared to the wavelength of the electromagnetic wave λ which is passing through the particle, the phase shift in the electromagnetic wave will be constant and $2\pi\sqrt{\varepsilon_p}d/\lambda \ll 1$. Therefore, the electric field inside the particles can be obtained using the quasi-static approximation:[265]

$$\vec{E}_p = \frac{3\varepsilon_m}{(\varepsilon_p + 2\varepsilon_m)} \vec{E}_m. \quad \text{Eq. 4-3}$$

Using Eq. 4-1 to Eq. 4-3, the M-G effective medium equation can be obtained as shown in Eq. 4-4:

$$\varepsilon_{eff} = \varepsilon_m \left[1 + \frac{3\varphi_p(\varepsilon_p - \varepsilon_m)}{(\varepsilon_p + 2\varepsilon_m) - \varphi_p(\varepsilon_p - \varepsilon_m)} \right]. \quad \text{Eq. 4-4}$$

In the visible spectral region far from the absorption bands, the RI can be approximated accurately by the square root of the dielectric constant according to Maxwell's electromagnetic theory $\varepsilon^{1/2} = n$.[266] Therefore, Eq. 4-4 can also be written as a function of RIs:

$$n_{eff}^2 = n_m^2 \left[1 + \frac{3\varphi_p(n_p^2 - n_m^2)}{(n_p^2 + 2n_m^2) - \varphi_p(n_p^2 - n_m^2)} \right] \quad for\ \varphi_p < 0.1 \quad \text{Eq. 4-5}$$

In the case of ligand-capped NPs, we assume that the ligand molecules have been uniformly adsorbed at the surface of the NPs while solvent molecules can penetrate the ligand layer assuring the dispersibility of the NPs in the dispersion. The ligand layer can be therefore considered as a mixture of ligand molecules in the solvent molecules where the RI of close-packed ligand molecules at $\lambda = 587\ nm$ is ($n_{oleic\ acid}^{20} = n_{oleylamine}^{20} = 1.459$) that is quite close to the RI of the solvent($n_{toluene}^{20} = 1.496$ or $n_{butylbenzene}^{20} = 1.489$). Then the RIs of the ligand molecules are assumed to be matched with the RIs of the solvents and thus, the ligand layer can be approximated well to have the same dielectric properties as the solvent. Therefore, we only considered bare titania NRs for the particle volume fraction used in the effective medium models. Using this assumption, the volume fraction used in our calculations φ_p is $\frac{V_{core}}{V_{core}+V_{ligand}+V_{solvent}}$ and the relative core volume, $V_i = \frac{W_i}{\rho_i}$ is

the volume of component i (with ρ_i and w_i denoting the density and mass of component i as measured in the Thermogravimetric Analysis (TGA)) we used.

As mentioned earlier, Eq. 4-5 generally assumes spherical particles. In the case of anisotropic particles, the geometry of the dispersed particles can be taken into account by introducing a depolarization factor, L, describing the deviation from sphericity. Then, the M-G equation can be written into a more general form:[259]

$$n_{eff}^2 = n_m^2\left[1 + \frac{\varphi_p(n_p^2 - n_m^2)}{L(1-\varphi_p)(n_p^2 - n_m^2) + n_m^2}\right] \quad for\ \varphi_p < 0.1 \qquad \text{Eq. 4-6}$$

Different values for the depolarization factors have been calculated for several geometries in the literature[255] and can be found below in Table 4-1. If $L = 0.33$, Eq. 4-6 turns back to that of spherical particles shown in Eq. 4-5.

Table 4-1. The equivalent depolarization factors of clusters build-up from spheres with various geometries.[255]

Geometrical configuration	Equivalent depolarization factors		
	L1	L2	L3
Single sphere	1/3	1/3	1/3
Double sphere	0.250	0.375	0.375
Single-strand chain	0.133	0.435	0435
Double-strand chain	0.139	0.342	0.518

4.2.1.2 Bruggeman's equation

In 1935, Bruggeman proposed an improvement for the mixing rules as an extension of the Lorentz-Lorenz equation. The main reason for doing this is that the M-G model treats the constituents asymmetrically such that one component constitutes particles while the other constitutes the host. Hence, the M-G model only would apply to composites with a small volume fraction of the filling material ($\varphi_p < 0.1$).[259,267] However, the

Bruggeman model avoids this problem by treating the constituents symmetrically and considering domains of materials randomly interspersed.[264,267] The commonly known Bruggeman's formula is shown in Eq. 4-7:[262]

$$\varphi_p \frac{n_p^2 - n_{eff}^2}{n_p^2 + 2n_{eff}^2} + (1-\varphi_p)\frac{n_m^2 - n_{eff}^2}{n_m^2 + 2n_{eff}^2} = 0 \qquad \text{Eq. 4-7}$$

Bruggeman's integration method can be seen as an extended mixing rule permitting the assessment of the overall electrical response at higher content of spherical particles as well. This is mainly interesting for a disordered system where dispersed particles may come close to each other ($\varphi_p > 0.1$). Under these assumptions, the solution of a differential equation obtained from either Eq. 4-5 or Eq. 4-7 would lead to the final Bruggeman's equation:[259]

$$\frac{n_p^2 - n_{eff}^2}{n_{eff}^{(2/3)}} = \frac{(1-\varphi_p)(n_p^2 - n_m^2)}{n_m^{(2/3)}} \quad \varphi_p < 0.5 \qquad \text{Eq. 4-8}$$

Although this equation is expected to hold for volume fractions up to 50 vol.%, it is valid only if the dispersed particles have not formed a percolative path throughout the medium.

4.2.2 Kerr effect and electric field-induced birefringence

In this section, we first recall the theoretical background that is necessary to interpret the experiments conducted. To this aim and because of similarities with our experimental conditions and studied colloidal dispersions, we mainly follow theoretical approaches that were successfully employed and confirmed by experimental reports from our research group[268,269] as well as other reports by Dozov et al.[270–272], Grelet et al.[273,274], Fontana et al.[238,244–246], Ponterio et al.[275,276], and, and Neyts et al.[243,277] Then in section 4.3.2, we evaluate our preliminary results regarding the characteristic times determining the alignment of titania NRs in the isotropic dispersion under the applied electric field.

When dispersions of anisotropic NPs (in our case NRs) are exposed to external stimuli such as electric fields, they exhibit electro-optical effects.[26,58,242,271,278]

Robust coupling of the NRs' orientation with an applied electric field (E), and the strong optical anisotropy of these NRs, either due to intrinsic properties and/or their shape anisotropy, are known to be the main factors corresponding to these electro-optical effects.[16,243] Principally, dispersed NRs align individually by the field resulting in an induced nematic-like LCs to a degree described by an order parameter $S(E)$. This order parameter is field-dependent such that at relatively weak fields, known as the Kerr region, $S(E)$ varies as a function of E^2 while at very strong fields, it saturates to an asymptotic value, +1 when all the rod-like particles are aligned in the same direction.[272] The preferential alignment in the applied external field is mainly dependent on the electric anisotropy within the particles for low volume fractions.[270] For dielectric NRs, it has been observed experimentally and theoretically[279] that they often typically align with their long axis along the field direction, although especially with magnetic particles there are also exceptions to this behavior.[280] This could arise from the anisotropy of the induced dipole moments and/or, in certain cases, the existence of a permanent dipole moment along the long axis of the dielectric NRs (e.g. CdSe/CdS,[243] CdSe,[281] TiO_2,[275,282] and cellulose NRs[283]). Metallic NRs, where ε has a strong frequency dispersion caused by coupling of the field with the conduction electrons, tend to align perpendicular or parallel to the field depending on the field frequencies.[244,284,285]

In general, three main mechanisms contribute to the induced dipole moment of a particle in an electric field:[271–273,286] **1)** Dielectric polarization, where the dielectric mismatch between the particle ε_p and the surrounding host medium ε_m gives rise to an accumulation of bound (polarization) charges on the particle/solvent interface proportional to the applied electric field.[243] **2)** The Maxwell-Wagner (M-W) mechanism originating from a contrast in the conductivities of the particles κ_p and surrounding host medium κ_m. This difference results in an induced dipole via accumulation of free charges on the particle/solvent interface. **3)** The Maxwell-Wagner-O'Konski (M-W-O) mechanism is due to the mobile counterions around the particles in the electrical double layer (EDL) and is important for charged colloidal particles.[287,288] In O'Konski's approach these ions are modeled by a surface conductivity of the colloids. The M-W-O mechanism describes the polarization of the ions in the EDL. We note that in the case of charged colloidal particles, the M-W-O mechanism often has been found to

be the most dominant mechanism for the dynamics of anisotropic particles in an electric field[271–273,286], even in apolar media [270,272].

Here, to assess the dielectric polarizability of titania NRs, we approximate them as ellipsoidal particles for which the theoretical description is easier to model.[268] It has been shown that the difference in the dielectric polarizability of cylinders (shapes similar to our titania NRs) and ellipsoids, with aspect ratios up to 10, is less than 10%.[289] Hence, when a cylindrical NR, approximated as an ellipsoid, is exposed to a homogeneous external field E in a host medium with a dielectric constant ε_m, the induced dipole moment $\boldsymbol{p_{ind}}$ with respect to the host medium is given by:[290]

$$\boldsymbol{p_{ind}} = \alpha_a \varepsilon_0 E_{\parallel} \boldsymbol{u}_{a,\parallel} + \alpha_b \varepsilon_0 E_{\perp} \boldsymbol{u}_{b,\perp} \qquad \text{Eq. 4-9}$$

where the unit vector $\boldsymbol{u}_{a,\parallel}$ points along the long axis of the ellipsoid, $\boldsymbol{u}_{b,\perp}$ and $\boldsymbol{u}_{c,\perp}$ points along the short axes, and $E_{\parallel}$ and $E_{\perp}$ are the electric field components projected on the unit vectors $\boldsymbol{u}_{a,\parallel}$ and $\boldsymbol{u}_{b,\perp}$, respectively. For an ellipsoidal particle with dielectric constants $\varepsilon_{NR,\parallel}$ and $\varepsilon_{NR,\perp}$, the polarizabilities along the long axis, $\alpha_{\parallel}$, and short axis, $\alpha_{\perp}$, are given by:[243,290]

$$\alpha_{\parallel} = \frac{\varepsilon_{NR,\parallel} - \varepsilon_m}{\varepsilon_m + L_{\parallel}(\varepsilon_{NR,\parallel} - \varepsilon_m)} V$$
$$\alpha_{\perp} = \frac{\varepsilon_{NR,\perp} - \varepsilon_m}{\varepsilon_m + L_{\perp}(\varepsilon_{NR,\perp} - \varepsilon_m)} V \qquad \text{Eq. 4-10}$$

Here V is the volume of the NR and $L_{\parallel}$ and $L_{\perp}$ represent the depolarization factors for fields parallel and perpendicular to the ellipsoidal particle (here NR long axis), respectively, as described in Eq. 4-11:[243]

$$L_{\parallel} = \frac{b^2}{a^2 - b^2}\left(\frac{a}{2\sqrt{a^2 - b^2}} ln\left(\frac{a + \sqrt{a^2 - b^2}}{a - \sqrt{a^2 - b^2}}\right) - 1\right)$$
$$L_{\perp} = \frac{1 - L_{\parallel}}{2} \qquad \text{Eq. 4-11}$$

where a and b are the length of the semi-axes in the ellipsoid. Due to the polarization, an induced torque is expected on the NRs that is equal to:

$$\boldsymbol{T_{induced}} = \boldsymbol{p_{ind}} \times \boldsymbol{E} = \frac{1}{2}(\alpha_{\parallel} - \alpha_{\perp})\, sin\, 2\theta\, \varepsilon_0 \boldsymbol{E}^2 \boldsymbol{u}'_{b,\perp} \qquad \text{Eq. 4-12}$$

Here, θ is the angle between the long axis of the ellipsoid and the electric field while $\boldsymbol{u}'_{b,\perp}$ is the unit vector orthogonal to both $\boldsymbol{u}_{a,\parallel}$ and $\boldsymbol{u}_{b,\perp}$.[243]

By considering a permanent dipole moment $\boldsymbol{p_{per}}$ along the long axis of the NRs, an additional dipolar torque arises as a result of an external electric field (Eq. 4-13). If we include the two torques into the reorientation equation of the ellipsoids, the resulting differential equation shown in Eq. 4-14 for the orientation angle θ can be derived:[243,284]

$$\boldsymbol{T_{per}} = \boldsymbol{p_{per}} \times \boldsymbol{E} = \boldsymbol{p_{per}} \boldsymbol{E}\, sin\, \theta\, \boldsymbol{u}'_{b,\perp} \qquad \text{Eq. 4-13}$$

$$I\frac{d^2\theta}{dt^2} + \gamma_r \frac{d_\theta}{d_t} = \sqrt{k_B T \gamma_r}\,\delta(t) + \boldsymbol{p_{per}} \boldsymbol{E}\, sin\, \theta + \frac{1}{2}(\alpha_{\parallel} - \alpha_{\perp})\, sin\, 2\theta\, \varepsilon_0 \boldsymbol{E^2} \qquad \text{Eq. 4-14}$$

The torque due to Brownian motion with k_B the Boltzmann constant, T the absolute temperature, and γ_r the rotational friction coefficient is presented in the first term on the right side.[291] I is the moment of inertia which can be neglected for small ellipsoids at frequencies lower than ~MHz. In this condition, the excess electrostatic energy of an ellipsoid in the external electric field and the corresponding field-induced orientational order parameter, *S(E)*, can be expressed in Eq. 4-15 and Eq. 4-16, respectively:[243,273]

$$U_e = -\boldsymbol{pE}\, cos\, \theta - \frac{1}{2}(\alpha_{\perp} + (\alpha_{\parallel} - \alpha_{\perp}) cos^2\theta)\varepsilon_0 \boldsymbol{E}^2 \qquad \text{Eq. 4-15}$$

$$S(E) = \frac{3}{2}\langle cos^2\theta \rangle - \frac{1}{2} = \frac{1}{2}\frac{\int_{-1}^{1}(3cos^2\theta - 1)\, exp(-U_e(cos\theta/kT))dcos\theta}{\int_{-1}^{1} exp(-U_e(cos\theta/kT))dcos\theta} \qquad \text{Eq. 4-16}$$

As we showed above, dispersed NRs in a solvent experience a reorientation with an order parameter ranging from 0 to 1, corresponding to randomly oriented NRs and fully aligned NRs, respectively. This uniaxial induced order is known as a (para)nematic phase (nematic-like orientational order). The birefringence of this phase and the effective applied electric field are related via a quadratic law, known as Kerr's law. As the field strength increases the orientation of the dispersed NRs gradually approaches the field

direction until they are fully aligned. Using Eq. 4-15 and Eq. 4-16, the induced birefringence can be expressed in Eq. 4-17:[273]

$$\Delta n = \Delta n_{sat}\left(1 - exp\left[\left(-\frac{E}{E_{sat}}\right)^2\right]\right) \cong \lambda B E^2 \qquad if\ E \ll E_{sat} \qquad \text{Eq. 4-17}$$

As shown in Eq. 4-17, Kerr's law can be approximated in a simpler form if field strengths are in the weak region or Kerr region where $E \ll E_{sat}$. In Eq. 4-17, λ is the the light wavelength used for observations, Δn_{sat} and E_{sat} are the saturated birefringence and its corresponding field strength, respectively. B is the Kerr coefficient which quantifies the coupling between the Δn and E. Since the Kerr coefficient has a quadratic dependence on Δn at low electric fields, it can be deduced from the slope of the equilibrium birefringence value as a function of the field. It can also be obtained when saturation is observed in the induced birefringence:[273]

$$B = \frac{\Delta n_{sat}}{\lambda E_{sat}^2} \qquad \text{Eq. 4-18}$$

It is worth noting that in the case of TiO_2 NPs, experimental observations by Pochylski et al. have confirmed 5 orders of magnitude increase in the Kerr coefficients for the TiO_2 NPs they studied with respect to their pure solvents, $B_{TiO2/silicone\ oil} = -9.23 \times 10^{-10}\ mV^{-2}$ and $B_{TiO2/octanoic\ acid} = -4.76 \times 10^{-10}\ mV^{-2}$), which is close to values usually observed for molecular commercial LCs (e.g., $B_{5CB\ LCs} = 1.12 \times 10^{-10}\ mV^{-2}\ at$ 35.6 ℃).[275]

Also, we note that E_{sat}, Δn_{sat}, and B values provide important information about the anisotropy of the excess polarizability of the NRs. For rod-like particles, Dozov et al. showed that the anisotropy of the excess polarizability can be written as follows:[271,272]

$$\Delta A = \frac{\Delta \alpha}{kT} = \frac{15}{E_{sat}^2} \qquad \text{Eq. 4-19}$$

Here, the coupling parameter ΔA is the anisotropy of the excess polarizability of the NRs, whereas all the above-mentioned three mechanisms (dielectric mechanism, MW, and MWO mechanisms) may have contributions to the coupling parameter.

4.2.3 Rise and decay times in TiO_2 dispersions based on the rotational diffusion coefficients of the dispersed TiO_2 NRs

In general, there are three different relaxation times involved in the rotational diffusion process in an electric field. The first one, $1/(6D_{\perp}^{r})$, is related to the rotational diffusion of the particles and describes the alignment of the polarizability of the particle, α. Two other terms are $1/(2D_{\perp}^{r})$ and $1/(D_{\perp}^{r}+D_{\parallel}^{r})$ and are associated with the relaxation times of the longitudinal and transverse components of the permanent dipole moment of the particle, respectively. When the electric field is switched on, all of these three rotational diffusion components can be involved based on the characteristics of the studied material system whereas in the decay times, when the field is off only $1/(6D_{\perp}^{r})$ is involved.[270]

As we showed in section 4.2.2 in Eq. 4-13 and Eq. 4-14, by assuming a dipole moment $\boldsymbol{p}$ along the long axis of the titania NRs, an additional dipolar torque is present in an external electric field associated with a parameter, γ_r, representing the viscous torque. γ_r can be approximated as follows:[284]

$$\gamma_r = \frac{16\pi\eta\sqrt{a'^2-b'^2}(a'^4-b'^4)}{3(a'^2-\frac{b'^2}{2})\ln(\frac{a'+\sqrt{a'^2-b'^2}}{a'-\sqrt{a'^2-b'^2}})-(a'\sqrt{a'^2-b'^2})} \qquad \text{Eq. 4-20}$$

where η is the dynamic viscosity of the medium (in Pa.s), and a' and b' are the semi-axes of ellipsoidal titania NR for which the ligands molecules have been taken into account (ligand length of 1.5 nm). Neyts et al. showed that the time to align a spheroid when a sufficiently strong electric field is switched on, τ_{ON}, can be approximated well by neglecting the Brownian term in Eq. 4-14, replacing the derivative by the ratio $\Delta\theta/\tau_{ON}$, and setting $\Delta\theta=\pi/4$:

$$\tau_{ON} = \frac{\pi\gamma_r}{2(\sqrt{2}\boldsymbol{pE}+(\alpha_{\parallel}-\alpha_{\perp})\varepsilon_0\boldsymbol{E}^2)} \qquad \text{Eq. 4-21}$$

Furthermore, the relaxation time, τ_{OFF}, which is generally longer than τ_{ON}, can be measured when the electric field is switched off. The relaxation time and corresponding birefringence relaxation back to an isotropic state originates from the thermal diffusion

randomizing the particle orientations and can be estimated using the Debye-Perrin model:[243]

$$\tau_{OFF} = \frac{\gamma_r}{k_B T} \qquad \text{Eq. 4-22}$$

In addition to the aforementioned approaches, we can also validate measured switching times by calculating the rotational diffusion coefficient $D_{\perp}^{r}$. There are many different relations suggested for calculating the diffusion coefficients of rod-shaped particles in dilute dispersions that are mainly based on modifications to the Stokes-Einstein equations for spheres.[292] In this regard, two expressions for the rotational diffusion coefficient $D_{\perp}^{r}$ and the translational diffusion coefficient $D_{\parallel}^{r}$ of long thin rods with a given length l and diameter d have been approximated by Kirkwood-Riseman:[292]

$$D_{\perp}^{r} = \frac{3k_B T}{\pi\eta l^3} ln(l/d) \qquad \text{Eq. 4-23}$$

$$D_{\parallel}^{r} = \frac{k_B T}{3\pi\eta l} ln(l/d) \qquad \text{Eq. 4-24}$$

Here it has been assumed that the rods behave in a viscous medium with viscosity η. Later, Tirado and de la Torre carried out a numerical evaluation of the translational and rotational diffusion coefficients of cylinders based on a more rigorous approach than the Kirkwood-Riseman results given above. Their results were in excellent agreement with experimental data for short microscopic cylinders. Therefore, for dilute dispersions of finite rods ($2 < l/d < 30$) modeled as cylinders, the expressions for the diffusion coefficients can are given by:[27,293]

$$D_{\perp}^{r} = \frac{3k_B T\,(ln(l/d) + \delta_{\perp})}{\pi\eta l^3} \quad where:\ \delta_{\perp} = -0.662 + 0.917\left[\frac{d}{l}\right] - 0.05\left[\frac{d}{l}\right]^2 \qquad \text{Eq. 4-25}$$

$$D_{\parallel}^{r} = \frac{k_B T\,(ln(l/d) + \nu)}{3\pi\eta l} \quad where:\ \nu = 0.312 + 0.565\left[\frac{d}{l}\right] - 0.1\left[\frac{d}{l}\right]^2 \qquad \text{Eq. 4-26}$$

One can expect that by increasing the concentration of the NRs in the dispersion, the motion of each rod becomes hindered by its neighbors, followed by a reduction in the translational and rotational diffusion coefficients. In this regard, Doi and Edwards have

presented a theory for the diffusion coefficients of rods with number concentration ($c = \varphi_p/V_p$) where $1/l^3 \ll c < 2\pi/dl^2$.[294,295] They assumed that the rods are still oriented randomly but their motions are strongly hindered by steric repulsions between rods. Also, the translational motion parallel to the rod's axis is unhindered (such as for thin rod-like macromolecules with large aspect ratios) and equal to its infinite dilution value ($D_{\parallel}^r$ in Eq. 4-26). Then, the rotational diffusion coefficient in the semi-dilute region is given by:[292,296]

$$D_{\perp}^r = \beta k_B T \frac{ln(l/d)}{\eta c^2 l^9} = \beta k_B T \frac{ln(l/d)}{\eta (\varphi_p/V_p)^2 l^9} \qquad \text{Eq. 4-27}$$

where β is a proportionality constant and has been reported to be approximately $\beta \simeq 0.5$ for NRs with aspect ratios smaller than 10.[273] Doi and Edwards also noted that in the concentrated region ($c \gg 1/l^3$), $D_{\perp}^r$ becomes (much) smaller due to non-Newtonian viscoelasticity. Thus, the viscosity of more concentrated dispersions becomes signficantly greater than the solvent viscosity as a result of rotational degrees of freedom of the dispersed rods and can be approximated by:[295]

$$\eta_{concentrated} = \eta_{solvent}[1 + (\varphi_p/V_p)^3 l^9] \qquad \text{Eq. 4-28}$$

4

4.3 Results and discussion

4.3.1 Refractive indexes of anatase and brookite colloidal dispersions

In Figure 4-1, we show the effective RIs of two different titania colloidal dispersions in magenta square markers measured using an Abbe refractometer at the wavelength of $\lambda = 589.6\ nm$. Additionally, the trends predicted on the basis of the M-G effective medium theories for spherical and anisotropic particles, are depicted. To validate our observations with the theory, as mentioned in section 4.2.1.1, the following assumptions were taken:

We assumed for the calculations of the volume fractions that the bare crystals of anatase and brookite NRs were dispersed in toluene and butylbenzene, respectively, and neglected small differences in the index of the ligand layer as detailed in the following.

The RIs of the bare crystals of anatase and brookite NRs at $\lambda = 589.6\,nm$ are known to be ($n_{ana,ext} = 2.488$ and $n_{ana,ord} = 2.561$) and ($n_{bro,ext} = 2.700$ and $n_{bro,ord} = 2.583$), respectively.[297][298] As was already mentioned before regarding the index of the ligand layer, since the solvent molecules simply penetrate in this layer to assure the dispersibility of the NRs in the dispersion, the whole ligand layer can be presumed as a mixture of ligand molecules in the solvent molecules. The RI of the ligand molecules ($n^{20}_{OLAC} = n^{20}_{OLAM} = 1.459$) is close to the RI of the solvents ($n^{20}_{toluene} = 1.496$ or $n^{20}_{butylbenzene} = 1.489$) and therefore the RI of the ligand molecules is closely matched with the RI of the solvents used. To calculate the effective RIs of the dispersions based on the M-G model for anisotropic particles (Eq. 4-6), we approximated our NRs as equivalent ellipsoids with the same volume and axial ratios.[299] In the case of the bare anatase NRs, the average dimensions, measured from TEM images, was $l = 24.6\,nm$ and $d = 3.6\,nm$ which translated into the equivalent ellipsoid size of $2a = 28.3\,nm$ and $2b = 2c = 4.14\,nm$. The same concept was also considered for bare brookite NRs where the average NRs size was $l = 27.4\,nm$ and $d = 3.4\,nm$ and the equivalent ellipsoid size was NRs $2a = 31.5\,nm$ and $2b = 2c = 3.9\,nm$. Moreover, specific depolarization factors for these ellipsoids were employed from Table 4-2 which were calculated for fields parallel and perpendicular to the ellipsoidal particles.

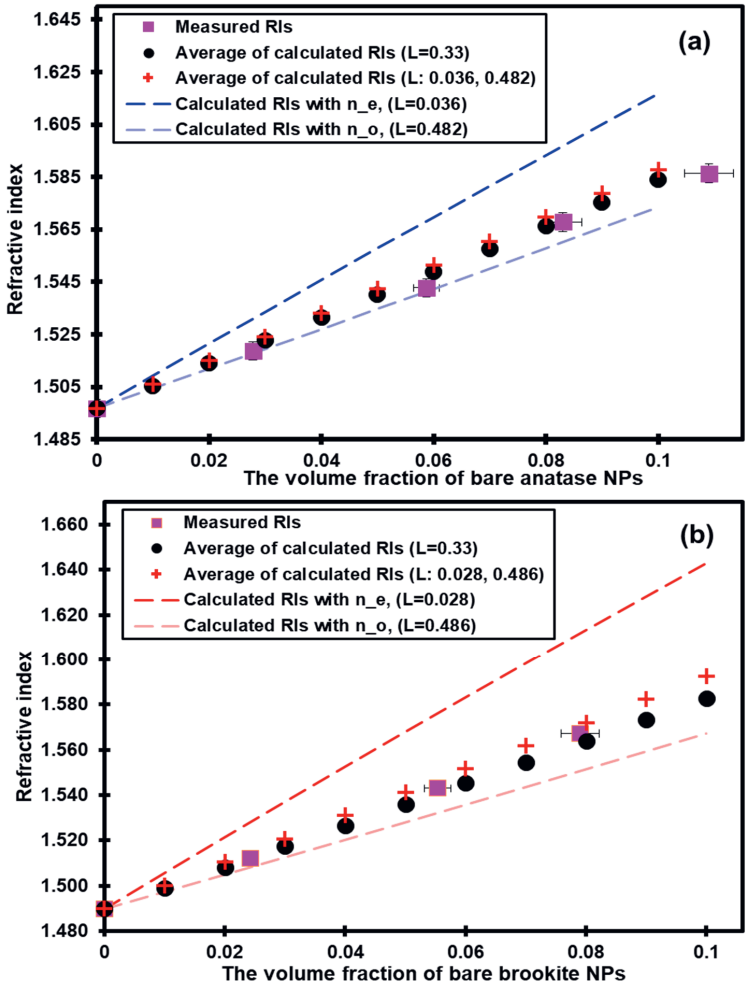

Figure 4-1. Dependence of RIs on TiO_2 NRs volume fractions in two different titania colloidal dispersions composed of rods with different crystal structure: brookite and anatase. (a) Anatase colloidal dispersions in toluene with volume fractions based on the bare crystalline anatase NRs. Magenta square markers correspond to the measured values of RIs of the anatase colloidal dispersions. Black and red markers are corresponding to the average of the calculated RIs using the M-G theory. For anatase NPs assumed as spheres with depolarization factor (L=0.33), they are shown in black markers. For anatase NPs assumed as anisotropic particles with depolarization factor ($L_\perp$ = 0.482 and $L_\parallel$ = 0.036), the averaged RI values are shown in red crosses while the calculated values for n_e and n_o in this condition are presented in dark and light dashed blue lines, respectively. (b) brookite colloidal dispersions with similar description in panel (a) but for brookite NPs. The employed depolarization factor for brookite NRs were $L_\perp$ = 0.486 and $L_\parallel$ = 0.028. The meausrements were performed in wavelength 589 nm and at 20.0 °C.

As can be seen in both panels in Figure 4-1, the measured RIs of the colloidal dispersions, shown in magenta markers, are observed between two dashed lines as lower and upper limits. These lines represent the lowest and highest expected RIs of the colloidal dispersions based on the M-G model for anisotropic particles. To calculate the lower dashed lines, as lower limits shown in light colors, we employed the ordinary RIs of the anatase and brookite NPs as well as $L_\perp = 0.482$ and $L_\perp = 0.486$ for the short axis of anatase and brookite NPs, respectively, as provided in Table 4-2. On the other hand, for the upper limits, shown in dark dashed lines, the extraordinary RIs of titania NPs were employed as RIs in Eq. 4-6 and $L_\parallel = 0.036$ for anatase and $L_\parallel = 0.028$ for brookite particles were used as parallel depolarization factors (for the long axis). The difference between these two limits can be assumed as the maximum intrinsic birefringence that can be expected in these colloidal dispersions. Since the M-G model is valid up to ~10 vol.% of the filling particles, hence, the estimated birefringence values for ligand-capped TiO_2 NRs dispersions with ca. 28.0 vol.% (equivalent to ca. 10.0 vol.% bare TiO_2 NRs) are $\Delta n_{ana,dispersion} = 0.043$ and $\Delta n_{bro,dispersion} = 0.075$. Hard rods with aspect ratios as for our experimental systems are expected to become LC phases at volume fraction of 50.0 vol.% for anatase NRs ($l/d = 4.18$) and 48.5 vol.% for brookite NRs ($l/d = 4.75$).

Since our experimentally observed RIs correspond to the RI of the colloidal dispersion, where colloidal NRs move randomly in the solvent, we also plotted the rotationally averaged RIs based on these two limits. In this way, we could approximate the contribution of both extraordinary and ordinary RIs from the anisotropic particles to the final RIs of the colloidal dispersions and thereby compare it with our measured values. Red cross markers in both panels in Figure 4-1 show these averaged RIs. In the calculation of averaged RIs in these dispersions, one should take into account that anatase and brookite are both intrinsically birefringent and thereby they have an extraordinary RI in the c crystallographic direction (along the long axis of NRs) and an ordinary RI in a and b crystallographic directions. Therefore, the averaged RI of these dispersions was calculated by considering 1/3 contribution from the dispersion's RI obtained by the extraordinary value (upper limit in dark dashed line) and 2/3 of the dispersion's RI obtained by the ordinary value (lower limit in light dashed lines). In the last step and in order to compare the geometry's effect in the M-G model, we calculated the averaged RIs of the dispersions based on the simplest approach in the M-G theory, the version for

spherical particles with $L = 0.33$ in Eq. 4-6. In the case of spherical particles, we have only shown the averaged RI values that are black solid markers in Figure 4-1. Calculation steps were quite similar to the anisotropic particles in the M-G model such that the upper limit was calculated by considering the extraordinary RI of these NPs and the lower limit by using the ordinary RI values. Finally, they were averaged by 2/3 contribution from ordinary RIs and 1/3 contribution from extraordinary RIs.

As can be seen in both panels in Figure 4-1, the averaged RI values for both spherical and anisotropic particles in the M-G theory are quite close to each other in the small filling factor approximation. Furthermore, an excellent agreement can be observed between our measured RI values and the theoretically averaged RIs up to the third decimal supporting the uniform distribution of the anatase and brookite NRs in the droplet of the colloidal dispersion as it was assumed in the M-G theory. Our experimental results show a linear correlation between the RI and concentration for both anatase NRs colloidal dispersions with volume fractions up to 29.8 vol.% (equivalent to 10.9 vol.% bare anatase nanocrystals) and brookite NRs up to 22.9 vol.% (equivalent to 9.3 vol.% bare brookite nanocrystals). The linear dependence of the square root of the dielectric function (RI in the visible spectral region) of organic matrixes filled with inorganic fillers has been observed in similar titania-polymer nanocomposites, as well.[198,263,265,300] We note that some experimental uncertainties during the RIs measurements such as solvent evaporation could have caused the errors in the actual concentration of the dropcast liquid layers thereby explaining the small deviations from the anticipated linear trend. To estimate the effective RIs of the colloidal dispersions at higher volume fractions of titania NRs, we employed Bruggeman's model (results shown in Supplementary Information). Although reaching volume fractions of 50 vol.% (the upper limit in Bruggeman's model) is practically too difficult in colloidal dispersions, achieving these concentrations in dried states (i.e. spin-coated thin films) is possible. By extrapolating the linear fit in Bruggeman's plots for anatase and brookite colloidal dispersions, we calculated RIs at $\varphi = 1.0$ equal to be 2.519 and 2.452, respectively. Although these values are smaller than reported RI values of anatase and brookite crystals in the literature, it shows a close match with the measured values and hence confirming the influence by low RI ligands.[301]

4.3.2 Switching of the birefringence of TiO_2 colloidal dispersions in external electric fields

To investigate the characteristic switching times and alignment behavior of the dispersed colloidal anatase and brookite NRs in electric fields, we dropcast dispersions of these NRs on in-plane switching cells and sandwiched them using a coverslip as described in the experimental part and can be seen in Polarized Optical Microscopy (POM) images in Figure 4-2. From the transmission measurements, we could measure the light intensity passing through the cell loaded with NRs dispersions. The area of interest was ca. 2560 square pixels (approximately 1380 μm^2) where the background intensity was substracted from the measured intensity. The change in this intensity could be correlated to the characteristic switching times of the system. However, the field-induced birefringence, Δn, was not measured since it would require a more accurate polarimeter and extra devices such as compensators that were not available. Furthermore, we could not measure zeta potential charges for anatase and brookite NRs in toluene and butylbenzene dispersions, respectively. Nevertheless, we did find spontaneous charging of these NRs in cyclohexylbromide without the addition of more charge-inducing agents. This will be discussed in more details in the next chapter. Thus, we think that if there is any charge on these NRs in 'pure' toluene and butylbenzene, it is probably less than $\sim 5\ mV$, since we could still observe reliably small charges on the NRs in cyclohexylbromide which has similar refractive index contrast. As is known for charged colloidal particles, the mobile charges in the dispersion have a relaxation frequency equal to $f_{charge} = \frac{\kappa_{solvent}}{2\pi\varepsilon_0\varepsilon_{solvent}}$ where $\kappa_{solvent}$ and $\varepsilon_{solvent}$ are the conductivity and the dielectric constant of the solvent, respectively.[272] If the applied electric field has lower frequencies than the charge relaxation frequency ($f < f_{charge}$), the field is completely screened by the charges accumulated in the dispersion in front of the electrodes. Hence, by applying square pulse a.c. fields with high frequencies (in kHz regime in our case), we could avoid artifacts caused by the charged NRs' drifting to the electrodes and their accumulation in front of the electrodes. Although by applying a.c. fields, we could reach a maximum value for brightness intensity (as shown in Figure 4-2), detecting the characteristic switching times, τ_{ON} and τ_{OFF}, in the a.c. fields was not possible. Therefore, we applied square pulse d.c. fields with a pulse width of 5000 μs and a duty cycle of 50%, shown in Figure 4-3, to probe the NRs reorientations dynamics more precisely.

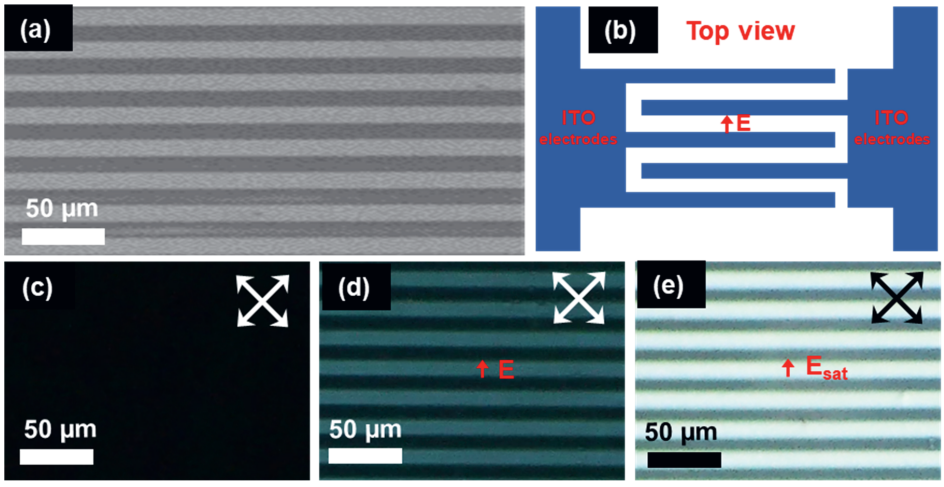

Figure 4-2. Scanning electron microscopy image of the in-plane switching cells utilized for the electro-optical experiments on anatase and brookite NRs colloidal dispersions. (b) Schematic representation of the in-plane switching cells. As an example, in panels (c-d), POM images of an in-plane switching cell are shown with an isotropic dispersion of the anatase NRs sandwiched between the cell and a cover slip. Samples were placed between cross-polarizers. Through a progressive increase of the electric field, the induced birefringence (Kerr effect) was observed. In (c) no electric field was applied (off-state), while in (d), we applied weak fields up to $E = 2\ V/\mu m$. In (e), we increased the field strength such that no further increment in brightness was detected to determine the saturation field of the index $E_{sat} = 5\ V/\mu m$ (a.c. fields, square wave, f = 1 kHz).

In Table 4-2, the depolarization factors and dielectric polarizabilities of anatase and brookite NRs were calculated approximating the NRs as ellipsoids, as mentioned in the previous section.[299] Using these values, we could predict the rise and decay times of the NRs in the pulsed d.c. fields as well as estimate the induced dipole moments of the NRs. For a better comparison, these estimated values were plotted as a function of different field strengths in Figure 4-4. In these calculations, we only used the pure solvent viscosities. Furthermore, we did not consider any contribution from a permanent dipole moment of TiO_2 NRs since these values were not available. A contribution of the electric polarizabilities of the titania NRs, $\Delta\alpha$, formulated in the extended Maxwell–Wagner framework was taken into account. We note that although TiO_2 is known to have a charge-neutral crystalline structure, permanent dipoles have recently been found to exist in TiO_2 NPs.[282,302] For instance, Gonzalo-Juan et al. reported a dipole moment of ca. 990 Debye for short anatase NRs ($l = 4.6\ nm$ and $d = 2.6\ nm$) ligand-capped with oleic acid in hexane and this value was almost 10 times smaller (ca. 100 Debye) for anatase

nanospheres in the same experimental conditions.[282] In another study by Pochylski et al., large permanent dipole moments of ca. 113 and 220 kilo-Debye for 32.0 nm anatase NPs in octanoic acid and silicon oil, respectively.[275] They linked these measured permanent dipole moments to ion distribution at the particles' surfaces as well as ligands groups, which affected significantly NPs' behavior at the nanoscale.[302–304] As we showed in previous chapters, surface defects at the atomic level were often observable for both anatase and brookite NRs and could cause a permanent dipole due to the inhomogeneous charge and/or atomic dipole distributions at NRs' surfaces.[275] Therefore, for a full description of the rotational dynamics, the presence of a permanent dipole moment of also our TiO_2 NRs has to be established and measured.

In addition to the abovementioned factors, a contribution of Maxwell-Wagner-O'Konski (M-W-O) polarization in the NRs' reorientation dynamics in our systems should not be ruled out as well especially since the NRs were found to be charged in the solvents studied. Although we did not have enough information to evaluate the M-W-O mechanism, it has been shown in several reports that due to the polarization of the counter-ions in the EDL around charged colloidal NPs, the M-W-O influence can be even significantly larger than the contribution of other mechanisms.[272,273] For instance, Dozov et al. illustrated that when dielectric pigment NRs were dispersed in dodecane ($\varepsilon_{dodecane} = 2.01$), although the surface conductivity and surface charge density of the NRs were small, the equivalent conductivity of the NRs was still approximately three orders of magnitude larger than the bulk conductivity of the solvent. This was in the work contributed due to the polarization of the counterions in the EDL.[271–273]

Table 4-2. Obtained calculated results for anatase and brookite dispersions

Anatase colloidal dispersions			
NRs dimensions	TEM [nm]	NRs sizes: $l = 24.6,\ d = 3.6$ Equivalent ellipsoid: $2a = 28.3\ ,\ 2b = 2c = 4.14$	
Anatase dielectric constants	Ref [305]	$\varepsilon_{\parallel} = 22.7$	$\varepsilon_{\perp} = 45.1$
Depolarization factors	Eq. 4-11	$L_{\parallel} = 0.036$	$L_{\perp} = 0.482$
Dielectric polarizabilities	Eq. 4-10	$\alpha_{\parallel} = 1.7 \times 10^{-24}\ m^3$	$\alpha_{\perp} = 4.7 \times 10^{-25}\ m^3$
$\boldsymbol{\tau_{ON}}$ in toluene $(\boldsymbol{\varepsilon_{toluene} = 2.38})$ $(\boldsymbol{\eta_{toluene} = 0.59 \times 10^{-3} Pa.s})$	Eq. 4-21	$\boldsymbol{E} = 3\ V/\mu m \longrightarrow \tau_{ON} = 298.2\ \mu s$	
		$\boldsymbol{E} = 7\ V/\mu m \longrightarrow \tau_{ON} = 54.8\ \mu s$	
		$\boldsymbol{E} = 10\ V/\mu m \longrightarrow \tau_{ON} = 26.8\ \mu s$	
$\boldsymbol{\tau_{OFF}}$ in toluene $(\boldsymbol{\eta_{toluene} = 1.88 \times 10^{-3} Pa.s})$	Eq. 4-22	$\tau_{OFF} = 13.9\ \mu s \longrightarrow D_{\perp}^{r} = 11.9 \times 10^{3}\ s^{-1}$	
Estimated induced dipole moment	Eq. 4-9	11.9 Debye at $(\boldsymbol{E} = 3\ V/\mu m)$	
		27.9 Debye at $(\boldsymbol{E} = 7\ V/\mu m)$	
		40.1 Debye at $(\boldsymbol{E} = 10\ V/\mu m)$	
Brookite colloidal dispersions			
NRs dimensions	TEM [nm]	NRs sizes: $l = 27.4,\ d = 3.4$ Equivalent ellipsoid: $2a = 31.5\ ,\ 2b = 2c = 3.9$	
Brookite dielectric constants	Ref [306]	$\varepsilon_{\parallel} = 86.7$	$\varepsilon_{\perp} = 55.2$
Depolarization factors	Eq. 4-11	$L_{\parallel} = 0.028$	$L_{\perp} = 0.486$
Dielectric polarizabilities	Eq. 4-10	$\alpha_{\parallel} = 4.5 \times 10^{-24}\ m^3$	$\alpha_{\perp} = 4.7 \times 10^{-25}\ m^3$
$\boldsymbol{\tau_{ON}}$ in butylbenzene $(\boldsymbol{\varepsilon_{butylbenzene} = 2.36})$ $(\boldsymbol{\eta_{butylbenzene} = 0.95 \times 10^{-3} Pa.s})$	Eq. 4-21	$\boldsymbol{E} = 3\ V/\mu m \longrightarrow \tau_{ON} = 178.6\ \mu s$	
		$\boldsymbol{E} = 7\ V/\mu m \longrightarrow \tau_{ON} = 32.8\ \mu s$	
		$\boldsymbol{E} = 10\ V/\mu m \longrightarrow \tau_{ON} = 16.1\ \mu s$	
$\boldsymbol{\tau_{OFF}}$ in butylbenzene $(\boldsymbol{\eta_{butylbenzene} = 0.95 \times 10^{-3} Pa.s})$	Eq. 4-22	$\tau_{OFF} = 28.2\ \mu s \longrightarrow D_{\perp}^{r} = 5.9 \times 10^{3}\ s^{-1}$	
Estimated induced dipole moment	Eq. 4-9	27.8 Debye at $(\boldsymbol{E} = 3\ V/\mu m)$	
		65.1 Debye at $(\boldsymbol{E} = 7\ V/\mu m)$	
		92.1 Debye at $(\boldsymbol{E} = 10\ V/\mu m)$	

Figure 4-3 shows the rise and decay times of our TiO_2 NRs dispersions for various field strengths when short square pulses were applied. As can be observed in Figure 4-3a, for all of the field strengths, the transmitted light intensity rapidly reached its maximum value indicating that all NRs become aligned relatively quickly. The utilized camera in

our experiments could record the transmitted light intensity with 4000 frames per second providing a resolution of 1 measurement (collected data point) per 250 μs. We show in both Table 4-2 and Figure 4-4 that except at lower fields (3 $V/\mu m$), at all of the higher field strengths for both anatase and brookite NRs dispersions, τ_{ON} is expected to be less than 250 μs. However, in our experiments, we could collect only one data point in the rise period after applying square pulse bursts of field strengths 3, 7, and 10 $V/\mu m$, which confirms that ca. 90% of the maximum intensity was achieved within 250 μs. Therefore, we conclude that the τ_{ON} is less than 250 μs.

In Figure 4-3b, the decay times associated with the relaxation of the Kerr induced birefringence can be observed. Similar to the rise time observations in panel (a) in Figure 4-3, the applied square pulse has a width of 5000 μs. We could again collect only one data point when the voltage dropped, which was after 250 μs; the light intensity decreased in this time span for more than 70%. As mentioned before, the relaxation of the Kerr induced birefringence back to the isotropic liquid state stems from the thermal rotational diffusion randomizing the NRs' orientation initially created by the applied electric field. Thus, τ_{OFF} only depends on the host medium as well as geometrical properties of the NRs, at volume fractions where interactions between them can be neglected.[244] As we showed in Table 4-2, τ_{OFF} values were estimated by the Debye-Perrin model (Eq. 4-22) to be ca. 14 μs and 28 μs for the anatase and brookite NRs, respectively. In this model, the rotational diffusion coefficient (γ_r), dynamic viscosity of the solvent (η), and the modified semi-axes of the ellipsoidal titania NRs covered with 1.5 nm organic ligand molecules were taken into account. By considering τ_{OFF} values from the Debye-Perrin model, the rotational relaxation frequencies of anatase and brookite NRs are ca. $f_{relaxation} = 35.7\ kHz$ and $f_{relaxation} = 17.7\ kHz$, respectively, which are on a time scale much shorter than the 5000 μs periods of the applied pulses. Therefore, all the applied fields (either pulsed d.c. fields or a.c. fields) with a frequency well below $f_{relaxation}$ would provide the NRs enough time to follow the variation of the electric field. The only difference between frequencies well below $f_{relaxation}$ and higher frequencies close to $f_{relaxation}$ that we can expect is that the latter makes the NRs switch faster from the 0° to 180° orientation. However, since the resolution of each measurement in our setup was 250 μs, we were not able to track the actual decay time or faster rise times below 250 μs. It is expected that at frequencies above $f_{relaxation}$, the distribution of the NRs will not

return to random alignment and therefore the minimum transmission cannot become equal to zero-field transmitted light intensity. Moreover, if a.c. fields would be applied, it is expected that the NRs will stop responding to the field once the frequency exceeds the rise time frequencies, f_{rise}, which are approximated to be $f_{rise,ana} \approx 5.9\ kHz$ and $f_{rise,bro} \approx 9.8\ kHz$ at $E = 10\ V/\mu m$.

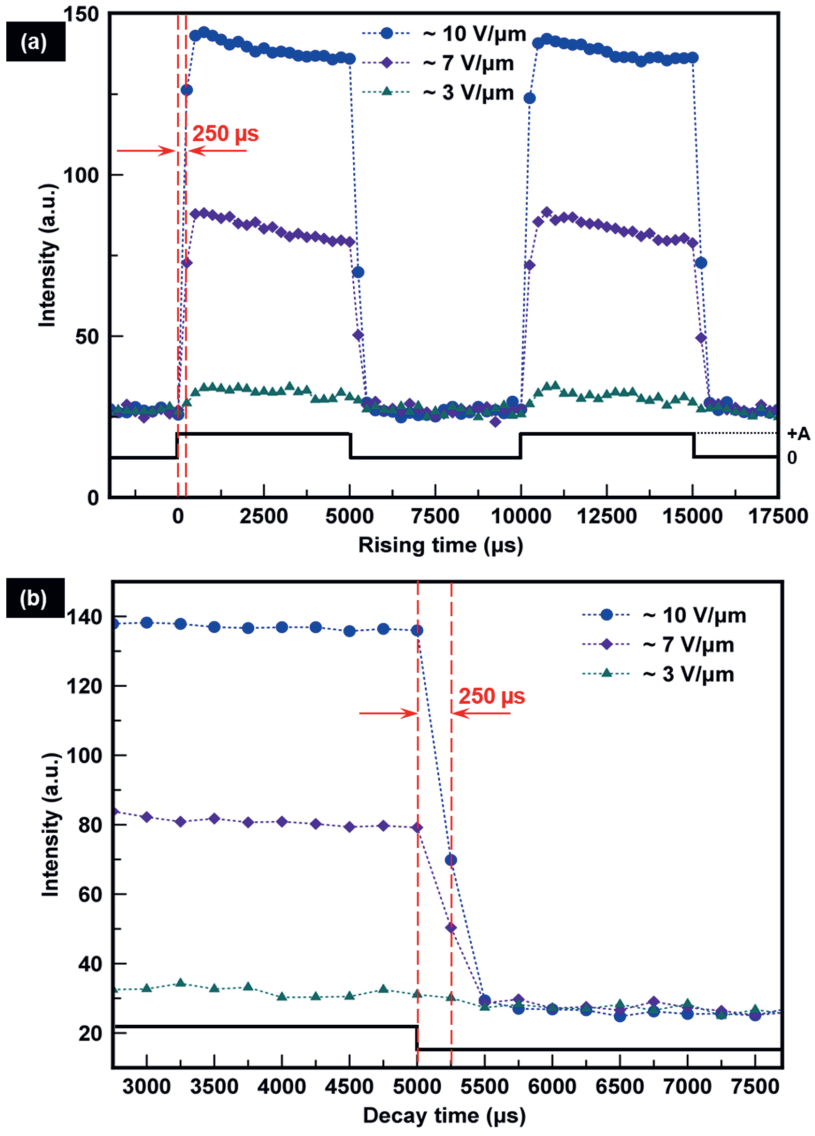

Figure 4-3. (a) Transmitted light intensity in cross-polarized in-plane switching cells versus time for TiO_2 NRs colloidal dispersions when square d.c. pulses with a pulse width of 5000 μs and a duty cycle of 50% are applied at 3, 7, and 10 $V/\mu m$ field strengths. (b) A zoomed-in plot from panel (a) with emphasis on decay times in cross-polarized in-plane switching cells as a function of time for TiO_2 NRs colloidal dispersions when a square pulse with 3, 7, and 10 $V/\mu m$ are relaxed to zero amplitude. The dashed vertical line in red color is depicting the time interval between the two data points during the decay times in all field strengths.

In Figure 4-4 we show that τ_{ON} is strongly dependent on the applied electric field. By tuning the field strength from 3 to 10 $V/\mu m$, τ_{ON} is expected to decreases from ca. 298 μs to 27 μs for the anatase NR dispersion and from ca. 178 μs to 16 μs for the brookite NR dispersions. These mentioned values for τ_{ON} are underestimates because only a dielectric torque on the titania NRs was taken into account. Nevertheless, the observed τ_{ON} in Figure 4-3a (shown with red vertical dashed lines) are in agreement with the estimated values from Figure 4-4. Since τ_{ON} depends on the electric field strengths, even faster τ_{ON} could be achievable by applying higher voltages. In this regard, several studies were conducted on the rotational dynamics of diverse colloidal NRs in electric fields by employing transient birefringence measurements or by fiber optofluidic devices. All these studies confirmed that if sufficiently high field strengths were applied (i.e. even up to 32 $V/\mu m$)[245] in the colloidal dispersions of various types of NRs with hard-core potentials (i.e. CdSe NRs,[242,281] CdSe/CdS NRs,[243] Au NRs,[238,244,245] and pigment red 176 NRs[272]), NRs' alignment would occur in several microseconds or even sub-microsecond timescales (all occurred in sophisticated fiber optofluidic devices).[245] Although ultrafast switching times were achieved in these studies, the colloidal dispersions measured were always in very dilute regimes.[238,242–245,272,281] On the other hand, when the colloidal dispersions were more concentrated close to volume fractions where LC phases would form, the observed switching times increased to the order of milliseconds or even several minutes as the result of increased interactions and (much) higher viscosities.[272–274,307–309] To the best of our knowledge, we believe that our results are the first experimental investigation confirming microsecond switching times in colloidal dispersions with relatively high volume fractions close to the isotropic-nematic phase transition.

In addition to smaller values for τ_{ON}, which could be achieved via increasing the field strengths, we expect that the magnitude of the induced dipole moments could be tuned from ca. 12 Debye in $3 V/\mu m$ for anatase NRs to ca. 92 Debye in $10 V/\mu m$ for brookite NRs. Typically, brookite NRs exhibit higher induced dipole moments in comparison to their anatase counterparts due to the higher complex dielectric mismatch between the solvent and the brookite NRs. Our induced dipole moments are reasonably close to the reported values by Neyts et al. for somewhat similar semiconductor colloidal dispersions. In their experiments, they reported an induced dipole moment of 100 Debye

for CdSe/CdS NRs with $l = 51.5\ nm$ and $d = 4.8\ nm$ in dodecane at a field strength of $E = 17\ V/\mu m$).[243]

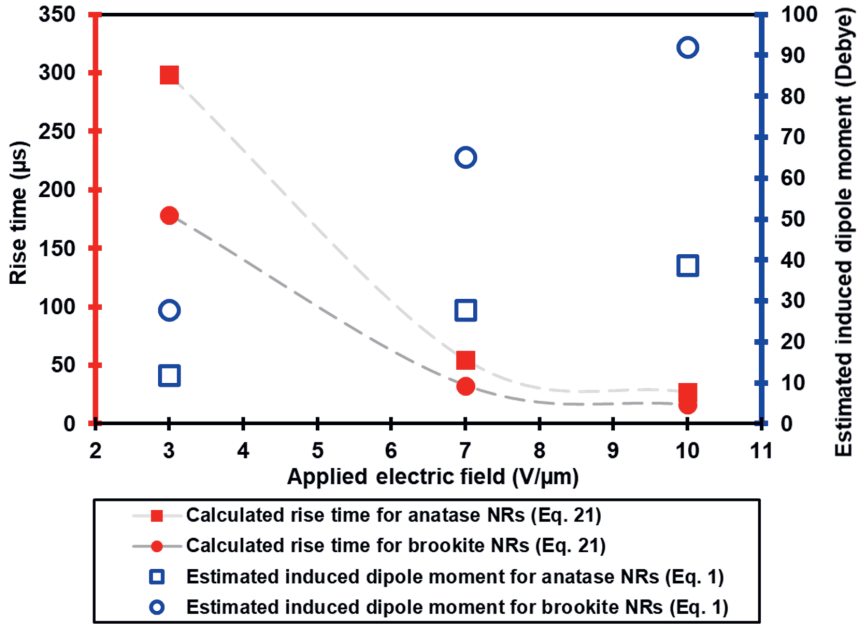

Figure 4-4. Switching speed predictions as function of field strength. On the left vertical red axis, estimated rise times for our anatase NRs (red square solid markers) and brookite NRs (red circle solid markers) as a function of different applied amplitutdes. On the right vertical blue axis, the estimated induced dipole moment of anatase NRs (blue empty square markers) and brookite NRs (blue circle empty markers) are plotted as a function of different applied field strengths.

In the next step, we try to assess the effects of the interactions between the NRs on their rotational dynamics. We calculated NR decay times based on theories to predict NR rotational dynamics in both dilute and semi-dilute conditions. As can be observed in Table 4-3, $D_{\perp}^{r}$ of the ligand-capped anatase and brookite NRs were firstly calculated in the dilute limit where the particles do not interact. Accordingly, the decay time was extracted from the calculated $D_{\perp}^{r}$ via $\tau_{OFF} = 1/(6D_{\perp}^{r})$.[310] This calculation resulted in decay times of ca. $0.7\ \mu s$ and $1.5\ \mu s$ for anatase and brookite NRs, respectively, which are the fastest decay times we could expect for these NRs in the dilute limit. However, since our colloidal dispersions are concentrated, we also calculated $D_{\perp}^{r}$ values in the semi-dilute limit by employing an equation (Eq. 4-27) by Doi and Edwards. In this equation, it is assumed

that the NRs can still orient randomly but their motions are strongly hindered by steric repulsions forces between NRs. We should also keep in mind that in this equation, it is assumed the rods are thin rods, as mentioned before. However, our titania NRs are not that thin and have aspect ratios around 4.5, and thereby the real decay times are most likely in between values obtained from the dilute dispersion and semi-dilute dispersion calculations. Nevertheless, several experimental reports have shown the validity of Eq. 4-27 for colloidal NRs with aspect ratios smaller than 10.[273,292,296] As reported in Table 4-3, by assuming the Doi and Edwards approach in the semi-dilute regime, decay times of ca. 120 μs and 238 μs are estimated for our anatase and brookite NRs dispersions, respectively. These values are reasonable when compared with our collected data. Hence, to get an idea regarding various decay times at different volume fractions in our systems, we calculated decay times by using the Doi and Edwards approach as a function of volume fraction, which are presented in Figure 4-5. For this approximation, the lowest volume fraction considered was 1 vol.% as it has been shown by Grelet et al. that this approach could still result in reasonable relaxation times in colloidal NRs dispersion of ca. 0.9 vol.%.[273]

Table 4-3. Estimated decay times for TiO_2 NRs dispersions in dilute and semi-dilute limits

Anatase colloidal dispersions		
NRs dimensions	TEM [nm]	NRs sizes: l+ (3.0 nm ligands length): 27.6 nm d + (3.0 nm ligands length): 6.6 nm
		Equivalent ellipsoid: $2a$ + (3.0 nm ligands length): 31.3 nm $2b = 2c$ = 4.14 + (3.0 nm ligands length): 7.14 nm
$\boldsymbol{D_{\perp}^{r}}$ in dilute region ($\boldsymbol{\eta_{toluene} = 0.59 \times 10^{-3} Pa.s}$)	Eq. 4-25	$D_{\perp}^{r} = 2.18 \times 10^{5}\ s^{-1} \rightarrow \tau_{OFF} = 0.76\ \mu s$
$\boldsymbol{D_{\perp}^{r}}$ in semidilute region ($\boldsymbol{\varphi_{dispersion} = 0.298}$)	Eq. 4-27	$D_{\perp}^{r} = 1.38 \times 10^{3}\ s^{-1} \rightarrow \tau_{OFF} = 120.7\ \mu s$
Estimated viscosity for concentrated dispersions ($\boldsymbol{\varphi_{dispersion} = 0.298}$)	Eq. 4-28	$\eta_{dispersion} = 0.77\ Pa.s$
Brookite colloidal dispersions		
NRs dimensions	TEM [nm]	NRs sizes: l + (3.0 nm ligands length): 30.4 nm d + (3.0 nm ligands length): 6.4 nm
		Equivalent ellipsoid: $2a$ + (3.0 nm ligands length): 34.5 nm $2b = 2c$ = 3.9 + (3.0 nm ligands length): 6.9 nm
$\boldsymbol{D_{\perp}^{r}}$ in dilute region ($\boldsymbol{\eta_{butylbenzene} = 0.95 \times 10^{-3} Pa.s}$)	Eq. 4-25	$D_{\perp}^{r} = 1.11 \times 10^{5}\ s^{-1} \rightarrow \tau_{OFF} = 1.49\ \mu s$
$\boldsymbol{D_{\perp}^{r}}$ in semidilute region ($\boldsymbol{\varphi_{dispersion} = 0.229}$)	Eq. 4-27	$D_{\perp}^{r} = 6.97 \times 10^{2}\ s^{-1} \rightarrow \tau_{OFF} = 238.8\ \mu s$
Estimated viscosity for concentrated dispersions ($\boldsymbol{\varphi_{dispersion} = 0.229}$)	Eq. 4-28	$\eta_{dispersion} = 1.24\ Pa.s$

In Figure 4-5, it is clearly observed that diluting the dispersion would significantly improve the decay times for both NRs' dispersions in the semi-dilute region. In this plot, the highest volume fractions for both dispersions were chosen close to the actual volume fractions that resulted in ca. 114 μs for 29.0 vol.% anatase NRs colloidal dispersions in toluene and ca. 241 μs for 23.0 vol.% brookite NRs colloidal dispersions in butylbenzene. The difference in these relaxation times is associated with dissimilarities in anatase and

brookite NRs colloidal systems such as NRs sizes, volume fractions, and solvent viscosity. Moreover, Doi and Edwards showed that for thin rod-like dispersions in the concentrated region ($c \gg 1/l^3$), where they still have rotational degrees of freedom, the viscosity of the dispersion becomes much greater than the solvent viscosity, resulting furthermore in non-Newtonian viscoelasticity.[295] Hence, to get a rough estimate, we also calculated the viscosity of the concentrated NRs dispersions (Eq. 4-28), as shown in Table 4-3. The calculated viscosities are nearly three orders of magnitude larger than solvent viscosities which rationalizes the notable decrease in relaxation times of NRs from the dilute limit to semi-dilute dispersions. Nevertheless, these results suggest that if sufficiently high field strengths are provided (at least $3\,V/\mu m$ in our colloidal dispersions), these colloidal NRs will be fully aligned for almost all of the time in the a.c. fields, except for very short time intervals which are on the order of microseconds. We note that this characteristic of the system can also be valuable for applications that need to *freeze* colloidal NRs at a specific orientation, for example by employing a triggered polymerization of the surrounding medium.[311–315] Submicrosecond relaxation times are also achievable at volume fractions below 3.0 vol.%. Although microsecond relaxation times are apparently reachable in a broad range of volume fractions, further investigations are necessary to find the critical volume fraction at which a collective induced birefringence (Kerr effect) becomes observable. We believe these promising electro-optical properties demonstrated in our material systems are of great interest in several fast switchable optical devices. By employing these NRs dispersions, not only we can benefit from the athermal LC behavior of these highly stable colloidal systems, but also from their unique stability under irradiation with high powers of light.

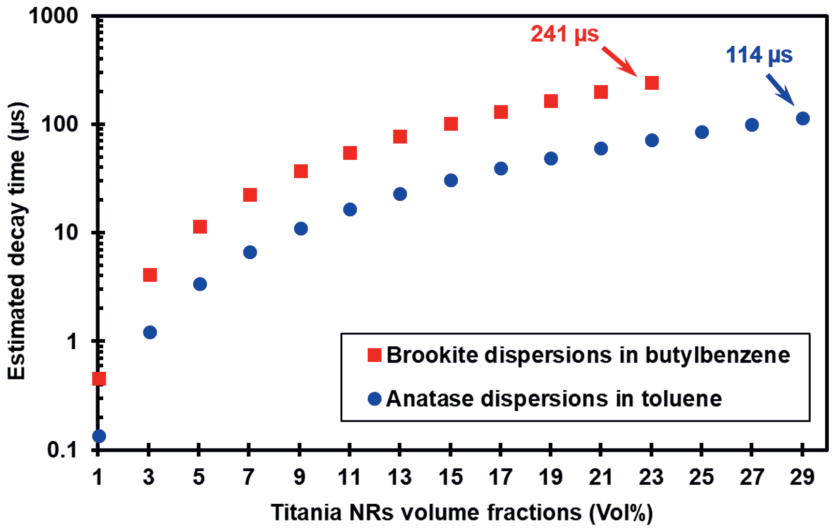

Figure 4-5. Estimated decay times shown on a logarithmic scale for anatase and brookite NRs as a function of their volume fractions. For this approximations, the rotational diffusion coefficient in a semi-dilute regime, proposed by Doi and Edwards, was employed from Eq. 4-27.

4.4 Conclusions and outlook

In summary, we demonstrated electric field induced birefringence (Kerr effect) and (para)nematic LC phases, in concentrated dispersions of anatase and brookite NRs in toluene and butylbenzene, respectively, that were initially in an isotropic liquid state. We probed the response of these colloidal dispersions in in-plane switching cells where the electrodes were in direct contact with the NRs' dispersions. To assess the reorientation of the TiO_2 NRs under pulsed d.c. electric fields, the estimated induced dipole moments of anatase and brookite NRs were calculated for different field strengths. Besides that, other possible mechanisms contributing to the reorientation of these NRs were discussed. By considering the electric polarizabilities of titania NRs in various electric fields, we calculated induced dipole moments ranging from ca. 12 Debye in $3\,V/\mu m$ for anatase NRs in toluene to ca. 92 Debye in $10\,V/\mu m$ for brookite NRs in butylbenzene. We found that the brookite NRs exhibited higher induced dipole moments in comparison to their anatase counterparts which is as expected from the higher complex dielectric mismatch between the solvent and the brookite NRs. Nevertheless, since our TiO_2 NRs were

measured to be charged colloids in the solvents we used, we believe that the polarization of the electrical double layer via the Maxwell–Wagner–O'Konski mechanism is probably contributing significantly to the mechanisms of the alignment dynamics of the NRs, although further detailed investigations are required to exactly determine how large this contribution is. We showed that both anatase and brookite NRs could be aligned into the direction of the applied electric fields in various field strengths within ca. 250 μs which is at least one order of magnitude faster than commercial Freedericksz-based LCs (i.e. E7 LCs). However, these measured switching times were limited by the resolution of our setup. By validating our experimental parameters with theories, we believe that rise times in these TiO_2 dispersions are in the order of ca. 30 to 60 μs for $E = 10\,V/\mu m$ while relaxation times of ca. 120 to 240 μs are expected in these semi-dilute TiO_2 NRs dispersions. Furthermore, to estimate the refractive index of our TiO_2 dispersions and determine the birefringence observed in an electric field, we measured the refractive indexes of our anatase and brookite dispersions in various volume fractions of TiO_2 NRs and compared these with effective medium models such as Maxwell-Garnett and Bruggeman theories. The largest estimated intrinsic birefringence for our ligand-capped TiO_2 NRs dispersions with ca. 28.0 vol.% (equivalent to ca. 10.0 vol.% bare NRs) measured were $\Delta n_{ana,dispersion} = 0.043$ and $\Delta n_{bro,dispersion} = 0.075$. At these largest volume fractions we expect to be relatively close to a phase transition to a nematic LC phase. The measured refractive indexes for both TiO_2 dispersions showed a linear correlation with the volume fractions of the NRs and were in excellent agreement with a Maxwell-Garnett effective medium theory. We believe that the high-speed switching times of these non-aqueous transparent colloidal dispersions even at relatively high volume fractions coupled with high degrees of induced birefringence make them highly suitable for ultrafast optical switches, spatial light modulators, switchable gradient index lenses (such as switchable Fresnel lenses)[164,166], remote sensing, and signaling applications.

4.5 Experimental

4.5.1 TiO_2 NRs dispersions preparation

Anatase and brookite NRs colloidal dispersions were prepared as described in previous chapters and references [188,316]. Concentrated colloidal dispersions were prepared by careful solvent evaporation. We emphasize that solvent evaporation should take place gradually while the colloidal dispersions are shaken to prevent NRs agglomeration on the wall of the vials. In order to prevent fast solvent evaporation during electro-optical experiments, brookite NRs dispersions were prepared in butylbenzene. Butylbenzene has a boiling point of 183 $°C$ and $n^{20}_{butylbenzene} = 1.489$.

4.5.2 Refractive index measurements

Refractive index measurements for TiO_2 NRs colloidal dispersions were taken with an Abbe refractometer (Atago-3T). This refractometer can measure the refractive indices to an accuracy of ± 0.0001. A sodium lamp of wavelength 589 nm was used to illuminate the prisms and sample. The temperature was controlled at 20.0 $°C$ by a circulating water bath, which maintained the temperature stable to $\pm 0.05\ °C$. For each measurement, we dropcast 70.0μL of the NRs colloidal dispersions with known volume fractions on the sample holder. After each measurement, we cleaned the sample holder by using the same pure solvent of the dispersion and Whatman lens cleaning tissues. In this way, we removed the leftover and dried NRs and finally cross-checked it by measuring the refractive index of the solvent. Once the refractive index of the solvent was correct, we could measure refractive indexes for other volume fractions. Each measurement was repeated 3 times and the results are shown as a mean value.

4.5.3 Electro-optical experiments

Our electro-optical cells were commercial in-plane switching substrates that contained interdigitated comb-like electrode structures made of Indium Tin Oxide (ITO) from Instec Inc. Electric contacts between ITO electrodes and wires were made by using a silver lacquer. The cell was then connected to a function generator (Agilent 33250A Arbitrary Wave Generator) through an electric amplifier (Krohn-Hite Model 7602) which provides a voltage gain of a factor 20 for frequencies up to 400 kHz. The input and output signals were monitored on a TEKTRONIX TDS3012B oscilloscope. We investigated the

characteristic switching times and alignment behavior of the dispersed colloidal anatase and brookite NRs by electric fields by dropcasting 10.0 μL dispersions of these NRs on the in-plane switching cells and sandwiching them with a coverslip (9.0 mm diameter from Fisher scientific). The whole area under the coverslip was filled by capillary forces resulting in a thin layer of approximately 150 μm of colloidal dispersion. The sample was then placed between crossed polarizers and illuminated by a stabilized light source from below. To measure the light intensity in POM images caused by Kerr induced birefringence in the samples, the images were captured via a Nikon D90 digital camera. This camera could provide 4000 frames per second resulting in a resolution of 1 measurement per 250 μs. Individual frames from the movies and images were analyzed using ImageJ software. In all of the measurements, the light intensity of the background was taken into account according to the totally cross-polarized state and not being cross-polarized. When the electric field is applied between two infinite parallel planes, the electric field strength (E) is the result of the ratio between the operating voltage and the inter-electrode distance (d). Since we were interested in detecting the characteristic switching times, τ_{ON} and τ_{OFF}, we applied square pulse d.c. fields with a pulse width of 5000 μs and a duty cycle of 50%.

4.6 Acknowledgments

I would like to thank my Bachelor's student, Winnie Kong, for her perseverance on her Bachelor's project in the SCM group and her contributions on preliminary observations on the Kerr induced birefringence LCs that were performed under the supervision of Alfons van Blaaderen, Anna Nikolaenkova, and me. I would like to thank Anna Nikolaenkova for collecting data on switching experiments and her help with the refractive index measurements. We thank Peter Helfferich for his technical assistance with the electro-optical setup.

5

Charging behavior of TiO_2 nanorods in nonaqueous media

Charged colloidal particles dispersed in apolar media are of great interest in a broad variety of applications ranging from paints to electrophoretic displays. Control over the charge of nanoparticles in apolar media can be essential for stability, phase behavior, and to manipulate colloidal TiO_2 nanorods by external electric fields providing tunable optical properties. Nevertheless, ion formation and separation as well as creating conductivity are known challenges in apolar systems in comparison to their aqueous counterparts. Here, we demonstrate the charging behavior of ligand-capped brookite and anatase TiO_2 nanorods in toluene (an apolar solvent) and cyclohexylbromide (representing more polar solvents) by introducing nonionic surfactants (Span80 and OLOA1200). Electrophoretic mobilities and corresponding zeta potentials in these apolar media are reported as a function of surfactant concentration, as measured by the phase analysis light scattering (PALS) technique. We show that the sign of the particle charge can be tuned as a result of an ion transfer between the TiO_2 nanorods' surfaces and the surfactant and found the charges resulting on the rods to be inline with an acidic behavior of Span80 resulting in positively charged rods and basic behavior of OLOA1200 resulting in negatively charged rods. In "pure" cyclohyxelbromide the rods became positively charged while in toluene the charges were too small to measure.

5.1 Introduction

Paints, coatings, oil-based printing toners, inks, cosmetics, and pharmaceuticals are just a few examples of commercial products that are developed from either aqueous or nonaqueous colloidal dispersions.[317–321] In all of these colloidal dispersions, it is important to prevent aggregation of colloidal particles by two main repulsion mechanisms: *steric* repulsion and/or *electrostatic* repulsion. In steric repulsion, which is regularly used for nanoparticles (NPs), ligand-capped NPs are strongly repelled as the ligand layers begin to overlap.[92] However, in electrostatic repulsion, electrical double layers (EDLs), resulting from differences in ion concentrations around charged particles by a competition between entropy and electrostatic interactions, cause repulsions when these EDLs begin to overlap. A combination of electrostatic and steric repulsion can also occur which is known as *electrosteric* stabilization.[322] In this case, the energy-distance curve can have two minima, one low maximum, which is described by the DLVO theory (Deryaguin, Landau, Verwey, and Overbeek), and a rapid increase at distances smaller than twice the ligand length as a result of steric repulsion (Figure 5-1).[323]

The main motivation to achieve electrostatic stabilization in addition to steric

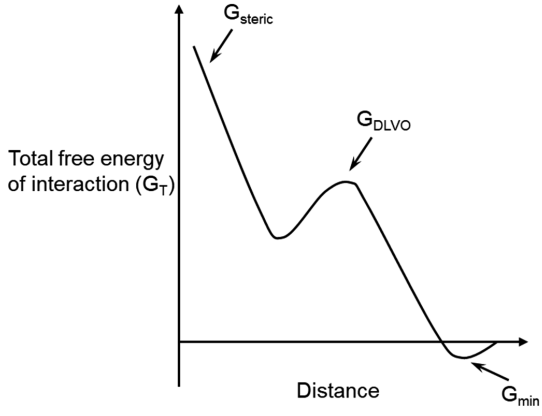

Figure 5-1. Total free energy of interaction (G_T) vs. distance curve for electrosteric stabilization, from reference [323].

stabilization in colloidal NPs dispersions in apolar media is that although the steric repulsion may guarantee colloidal stability, there are many applications such as e-ink displays (i.e., the Amazon Kindle®) and digital printers (i.e., HP Indigo®) where charged

NPs are used in successful products.[324] Energetically it is the dielectric constant which is limiting the creation of charges in the apolar media and thereby it is a disfavored process. As mentioned, the low dielectric permittivity of the apolar solvents (with typical $\varepsilon_s \approx 2$), makes it much harder than in polar solvents to achieve charge separation in these media as the charges are much less screened in these media.[325] For a more quantitative view, one may consider the separation distance that is characterizing charge recombination and neutralization: the Bjerrum length (λ_B). This length, λ_B, is defined as the distance between two oppositely charged monovalent ions at which the Coulombic attraction energy is equal to the thermal energy $k_B T$ and is given by:[145]

$$\lambda_B = \frac{e^2}{4\pi\varepsilon_s\varepsilon_0 k_B T} \qquad \text{Eq. 5-1}$$

where e is the elementary charge ($1.602 \times 10^{-19}\, C$), ε_0 is the electric permittivity in vacuum ($8.854 \times 10^{-12}\, C^2.N^{-1}.m^{-2}$), k_B is the Boltzmann constant ($1.38 \times 10^{-23}\, J.K^{-1}$), and T is the absolute temperature. By considering Eq. 5-1 for water with $\varepsilon_s \approx 80$ at room temperature, λ_B is about $0.7\, nm$ which is fairly close to the center-to-center distance, ca. $0.28\, nm$, in the NaCl rocksalt crystal). This is on the order of the size of a hydration layer of water molecules, which allows ions to freely dissociate and be held apart by tightly bound water molecules on both the cation and anion. However, in apolar solvents such as saturated hydrocarbons and toluene with $\varepsilon_s \approx 2$, λ_B is about $28\, nm$, two orders of magnitude larger. This means that the solvent molecules have to form a tightly bound shell around the present ions with a thickness of at least $14\, nm$. This evidently does not occur in pure apolar media, and thus prevents the free dissociation of most ions.[326] Hence, ions in apolar media can remain dissociated and stay stable only if they are large or contained in large structures (i.e., polymers, co-polymers, or most commonly, inverse micelles) that are significantly larger than hydration layers.[327]

Micelle formation in hydrocarbon solvents was already reviewed by Mathews and Hirschhorn in the early 1950s.[328] Afterwards, many reports were devoted to investigating the complex solubilization and interactions mechanisms of polar molecules, micelles, and polymers in nonaqueous media.[329–335] Along with these studies and especially in the last two decades, extensive reports and reviews have been published in the area of charge stabilization in apolar media focused on the presence of ion pairs and

reverse micelles by Morrison,[327] Lyklema,[336] Dukhin et al.,[337,338] Smith and Eastoe,[326,339–341] Bartlett et al.,[340,342,343] Weitz et al.,[344–346] Behrens et al.,[347–350] and Berg et al.[324,325,351,352] The majority of these investigations showed that the origin of the charge is system-dependent, which also makes it less clear to what exentend what mechanism is in operation and/or of importance.[326,350] As a consequence, several hypotheses have been suggested to rationalize the underlying particle charging mechanisms, some of these are: an *acid-base mechanisms*, *preferential adsorption*, and *site-binding mechanisms*.[325–327]

An acid-base mechanism was primarily suggested by Fowkes et al.[353] in 1984 and then promoted in experimental works of a several research groups.[347–350] It involves three key steps: 1) electrically neutral surfactants adsorb to the particle surfaces; 2) protons or electrons are donated or accepted based on the relative donor/acceptor (acid/base) characteristics of the surfactant and particle; and 3) charged surfactant monomers desorb from the particle surface leaving the opposite charge on the surface of the particles.[325] It has been shown that such acid-base mechanisms are predominantly applicable to nonionic surfactants which are surfactants that lack ionizable groups.[326] In the second mechanism, known as preferential adsorption, inverse micelles that are formed in the ionic surfactant solution and have charges of opposite sign in their polar cores, adsorb asymmetrically onto the particle surface, and thereby a net surface charge is generated.[342] Besides that, this mechanism may also occur at specific surfactant concentrations such as Aerosol-OT (AOT, sodium bis(2-ethyl-1-hexyl) sulfosuccinate), where individual ionic surfactant molecules (i.e., AOT^- anions) adsorb onto the particles' surface resulting in a net surface charge while Na^+ counterions are stabilized in inverse micelles.[354] In the third mechanism, known as the site-binding model, the combination of both mentioned models (acid-base interactions and preferential adsorption) occurs. At low surfactant concentrations, charged premicellar aggregates of one to three surfactant monomers adsorb to the particle surface based on the acid-base mechanism. However, at higher concentrations, inverse micelles of oppositely charged species begin to adsorb according to a preferential adsorption mechanism.[326,355,356] However, these mechanisms are known to explain and predict the generated electrical charges in apolar media well apriori, and several inconsistencies have been pointed out against the general

concept of the acid-base mechanism by Behrens et al.[347,348,350] In the notion of such discrepancies, they demonstrated that the (Lewis) acid-base character of the colloids (especially colloidal polymers) or its combination with ionizable functional surface headgroups would mainly determine the nature of electrical charges.[348,357] Nevertheless, they admitted that the classical inverse micelle acid-base charging mechanism in apolar media is applicable to several mineral oxides, clays, and similar pigments, which were thus consistent with Berg et al. observations.[324–326,350,351] It should be mentioned here that most of these models, including the 'acid-base' mechanism, were developed to explain the surface charge when ligands/charge-inducing agents like Span80 and OLOA1200 (see Fig. 5.2) were used to disperse 'bare' inorganic nanoparticles and not like we did in this study. Our NRs are already coated by ligands (oleic acid and/or oleylamine) that themselves are charge-inducing agents. This fact makes application of any theory a lot more difficult.

Next to apolar media, surface charges can play an important role also in low-polar solvents where $5 < \varepsilon_s < 15$ while ion concentrations are still extremely low.[327,358,359] Despite that the total amount of generated charges is still limited in these media, spontaneous charging is often observed for colloidal model systems like alkyl-coated silica dispersions and sterically stabilized polymethylmethacrylate (PMMA) particles [102,359–361], the ionic strength is often low making double layers extended ($\kappa^{-1} \gg a$, with a equals to the particle's diameter). As we also saw in this study, this allows the creation of charged particles without the need to add charge-inducing agents even to get surface potentials that are analogous in magnitude to those detected in aqueous dispersions.[358–361] Additionally, compared to apolar solvents these dispersions are much more sensitive to trace amounts of water [362,363]. For that reason, investigating diverse non-aqueous colloidal systems in both apolar or low-polar solvents has attracted much attention in the last decade.[363–365]

As mentioned in this chapter we investigated and show the formation of electric charges on ligand-capped brookite and anatase TiO_2 NRs in the presence of nonionic surfactants (Span80 and OLOA1200). The charging behavior of these colloidal nanorods was studied in toluene (as an apolar solvent with $\varepsilon = 2.38$) and cyclohexylbromide CHB (as a low-polar solvent with $\varepsilon = 7.92$). Despite the presence of charge inducing agents as

ligands already being present on our particles, we found the particle charges that we observed were in accordance with an often reported acidic behavior of Span80[325] creating positively charged titania NRs and basic behavior of OLOA1200[325] making the particles negatively charged.

5.2 Results and discussion

We investigated the surfactant-mediated charging of TiO_2 NRs by measuring their electrophoretic mobility in apolar and low-polar solvents using a Malvern Zetasizer. The brookite TiO_2 NRs had an average size of 27.4 nm (L) × 3.4 nm (D) and were stabilized with oleic acid and oleylamine ligand molecules. The anatase TiO_2 NRs had an average size of 24.6 nm (L) × 3.6 nm (D) and were stabilized with oleic acid molecules. Toluene with a dielectric constant of $\varepsilon = 2.38$ and refractive index of $n^{20}_{toluene} = 1.496$ at $\lambda = 587\ nm$ was used as an apolar solvent.[366] Its relatively high refractive index and boiling point in comparison with saturated hydrocarbons (i.e. hexane, heptane, decane) or commercial synthetic isoparaffinic fluids counterparts ensures weaker van der Waals attractions in TiO_2 NRs dispersions in our measurements. Cyclohexylbromide ($C_6H_{11}Br$, CHB) was used as a low-polar solvent with $\varepsilon = 7.92$, in which λ_B is about $7.2\ nm$ at room temperature ($T = 293\ °K$) and charge dissociation can still occur spontaneously with the ligands employed (ligand length of 1.5 to 2.0 nm in good solvents), contrary to truly apolar solvents with $\varepsilon \approx 2$. It has been reported that CHB solvent can show a considerable intrinsic conductivity, from several tens to thousands of $pScm^{-1}$ (for comparison, purified water has a conductivity in the μScm^{-1} range).[361,363] As can be observed in Table 5-1, electrical charges of different signs were observed in the dispersions of the titania NRs in the presence of Span80 and OLOA1200, which confirms the system dependency of the formed charges in the apolar media. We did find spontaneous charging of our NRs in CHB without the addition of more charge-inducing agents that were already used as ligands, while charges in 'pure' toluene were too small to be measured. We think that if there is any charge on these particles in 'pure' toluene, it is probably less than $\pm 5\ mV$, since we could still observe reliably small charges on the NRs in CHB which has similar

refractive index contrast. In order to rationalize the nature of the generated charges, both of these nonionic surfactants are described in some more detail.

Span80 (sorbitan monooleate) is a nonionic fatty acid ester from the commercial surfactants family of the sorbitan esters (Span) (Figure 5-2). It has a C_{17} tail, but with a double bond halfway down its length. The critical micelle concentration (CMC) of Span80 in apolar solvents (such as decane and Isopar L) has been reported to be 0.042 ± 0.001 mM, based on conductometric measurements.[352,367] This surfactant usually contains ca. 40.0 wt.% of other fatty acids such as oleic, linolenic, and palmitic acids as well as less than 1.0 wt.% water as impurities.[368–370] It has been shown that these ionogenic impurities such as oleic acid and residual water play a vital role in the generation of charged micelles in Span80 solutions, however, Span80 molecules are still known as limiting factors in the ionization process.[369] Dukhin and Goetz reported a diameter of 29 nm in kerosene oil for Span80 inverse micelles. Whereas in dry conditions, spherical inverse micelles of ca. 5.5 nm were observed for Span80 molecules in apolar solvents (e.g. decane, isoparaffin). As mentioned above, this diameter can vary notably in the same medium with respect to the present trace water ranging from 6 to 80 nm in diameter which has been confirmed by dynamic light scattering (DLS), small-angle x-ray scattering (SAXS), and small-angle neutron scattering (SANS) techniques in previous studies.[324,352] The acidity of Span80 has been reported by its manufacturer by an acid number of ca. 8 which is determined via a 'standard' industrial method suggested by the American Society for Testing Materials (ASTM). According to ASTM D664 suggested for describing acid-base characteristics of petroleum products, lubricants, and especially surfactants, an acid number is defined as the amount of KOH (in milligrams) required to neutralize one gram of an acid of interest.[371] These typical numbers are mostly measured via a potentiometric titration where the acid number is obtained through titration of KOH in the mixture of 2-propanol and toluene and the base number is achieved by the titration of perchloric acid.[372] Span80 is often observed to act as an acid creating positively charged nanoparticles. Despite of the fact that the surface of our brookite and anatase NR system are already coated with ligands, Span80 was still seen to induce positive charges on both our NR systems in both toluene and CHB.

OLOA1200 is a nonionic polyisobutylene succinimide (PIBS) surfactant ($M_w \cong 1200\ g/mol$) with a polyamine headgroup and thereby exhibits a basic nature (Figure 5-2).[373] PIBS surfactants are available commercially as OLOA family (Oronite Lubricating Oil Additive as a patented material) and the exact number of repeat units in the PIB tail and the polyamine head is not known very well and may differ based on the OLOA version (i.e. OLOA371, 1200, and 11000 are all cited in the literature as similar PIBS surfactants).[373] Fowkes et al. reported the following three-section structure for OLOA1200 molecules: 1) a section of multiple amine groups even though there is discrepancy whether it contains a pentamine or triamine,[373] 2) a long polyisobutylene tail including approximately 70 carbon atoms attached, and 3) a succinimide group linking the first two parts. In general, the polar head is expected to be ca. 1 nm while the apolar tail should be around 5 nm yielding an inverse micelle of approximately 10 nm.[353,373] Therefore, OLOA1200 inverse micelles are almost two times larger than the Span80 inverse micelles in dry conditions. The concept of CMC in apolar media should be used with caution, as the transition occurs not as sharp as it does in aqueous systems. Furthermore, small amounts of water or impurities are expected to influence the formation of the inverse micelles in apolar solutions or possibly induce the formation of premicellar aggregates.[325,349,374]

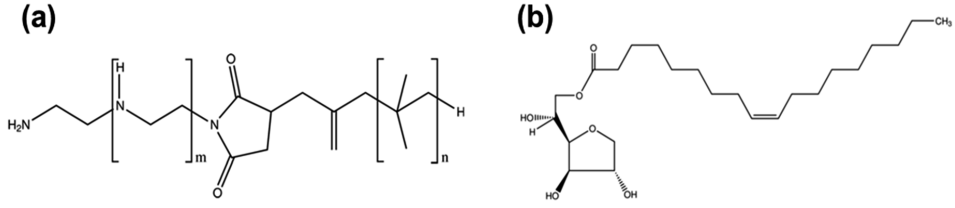

Figure 5-2. Chemical structure of (a) the commercial polyisobutylene succinimide polyamines (commercially distributed as OLOA charging agent surfactants) from reference [326] and (b) Span® 80.

In addition to the properties of the surfactants, we note that the crystalline titania NRs, such as brookite and anatase TiO_2 NRs, have several acid sites such as Lewis acid sites (Ti^+) and Brønsted acid sites ($Ti-OH$) on their surface. Both of these acid sites are

known to adsorb with the polar groups carboxylic acids and amines (in our cases oleic acid and oleylamine ligand molecules) to the hydroxylated oxide surfaces of the NRs ensuring steric stabilization.[375] We have shown in our earlier report that the TiO_2 NRs are covered with ligand molecules with an average ligand density of 2.3 to 2.7 molecules/nm^2.[188] On the other hand, the surface hydroxyl groups density on TiO_2 nanocrystals (ca. 30.0 nm in diameter) has been reported to be around 3.3 OH/nm^2.[376] Therefore, the TiO_2 NRs still have $-$OH sites on their surfaces that are not connected to ligand molecules.

Table 5-1. Various electrical charges were observed in the dispersions of brookite and anatase NRs in the presence of Span80 (acidic surfactant) and OLOA1200 (basic surfactant) and pure solvents. In pure toluene, the electric charge was not measurable.

Apolar dispersions ($\varepsilon = 2.38$)		
Surfactant solutions	**Brookite (TiO_2)**	**Anatase (TiO_2)**
Toluene / OLOA1200	Negative	Negative
Toluene / Span80	Positive	Positive
Toluene	Too small to measure	Too small to measure
Low-polar dispersions ($\varepsilon = 7.92$)		
Surfactant solutions	**Brookite (TiO_2)**	**Anatase (TiO_2)**
CHB / OLOA1200	Negative	Negative
CHB / Span80	Positive	Positive
CHB	Positive	Positive

Again, despite the more complex surface covering of our titania NR systems as compared to 'bare' NPs systems, we observed negatively charged NRs in both toluene and CHB caused by the basic OLOA1200. As mentioned, for the apolar samples dispersed in toluene, due to low signal-to-noise ratio of the zeta potential measurements, it was not possible to detect any mobility in this pure apolar solvent. If there was any charge on these dispersions it was likely less than 5 mV. On the other hand, we observed that dispersed TiO_2 NRs in CHB became positively charged even without additional charge-inducing agents for both the NR systems. This spontaneous charging is also observed for other (silica, PMMA) colloidal model systems in this type of solvent. To speculate about the possible origins of this charging: it is known that CHB as a solvent can slightly decompose forming HBr and likely cyclohexene:

$$C_6H_{11}Br \rightarrow C_6H_{10} + HBr \qquad \text{Eq. 5-2}$$

Moreover, the solvent had a slight yellow appearance, which could be caused by the formation of small amounts of bromine (Br_2) as a side product. Hydrobromic acid has

a finite solubility in CHB and even though HBr is a strong acid in the water, it will only partially dissociate in CHB and thus behaves as a weak acid.[362] On the other hand, the available surface hydroxyl groups in TiO_2 NRs are capable of either accepting a proton (electron donor) or donating a proton (electron acceptor). Since TiO_2 surface is only weakly acidic in aqueous media, it could behave relatively basic in the presence of HBr in CHB.

In Figure 5-3 the charging behavior of our brookite and anatase TiO_2 NRs are shown in terms of the NRs' electrophoretic mobility (μ) and their corresponding zeta potentials (ζ) in the apolar and low-polar dispersions at various surfactant concentrations. Since the electrophoretic measurements were performed in dilute dispersions and the solvents had relatively low dielectric constants ($\varepsilon_{toluene} \approx 2.3$ and $\varepsilon_{CHB} \approx 7.9$), our systems were considered in the limit of thick double layers ($\kappa a \ll 1$) and the zeta potentials were obtained via the Hückel equation in Eq. 5-3:[360]

$$\zeta = \frac{3\eta\mu}{2\varepsilon_s\varepsilon_0} \qquad \text{Eq. 5-3}$$

where ε_s is the solvent dielectric constants, ε_0 is the electric permittivity in vacuum and η is the viscosity of the solvent. Here, in order to compare our material systems with similar systems (either titania or similar metal oxide NPs in apolar media) reported in the literature,[324,325,368,377,378] we selected surfactant concentration ranges from them (above CMC) which were known to impart measurable electrophoretic mobilities and zeta potentials to the dispersed NRs. In addition to surfactant concentration, it is known that the applied electric field strength can also affect the particle's electrophoretic mobility at higher field strengths. Therefore, we avoided misinterpretations by employing the commonly used strategy of extrapolating the field-dependent mobility to zero field strength,[325,347,349,379], and therefore the values shown in Figure 5-3 are 'zero-field' electrophoretic mobilities. As mentioned, in the entire concentration range, Span80 (acidic surfactant) charged both the brookite and anatase TiO_2 NRs positively in both toluene and CHB. On the other hand, both of these polymorphs of TiO_2 were charged negatively in the presence of the basic OLOA1200 surfactant. The measured electrophoretic mobilities are of the same order and analogous to reported mobilities for mineral oxide NPs and polymer colloidal NPs in apolar solvents.[324,347,348,357,367]

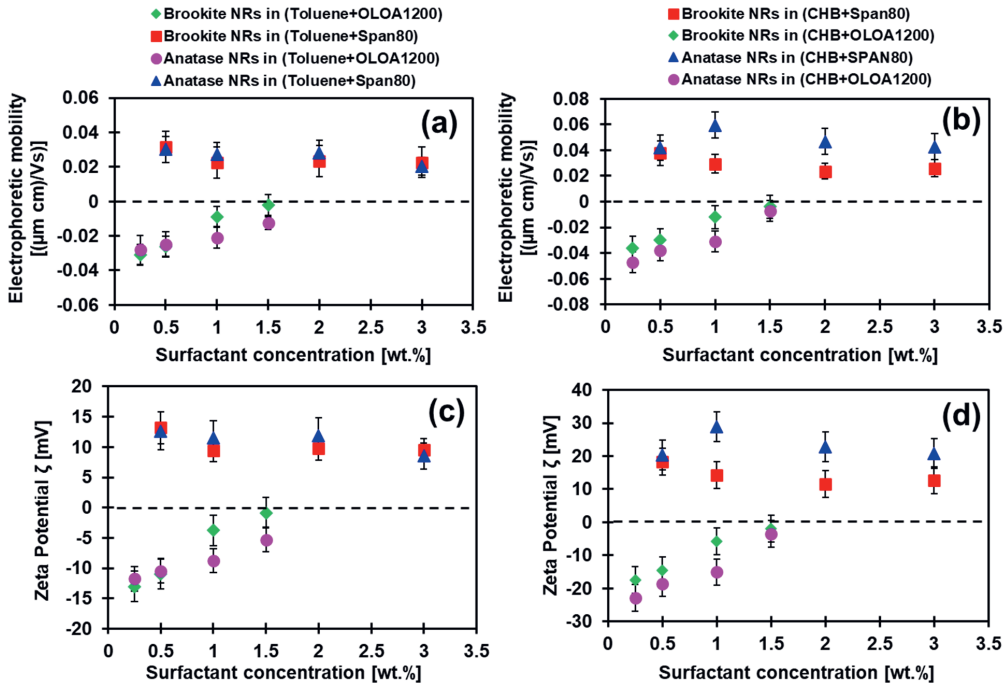

Figure 5-3. (a and c) Zero field electrophoretic mobility and corresponding zeta potential (in the Hückel limit) of brookite and anatase NRs in the apolar solvent solutions (toluene) and (b and d) in low-polar solvent solutions (CHB) with various surfactants. Blue and red markers are shown for solutions containing diverse concentrations of Span80 (0.5 to 3 wt.% equal to ca. 10 to 60 mM, acidic surfactant) in toluene and CHB dispersions, respectively. Green and magenta markers are illustrating OLOA1200 (0.25 to 1.5 wt.% equal to ca. 3.9 to 24.0 mM, basic surfactant) concentrations in toluene and CHB dispersions, respectively.

5.3 Conclusions and outlook

In summary, we successfully created oppositely charged titania NRs by using either charge-inducing agents with an acid character Span 80 creating positively charged particles of basic character, OLOA 1200 creating negatively charged oleylamine and oleic acid stabilized brookite and anatase NRs.. The same charging behavior of these colloidal nanorods was shown in toluene (representing an apolar solvent) and CHB (representing

a low-polar solvent). Moreover, we observed positively charged TiO_2 NRs in pure CHB dispersions which is hypothesized to be due to protonation from traces of HBr (formed by CHB decomposition). Particle charges were too low to measure in pure toluene. The fact that we can create oppositely charged TiO_2 dispersions using commercially available charge-inducing agents turns these dispersions into interesting model particles to investigate the effects of particle charging on for instance their alignment dynamics as was already investigated in Chapter 4 for (almost) uncharged titania NRs inside toluene.

5.4 Experimental

5.4.1 TiO_2 NRs Dispersions Preparation

Ligand-capped anatase and brookite NRs colloidal NRs were prepared as described in previous chapters and references [188,316]. Two oil-soluble surfactants were used in this study. The basic OLOA1200 was obtained from Chevron Oronite (San Ramon, CA). The company describes it as a mixture of 50 wt.% mineral oil and 50 wt% polyisobutylene succinimide. The acidic surfactant, Span80, sorbitan monooleate, was purchased from Sigma-Aldrich. Toluene and CHB were purchased from Sigma-Aldrich and were used as received.

The surfactant solutions were formulated in two different series. Four concentrations (0.25, 0.5, 1.0, 1.5 wt.%) for OLOA1200 and four concentrations (0.5, 1.0, 2.0, and 3.0 wt.%) for Span80 were prepared, both in toluene and in CHB. Then 15.0 μL from the dispersions of brookite and anatase NRs with an initial volume fraction of 20.0 vol.% were added to 3.0 mL of the various surfactant solutions. In this way, we could prevent interparticle interactions and multiple scattering during the electrophoretic mobility measurements which were cross-checked by controlling the attenuation index in DLS measurements to be less than 11. The dispersions were then sonicated for 3 h. To avoid overheating, the sample was removed from the sonicator for cool-down at different time intervals. Then samples were left rolling for 3 h and allowed to equilibrate for at least a few days.

5.4.2 Dynamic light scattering (DLS) and Electrophoretic Mobility Measurements

Dynamic light scattering (DLS) measurements were performed on a Zetasizer Nano ZS (Malvern) with a backscatter detector at 175° angle to maximize the scattering volume and signal intensity and reduce multiple scattering effects. By employing solvent viscosity and refractive index together with the surfactants and particles' refractive indexes, Zetasizer algorithms determined a diffusion coefficient from the decay rate of the correlation function of a sample's scattering intensity fluctuations over time. Using this information, the hydrodynamic diameters of the inverse micelles and dispersed NRs were measured as a size distribution from the Einstein-Stokes relation.

The electrophoretic mobilities in nonaqueous dispersions as an indicator of particle surface charging was measured by phase analysis light scattering (PALS) using the same Zetasizer Nano ZS machine. The prepared dispersions were loaded into a glass cuvette (10 mm square optical glass cell), and a dip cell with two planar palladium electrodes spaced by 2 mm was submerged in the sample. Before each measurement, the glass cuvette and dip cell were washed and rinsed with hexane and then dried with an airflow. An a.c electric field was applied across the electrodes under systematic variations of field strength (7.5–40.0 kV/m), and the field-dependent electrophoretic mobility of particles was measured based on phase information of light scattered by the particles. To prevent misinterpretations, we employed the commonly used strategy of extrapolating the field-dependent mobility to zero-field strength.[325,347,349,379] The Zetasizer ran both slow and fast field reversals to measure the mobility of the NRs from the phase analysis light scattering. Zeta potentials were calculated via the Hückel equation (shown in Eq. 5-3) with error bars for an average of three measurements.

5.5 Acknowledgments

I would like to thank my Bachelor's student, Dagney Mackaaij, for her contributions on anatase titania synthesis experiments, DLS and electrophoretic mobility measurements

Summary and outlook

This thesis deals with the synthesis, characterization, and optimization of TiO_2 nanorods colloidal dispersions. Two polymorphs of TiO_2 nanorods are developed in the form of highly stable colloidal dispersions that are further investigated for advancing inorganic-based liquid crystalline phases utilized for switchable optics applications.

In **chapter 1**, we provide a brief background on inorganic liquid crystals and TiO_2 nanoparticles, known as one of the most functional building blocks in the colloidal industry. In **chapter 2** we explain the synthesis of fairly monodisperse brookite TiO_2 nanorods in a scaled-up version of a literature method such that the liquid crystalline phase behavior of the resulting nanorods dispersions can be investigated. Furthermore, the role of the surface ligands' density is highlighted, which was found to be crucial to minimize the detrimental effects of destabilizing attractions between the dispersed nanorods. A post-synthesis-treatment step is thus designed and coupled with the scaled-up procedure to ensure more hard-rod-like phase behavior as well as maintaining colloidal stability even at relatively high volume fractions in the apolar organic solvents. Then various self-assembled liquid crystalline structures formed on a liquid interface and in bulk are investigated by utilizing transmission electron microscopy and polarized optical microscopy techniques. Self-assembled structures of the brookite nanorods are qualitatively similar to the nematic and smectic liquid crystalline phases predicted for hard rod-shaped particles. Interestingly, it is also observed that the ordering within the smectic layers can be tuned from hexagonal to tetragonal reflected by the shape of the brookite nanorods' hard cores.

In **chapter 3** the synthesis of nanorods of another polymorph of TiO_2 phase, anatase, is described. This is performed via a single step nonhydrolytic sol-gel route using oleic acid as the solvent, reagent, and surface ligands and titanium (IV) isopropoxide as the titanium precursor. Along with the formation of monodisperse anatase TiO_2 nanorods, some semi-spherical TiO_2 nanocrystals mainly of TiO_2(B) phase, are grown that can be

removed by size-selective precipitation. It is found that the average length of the initially grown nanorods decreases during the synthesis and possible reasons for this unusual growth path, partially based also on high-resolution electron microscopy observations during the growth, are discussed. Analogous to brookite TiO_2 nanorods dispersions, the dispersion of anatase TiO_2 nanorods are capable of spontaneous formation of lyotropic liquid crystals in bulk and at the liquid interface.

In **chapter 4** we demonstrate the electric-field-induced birefringence, known as the Kerr effect, due to the formation of (para)nematic liquid crystalline phases in previously developed isotropic dispersions of brookite and anatase TiO_2 nanorods in external electric fields. Both of these nanorod dispersions exhibit outstanding electro-optical responses probed in in-plane alternating current electric fields. In our preliminary results, it is observed that both of these nanorods can be aligned into the direction of the applied electric field within ca. $250\,\mu s$ switching times in various field strengths, one order of magnitude faster than commercial Freedericksz-based liquid crystals. Possible mechanisms contributing to the reorientation of TiO_2 NRs are discussed among which the polarization of the electrical double layer in the framework of the Maxwell–Wagner–O'Konski mechanism is proposed to contribute larger than other mechanisms. Furthermore, experimental observations are confirmed with theories and thus it is surmised that rise times in these TiO_2 dispersions are in the order of ca. $50\,\mu s$ for $E = 10\,V/\mu m$ whereas the relaxation times are approximated to be ca. $100\,\mu s$. Finally, to estimate the refractive index of TiO_2 dispersions and possible birefringence observed in the electric field, refractive indexes of anatase and brookite colloidal dispersions at various volume fractions are measured and subsequently compared with effective medium models such as Maxwell-Garnett and Bruggeman theories. The largest estimated birefringence for utilized anatase and brookite NRs dispersions are approximated to be 0.025 and 0.034, respectively.

Last but not least, in **chapter 5**, the possibility of charging such colloidal nanorods in apolar and low-polar media is shown. Our results confirm that both TiO_2 NRs are charged positively in toluene (as an apolar solvent) and cyclohexylbromide (as a low-polar solvent) if Span80 (an acidic nonionic surfactant) is used and are charged negatively if OLOA1200 (basic nonionic surfactant) is present. The ion formation and sustaining electric charges are believed to be caused by introducing reverse micelles formed by added

surfactants. Moreover, we observe positively charged TiO_2 NRs in pure CHB dispersions, which may be assigned to its relatively high dielectric permittivity in comparison to toluene as well as formed HBr by CHB decomposition. Although electrophoretic measurement does not provide any insights in apolar solvent without the addition of surfactant, we think there may be some charge on these NRs in 'pure' toluene but it is too small to measure, since we could still observe reliably small charges on the NRs in CHB which has similar refractive index contrast. Nevertheless, we believe this charge has been promoted and sustained in the bulk solution via the reverse micelles formed by the existence of desorbed ligand molecules in the solution. Finally, we believe that our demonstrated results provide experimental supports for the well-known theory of acid-base charging in the nonaqueous media.

In the **outlook**, we would like to point out that as mentioned in this thesis, we introduce brookite and anatase TiO_2 nanorods dispersions in nonaqueous media as promising candidates beneficial for many fields in the optical industry. We show that by engineering the ligand density at the surface of TiO_2 nanorods and optimizing experiment conditions, relatively monodisperse TiO_2 nanorods with tunable aspect ratios and lengths less than 100 nm can be achieved at a high yield at the colloidal level. These NRs are small enough not to strongly scatter light, but their high refractive indexes and anisotropies can be utilized to manipulate (polarized) light. Our preliminary results show the emergence of (para)nematic ordering reversibly induced in isotropic dispersions of TiO_2 nanorods at relatively high volume fractions while external electric fields are applied. The switching dynamics in our dispersions are remarkably faster than their commercial Freedericksz-based liquid crystals counterparts. We strongly believe that these fast switching dynamics, coupled with the changes in the effective refractive index of these dispersions manipulated by external electric fields (e.g. by changing the orientation of the rods and/or the local concentration by (di)electrophoresis), offer a brilliant perspective in many optical applications such as ultrafast optical switches, spatial light modulators, switchable gradient index lenses, shutters, remote sensors, diffusers, and signaling industries

Samenvatting en vooruitzicht

Dit proefschrift beschrijft de synthese, het karakteriseren en het optimaliseren van colloïdale dispersies van TiO_2 nanostaafjes. Twee versies van TiO_2 nanostaafjes met verschillende kristalstructuren zijn ontwikkeld in de vorm van stabiele colloïdale dispersies die verder onderzocht zijn om vloeibare kristallen gebaseerd op anorganische nanodeeltjes te ontwikkelen die bedoeld zijn voor schakelbare optische toepassingen.

In **hoofdstuk 1** geven we een korte achtergrond over anorganische vloeibare kristallen en TiO_2 nanodeeltjes, die bekend staan als een van de meest bestudeerde colloïdale systemen voor een groot bereik aan toepassingen, van katalytische tot optische.

In **hoofdstuk 2** beschrijven we de synthese van relatief monodisperse brookite TiO_2 nanostaafjes in een opgeschaalde versie van een methode uit de literatuur. Met deze dispersie van nanostaafjes konden we onderzoeken hoe de vloeibaar kristallijne fase zich gedraagt. Bovendien laten we de rol van de dichtheid van de liganden op de oppervlakte zien, wat cruciaal bleek om nadelige effecten van destabiliserende aantrekkingen tussen deze nanostaafjes te minimaliseren. Een behandelingsstap na de synthese werd ontworpen en gecombineerd met een opschalingsprocedure om het fasengedrag meer zoals dat van harde staafjes te maken. Eveneens werd zo de colloïdale stabiliteit gewaarborgd, zelfs bij relatief hoge volumefracties in apolaire vloeistoffen. De staafjes vormden verscheidene zelf-geassembleerde vloeibare kristal fasen op een vloeistofoppervlak en in bulk. Deze structuren zijn onderzocht met behulp van transmissie elektronen microscopie en optische microscopie technieken met gepolariseerd licht. Zelf-geassembleerde structuren van de brookite nanostaafjes vormden fasen die kwalitatief overeen kwamen met nematische en smectische vloeibare kristalfasen zoals die voor harde staafvormige deeltjes worden voorspeld. Het bleek dat de symmetrie binnen de smectische lagen ook veranderd kon worden van een hexagonale naar een tetragonale symmetrie, wat komt door de vorm van de kern van de brookite nanostaafjes.

In **hoofdstuk 3** beschrijven we de synthese van nanostaafjes van anatase, hetgeen een andere kristalstructuur van TiO_2 is. Deze werden gemaakt via een 'nonhydrolitic sol-gel' route met oliezuur als het oplosmiddel, reagens en als oppervlakte ligand en titanium (IV) isopropoxide als de titanium precursor. Samen met de formatie van monodisperse anatase TiO_2 nanostaafjes groeiden er ook sommige semi-bolvormige TiO_2 nanokristallen van hoofdzakelijk de TiO_2(B) fase, die verwijderd zijn met grootte-selectieve precipitatie. We observeerden dat de gemiddelde lengte van de initieel gegroeide nanostaafjes afnam tijdens de synthese. Mogelijke redenen voor dit ongewone groei proces worden besproken, mede op basis van hoge resolutie elektron microscopie observaties tijdens de groei. Net zoals de brookite TiO_2 nanostaafjes dispersies konden de dispersies van anatase TiO_2 nanostaafjes ook spontaan lyotrope vloeibare kristallen vormen, zowel in de bulk als op een vloeistofoppervlak.

In **hoofdstuk 4** demonstreren we de 'birefringence', ofwel dubbelbreking, die opgewekt wordt door een elektrisch veld, in de eerder ontwikkelde isotrope dispersies van brookite en anatase TiO_2 nanostaafjes met externe elektrische velden. Dit staat ook wel bekend als het Kerr effect, ofwel het ontstaan van een (para)nematische vloeibare kristal fase in een elektrisch veld. Beide dispersies van nanostaafjes vertoonden uitstekende elektro-optische eigenschappen, die onderzocht werden met 'in-plane' wisselstroom elektrische velden. In onze eerste resultaten konden beide systemen van nanostaafjes worden uitgericht in de richting van het aangelegde elektrische veld binnen een schakeltijd van ca. $250\,\mu s$. Dit is een orde van grootte sneller dan commerciële moleculaire vloeibare kristallen, waar het schakelen gebaseerd is op de collectieve Freedericksz transitie. Mogelijke mechanismen die bijdragen aan de heroriëntatie van de TiO_2 nanostaafjes worden besproken, waaronder de polarisatie van de elektrische dubbellaag in het kader van het Maxwell–Wagner–O'Konski mechanisme, dat voorgesteld wordt als belangrijker dan andere mechanismen. Verder werden de experimentele observaties bevestigd met theorieën en dus vermoeden we dat de tijdschaal voor het opkomen van de uitlijning van de TiO_2 dispersies van de orde van ca. $50\,\mu s$ is bij $E = 10\,V/\mu m$, terwijl$100\,\mu s$ is. Tenslotte, om de brekingsindex van de TiO_2 dispersies en de dubbelbreking af te schatten zoals geobserveerd in de elektrische velden, werden de brekingsindices van colloïdale anatase en brookite dispersies gemeten voor verschillende

volumefracties en vervolgens vergeleken met ”effectieve medium” modellen zoals Maxwell-Garnett en Bruggeman theorieën. De grootste ‘dubbelbreking’ effecten voor dispersies van anatase en brookite nanostaafjes waren respectievelijk 0.025 en 0.034.

‘Last but not least’, in **hoofdstuk 5** wordt de mogelijkheid van het opladen van zulke colloïdale nanostaafjes in apolaire en laag-polaire media onderzocht. Onze resultaten bevestigden dat beide typen TiO_2 nanostaafjes positief geladen waren in tolueen (een apolair oplosmiddel) en cyclohexylbromide (CHB) (een laag-polair oplosmiddel) als Span80 (niet-ionisch oppervlakte-actieve stof) gebruikt werd en negatief geladen waren als OLOA1200 (niet-ionische oppervlakte-actieve stof) aanwezig was. Het vormen van ionen en de elektrische ladingen werden waarschijnlijk mogelijk gemaakt en gestabiliseerd door de introductie van omgekeerde micellen die gevormd worden door de toegevoegde oppervlakte-actieve stoffen. Bovendien observeerden we TiO_2 nanostaafjes die positief geladen waren in pure CHB dispersies. Dat komt wellicht door de hogere relatieve diëlektrische permittiviteit vergeleken met tolueen, en ook door HBr dat gevormd wordt door CHB decompositie. Hoewel elektroforetische metingen geen duidelijk resultaat gaven in dit apolaire oplosmiddel zonder toevoeging van de oppervlakte-actieve stof, is het mogelijk dat er enige lading op deze NRs in 'puur' tolueen is, maar dat die te klein is om te meten aangezien lading op NRs in CHB wel betrouwbaar te meten was bij een vergelijkbare brekingsindexcontrast. We denken dat deze negatieve lading gecreëerd is in de bulk via omgekeerde micellen, die gevormd waren door gedesorbeerde ligand moleculen in het oplosmiddel. Tenslotte geloven we dat onze resultaten experimentele ondersteuning geven aan de theorie van zuur-base oplading in dit niet-waterige oplosmiddel.

Als **vooruitzicht** benadrukken we dat dispersies van brookite en anatase TiO_2 nanostaafjes in niet-waterige media geïntroduceerd werden als veelbelovende kandidaten voor vele toepassingen binnen het veld van (schakelbare) optica. We hebben laten zien dat we door het aanpassen van de ligand dichtheid op het oppervlak van de TiO_2 nanostaafjes en het optimaliseren van de experimentele condities redelijk monodisperse TiO_2 nanostaafjes kunnen maken met aanpasbare aspect ratio en met lengtes korter dan 100 nm met een hoge opbrengst. Deze nanostaafjes zijn klein genoeg om niet teveel licht te verstrooien, terwijl hun hoge brekingsindex en anisotropie kunnen worden gebruikt

om (gepolariseerd) licht te manipuleren. Onze voorlopige resultaten lieten zien dat (para)nematische orde reversibel aangebracht kon worden in isotrope dispersies van de TiO_2 nanostaafjes, bij relatief hoge volumefracties, door het aanleggen van externe elektrische velden. De schakeldynamica van onze dispersies zijn duidelijk (veel) sneller dan commerciële moleculaire vloeibare kristallen waar het schakelen gebaseerd is op de Freedericksz transitie. We geloven er sterk in dat deze snelle oplijningsdynamica gekoppeld met de opmerkelijke veranderingen in de effectieve brekingsindex van deze dispersies wanneer deze gemanipuleerd worden door externe elektrische velden (bijvoorbeeld door het veranderen van de oriëntatie van de staafjes en/of de lokale concentratie door (di)elektroforese) deze dispersies interessant maken voor vele optische toepassingen, zoals schakelbare (gradiënt brekingsindex) lenzen, ultrasnelle optische schakelaars, ruimtelijke licht modulatoren, sluiters, 'remote sensing', diffusors en in beeldschermen.

Acknowledgments

Although I am writing the very last pieces of my thesis, it is certainly hard for me to believe that it is done and I could make it! Even though I started my Ph.D. in 2016, to be more precise, this journey started a bit earlier in 2015 from Iran where I applied for a Ph.D. position in the SCM group with the job title "*Responsive Colloids for Switchable Optics*" funded by STW. As a person with an engineering background who was passionate about applications, it was a perfect match for me to work in the field of synthesis and characterization of nanoparticles which could be ultimately used for optical applications. Back then, as I expect for most PhDs, I had no idea how my adventure will take place, nevertheless, I am glad that I could deliver my objectives and learn many valuable things along this journey. I am grateful to all of the people who participated in various ways in the work described in this thesis and I hope I do not miss any of them in the acknowledgment otherwise, my apologies in advance!

First of all, I am absolutely grateful that during my Ph.D., I was supervised by three nice scientists who always treated me like a *friend* and not like a *boss*! I would like to thank my supervisors who accompanied me step by step over the last 6 years, Alfons van Blaaderen, Arnout Imhof, and Patrick Baesjou. **Alfons**, thank you for trusting in me and giving me the opportunity to work on this project. Your broad view on various topics coupled with strong scientific memory and rich knowledge of even detailed practical tricks in the lab have always fascinated me. Although different supervisors may have different styles for their supervision which may seem to be more or less supportive when they are compared with each other, I learned from you to be an independent researcher who must take a deep dive into the literature and solve the problems either independently or by setting up collaborations with people in the field. Apart from the scientific aspects, I would like to thank you for your consistent support of the social aspects of the SCM group which guaranteed a pleasant atmosphere for the SCM group. **Arnout**, thanks a lot for your constant calm positive attitude and all of your support. It has been an honor working under your supervision where I learned from you how to simplify different problems to find logical solutions. We went through all of the Ph.D. reports as well as thesis chapters together and had many fruitful discussions. Furthermore, in the last step of my Ph.D., together with you and Alfons, we were awarded the "Take-off" grant by NWO-TTW which was not possible if your always present kind support would not be there. **Patrick**, with no doubt, I owe you my practical skills and confidence in the lab. I was very fortunate to have you as my daily advisor. Your scientific knowledge and valuable experience from years of working in cutting-edge research at Philips labs have always inspired me to become a decent scientist. I hope I could fulfill your expectations for this project.

In the next step, I would like to thank the scientific staff of the SCM and Molecular Biophysics group: Marjolein Dijkstra, René van Roij, Laura Filion, Marijn van Huis, Joost de Graaf, Frank Smallenburg, Freddy Rabouw, Lisa Tran, Michiel Hermes, Krassimir Velikov, Hans Gerritsen, Gerhard Blab, and Jan Lipfert. Many thanks for the helpful remarks and suggestions you gave me during my Ph.D. in various occasions. **Marjolein** and **René**, although I was an experimentalist, your comments and questions in work discussions were always insightful for me and I am grateful for them. **Marijn**, thanks for your support on high-resolution microscopy measurements that enriched my thesis and helped me to collaborate with two of your students which resulted in three publications for us. **Laura**, it has been always a pleasure talking to you (even sometimes while biking home since we were neighbors for a while during my Ph.D.!) about scientific and non-scientific topics. **Freddy**, thank you for your kind help and discussions on the data analysis of the SAXS results we acquired from the X-ray measurements in the Diamond Light Source synchrotron facilities in the UK. Furthermore, I would like to thank

you for allowing us to use your optical set-up for optical switching measurements. **Gerhard**, a warm *salam* to you and thank you for sharing tasty Austrian sweets with us. **Lisa**, you joined the SCM group when my Ph.D. project was almost finished. I wish you lots of success with the Tran's group.

In the next step, I would like to heartily thank our administrative support staff members: Marion Wijburg, Hester van der Putte, Dianne Ickenroth, Linda Kumeling, Mijke Heldens, and Mirna Marrink. **Marion**, thank you for your assistance with all administrative matters, especially at the beginning of my Ph.D. Dear **Hester**, thanks for your constant positive attitude in the SCM group. I sincerely thank you for giving order to many detailed administrative tasks and taking care of them carefully which helped me to submit my thesis smoothly. I wish you and *Momo* lots of fun together. **Dianne, Mirna,** and **Mijke** are warmly thanked for their help in facilitating my contract procedures in collaboration with the HR department during my Ph.D. and Postdoc.

As an experimentalist, it happened so often that my daily practical matters were smoothly handled with the help of our friendly technical staff: Peter Helfferich, Relinde Moes-van Dijk, Elleke van Harten, Dave van den Heuvel, Chris Schneijdenberg, Hans Meeldijk, and Judith Wijnhoven. **Peter**, I gratefully thank you for all of your kind support in various aspects that I received from you. Thanks for being always there and to help the SCM group keep running! **Relinde** and **Elleke**, I warmly thank you for your technical/chemical support and feedback in the lab. **Dave**, thank you for the interesting discussions during the coffee breaks on various topics ranging from aikido to cultures. **Chris** and **Hans**, it is almost impossible to imagine the microscopy center running without your assistance! Thanks a lot for all of those trainings, troubleshootings, and even late evening calls to get technical tips from you! Although **Judith** is not among us anymore, I would like to thank her for different safety suggestions and instructions for the labs and I hope she is resting in peace.

Next, my appreciation goes to all of the people I have collaborated with: Albert, Anna, my bachelor students (Dagney and Winnie), Xiaobin, Xiaodan, Marijn. **Albert**, thank you for your positive mood, *artistic* skills, and supportive attitude. Working with you was a pleasant experience for me. **Anna**, thank you for advising Winnie with electric field measurements. Besides that, thanks for sharing *Dominique* and other memorable gifts from different parts of the world with me. **Dagney** and **Winnie**, I am proud of your achievements in your bachelor projects which resulted in two chapters of my thesis. **Xiaobin**, thank you for helping me with all the high-resolution microscopy images. **Xiaodan**, thanks a lot for high resolution and in-situ heating microscopy measurements on titania particles which resulted in three nice papers for both of us.

In addition to my collaborators in the SCM group, I would like to cordially thank other people who helped me at various stages of my thesis: Great appreciation goes to **Dr. Matteo Cargnello** at Stanford University for his absolutely useful tips and suggestions on the synthesis of brookite nanorods. I was honored to discuss many details about colloidal liquid crystals with a great scientist in the field of physical chemistry, **Prof. Henk Lekkerkerker**. **Henk**, your constant positive and kind support during the writing stage of my thesis motivated me to never give up and keep the momentum. All the best wishes to you and **Loes**! In the last stage of my Ph.D., via Henk's scientific network, I was honored to get in touch with two nice scientists, **Dr. Patrick Davidson** and **Dr. Ivan Dozov**, in Laboratoire de Physique des Solides of Université Paris-Sud in Orsay. I would like to warmly thank you for collaborating with us on studying the dynamics of titania nanorods in the external electric fields and all of those subsequent fruitful discussions. I hope the collaborations between the SCM group and you will be continued in the future. Also, I would like to kindly thank **Prof. Dick Broer** and his Ph.D. student, **Wei Feng** for

having me in TU/Eindhoven for very beneficial discussions on liquid crystals as well as for being a valued member of the assessment committee of my thesis. **Koen Demeyer** from **Anteryon B.V.** is greatly appreciated for supporting our project, especially their generous financial support during the last 3 months of my Ph.D. project. Furthermore, I would like to thank **Roel van de Belt** from **Kriya-Materials B.V.** for fruitful discussions on industrial aspects of titania nanoparticles synthesis as well as for connecting me to **Dr. Jonathan van den Ham** in TNO/Eindhoven to get valuable consultations on ellipsometry measurements. In the last stage of my Ph.D., together with Alfons and Arnout, we were awarded a "take-off" grant for the feasibility study of my start-up idea. A great appreciation goes to **Hans** and **Steven** from Nascent Ventures who believed in me and supported me with their excellent support letter for the grant application. Along with this process, I received strong positive support from **Bas**, **Frederieke**, and **Pieter** and I am absolutely grateful for that.

Next, I would like to thank my friends in the SCM group with whom I shared many memories over the last several years. **Raghu** (**Rama**), *my brother*, I am absolutely grateful for having you as my buddy in the group. Not only did we talk about serious topics in chemistry with each other and I learned very much from you, but also we shared lots of fun memories in different times such as playing foosball, struggling with TA duties, parties on weekends/holidays, *Holi* festival, concerts, spring schools, conferences, and many more. Thanks for all of those philosophical comments on life and random topics:) Special thanks to you, **Sarita**, and your lovely family in India for inviting us and having us in your extraordinary wedding ceremony which will last in our minds forever! Thanks to you and Sarita for the great time you shared with us in Warsaw! And thanks for our amazing adventure in Japan and all of those beautiful unique memories! All the best wishes for you, Sarita, and your lovely daughter, **Githa**.

Since lots of nice moments can be categorized by their events and occasions where I was sharing with others, I try to acknowledge my companions per event. Certainly, one of the best entertainment we had in the SCM group was playing foosball. Great thanks to **Guido, Simone, Nick, Wessel, Ernest, Vassilis, Douglas, Tonni, Giulia, Carmine, Massi, Gabriele, Emanuele, Pepijn, Sina, Albert, Srivatssan, Siddarth, and Wiebke** for all of those fun moments in the basement, playing foosball to get rid of daily stress that we had in our projects.

During my Ph.D., I had an amazing journey to India not only to attend glorious Rama's wedding but also to discover this beautiful country with lovely friends: **Samaneh, Massi, Gabriele, Chris, Doug, and Tonni.** It was absolutely a great pleasure traveling with you all, especially my dearest **Samaneh**, *azizam*, since we started the very first stages of our life there. **Massi**, we owe you all the nice memories in India for organizing our daily adventure step by step. **Gabriele**, *junam*, thanks for capturing great pictures from our Indian adventures in Kerala, Munnar, and Agra. **Doug, Tonni,** and **Chris,** thanks for all of those jokes and funny memories in the first week of our stay in India. It would not be better than this I guess. In addition to the Indian trip, I would like to thank you guys for all the happy memories in and after my Ph.D. from dinners and drinks, Turkish brunches in Mado, and parties on weekends.

Traveling to Japan was another unforgettable journey in my Ph.D. where I shared wonderful memories with **Tom**, **Kanako**, and **Rama**. **Tom** and **Kanako**, thanks for facilitating our stay in Okinawa, accompanying us in visiting beautiful places there, and for all the useful tips for the rest of our journey in Kyoto and Osaka which made it memorable. Furthermore, thank you for having us at the international dinner festival in your place with delicious foods. A special thank goes to **Tom** who generously helped me with translating my English summary to a decent 'Samenvatting' in Dutch. *Hartelijk bedankt!*

I went to several concerts and music festivals among which one was very unique and memorable: Thanks to **Samaneh**, **Aliyeh**, **Amin**, **Rama**, **Doug, Tonni,** and **Siddarth** for the good vibes at Shakira's concert in Amsterdam where we had a wonderful time there.

Having dinner, drinks, and board games with friends after work in OL was part of the Ph.D. time which would happen with great people occasionally. Many thanks go to **Wessel** for having us in his place in Amsterdam, **Guido, Giulia,** and **Massi** for lovely Italian foods and board games**, Anna** for initiating innovative games, and having a real *magician (Pritam)* at her parties as an entertainer, **Douglas, Tonni**, **Pepijn**, **and Chris** for very spontaneous gatherings and BBQs, **Simone** and **Jessi**, for their warm hospitality, playing board games, and having us in special occasions such as New Year's eve, **Ernest** and **Wiebke** for nice drinks and friendly chats, **Rama, Somil**, **Harith**, and **Srivatssan** for warmly sharing great Indian foods with us, and **Fabian** for having us kindly in his place and sharing good memories with us.

I am also grateful for many nice dutch friends who were in the group when I joined and generously gave me friendly tips in various ways from filling forms in Dutch and listening to Dutch answering machines(!) to correcting exam papers and problems for TA duties: **Ernest, Wessel, Henriëtte, Jessi, Fabian, Stijn, Maarten, Tom, Kelly, Roy, Erik,** and **Rik**. *Hartelijk bedankt voor jullie hulp, inspiratie, aanmoediging, tijd, tips en ideeën*. **Kelly en Maarten**, *bedankt dat jullie met me in het Nederlands hebben gepraat!* **Ernest, Wessel**, and **Fabian**, thanks a lot for sharing life tips in the Netherlands, and helping new members like me to feel comfortable in the SCM group.

Carmine, we shared our office for a long time during this journey. Thanks for all of those fun memories in Utrecht, chitchats on football, nostalgic memories, politics, and history. I learned many things about liquid crystals from you and thanks for being a good listener. **Chris** and **Eke,** thanks for the pleasant chats during Turkish brunches every now and then. Besides that, Thanks **Chris** for being always open to helping and sharing your knowledge scientifically and non-scientifically. **Maryam**, we both came from the same hometown and thus talked so often in our Isfahanian accent with each other. Thanks for being a nice friend in the CMI group and connecting me with other nice friends there such as **Jaco**, **Mijke**, **Tim**, and **Serena**. Thank you **Serena** for being another nice Italian friend to me. I would like to kindly thank **Tim** and **Mark** who helped me with the data collection and analysis of the SAXS results we acquired from the X-ray measurements in the Diamond Light Source synchrotron facilities in the UK.

During these years in the SCM group (my Ph.D. and also Postdoc), I had many other nice colleagues and friends who made the working atmosphere in the SCM group more pleasant. I would like to sincerely thank José, Frankje, Berend, Harini, Nick, Da, Srivatssan, Erik, Kelly, Roy, Mark, Sander, Yang, Murphy, Dyaneshwar, Alberto, Sina, Stijn, Robin, Federico, Giuseppe, Sajjad, Jantina, Ravi, Ajoy, Arya, Harith, Willem, Marjolein, Mengwei, Zahra, Sepideh, Diogo, Alptuğ, Thomas, Chaohong, Ruihzi, Yunhan, Rodolfo, Fabrizio, Gerardo, Giuliana, Ethan, Susana, Tor, Braulio, Rafael, Alberto, Tjom, and all the Master and Bachelor students in the group. Thanks to **Zahra** and **Harith** for fun moments and chitchats at coffee/lunch breaks and best wishes for the rest of your Ph.D. journey. I appreciate **Ethan** for his patience with my endless questions about liquid crystals and his nice feedback. *Mijn hartelijk dank voor alle hulp tijdens mijn verblijf in de SCMgroep!*

I was also very lucky to meet great Iranian/international friends out of university with whom I spent amazing times over the last several years in numerous occasions such as BBQs, incredible Persian foods, outgoings, canoeing, billiard, bowling, laser tag, biking, hiking, swimming, and many other things. **Fahimeh** (*Fallahi joon*), **Mahdi** (*Shishavan*), **Yasi** (*Zan dadash*), **Maurits** (*Dadash Mautje*), **Sina** & **Shahrzad**, **Soheil** & **Nafiseh (**& **Elara joon), Amin** & **Sanaz, Sepideh** & **Yadi**, **Behrad**, **Zahra** & **Ali**, **Siamak**, **Farzaneh** & **Mehdi** (& **Arian joon)**, **Yeganeh** &

Behzad, **Mohsen** & **Nasim**, **Ali** & **Behnaz** (in Meppel), **Maarten** (Jensen), **Davide** (Dell'Anna), **Marjan** & **Mathijs**, **Elahe**, **Nazila**, **Neshat** & **Moslem**, **Sajjad** & **Zakiyeh**, and **Aghaye Jafari**, thanks a lot for all of those wonderful weekends, fun memories, and unforgettable moments you created for me to make the life much nicer. Thank you **Sajjad** and **Zakiyeh** for helping me in my very first days in the Netherlands and for all the delightful memories we shared in Denmark and Germany! Thanks to **Reza** and **Zsuzsanna joon** for having us in their lovely place and offering delicious Hungarian dishes. Special thanks to **Khaleh Mina**, **Amoo Nader**, **Laleh joon**, and their lovely family for having us generously in their open hugs and making Holland like home for us. Thanks to our friends **Saeid Sarafrazian**, **Soheil Mojiri** & **Samira** for their hospitality and a great time in Germany! And a special thanks to **Soheil** for always being there like a brother and sharing his worthful knowledge with me. Many thanks to my lovely friends in the salsa dance class (**Jet**, **Wieke**, **Giorgio**, **Michael**, **Melanie**, and **Angela**) where we had lots of fun together. **Aliyeh**, thanks for motivating us for going to Shakira's concert and Lady Gaga's concert! *Beste Bep, u bent de allerbeste lerares/taalmaatje ooit! Dank u wel voor uw positieve bijdrage aan onze ontwikkeling en gezellige vrijdagavonden!*

Next, I would love to thank my family, my dearest mother, dear Nazaneen, and dear Majid, and all support from my relatives in homeland. **Maman joon**, ***azizam***, with no doubt, if I am here now, it is because of you since you devoted your youth life and fought against life challenges to support us in every single moment and dedicate a bright future to us. Your love, positive vibes, and kind support were unconditional and I hope I could make you proud. *I love you very much*. **Baba joon**, your thoughts were always with me. *I love you very much*. My dearest **Nazaneen** and **Majid**, ***azizanam***, you were my heroes and your kind support started even before my Ph.D. by giving me super valuable consultations. I am grateful for such a lovely family where we could always talk and brainstorm on any topic and help each other in any direction. Your presence never let me feel alone. *I love you both*. From the middle of my Ph.D., my family members extended and I am grateful for being part of Heidaris, as well. **Baba jan** (*Ahmad*)**, Maman jan** (*Foziyeh*)**, Sobhan, Sajjad, Hadis, Fatemeh, and Peyman** *aziz*, thank you very much for your positive energy over the last several years.

And finally, I would love to thank my dearest **Samaneh**. ***Azizam***, as you do know, my life in the Netherlands divides into two main parts: before our relationship and after that. I would not even imagine that I could be that much lucky to find a beautiful, kind, energetic, well-tempered, and brilliant partner in the Netherlands from the same roots. Thank you for everything that I have, for being a good listener, for your patience in all of those hard times, for sharing with me unforgettable memories in my Ph.D. journey, for your constant positive vibes, for lovely smiles, and for making my life cheerful more than ever. *I love you and I'll always remember us this way!*

*به پایان آمد این دفتر حکایت همچنان باقی به صد دفتر نشاید گفت حسب الحال مشتاقی "سعدی شیرازی"

**Although this book has reached its end, the story continues and it cannot be written down even in hundred books! "Saadi Shirazi"*

Naveed (July 2022, Utrecht)

References

1. Kelly, S.M.; O'Neill, M. *Liquid crystals for electro-optic applications*; 2001; Vol. 7; ISBN 0125137575.
2. Li, Q. *Anisotropic Nanomaterials Preparation, Properties, and Applications*; Springer, 2015; ISBN 9783319182926.
3. Carsten Tschierske, E. *Liquid Crystals Materials Design and Self-Assembly*; 2012; Vol. 318; ISBN 978-3-642-27590-6.
4. O'Neill, M.; Kelly, S.M. Liquid crystals for charge transport, luminescence, and photonics. *Adv. Mater.* **2003**, *15*, 1135–1146, doi:10.1002/adma.200300009.
5. Fleischmann, E.K.; Zentel, R. Liquid-Crystalline Ordering as a Concept in Materials Science: From Semiconductors to Stimuli-Responsive Devices. *Angew. Chemie - Int. Ed.* **2013**, *52*, 8810–8827, doi:10.1002/anie.201300371.
6. Miller, D.S.; Carlton, R.J.; Mushenheim, P.C.; Abbott, N.L. Introduction to optical methods for characterizing liquid crystals at interfaces. *Langmuir* **2013**, *29*, 3154–3169, doi:10.1021/la304679f.
7. Dierking, I. 1.1 What are Liquid Crystals? In *Soft Matter Series: Polymer-modified Liquid Crystals*; The Royal Society of Chemistry, 2019; pp. 1–18 ISBN 9781788013321.
8. Bisoyi, H.K.; Kumar, S. Liquid-crystal nanoscience: An emerging avenue of soft self-assembly. *Chem. Soc. Rev.* **2011**, *40*, 306–319, doi:10.1039/b901793n.
9. Reinitzer, F. Beitr ge zur Kenntniss des Gholesterins. *Monatshefte für Chemie* **1888**, *9*, 421–441.
10. Lehmann, O. Über fliessende Krystalle. *Zeitschrift für Phys. Chemie* **1889**, *4*, 462–472.
11. Dierking, I.; Neto, A.M.F. Novel trends in lyotropic liquid crystals. *Crystals* **2020**, *10*, 1–24, doi:10.3390/cryst10070604.
12. de Gennes, P.G.; Prost, J. *The Physics of Liquid Crystals*; Second Edi.; Clarendon Press: Oxford, 1993;
13. Dierking, I.; Al-Zangana, S. Lyotropic liquid crystal phases from anisotropic nanomaterials. *Nanomaterials* **2017**, *7*, doi:10.3390/nano7100305.
14. Sonin, A.S. Inorganic lyotropic liquid crystals. *J. Mater. Chem.* **1998**, *8*, 2557–2574, doi:10.1039/a802666a.
15. Lekkerkerker, H.N.W.; Vroege, G.J. Liquid crystal phase transitions in suspensions of mineral colloids: New life fromold roots. *Philos. Trans. R. Soc. A Math. Phys. Eng. Sci.* **2013**, *371*, doi:10.1098/rsta.2012.0263.
16. Gabriel, J.C.P.; Davidson, P. New trends in colloidal liquid crystals based on mineral moieties. *Adv. Mater.* **2000**, *12*, 9–20, doi:10.1002/(SICI)1521-4095(200001)12:1<9::AID-ADMA9>3.0.CO;2-6.
17. Davidson, P.; Gabriel, J.C.P. Mineral liquid crystals. *Curr. Opin. Colloid Interface Sci.* **2005**, *9*, 377–383, doi:10.1016/j.cocis.2004.12.001.

18. Zocher, H. Über Sole mit nichtkugeligen Teilchen. *Zeitschrift für Phys. Chemie* **1921**, *98U*, 293–337, doi:10.1515/zpch-1921-9821.

19. Zocher, H.; Jacobsohn, K. Ueber freiwillige Strukturbildung im Vanadinpentoxydsol. *Kolloid-Zeitschrift* **1927**, *41*, 220–222, doi:10.1007/BF01451342.

20. Coper, K.; Freundlich, H. The Formation of Tactoids Iron Oxide Sols. **1936**, 1–4.

21. Zocher, H.; Török, C. Crystals of higher order and their relation to other superphases. *Acta Crystallogr.* **1967**, *22*, 751–755, doi:10.1107/S0365110X67001495.

22. Onsager, L. the Effects of Shape on the Interaction of Colloidal Particles. *Ann. N. Y. Acad. Sci.* **1949**, *51*, 627–659, doi:10.1111/j.1749-6632.1949.tb27296.x.

23. Oster, B.Y.G. Two-Phase Formation In Solutions Of Tobacco Mosaic Virus And The Problem Of Long-Range Forces. **1949**, 445–473.

24. Wierenga, A.; Philipse, A.P.; Lekkerkerker, H.N.W.; Boger, D. V. Aqueous Dispersions of Colloidal Boehmite: Structure, Dynamics, and Yield Stress of Rod Gels. *Langmuir* **1998**, *14*, 55–65, doi:10.1021/la970376z.

25. Maeda, Y.; Hachisu, S. Structure of Schiller layers in β-FeOOH sols: Observation by scanning electron microscope. *Colloids and Surfaces* **1983**, *7*, 357–360, doi:10.1016/0166-6622(83)80062-6.

26. Lemaire, B.J.; Davidson, P.; Ferré, J.; Jamet, J.P.; Panine, P.; Dozov, I.; Jolivet, J.P. Outstanding Magnetic Properties of Nematic Suspensions of Goethite (a -FeOOH) Nanorods a) b). **2002**, *88*, 2–5, doi:10.1103/PhysRevLett.88.125507.

27. Kuijk, A.; Byelov, D. V.; Petukhov, A. V.; van Blaaderen, A.; Imhof, A. Phase behavior of colloidal silica rods. *Faraday Discuss.* **2012**, *159*, 181–199, doi:10.1039/c2fd20084h.

28. McGrother, S.C.; Williamson, D.C.; Jackson, G. A re-examination of the phase diagram of hard spherocylinders. *J. Chem. Phys.* **1996**, *104*, 6755–6771, doi:10.1063/1.471343.

29. Dussi, S. *When shape is enough.*; 2016; ISBN 9789039365724.

30. Dussi, S.; Chiappini, M.; Dijkstra, M. On the stability and finite-size effects of a columnar phase in single-component systems of hard-rod-like particles. *Mol. Phys.* **2018**, *116*, 2792–2805, doi:10.1080/00268976.2018.1471231.

31. Bruggen, M.P.B. van; Kooij, F.M. van Der; Lekkerkerker, H.N.W. Liquid crystal phase transitions in dispersions of rod-like colloidal particles. *J. Phys. Condens. Matter* **1999**, *8*, 9451–9456, doi:10.1088/0953-8984/8/47/044.

32. Lekkerkerker, H.N.W.; Vroege, G.J. Theory of the isotropic-nematic-nematic phase separation for a solution of bidisperse rodlike particles. *J. Phys. Chem.* **1993**, *97*, 3601–3605, doi:10.1021/j100116a026.

33. Bolhuis, P.G.; Stroobants, A.; Frenkel, D.; Lekkerkerker, H.N.W. Numerical study of the phase behavior of rodlike colloids with attractive interactions. *J. Chem. Phys.* **1997**, *107*, 1551–1564, doi:10.1063/1.474508.

34. van der Kooij, F.M.; Lekkerkerker, H.N.W. Formation of Nematic Liquid Crystals in Suspensions of Hard Colloidal Platelets. *J. Phys. Chem. B* **1998**, *102*, 7829–7832, doi:10.1021/jp981534d.

35. van der Kooij, F.M.; Vogel, M.; Lekkerkerker, H.N.W. Phase behavior of a mixture of platelike colloids and nonadsorbing polymer. *Phys. Rev. E - Stat. Physics, Plasmas, Fluids, Relat. Interdiscip. Top.* **2000**, *62*, 5397–5402, doi:10.1103/PhysRevE.62.5397.

36. Buining, P.A.; Lekkerkerker, H.N.W. Isotropic-Nematic Phase Separation of Dispersion of Organophilic Boehmite Rods D / L. **1993**, 11510–11516, doi:10.1021/j100146a027.

37. Frenkel, D.; Lekkerkerker, H.N.W.; Stroobants, A. Thermodynamic stability of a smectic phase in a system of hard rods. *Nature* **1988**, *332*, 822–823.

38. Vroege, G.J.; Lekkerkerker, H.N.W. Phase transitions in lyotropic colloidal and polymer liquid crystals. *Reports Prog. Phys.* **1992**, *55*, 1241–1309, doi:10.1088/0034-4885/55/8/003.

39. Frenkel, D.; Mulder, B.; McTague, J.P. Phase Diagram of a System of Hard Ellipsoids. **1984**, *52*, 287–290.

40. Bates, M.A.; Frenkel, D. Phase behavior of two-dimensional hard rod fluids. *J. Chem. Phys.* **2000**, *112*, 10034–10041, doi:10.1063/1.481637.

41. Bolhuis, P.; Frenkel, D. Tracing the phase boundaries of hard spherocylinders. *J. Chem. Phys.* **1997**, *106*, 666–687, doi:10.1063/1.473404.

42. Frenkel, D.; Schilling, T. Smectic filaments in colloidal suspensions of rods. *Phys. Rev. E - Stat. Physics, Plasmas, Fluids, Relat. Interdiscip. Top.* **2002**, *66*, 5, doi:10.1103/PhysRevE.66.041606.

43. Bates, M.A.; Frenkel, D. Influence of polydispersity on the phase behavior of colloidal liquid crystals: A Monte Carlo simulation study. *J. Chem. Phys.* **1998**, *109*, 1208–10034, doi:10.1063/1.481637.

44. Veerman, J.A.C.; Frenkel, D. Phase behavior of disklike hard-core mesogens. *Phys. Rev.* **1992**, *45*.

45. van Roij, R.; Bolhuis, P.; Mulder, B.; Frenkel, D. Transverse interlayer order in lyotropic smectic liquid crystals. *Phys. Rev. E.* **1995**, *52*, 1277–1281, doi:10.1103/PhysRevE.52.R1277.

46. Dussi, S.; Tasios, N.; Drwenski, T.; van Roij, R.; Dijkstra, M. Hard competition: stabilizing the elusive biaxial nematic phase in suspensions of colloidal particles with extreme lengths. **2018**, doi:10.1103/PhysRevLett.120.177801.

47. Chiappini, M.; Drwenski, T.; van Roij, R.; Dijkstra, M. Biaxial, Twist-bend, and Splay-bend Nematic Phases of Banana-shaped Particles Revealed by Lifting the "smectic Blanket." *Phys. Rev. Lett.* **2019**, *123*, 1–6, doi:10.1103/PhysRevLett.123.068001.

48. Ni, R.; Belli, S.; van Roij, R.; Dijkstra, M. Glassy dynamics, spinodal fluctuations, and the kinetic limit of nucleation in suspensions of colloidal hard rods. *Phys. Rev. Lett.* **2010**, *105*, 7–10, doi:10.1103/PhysRevLett.105.088302.

49. Savenko, S. V.; Dijkstra, M. Sedimentation and multiphase equilibria in suspensions of colloidal hard rods. *Phys. Rev. E* **2004**, *70*, 51401, doi:10.1103/PhysRevE.70.051401.

50. Savenko, S. V.; Dijkstra, M. Phase behavior of a suspension of colloidal hard rods and nonadsorbing polymer. *J. Chem. Phys.* **2006**, *124*, doi:10.1063/1.2202853.

51. Belli, S.; Patti, A.; Dijkstra, M.; Roij, R. van Polydispersity Stabilizes Biaxial Nematic Liquid Crystals. **2011**, *148303*, 1–4, doi:10.1103/PhysRevLett.107.148303.

52. de Mello Donegá, C. Synthesis and properties of colloidal heteronanocrystals. *Chem. Soc. Rev.* **2011**, *40*, 1512–1546, doi:10.1039/c0cs00055h.

53. Mourdikoudis, S.; Liz-Marzán, L.M. Oleyamine in Nanoparticle Synthesis. *Chem. Mater.* **2013**, *25*, 1465, doi:10.1021/cm4000476.

54. Niederberger, M.; Garnweitner, G.; Ba, J.; Polleux, J.; Pinna, N. Nonaqueous synthesis, assembly and formation mechanisms of metal oxide nanocrystals. *Int. J. Nanotechnol.* **2007**, *4*, 263–281, doi:10.1504/IJNT.2007.013473.

55. Niederberger, M.; Pinna, N. *Metal Oxide Nanoparticles in Organic Solvents: Synthesis, Formation, Assembly and Application*; Springer, London, 2009; ISBN 9781848826700.

56. Niederberger, M. Nonaqueous Sol – Gel Routes to Metal Oxide Nanoparticles. *Acc. Chem. Res.* **2007**, *40*, 793–800, doi:10.1021/ar600035e.

57. Ma, Y.; Wang, X.L.; Jia, Y.S.; Chen, X.B.; Han, H.X.; Li, C. Titanium Dioxide-Based Nanomaterials for Photocatalytic Fuel Generations. *Chem. Rev.* **2014**, *114*, 9987–10043, doi:10.1021/cr500008u.

58. Park, S.; Mundoor, H.; Fleury, B.; Davidson, P.; van de Lagemaat, J.; Smalyukh, I.I. Liquid Crystalline Order and Electric Switching of Upconversion Luminescence in Colloidal Nanorod Suspensions. *Adv. Opt. Mater.* **2019**, *7*, 1–8, doi:10.1002/adom.201900041.

59. Diroll, B.T.; Greybush, N.J.; Kagan, C.R.; Murray, C.B. Smectic nanorod superlattices assembled on liquid subphases: Structure, orientation, defects, and optical polarization. *Chem. Mater.* **2015**, *27*, 2998–3008, doi:10.1021/acs.chemmater.5b00355.

60. Zanella, M.; Gomes, R.; Povia, M.; Giannini, C.; Zhang, Y.; Riskin, A.; van Bael, M.; Hens, Z.; Manna, L. Self-assembled multilayers of vertically aligned semiconductor nanorods on device-scale areas. *Adv. Mater.* **2011**, *23*, 2205–2209, doi:10.1002/adma.201100539.

61. Fukagawa, T.; Tanaka, H.; Morikawa, K.; Tanaka, S.; Hatakeyama, Y.; Hino, K. Spatial Ordering of the Structure of Polymer-Capped Gold Nanorods under an External DC Electric Field. *J. Phys. Chem. Lett.* **2020**, *11*, 2086–2091, doi:10.1021/acs.jpclett.0c00566.

62. Murphy, C.J.; Gole, A.M.; Hunyadi, S.E.; Orendorff, C.J. One-Dimensional Colloidal Gold and Silver Nanostructures Catherine. *Inorg. Chem.* **2006**, *45*, 7544–7554.

63. Pérez-Juste, J.; Pastoriza-Santos, I.; Liz-Marzán, L.M.; Mulvaney, P. Gold nanorods: Synthesis, characterization and applications. *Coord. Chem. Rev.* **2005**, *249*, 1870–1901, doi:10.1016/j.ccr.2005.01.030.

64. Vanmaekelbergh, D. Self-assembly of colloidal nanocrystals as route to novel classes of nanostructured materials. *Nano Today* **2011**, *6*, 419–437, doi:10.1016/j.nantod.2011.06.005.

65. De Mello Donegá, C. *Nanoparticles: Workhorses of nanoscience*; 2014; Vol. 9783662448; ISBN 9783662448236.

66. Berends, A.C.; De Mello Donega, C. Ultrathin One- and Two-Dimensional Colloidal Semiconductor Nanocrystals: Pushing Quantum Confinement to the Limit. *J. Phys. Chem. Lett.* **2017**, *8*, 4077–4090, doi:10.1021/acs.jpclett.7b01640.

67. Steiner, D.; Dorfs, D.; Banin, U.; Sala, F.D.; Manna, L.; Millo, O. Determination of band offsets in

heterostructured colloidal nanorods using scanning tunneling spectroscopy. *Nano Lett.* **2008**, *8*, 2954–2958, doi:10.1021/nl801848x.

68. Costi, R.; Saunders, A.E.; Banin, U. Colloidal hybrid nanostructures: A new type of functional materials. *Angew. Chemie - Int. Ed.* **2010**, *49*, 4878–4897, doi:10.1002/anie.200906010.

69. Klöckner, B.; Daniel, P.; Brehmer, M.; Tremel, W.; Zentel, R. Liquid crystalline phases from polymer functionalized ferri-magnetic Fe3O4nanorods. *J. Mater. Chem. C* **2017**, *5*, 6688–6696, doi:10.1039/c7tc01106g.

70. Halpert, J.E.; Porter, V.J.; Zimmer, J.P.; Bawendi, M.G. Synthesis of CdSe / CdTe Nanobarbells. **2006**, 12590–12591.

71. Zorn, M.; Zentel, R. Liquid crystalline orientation of semiconducting nanorods in a semiconducting matrix. *Macromol. Rapid Commun.* **2008**, *29*, 922–927, doi:10.1002/marc.200800165.

72. Zorn, M.; Meuer, S.; Tahir, M.N.; Khalavka, Y.; Sönnichsen, C.; Tremel, W.; Zentel, R. Liquid crystalline phases from polymer functionalised semiconducting nanorods. *J. Mater. Chem.* **2008**, *18*, 3050, doi:10.1039/b802666a.

73. Kudera, S.; Carbone, L.; Casula, M.F.; Cingolani, R.; Falqui, A.; Snoeck, E.; Parak, W.J.; Manna, L. Selective growth of PbSe on one or both tips of colloidal semiconductor nanorods. *Nano Lett.* **2005**, *5*, 445–449, doi:10.1021/nl048060g.

74. Casavola, M.; Grillo, V.; Carlino, E.; Giannini, C.; Gozzo, F.; Pinel, E.F.; Garcia, M.A.; Manna, L.; Cingolani, R.; Cozzoli, P.D. Topologically controlled growth of magnetic-metal-functionalized semiconductor oxide nanorods. *Nano Lett.* **2007**, *7*, 1386–1395, doi:10.1021/nl070550w.

75. Robinson, R.D.; Sadtler, B.; Demchenko, D.O.; Erdonmez, C.K.; Wang, L.W.; Alivisatos, A.P. Spontaneous superlattice formation in nanorods through partial cation exchange. *Science (80-.).* **2007**, *317*, 355–358, doi:10.1126/science.1142593.

76. Zorn, M.; Meuer, S.; Tahir, M.N.; Tremel, W.; Char, K.; Zentel, R. Orientation of polymer functionalized nanorods in thin films. *J. Nanosci. Nanotechnol.* **2010**, *10*, 6845–9, doi:10.1166/jnn.2010.2946.

77. Meuer, S.; Oberle, P.; Theato, P.; Tremel, W.; Zentel, R. Liquid crystalline phasees from polymr-functionalized TiO2 nanorods. *Adv. Mater.* **2007**, *19*, 2073–2078, doi:10.1002/adma.200602516.

78. Zhang, H.; Banfield, J.F. Structural characteristics and mechanical and thermodynamic properties of nanocrystalline TiO2. *Chem. Rev.* **2014**, *114*, 9613–9644, doi:10.1021/cr500072j.

79. Muscat, J.; Swamy, V.; Harrison, N.M. First-principles calculations of the phase stability of TiO2. *Phys. Rev. B - Condens. Matter Mater. Phys.* **2002**, *65*, 2241121–22411215, doi:10.1103/PhysRevB.65.224112.

80. Chen, X.; Mao, S.S. Titanium Dioxide Nanomaterials : Synthesis , Properties , Modifications , and Applications. *Chem. Rev.* **2007**, *107*, 2891–2959, doi:10.1021/cr0500535.

81. Feynman, R.P. There's plenty of room at the bottom. *Eng. Sci.* 1960, 22–36.

82. Rueda-Romero, C.; Hernández-Pérez, G.; Ramos-Godínez, P.; Vázquez-López, I.; Quintana-Belmares, R.O.; Huerta-García, E.; Stepien, E.; López-Marure, R.; Montiel-Dávalos, A.; Alfaro-

Moreno, E. Titanium dioxide nanoparticles induce the expression of early and late receptors for adhesion molecules on monocytes. *Part. Fibre Toxicol.* **2016**, *13*, 1–13, doi:10.1186/s12989-016-0147-3.

83. de Boer, F.Y.; Imhof, A.; Velikov, K.P. Encapsulation of colorants by natural polymers for food applications. *Color. Technol.* **2019**, *135*, 183–194, doi:10.1111/cote.12393.

84. Hayden, D.R.; Kibbelaar, H.V.M.; Imhof, A.; Velikov, K.P. Fully-biobased UV-absorbing nanoparticles from ethyl cellulose and zein for environmentally friendly photoprotection. *RSC Adv.* **2018**, *8*, 25104–25111, doi:10.1039/c8ra02674b.

85. Hayden, D.R.; Imhof, A.; Velikov, K.P. Biobased Nanoparticles for Broadband UV Protection with Photostabilized UV Filters. *ACS Appl. Mater. Interfaces* **2016**, *8*, 32655–32660, doi:10.1021/acsami.6b12933.

86. Katal, R.; Masudy-Panah, S.; Tanhaei, M.; Farahani, M.H.D.A.; Jiangyong, H. A review on the synthesis of the various types of anatase TiO2 facets and their applications for photocatalysis. *Chem. Eng. J.* **2020**, *384*, 123384, doi:10.1016/j.cej.2019.123384.

87. Magalhães, P.; Andrade, L.; Nunes, O.C.; Mendes, A. Titanium dioxide photocatalysis: Fundamentals and application on photoinactivation. *Rev. Adv. Mater. Sci.* **2017**, *51*, 91–129.

88. Kang, X.; Liu, S.; Dai, Z.; He, Y.; Song, X.; Tan, Z. *Titanium Dioxide: From Engineering to Applications*; 2019; Vol. 9; ISBN 8642726318.

89. Chen, D.; Caruso, R.A. Recent progress in the synthesis of spherical titania nanostructures and their applications. *Adv. Funct. Mater.* **2013**, *23*, 1356–1374, doi:10.1002/adfm.201201880.

90. Schneider, J.; Matsuoka, M.; Takeuchi, M.; Zhang, J.; Horiuchi, Y.; Anpo, M.; Bahnemann, D.W. Understanding TiO 2 Photocatalysis : Mechanisms and Materials. *Chem. Rev.* **2014**, *114*, 9919–9986, doi:10.1021/cr5001892.

91. Bai, J.; Zhou, B. Titanium Dioxide Nanomaterials for Sensor Applications. *Chem. Rev* **2014**, *114*, 10131–10176, doi:10.1021/cr400625j.

92. Cargnello, M.; Gordon, T.R.; Murray, C.B. Solution-Phase Synthesis of Titanium Dioxide Nanoparticles and Nanocrystals. *Chem. Rev.* **2014**, *114*, 9319–9345.

93. Cozzoli, P.D.; Kornowski, A.; Weller, H. Low-Temperature Synthesis of Soluble and Low-Temperature Synthesis of Soluble and Processable. *J. Am. Chem. Soc.* **2003**, *125*, 14539–14548, doi:10.1021/ja036505h.

94. Lee, K.; Mazare, A.; Schmuki, P. One-dimensional titanium dioxide nanomaterials: Nanotubes. *Chem. Rev.* **2014**, *114*, 9385–9454, doi:10.1021/cr500061m.

95. Green, M. The nature of quantum dot capping ligands. *J. Mater. Chem.* **2010**, *20*, 5797–5809, doi:10.1039/c0jm00007h.

96. Yang, L.; Zhou, Z.; Song, J.; Chen, X. Anisotropic nanomaterials for shape-dependent physicochemical and biomedical applications. *Chem. Soc. Rev.* **2019**, *48*, 5140–5176, doi:10.1039/c9cs00011a.

97. Liu, B.; Wu, Y.; Zhao, S. Anisotropic Colloids: From Non-Templated to Patchy Templated Synthesis.

Chem. - A Eur. J. **2018**, *24*, 10562–10570, doi:10.1002/chem.201705960.

98. Bouju, X.; Duguet, É.; Gauffre, F.; Henry, C.R.; Kahn, M.L.; Mélinon, P.; Ravaine, S. Nonisotropic Self-Assembly of Nanoparticles: From Compact Packing to Functional Aggregates. *Adv. Mater.* **2018**, *30*, 1–38, doi:10.1002/adma.201706558.

99. Sacanna, S.; Pine, D.J. Shape-anisotropic colloids: Building blocks for complex assemblies. *Curr. Opin. Colloid Interface Sci.* **2011**, *16*, 96–105, doi:10.1016/j.cocis.2011.01.003.

100. Quan, Z.; Fang, J. Superlattices with non-spherical building blocks. *Nano Today* **2010**, *5*, 390–411, doi:10.1016/j.nantod.2010.08.011.

101. Dierking, I. From colloids in liquid crystals to colloidal liquid crystals. *Liq. Cryst.* **2019**, *46*, 2057–2074, doi:10.1080/02678292.2019.1641755.

102. Liu, B.; Besseling, T.H.; van Blaaderen, A.; Imhof, A. Confinement Induced Plastic Crystal-to-Crystal Transitions in Rodlike Particles with Long-Ranged Repulsion. *Phys. Rev. Lett.* **2015**, *115*, 1–5, doi:10.1103/PhysRevLett.115.078301.

103. Dogic, Z.; Sharma, P.; Zakhary, M.J. Hypercomplex Liquid Crystals. *Annu. Rev. Condens. Matter Phys. is Annu. Rev. Condens. Matter Phys.* **2014**, *5*, 137–157, doi:10.1146/annurev-conmatphys-031113-133827.

104. Xue, B.; Li, T.; Wang, B.; Ji, L.; Yang, D.; Dong, A. Self-assembled Fe_3O_4 nanoparticle-doped TiO_2 nanorod superparticles with highly enhanced lithium storage properties. *Sustain. Energy Fuels* **2018**, 616–625, doi:10.1039/C7SE00460E.

105. Dessombz, A.; Pasquier, C.R.; Davidson, P.; Chanéac, C. Evidence for photoconductivity anisotropy in aligned TiO2 nanorod films. *J. Phys. Chem. C* **2010**, *114*, 19799–19802, doi:10.1021/jp1063275.

106. Rizzo, A.; Nobile, C.; Mazzeo, M.; De Giorgi, M.; Fiore, A.; Carbone, L.; Cingolani, R.; Manna, L.; Gigli, G. Polarized light emitting diode by long-range nanorod self-assembling on a water surface. *ACS Nano.* **2009**, *3*, 1506–1512, doi:10.1021/nn900063m.

107. Dessombz, A.; Chiche, D.; Davidson, P.; Panine, P.; Chanéac, C.; Jolivet, J.P. Design of liquid-crystalline aqueous suspensions of rutile nanorods: Evidence of anisotropic photocatalytic properties. *J. Am. Chem. Soc.* **2007**, *129*, 5904–5909, doi:10.1021/ja0684491.

108. Radhakrishnan, B.Y.T. The optical properties of titanium dioxide. *Proc. Indian Acad. Sci. (Math. Sci.).* **1951**, *35*, 117–125.

109. Gordon, T.R.; Cargnello, M.; Paik, T.; Mangolini, F.; Weber, R.T.; Fornasiero, P.; Murray, C.B. Nonaqueous synthesis of TiO2 nanocrystals using TiF4 to engineer morphology, oxygen vacancy concentration, and photocatalytic activity. *J. Am. Chem. Soc.* **2012**, *134*, 6751–61, doi:10.1021/ja300823a.

110. Cargnello, M.; Montini, T.; Smolin, S.Y.; Priebe, J.B.; Delgado Jaén, J.J.; Doan-Nguyen, V.V.T.; McKay, I.S.; Schwalbe, J.A.; Pohl, M.-M.; Gordon, T.R.; et al. Engineering titania nanostructure to tune and improve its photocatalytic activity. *Proc. Natl. Acad. Sci. U. S. A.* **2016**, *113*, 3966–3971, doi:10.1073/pnas.1524806113.

111. Bourikas, K.; Kordulis, C.; Lycourghiotis, A. Titanium dioxide (Anatase and Rutile): Surface chemistry, liquid-solid interface chemistry, and scientific synthesis of supported catalysts. *Chem.*

Rev. **2014**, *114*, 9754–9823, doi:10.1021/cr300230q.

112. Casavola, M.; Buonsanti, R.; Caputo, G.; Cozzoli, P.D. Colloidal strategies for preparing oxide-based hybrid nanocrystals. *Eur. J. Inorg. Chem.* **2008**, 837–854, doi:10.1002/ejic.200701047.

113. Dinh, C.; Nguyen, T.; Kleitz, F.; Do, T. Shape-Controlled Synthesis of Highly Crystalline Titania Nanocrystals. *ACS Nano* **2009**, *3*, 3737–3743, doi:10.1021/nn900940p.

114. Wu, B.; Guo, C.; Zheng, N.; Xie, Z.; Stucky, G.D. Nonaqueous production of nanostructured anatase with high-energy facets. *J. Am. Chem. Soc.* **2008**, *130*, 17563–17567, doi:10.1021/ja8069715.

115. De Nijs, B.; Dussi, S.; Smallenburg, F.; Meeldijk, J.D.; Groenendijk, D.J.; Filion, L.; Imhof, A.; van Blaaderen, A.; Dijkstra, M. Entropy-driven formation of large icosahedral colloidal clusters by spherical confinement. *Nat. Mater.* **2015**, *14*, 56–60, doi:10.1038/nmat4072.

116. Montanarella, F.; Geuchies, J.J.; Dasgupta, T.; Prins, P.T.; van Overbeek, C.; Dattani, R.; Baesjou, P.; Dijkstra, M.; Petukhov, A. V.; van Blaaderen, A.; et al. Crystallization of Nanocrystals in Spherical Confinement Probed by in Situ X-ray Scattering. *Nano Lett.* **2018**, *18*, 3675–3681, doi:10.1021/acs.nanolett.8b00809.

117. Boles, M.A.; Ling, D.; Hyeon, T.; Talapin, D. V. Erratum: The surface science of nanocrystals (Nature Materials (2016) 15 (141-153)). *Nat. Mater.* **2016**, *15*, 364, doi:10.1038/nmat4578.

118. Boles, M.A.; Talapin, D. V. Binary Assembly of PbS and Au Nanocrystals: Patchy PbS Surface Ligand Coverage Stabilizes the CuAu Superlattice. *ACS Nano* **2019**, *13*, 5375–5384, doi:10.1021/acsnano.9b00006.

119. Goodfellow, B.W.; Yu, Y.; Bosoy, C.A.; Smilgies, D.M.; Korgel, B.A. The Role of Ligand Packing Frustration in Body-Centered Cubic (bcc) Superlattices of Colloidal Nanocrystals. *J. Phys. Chem. Lett.* **2015**, *6*, 2406–2412, doi:10.1021/acs.jpclett.5b00946.

120. Kister, T.; Monego, D.; Mulvaney, P.; Widmer-Cooper, A.; Kraus, T. Colloidal Stability of Apolar Nanoparticles: The Role of Particle Size and Ligand Shell Structure. *ACS Nano* **2018**, *12*, 5969–5977, doi:10.1021/acsnano.8b02202.

121. Winslow, S.W.; Swan, J.W.; Tisdale, W.A. The Importance of Unbound Ligand in Nanocrystal Superlattice Formation. *J. Am. Chem. Soc.* **2020**, *142*, 39, doi:10.1021/jacs.0c01809.

122. Ye, X.; Chen, J.; Engel, M.; Millan, J.A.; Li, W.; Qi, L.; Xing, G.; Collins, J.E.; Kagan, C.R.; Li, J.; et al. Competition of shape and interaction patchiness for self-assembling nanoplates. *Nat. Chem.* **2013**, *5*, 466–473, doi:10.1038/nchem.1651.

123. Boles, M.A.; Talapin, D. V. Many-Body Effects in Nanocrystal Superlattices: Departure from Sphere Packing Explains Stability of Binary Phases. *J. Am. Chem. Soc.* **2015**, *137*, 4494–4502, doi:10.1021/jacs.5b00839.

124. Bian, K.; Choi, J.J.; Kaushik, A.; Clancy, P.; Smilgies, D.M.; Hanrath, T. Shape-anisotropy driven symmetry transformations in nanocrystal superlattice polymorphs. *ACS Nano* **2011**, *5*, 2815–2823, doi:10.1021/nn103303q.

125. Wang, Z.; Schliehe, C.; Bian, K.; Dale, D.; Bassett, W.A.; Hanrath, T.; Klinke, C.; Weller, H. Correlating superlattice polymorphs to internanoparticle distance, packing density, and surface lattice in assemblies of PbS nanoparticles. *Nano Lett.* **2013**, *13*, 1303–1311, doi:10.1021/nl400084k.

126. Lee, B.; Littrell, K.; Sha, Y.; Shevchenko, E. V. Revealing the Effects of the Non-solvent on the Ligand Shell of Nanoparticles and Their Crystallization. *J. Am. Chem. Soc.* **2019**, *141*, 16651–16662, doi:10.1021/jacs.9b06010.

127. Lau, C.Y.; Duan, H.; Wang, F.; He, C. Bin; Low, H.Y.; Yang, J.K.W. Enhanced ordering in gold nanoparticles self-assembly through excess free ligands. *Langmuir* **2011**, *27*, 3355–3360, doi:10.1021/la104786z.

128. Goodfellow, B.W.; Rasch, M.R.; Hessel, C.M.; Patel, R.N.; Smilgies, D.M.; Korgel, B.A. Ordered structure rearrangements in heated gold nanocrystal superlattices. *Nano Lett.* **2013**, *13*, 5710–5714, doi:10.1021/nl403458q.

129. Shah, P.S.; Holmes, J.D.; Johnston, K.P.; Korgel, B.A. Size-selective dispersion of dodecanethiol-coated nanocrystals in liquid and supereritical ethane by density tuning. *J. Phys. Chem. B* **2002**, *106*, 2545–2551, doi:10.1021/jp013931l.

130. Zhang, Z.; Wu, Q.; Johnson, G.; Ye, Y.; Li, X.; Li, N.; Cui, M.; Lee, J.D.; Liu, C.; Zhao, S.; et al. A Generalized Synthetic Strategy for Transition Metal Doped Brookite-Phase TiO2 Nanorods. *J. Am. Chem. Soc.* **2019**, *141*, 16548–16552, doi:10.1021/jacs.9b06389.

131. Wang, P.P.; Qiao, Q.; Zhu, Y.; Ouyang, M. Colloidal Binary Supracrystals with Tunable Structural Lattices. *J. Am. Chem. Soc.* **2018**, *140*, 9095–9098, doi:10.1021/jacs.8b05643.

132. Gomes, R.; Hassinen, A.; Szczygiel, A.; Zhao, Q.; Vantomme, A.; Martins, J.C.; Hens, Z. Binding of phosphonic acids to CdSe quantum dots: A solution NMR study. *J. Phys. Chem. Lett.* **2011**, *2*, 145–152, doi:10.1021/jz1016729.

133. Wilson, D.; Langell, M.A. XPS analysis of oleylamine/oleic acid capped Fe 3 O 4 nanoparticles as a function of temperature. *Appl. Surf. Sci.* **2014**, *303*, 6–13, doi:10.1016/j.apsusc.2014.02.006.

134. Ren, Z.; Chen, C.; Hu, R.; Mai, K.; Qian, G.; Wang, Z. Two-step self-assembly and lyotropic liquid crystal behavior of TiO 2 nanorods. *J. Nanomater.* **2012**, *2012*, doi:10.1155/2012/180989.

135. Cheng, F.; Verrelli, E.; Alharthi, F.A.; Kelly, S.M.; O'Neill, M.; Kemp, N.T.; Kitney, S.P.; Lai, K.T.; Mehl, G.H.; Anthopoulos, T. Lyotropic 'hairy' TiO 2 nanorods. *Nanoscale Adv.* **2018**, *1*, 254–264, doi:10.1039/C8NA00054A.

136. Jishkariani, D.; Elbert, K.C.; Wu, Y.; Lee, J.D.; Hermes, M.; Wang, D.; van Blaaderen, A.; Murray, C.B. Nanocrystal Core Size and Shape Substitutional Doping and Underlying Crystalline Order in Nanocrystal Superlattices. *ACS Nano* **2019**, *13*, 5712–5719, doi:10.1021/acsnano.9b01107.

137. Elbert, K.C.; Jishkariani, D.; Wu, Y.; Lee, J.D.; Donnio, B.; Murray, C.B. Design, Self-Assembly, and Switchable Wettability in Hydrophobic, Hydrophilic, and Janus Dendritic Ligand-Gold Nanoparticle Hybrid Materials. *Chem. Mater.* **2017**, *29*, 8737–8746, doi:10.1021/acs.chemmater.7b02928.

138. Diroll, B.T.; Weigandt, K.M.; Jishkariani, D.; Cargnello, M.; Murphy, R.J.; Hough, L.A.; Murray, C.B.; Donnio, B. Quantifying "softness" of Organic Coatings on Gold Nanoparticles Using Correlated Small-Angle X-ray and Neutron Scattering. *Nano Lett.* **2015**, *15*, 8008–8012, doi:10.1021/acs.nanolett.5b04011.

139. Jishkariani, D.; Diroll, B.T.; Cargnello, M.; Klein, D.R.; Hough, L.A.; Murray, C.B.; Donnio, B. Dendron-Mediated Engineering of Interparticle Separation and Self-Assembly in Dendronized Gold

Nanoparticles Superlattices. *J. Am. Chem. Soc.* **2015**, *137*, 10728–10734, doi:10.1021/jacs.5b06306.

140. Meuer, S.; Fischer, K.; Mey, I.; Janshoff, A.; Schmidt, M.; Zentel, R. Liquid crystals from polymer-functionalized TiO2 nanorod mesogens. *Macromolecules.* **2008**, *41*, 7946–7952, doi:10.1021/ma801369w.

141. Buonsanti, R.; Grillo, V.; Carlino, E.; Giannini, C.; Kipp, T.; Cingolani, R.; Cozzoli, P.D. Nonhydrolytic synthesis of high-quality anisotropically shaped brookite TiO2 nanocrystals. *J. Am. Chem. Soc.* **2008**, *130*, 11223–11233, doi:10.1021/ja803559b.

142. Krayzman, V.; Cockayne, E.; Johnston-Peck, A.C.; Vaughan, G.; Zhang, F.; Allen, A.J.; Kunz, L.Y.; Cargnello, M.; Friedman, L.H.; Levin, I. Local Structural Distortions and Failure of the Surface-Stress "core-Shell" Model in Brookite Titania Nanorods. *Chem. Mater.* **2020**, *32*, 286–298, doi:10.1021/acs.chemmater.9b03762.

143. Vold, M.J. Van der Waals' attraction between anisometric particles. *J. Colloid Sci.* **1954**, *9*, 451–459, doi:10.1016/0095-8522(54)90032-X.

144. Philipse, A.P.; Nechifor, A.M.; Patmamanoharan, C. Isotropic and Birefringent Dispersions of Surface Modified Silica Rods with a Boehmite-Needle Core. *Langmuir* **1994**, *10*, 4451–4458, doi:10.1021/la00024a013.

145. Israelachvili, J.N. *Intermolecular and Surface Forces: Third Edition*; Elsevier, 2011; ISBN 9780123919274.

146. Dong, A.; Chen, J.; Vora, P.M.; Kikkawa, J.M.; Murray, C.B. Binary nanocrystal superlattice membranes self-assembled at the liquid–air interface. *Nature* **2010**, *466*, 474–477, doi:10.1038/nature09188.

147. Paik, T.; Diroll, B.T.; Kagan, C.R.; Murray, C.B. Binary and Ternary Superlattices Self-Assembled from Colloidal Nanodisks and Nanorods. *J. Am. Chem. Soc.* **2015**, *137*, 6662–6669, doi:10.1021/jacs.5b03234.

148. Paik, T.; Ko, D.K.; Gordon, T.R.; Doan-Nguyen, V.; Murray, C.B. Studies of liquid crystalline self-assembly of GdF3 nanoplates by in-plane, out-of-plane SAXS. *ACS Nano* **2011**, *5*, 8322–8330, doi:10.1021/nn203049t.

149. Geuchies, J.J.; Soligno, G.; Geraffy, E.; Hendrikx, C.P.; Overbeek, C. van; Montanarella, F.; Slot, M.R.; Konovalov, O. V.; Petukhov, A. V.; Vanmaekelbergh, D. Unravelling three-dimensional adsorption geometries of PbSe nanocrystal monolayers at a liquid-air interface. *Commun. Chem.* **2020**, *3*, 1–10, doi:10.1038/s42004-020-0275-4.

150. Ye, B.; Qian, G.; Fan, X.; Wang, Z. Self-Assembled Superlattices from Colloidal TiO 2 Nanorods. *Curr. Nanosci.* **2010**, *6*, 262–268.

151. Baranov, D.; Fiore, A.; van Huis, M.; Giannini, C.; Falqui, A.; Lafont, U.; Zandbergen, H.; Cingolani, R.; Manna, L. Assembly of colloidal semiconductor nanorods in solution by depletion attraction. *Nano Lett.* **2010**, *10*, 743–749, doi:10.1021/nl903946n.

152. Li, W.; Hinton, C.H.; Lee, S.S.; Wu, J.; Fortner, J.D. Surface engineering superparamagnetic nanoparticles for aqueous applications: Design and characterization of tailored organic bilayers. *Environ. Sci. Nano.* **2016**, *3*, 85–93, doi:10.1039/c5en00089k.

153. Liang, Y.; Xie, Y.; Chen, D.; Guo, C.; Hou, S.; Wen, T.; Yang, F.; Deng, K.; Smalyukh, I.I.; Liu, Q. Symmetry control of nanorod superlattice driven by a governing force. *Nat. Commun.* **2017**, *8*, 1–8, doi:10.1038/s41467-017-01111-4.

154. Buining, P.A.; Lekkerkerker, H.N.W. Isotropic-Nematic Phase Separation of Dispersion of Organophilic Boehmite Rods D / L. *J. Phys. Chem.* **1993**, *97*, 11510–11516, doi:10.1021/j100146a027.

155. Bohle, A.M.; Hołyst, R.; Vilgis, T. Polydispersity and Ordered Phases in Solutions of Rodlike Macromolecules. *Phys. Rev. Lett.* **1996**, *76*, 1396–1399.

156. van Bruggen, M.P.B.; Dhont, J.K.G.; Lekkerkerker, H.N.W. Morphology and kinetics of the isotropic-nematic phase transition in dispersions of hard rods. *Macromolecules* **1999**, *32*, 2256–2264, doi:10.1021/ma981196e.

157. Vroege, G.J.; Petukhov, A. V.; Lemaire, B.J.; Davidson, P. Smectic liquid-crystalline order in suspensions of highly polydisperse goethite nanorods. *Adv. Mater.* **2006**, *18*, 2565–2568, doi:10.1002/adma.200601112.

158. John, B.S.; Juhlin, C.; Escobedo, F.A. Phase behavior of colloidal hard perfect tetragonal parallelepipeds. *J. Chem. Phys.* **2008**, *128*, doi:10.1063/1.2819091.

159. Zhang, Y.; Liu, F.M. Large-scale superlattices from colloidal TiO2nanorods: A facile self-assembly approach. *Appl. Surf. Sci.* **2016**, *367*, 559–562, doi:10.1016/j.apsusc.2016.01.218.

160. Li, L.S.; Alivisatos, A.P. Semiconductor nanorod liquid crystals and their assembly on a substrate. *Adv. Mater.* **2003**, *15*, 408–411, doi:10.1002/adma.200390093.

161. Piazza, R. Settled and unsettled issues in particle settling. *Reports Prog. Phys.* **2014**, *77*, 1–26, doi:10.1088/0034-4885/77/5/056602.

162. Prinsen, P.; van der Schoot, P. Shape and director-field transformation of tactoids. *Phys. Rev. E* **2003**, *68*, 11, doi:10.1103/PhysRevE.68.021701.

163. Niezgoda, I.; Jaworska, J.; Pociecha, D.; Galewski, Z. The kinetics of the E-Z-E isomerisation and liquid-crystalline properties of selected azobenzene derivatives investigated by the prism of the ester group inversion. *Liq. Cryst.* **2015**, *42*, 1148–1158, doi:10.1080/02678292.2015.1031198.

164. Lenssen, K.-M.H.; Baesjou, P.J.; Wilhelmus, M.H.; van Delden, M. In-plane Switching Electrophoretic Colour Display: US Patent Application Publication 2010.

165. van Blaaderen, A.; Dijkstra, M.; van Roij, R.; Imhof, A.; Kamp, M.; Kwaadgras, B.W.; Vissers, T.; Liu, B. Manipulating the self assembly of colloids in electric fields. *Eur. Phys. J. Spec. Top.* **2013**, *222*, 2895–2909, doi:10.1140/epjst/e2013-02065-0.

166. Baesjou, P.J.; Maria, L.J.; Nl, E. Light Modulator: US Patent Application Publication 2010.

167. Gindl, J.; Liu, F.Q.; Noltemeyer, M.; Schmidt, H.G.; Roesky, H.W. Carboxylates of Organotitanium Fluorides: Preparation of Cp- and Cp*-Fluorotitanium Trifluoroacetates and Pentafluorobenzoates. *Inorg. Chem.* **1995**, *34*, 5711–5714, doi:10.1021/ic00127a006.

168. Zhang, Z.; Zhong, X.; Liu, S.; Li, D.; Han, M. Aminolysis route to monodisperse titania nanorods with tunable aspect ratio. *Angew. Chemie - Int. Ed.* **2005**, *44*, 3466–3470, doi:10.1002/anie.200500410.

169. van Embden, J.; Chesman, A.S.R.; Jasieniak, J.J. The heat-up synthesis of colloidal nanocrystals. *Chem. Mater.* **2015**, *27*, 2246–2285, doi:10.1021/cm5028964.

170. Smith, S.J.; Stevens, R.; Liu, S.; Li, G.; Navrotsky, A.; Boerio-Goates, J.; Woodfield, B.F. Heat capacities and thermodynamic functions of TiO2 anatase and rutile: Analysis of phase stability. *Am. Mineral.* **2009**, *94*, 236–243, doi:10.2138/am.2009.3050.

171. Ranade, M.R.; Navrotsky, A.; Zhang, H.Z.; Banfield, J.F.; Elder, S.H.; Zaban, A.; Borse, P.H.; Kulkarni, S.K.; Doran, G.S.; Whitfield, H.J. Energetics of nanocrystalline TiO2. *Proc. Natl. Acad. Sci.* **2002**, *99*, 6476–6481, doi:10.1073/pnas.251534898.

172. Levchenko, A.A.; Li, G.; Boerio-Goates, J.; Woodfield, B.F.; Navrotsky, A. TiO2 stability landscape: Polymorphism, surface energy, and bound water energetics. *Chem. Mater.* **2006**, *18*, 6324–6332, doi:10.1021/cm061183c.

173. Gilbert, B.; Zhang, H.; Huang, F.; Finnegan, M.P.; Waychunas, G.A.; Banfield, J.F. Special phase transformation and crystal growth pathways observed in nanoparticlesPresented at the ACS Division of Geochemistry Symposium ?The Impact of Nanoparticle Growth and Transformation Processes on Contaminant Geochemical Cycling?, New Orleans, Mar. *Geochem. Trans.* **2003**, *4*, 20, doi:10.1039/b309073f.

174. Zhang, H.; Banfield, J.F. Understanding polymorphic phase transformation behavior during growth of nanocrystalline aggregates: Insights from TiO2. *J. Phys. Chem. B* **2000**, *104*, 3481–3487, doi:10.1021/jp000499j.

175. Joo, J.; Kwon, S.G.; Yu, T.; Cho, M.; Lee, J.; Yoon, J. Large-Scale Synthesis of TiO 2 Nanorods via Nonhydrolytic Sol - Gel Ester Elimination Reaction and Their Application to Photocatalytic Inactivation of E . coli. **2005**, 15297–15302, doi:10.1021/jp052458z.

176. Christie, W.W.; Han, X. Isolation of fatty acids and identification by spectroscopic and related techniques. *Lipid Anal.* **2013**, 181–211, doi:10.1533/9780857097866.181.

177. Humphrey, J.J.L.; Sadasivan, S.; Plana, D.; Celorrio, V.; Tooze, R.A.; Fermín, D.J. Surface Activation of Pt Nanoparticles Synthesised by "hot Injection" in the Presence of Oleylamine. *Chem. - A Eur. J.* **2015**, *21*, 12694–12701, doi:10.1002/chem.201501496.

178. Sopoušek, J.; Pinkas, J.; Brož, P.; Buršík, J.; Vykoukal, V.; Škoda, D.; Stýskalík, A.; Zobač, O.; Vřešťál, J.; Hrdlička, A.; et al. Ag-Cu Colloid Synthesis: Bimetallic Nanoparticle Characterisation and Thermal Treatment. *J. Nanomater.* **2014**, *2014*, 1–13, doi:10.1155/2014/638964.

179. Pinchuk, O.A.; Aubuchon, S.R.; Marks, C.; Dominey, R.; Dundar, F.; Deniz, O.F.; Ata, A.; Wynne, K.J. Thermally pretreated 46% pt/vulcan XC72: Characterisation by TGA/DSC/ TEM and cyclic voltammetry. *Fuel Cells* **2009**, *9*, 554–561, doi:10.1002/fuce.200800183.

180. Kim, F.; Kwan, S.; Akana, J.; Yang, P. Langmuir-Blodgett nanorod assembly [13]. *J. Am. Chem. Soc.* **2001**, *123*, 4360–4361, doi:10.1021/ja0059138.

181. Querner, C.; Fischbein, M.D.; Heiney, P.A.; Drndić, M. Millimeter-scale assembly of CdSe nanorods into smectic superstructures by solvent drying kinetics. *Adv. Mater.* **2008**, *20*, 2308–2314, doi:10.1002/adma.200800125.

182. Bai, Y.; Mora-Sero, I.; De Angelis, F.; Bisquert, J.; Wang, P. Titanium dioxide nanomaterials for

photovoltaic applications. *Chem. Rev.* **2014**, *114*, 10095–10130, doi:10.1021/cr400606n.

183. Kern, P.; Schwaller, P.; Michler, J. Electrolytic deposition of titania films as interference coatings on biomedical implants: Microstructure, chemistry and nano-mechanical properties. *Thin Solid Films* **2006**, *494*, 279–286, doi:10.1016/j.tsf.2005.09.068.

184. Sungur, Ş. Titanium Dioxide Nanoparticles. In *Handbook of Nanomaterials and Nanocomposites for Energy and Environmental Applications*; Springer, Cham, 2021; pp. 713–730 ISBN 978-3-030-36268-3.

185. Zhang, H.; Banfield, J.F. Thermodynamic analysis of phase stability of nanocrystalline titania. *J. Mater. Chem.* **1998**, *8*, 2073–2076, doi:10.1039/a802619j.

186. Mason, C.W.; Yeo, I.; Saravanan, K.; Balaya, P. Interconnected nanofibrous titanium dioxide bronze: An emerging lithium ion anode material for high rate performance. *RSC Adv.* **2013**, *3*, 2935–2941, doi:10.1039/c2ra22847e.

187. Voepel, P.; Seitz, C.; Waack, J.M.; Zahn, S.; Leichtweiß, T.; Zaichenko, A.; Mollenhauer, D.; Amenitsch, H.; Voggenreiter, M.; Polarz, S.; et al. Peering into the mechanism of low-temperature synthesis of bronze-type TiO2 in ionic liquids. *Cryst. Growth Des.* **2017**, *17*, 5586–5601, doi:10.1021/acs.cgd.7b01231.

188. Hosseini, S.N.; Grau-Carbonell, A.; Nikolaenkova, A.G.; Xie, X.; Chen, X.; Imhof, A.; van Blaaderen, A.; Baesjou, P.J. Smectic Liquid Crystalline Titanium Dioxide Nanorods: Reducing Attractions by Optimizing Ligand Density. *Adv. Funct. Mater.* **2020**, *30*, 1–11, doi:10.1002/adfm.202005491.

189. Trentler, T.J.; Denler, T.E.; Bertone, J.F.; Agrawal, A.; Colvin, V.L. Synthesis of TiO2 nanocrystals by nonhydrolytic solution-based reactions [9]. *J. Am. Chem. Soc.* **1999**, *121*, 1613–1614, doi:10.1021/ja983361b.

190. Chemseddine, A.; Moritz, T. Nanostructuring titania: Control over nanocrystal structure, size, shape, and organization. *Eur. J. Inorg. Chem.* **1999**, 235–245, doi:Doi 10.1002/(Sici)1099-0682(19990202)1999:2<235::Aid-Ejic235>3.0.Co;2-N.

191. Jun, Y.W.; Casula, M.F.; Sim, J.H.; Kim, S.Y.; Cheon, J.; Alivisatos, A.P. Surfactant-Assisted Elimination of a High Energy Facet as a Means of Controlling the Shapes of TiO2 Nanocrystals. *J. Am. Chem. Soc.* **2003**, *125*, 15981–15985, doi:10.1021/ja0369515.

192. Niederberger, M.; Bartl, M.H.; Stucky, G.D. Benzyl alcohol and titanium tetrachloride - A versatile reaction system for the nonaqueous and low-temperature preparation of crystalline and luminescent titania nanoparticles. *Chem. Mater.* **2002**, *14*, 4364–4370, doi:10.1021/cm021203k.

193. Arnal, P.; Corriu, R.J.P.; Leclercq, D.; Mutin, P.H.; Vioux, A. A Solution Chemistry Study of Nonhydrolytic Sol - Gel Routes to Titania. *Chem. Mater.* **1997**, *9*, 694–698, doi:10.1021/cm960337t.

194. Mutin, P.H.; Vioux, A. Nonhydrolytic processing of oxide-based materials: Simple routes to control homogeneity, morphology, and nanostructure. *Chem. Mater.* **2009**, *21*, 582–596, doi:10.1021/cm802348c.

195. Buonsanti, R.; Carlino, E.; Giannini, C.; Altamura, D.; De Marco, L.; Giannuzzi, R.; Manca, M.; Gigli, G.; Cozzoli, P.D. Hyperbranched Anatase TiO 2 Nanocrystals: Nonaqueous Synthesis, Growth

Mechanism, and Exploitation in Dye-Sensitized Solar Cells. *J. Am. Chem. Soc.* **2011**, *133*, 19216–19239, doi:10.1021/ja208418z.

196. Koo, B.; Park, J.; Kim, Y.; Choi, S.H.; Sung, Y.E.; Hyeon, T. Simultaneous phase- and size-controlled synthesis of TiO2 nanorods via non-hydrolytic sol-gel reaction of syringe pump delivered precursors. *J. Phys. Chem. B* **2006**, *110*, 24318–24323, doi:10.1021/jp065372u.

197. Levy, D.; Marcos, Z. *The Sol-Gel Handbook*; Levy, D., Marcos, Z., Eds.; Wiley-VCH Verlag GmbH & Co., 2015; ISBN 9783527338443.

198. Kobayashi, M.; Saito, H.; Boury, B.; Matsukawa, K.; Sugahara, Y. Epoxy-based hybrids using TiO2 nanoparticles prepared via a non-hydrolytic sol-gel route. *Appl. Organomet. Chem.* **2013**, *27*, 673–677, doi:10.1002/aoc.3027.

199. Murray, C. B., Kagan.R., and B.M.G. Synthesis And Characterization Of Monodisperse Nanocrystals And Close-Packed Nanocrystal Assemblies. *Annu. Rev. Mater. Sci.* **2000**, *30*, 545–610.

200. Penn, R.L.; Banfield, J.F. Morphology development and crystal growth in nanocrystalline aggregates under hydrothermal conditions: Insights from titania. *Geochim. Cosmochim. Acta* **1999**, *63*, 1549–1557, doi:10.1016/S0016-7037(99)00037-X.

201. Niederberger, M.; Garnweitner, G.; Pinna, N.; Neri, G. Non-aqueous routes to crystalline metal oxide nanoparticles: Formation mechanisms and applications. *Prog. Solid State Chem.* **2005**, *33*, 59–70, doi:10.1016/j.progsolidstchem.2005.11.032.

202. Deshmukh, R.; Niederberger, M. Nonhydrolytic Sol – Gel Methods, The Sol–Gel Handbook: Synthesis, Characterization, and Applications. **2015**, 29–69.

203. Dalmaschio, C.J.; Leite, E.R. Detachment induced by rayleigh-instability in metal oxide nanorods: Insights from TiO 2. *Cryst. Growth Des.* **2012**, *12*, 3668–3674, doi:10.1021/cg300473u.

204. Niederberger, M.; Bartl, M.H.; Stucky, G.D. Benzyl alcohol and transition metal chlorides as a versatile reaction system for the nonaqueous and low-temperature synthesis of crystalline nano-objects with controlled dimensionality. *J. Am. Chem. Soc.* **2002**, *124*, 13642–13643, doi:10.1021/ja027115i.

205. Li, X.L.; Peng, Q.; Yi, J.X.; Wang, X.; Li, Y. Near monodisperse TiO2 nanoparticles and nanorods. *Chem. - A Eur. J.* **2006**, *12*, 2383–2391, doi:10.1002/chem.200500893.

206. Jiang, D.; Xu, Y.; Hou, B.; Wu, D.; Sun, Y. A simple non-aqueous route to anatase TiO2. *Eur. J. Inorg. Chem.* **2008**, 1236–1240, doi:10.1002/ejic.200700650.

207. Zhu, J.; Zhang, J.; Chen, F.; Anpo, M. Preparation of high photocatalytic activity TiO2 with a bicrystalline phase containing anatase and TiO2 (B). *Mater. Lett.* **2005**, *59*, 3378–3381, doi:10.1016/j.matlet.2005.05.072.

208. Cargnello, M.; Cargnello, M.; Doan-nguyen, V.V.T.; Gordon, T.R.; Diaz, R.E.; Stach, E.A.; Gorte, R.J.; Fornasiero, P.; Murray, C.B. Control of Metal Nanocrystal Size Role for Ceria Catalysts. **2014**, *771*, 771–774, doi:10.1126/science.1240148.

209. Casavola, M.; Grillo, V.; Carlino, E.; Giannini, C.; Gozzo, F.; Pinel, E.F.; Garcia, M.A.; Manna, L.; Cingolani, R.; Cozzoli, P.D. Topologically controlled growth of magnetic-metal-functionalized semiconductor oxide nanorods. *Nano Lett.* **2007**, *7*, 1386–1395, doi:10.1021/nl070550w.

210. Barnard, A.S.; Curtiss, L.A. Prediction of TiO 2 nanoparticle phase and shape transitions controlled by surface chemistry. *Nano Lett.* **2005**, *5*, 1261–1266, doi:10.1021/nl050355m.

211. Da Silva, R.O.; Gonalves, R.H.; Stroppa, D.G.; Ramirez, A.J.; Leite, E.R. Synthesis of recrystallized anatase TiO2 mesocrystals with Wulff shape assisted by oriented attachment. *Nanoscale* **2011**, *3*, 1910–1916, doi:10.1039/c0nr01016b.

212. Dalmaschio, C.J.; Ribeiro, C.; Leite, E.R. Impact of the colloidal state on the oriented attachment growth mechanism. *Nanoscale* **2010**, *2*, 2336–2345, doi:10.1039/c0nr00338g.

213. Zhang, J.; Huang, F.; Lin, Z. Progress of nanocrystalline growth kinetics based on oriented attachment. *Nanoscale* **2010**, *2*, 18–34, doi:10.1039/b9nr00047j.

214. Nichols, F.A.; Mullins, W.W. Contributions to Morphological Changes Driven by Capillarity. *Trans. Met. Soc. AIME* **1965**, *233*.

215. Karim, S.; Toimil-Molares, M.E.; Ensinger, W.; Balogh, A.G.; Cornelius, T.W.; Khan, E.U.; Neumann, R. Influence of crystallinity on the Rayleigh instability of gold nanowires. *J. Phys. D. Appl. Phys.* **2007**, *40*, 3767–3770, doi:10.1088/0022-3727/40/12/031.

216. Qin, Y.; Lee, S.M.; Pan, A.; Gösele, U.; Knez, M. Rayleigh-instability-induced metal nanoparticle chains encapsulated in nanotubes produced by atomic layer deposition. *Nano Lett.* **2008**, *8*, 114–118, doi:10.1021/nl0721766.

217. Qin, Y.; Liu, L.; Yang, R.; Gösele, U.; Knez, M. General assembly method for linear metal nanoparticle chains embedded in nanotubes. *Nano Lett.* **2008**, *8*, 3221–3225, doi:10.1021/nl801548h.

218. Penn Lee, R.; Banfield F., J. Formation of rutile nuclei at anatase {112} twin interfaces and the phase transformation mechanism in nanocrystalline titania. *Am. Mineral.* **1999**, *84*, 871–876, doi:10.2138/am-1999-5-621.

219. Reddy, K.M.; Manorama, S. V.; Reddy, A.R. Bandgap studies on anatase titanium dioxide nanoparticles. *Mater. Chem. Phys.* **2003**, *78*, 239–245, doi:10.1016/S0254-0584(02)00343-7.

220. Holzwarth, U.; Gibson, N. The Scherrer equation versus the "Debye-Scherrer equation." *Nat. Nanotechnol.* **2011**, *6*, 534, doi:10.1038/nnano.2011.145.

221. Gonzalo-Juan, I.; McBride, J.R.; Dickerson, J.H. Ligand-mediated shape control in the solvothermal synthesis of titanium dioxide nanospheres, nanorods and nanowires. *Nanoscale* **2011**, *3*, 3799–804, doi:10.1039/c1nr10540j.

222. Kandiel, T.A.; Feldhoff, A.; Robben, L.; Dillert, R.; Bahnemann, D.W. Tailored titanium dioxide nanomaterials: anatase nanoparticles and brookite nanorods as highly active photocatalysts. *Chem. Mater.* **2010**, *22*, 2050–2060, doi:10.1021/cm903472p.

223. Li, J.G.; Ishigaki, T.; Sun, X. Anatase, brookite, and rutile nanocrystals via redox reactions under mild hydrothermal conditions: Phase-selective synthesis and physicochemical properties. *J. Phys. Chem. C* **2007**, *111*, 4969–4976, doi:10.1021/jp0673258.

224. Andreev, Y.G.; Panchmatia, P.M.; Liu, Z.; Parker, S.C.; Islam, M.S.; Bruce, P.G. The shape of TiO2-B nanoparticles. *J. Am. Chem. Soc.* **2014**, *136*, 6306–6312, doi:10.1021/ja412387c.

225. Wensink, H.H.; Vroege, G.J. Isotropic – nematic phase behavior of length- polydisperse hard rods.

J. Chem. Phys. **2003**, *119*, 6868–6882, doi:10.1063/1.1599277.

226. Pietra, F.; Rabouw, F.T.; Evers, W.H.; Byelov, D. V.; Petukhov, A. V.; De Mello Donegá, C.; Vanmaekelbergh, D. Semiconductor nanorod self-assembly at the liquid/air interface studied by in situ GISAXS and ex situ TEM. *Nano Lett.* **2012**, *12*, 5515–5523, doi:10.1021/nl302360u.

227. Ryan, K.M.; Mastroianni, A.; Stancil, K.A.; Liu, H.; Alivisatos, A.P. Electric-field-assisted assembly of perpendicularly oriented nanorod superlattices. *Nano Lett.* **2006**, *6*, 1479–1482, doi:10.1021/nl0608660.

228. An, K.; Lee, N.; Park, J.; Kim, S.C.; Hwang, Y.; Park, J.G.; Kim, J.Y.; Park, J.H.; Han, M.J.; Yu, J.; et al. Synthesis, characterization, and self-assembly of pencil-shaped CoO nanorods. *J. Am. Chem. Soc.* **2006**, *128*, 9753–9760, doi:10.1021/ja0608702.

229. Xie, Y.; Liang, Y.; Chen, D.; Wu, X.; Dai, L.; Liu, Q. Vortical superlattices in a gold nanorods' self-assembled monolayer. *Nanoscale* **2014**, *6*, 3064–3068, doi:10.1039/C3NR05992H.

230. Modlinska, A.; Alsayed, A.M.; Gibaud, T. Condensation and dissolution of nematic droplets in dispersions of colloidal rods with thermo-sensitive depletants. *Sci. Rep.* **2015**, *5*, 1–10, doi:10.1038/srep18432.

231. Wang, P.; MacLachlan, M.J. Liquid crystalline tactoids: ordered structure, defective coalescence and evolution in confined geometries. *Philos. Trans. R. Soc. A Math. Phys. Eng. Sci.* **2018**, *376*, 20170042, doi:10.1098/rsta.2017.0042.

232. Jamali, V.; Behabtu, N.; Senyuk, B.; Lee, J.A.; Smalyukh, I.I.; van Der Schoot, P.; Pasquali, M. Experimental realization of crossover in shape and director field of nematic tactoids. *Phys. Rev. E - Stat. Nonlinear, Soft Matter Phys.* **2015**, *91*, 1–7, doi:10.1103/PhysRevE.91.042507.

233. Green, M.J.; Parra-Vasquez, A.N.G.; Behabtu, N.; Pasquali, M. Modeling the phase behavior of polydisperse rigid rods with attractive interactions with applications to single-walled carbon nanotubes in superacids. *J. Chem. Phys.* **2009**, *131*, doi:10.1063/1.3204024.

234. Saliba, S.; Mingotaud, C.; Kahn, M.L.; Marty, J.D. Liquid crystalline thermotropic and lyotropic nanohybrids. *Nanoscale* **2013**, *5*, 6641–6661, doi:10.1039/c3nr01175e.

235. Lawrence, A.S.C.; Lekkerkerker, H.N.W. Colloid science. *Nature* **2002**, *416*, 811–815, doi:10.1038/168800a0.

236. Gast, A.P.; Russel, W.B. Simple ordering in complex fluids - Colloidal particles suspended in solution provide intriguing models for studying phase transitions. *Phys. Today* **1998**, *51*, 24–30, doi:10.1063/1.882495.

237. Andrienko, D. Introduction to liquid crystals. *J. Mol. Liq.* **2018**, *267*, 520–541, doi:10.1016/j.molliq.2018.01.175.

238. Fontana, J.; Da Costa, G.K.B.; Pereira, J.M.; Naciri, J.; Ratna, B.R.; Palffy-Muhoray, P.; Carvalho, I.C.S. Electric field induced orientational order of gold nanorods in dilute organic suspensions. *Appl. Phys. Lett.* **2016**, *108*, 081904, doi:10.1063/1.4942969.

239. Wu, S.T. Nematic liquid crystal modulator with response time less than 100 μs at room temperature. *Appl. Phys. Lett.* **1990**, *57*, 986–988, doi:10.1063/1.103533.

240. Clark, N.A.; Lagerwall, S.T. Submicrosecond bistable electro-optic switching in liquid crystals. *Appl. Phys. Lett.* **1980**, *36*, 899–901, doi:10.1063/1.91359.

241. Acharya, B.R.; Baldwin, K.W.; MacHarrie, R.A.; Rogers, J.A.; Huang, C.C.; Pindak, R. In-fiber nematic liquid crystal optical modulator based on in-plane switching with microsecond response time. *Appl. Phys. Lett.* **2002**, *81*, 5243–5245, doi:10.1063/1.1532532.

242. Dozov, I.; Goldmann, C.; Davidson, P.; Abécassis, B. Supporting Informatio: Probing permanent dipoles in CdSe nanoplatelets with transient electric birefringence. *Nanoscale* **2020**, *12*, 11040–11054, doi:10.1039/d0nr00884b.

243. Mohammadimasoudi, M.; Hens, Z.; Neyts, K. Full alignment of dispersed colloidal nanorods by alternating electric fields. *RSC Adv.* **2016**, *6*, 55736–55744, doi:10.1039/c6ra02620f.

244. Etcheverry, S.; Araujo, L.F.; da Costa, G.K.B.; Pereira, J.M.B.; Camara, A.R.; Naciri, J.; Ratna, B.R.; Hernández-Romano, I.; de Matos, C.J.S.; Carvalho, I.C.S.; et al. Microsecond switching of plasmonic nanorods in an all-fiber optofluidic component. *Optica* **2017**, *4*, 864, doi:10.1364/optica.4.000864.

245. Etcheverry, S.; Araujo, L.F.; Carvalho, I.C.S.; Margulis, W.; Fontana, J. Digital electric field induced switching of plasmonic nanorods using an electro-optic fluid fiber. *Appl. Phys. Lett.* **2017**, *111*, 1–5, doi:10.1063/1.5001702.

246. Zheng, X.; Fontana, J.; Pevnyi, M.; Ignatenko, M.; Wang, S.; Vaia, R.; Palffy-Muhoray, P. The effects of nanoparticle shape and orientation on the low frequency dielectric properties of nanocomposites. *J. Mater. Sci.* **2012**, *47*, 4914–4920, doi:10.1007/s10853-012-6364-8.

247. Levy, O. Dielectric response and electro-optical effects in suspensions of anisotropic particles. *Phys. Rev. E - Stat. Physics, Plasmas, Fluids, Relat. Interdiscip. Top.* **2002**, *66*, 1–6, doi:10.1103/PhysRevE.66.011404.

248. Gharde, R.; Bhave, M.G. The study of refractive indices of liquid crystal mixtures. *Mol. Cryst. Liq. Cryst.* **2015**, *613*, 1–15, doi:10.1080/15421406.2015.1032019.

249. Lagerwall, J.P.F. A phenomenological introduction to liquid crystals and colloids. In *Liquid Crystals with Nano and Microparticles*; pp. 11–93 ISBN 9789814619264.

250. Ozbek, H.; Ustunel, S.; Kutlu, E.; Cetinkaya, M.C. A simple method to determine high-accuracy refractive indices of liquid crystals and the temperature behavior of the related optical parameters via high-resolution birefringence data. *J. Mol. Liq.* **2014**, *199*, 275–286, doi:10.1016/j.molliq.2014.09.003.

251. Li, J.; Gauza, S.; Wu, S.T. Temperature effect on liquid crystal refractive indices. *J. Appl. Phys.* **2004**, *96*, 19–24, doi:10.1063/1.1757034.

252. Li, J.; Wu, S.T. Self-consistency of Vuks equations for liquid-crystal refractive indices. *J. Appl. Phys.* **2004**, *96*, 6253–6258, doi:10.1063/1.1812356.

253. Li, J.; Wu, S.T. Extended Cauchy equations for the refractive indices of liquid crystals. *J. Appl. Phys.* **2004**, *95*, 896–901, doi:10.1063/1.1635971.

254. Smith, G.B. Dielectric constants for mixed media. *J. Phys. D. Appl. Phys.* **1977**, *10*, 1–5, doi:10.1088/0022-3727/10/4/004.

255. Nan, C.W. Physics of inhomogeneous inorganic materials. *Prog. Mater. Sci.* **1993**, *37*, 1–116, doi:10.1016/0079-6425(93)90004-5.

256. Heller, W. The determination of refractive indices of colloidal particles by means of a new mixture rule or from measurements of light scattering. *Phys. Rev.* **1945**, *68*, 5–10, doi:10.1103/PhysRev.68.5.

257. Zakri, T.; Laurent, J.P.; Vauclin, M. Theoretical evidence for "Lichtenecker's mixture formulae" based on the effective medium theory. *J. Phys. D. Appl. Phys.* **1998**, *31*, 1589–1594, doi:10.1088/0022-3727/31/13/013.

258. Jayasundere, N.; Smith, B. V. Dielectric constant for binary piezoelectric 0-3 composites. *J. Appl. Phys.* **1993**, *73*, 2462–2466, doi:10.1063/1.354057.

259. Dang, Z.M.; Yuan, J.K.; Zha, J.W.; Zhou, T.; Li, S.T.; Hu, G.H. Fundamentals, processes and applications of high-permittivity polymer-matrix composites. *Prog. Mater. Sci.* **2012**, *57*, 660–723, doi:10.1016/j.pmatsci.2011.08.001.

260. Gehr, R.J.; Boyd, R.W. Optical properties of nanostructured optical materials. *Chem. Mater.* **1996**, *8*, 1807–1819, doi:10.1021/cm9600788.

261. Dang, A.; Ojha, S.; Hui, C.M.; Mahoney, C.; Matyjaszewski, K.; Bockstaller, M.R. High-transparency polymer nanocomposites enabled by polymer-graft modification of particle fillers. *Langmuir* **2014**, *30*, 14434–14442, doi:10.1021/la5037037.

262. Bodurov, I.; Yovcheva, T.; Sainov, S. Refractive index investigations of nanoparticles dispersed in water. *J. Phys. Conf. Ser.* **2014**, *558*, doi:10.1088/1742-6596/558/1/012062.

263. Wang, Z.; Lu, Z.; Mahoney, C.; Yan, J.; Ferebee, R.; Luo, D.; Matyjaszewski, K.; Bockstaller, M.R. Transparent and High Refractive Index Thermoplastic Polymer Glasses Using Evaporative Ligand Exchange of Hybrid Particle Fillers. *ACS Appl. Mater. Interfaces* **2017**, *9*, 7515–7522, doi:10.1021/acsami.6b12666.

264. Liu, C.; Hajagos, T.J.; Chen, D.; Chen, Y.; Kishpaugh, D.; Pei, Q. Efficient One-Pot Synthesis of Colloidal Zirconium Oxide Nanoparticles for High-Refractive-Index Nanocomposites. *ACS Appl. Mater. Interfaces* **2016**, *8*, 4795–4802, doi:10.1021/acsami.6b00743.

265. Sainov, S.; Vlaeva, I.; Yovcheva, T.; Dragostinova, V.; Stavrev, S. Dielectric function of polymer nanocomposites in small filling factor approximation. *J. Phys. Conf. Ser.* **2010**, *253*, 4–10, doi:10.1088/1742-6596/253/1/012067.

266. Maldovan, M.; Bockstaller, M.R.; Thomas, E.L.; Carter, W.C. Validation of the effective-medium approximation for the dielectric permittivity of oriented nanoparticle-filled materials: Effective permittivity for dielectric nanoparticles in multilayer photonic composites. *Appl. Phys. B Lasers Opt.* **2003**, *76*, 877–884, doi:10.1007/s00340-003-1209-4.

267. Moiseev, S.G. Optical properties of a Maxwell-Garnett composite medium with nonspherical silver inclusions. *Russ. Phys. J.* **2009**, *52*, 1121–1127, doi:10.1007/s11182-010-9349-6.

268. Kuijk, A.; Troppenz, T.; Filion, L.; Imhof, A.; van Roij, R.; Dijkstra, M.; van Blaaderen, A. Effect of external electric fields on the phase behavior of colloidal silica rods. *Soft Matter* **2014**, *10*, 6249–6255, doi:10.1039/c4sm00957f.

269. Liu, B.; Besseling, T.H.; Hermes, M.; Demirörs, A.F.; Imhof, A.; van Blaaderen, A. Switching plastic

crystals of colloidal rods with electric fields. *Nat. Commun.* **2014**, *5*, 3092, doi:10.1038/ncomms4092.

270. Dozov, I.; Goldmann, C.; Davidson, P.; Abécassis, B. Probing permanent dipoles in CdSe nanoplatelets with transient electric birefringence. *Nanoscale* **2020**, *12*, 11040–11054, doi:10.1039/d0nr00884b.

271. Dozov, I.; Paineau, E.; Davidson, P.; Antonova, K.; Baravian, C.; Bihannic, I.; Michot, L.J. Electric-field-induced perfect anti-nematic order in isotropic aqueous suspensions of a natural beidellite clay. *J. Phys. Chem. B* **2011**, *115*, 7751–7765, doi:10.1021/jp201201x.

272. Buluy, O.; Aryasova, N.; Tereshchenko, O.; Kurioz, Y.; Nazarenko, V.; Eremin, A.; Stannarius, R.; Klein, S.; Goldmann, C.; Davidson, P.; et al. Optical and X-ray scattering studies of the electric field-induced orientational order in colloidal suspensions of pigment nanorods. *J. Mol. Liq.* **2018**, *267*, 286–296, doi:10.1016/j.molliq.2018.02.003.

273. De La Cotte, A.; Merzeau, P.; Kim, J.W.; Lahlil, K.; Boilot, J.P.; Gacoin, T.; Grelet, E. Electric field induced birefringence in non-aqueous dispersions of mineral nanorods. *Soft Matter* **2015**, *11*, 6595–6603, doi:10.1039/c5sm01427a.

274. Kim, J.; de la Cotte, A.; Deloncle, R.; Archambeau, S.; Biver, C.; Cano, J.-P.; Lahlil, K.; Boilot, J.-P.; Grelet, E.; Gacoin, T. LaPO 4 Mineral Liquid Crystalline Suspensions with Outstanding Colloidal Stability for Electro-Optical Applications. *Adv. Funct. Mater.* **2012**, *22*, 4949–4956, doi:10.1002/adfm.201200825.

275. Pochylski, M.; Calandra, P.; Aliotta, F.; Ponterio, R.C. Electrically induced birefringence in nanoparticle dispersions for electrorheological applications. *J. Phys. D. Appl. Phys.* **2014**, *47*, doi:10.1088/0022-3727/47/46/465301.

276. Aliotta, F.; Calandra, P.; Pochylski, M.; Ponterio, R.C.; Salvato, G.; Vasi, C. Enhancement of electrorheological effect by particle-fluid interaction. *Phys. Rev. E - Stat. Nonlinear, Soft Matter Phys.* **2013**, *87*, 1–8, doi:10.1103/PhysRevE.87.062304.

277. Aubert, T.; Palangetic, L.; Mohammadimasoudi, M.; Neyts, K.; Beeckman, J.; Clasen, C.; Hens, Z. Large-Scale and Electroswitchable Polarized Emission from Semiconductor Nanorods Aligned in Polymeric Nanofibers. *ACS Photonics* **2015**, *2*, 583–588, doi:10.1021/acsphotonics.5b00068.

278. van der Zande, B.M.I.; Koper, G.J.M.; Lekkerkerker, H.N.W. Alignment of Rod-Shaped Gold Particles by Electric Fields. *J. Phys. Chem. B* **2002**, *103*, 5754–5760, doi:10.1021/jp984737a.

279. Titov, A. V; Kra, P. Modeling the Self-Assembly of Colloidal Nanorod Superlattices. *Nano Lett.* **2008**, *8*, 3605–3612, doi:10.1021/nl801530x.

280. Leferink op Reinink, A.B.G.M.; van den Pol, E.; Petukhov, A. V.; Vroege, G.J.; Lekkerkerker, H.N.W. Phase behaviour of lyotropic liquid crystals in external fields and confinement. *Eur. Phys. J. Spec. Top.* **2013**, *222*, 3053–3069, doi:10.1140/epjst/e2013-02075-x.

281. Li, L.; Alivisatos, A.P. Origin and Scaling of the Permanent Dipole Moment in CdSe Nanorods. *Phys. Rev. Lett.* **2003**, *90*, 097402, doi:10.1103/PhysRevLett.90.097402.

282. Gonzalo-Juan, I.; Krejci, A.J.; Rodriguez, M.A.; Zhou, Y.; Fichthorn, K.A.; Dickerson, J.H. Dipole moment-tuned packing of TiO2nanocrystals into monolayer films by electrophoretic deposition. *Appl. Phys. Lett.* **2014**, *105*, doi:10.1063/1.4896133.

283. Frka-Petesic, B.; Jean, B.; Heux, L. First experimental evidence of a giant permanent electric-dipole moment in cellulose nanocrystals. *EPL* **2014**, *107*, doi:10.1209/0295-5075/107/28006.

284. Ruda, H.E.; Shik, A. Nanorod dynamics in ac electric fields. *Nanotechnology* **2010**, *21*, 235502, doi:10.1088/0957-4484/21/23/235502.

285. Zhang, Y.; Liu, Q.; Mundoor, H.; Yuan, Y.; Smalyukh, I.I. Metal nanoparticle dispersion, alignment, and assembly in nematic liquid crystals for applications in switchable plasmonic color filters and E-polarizers. *ACS Nano* **2015**, *9*, 3097–3108, doi:10.1021/nn5074644.

286. Bertrand, E.A.; Endres, A.L. Complex dielectric response of ellipsoidal particles with surface conduction. *J. Chem. Phys.* **2009**, *130*, doi:10.1063/1.3139257.

287. O'Konski, C.T. Effect of interfacial conductivity on dielectric properties. *J. Chem. Phys.* **1955**, *23*, 15–16, doi:10.1063/1.1742372.

288. O'Konski, C.T. Electric Properties Of Macromolecules. V. Theory Of Ionic Polarization In Polyelectrolytes. *J. Phys. Chem.* **1960**, *64*, 605–619, doi:10.1017/9781316662205.006.

289. Venermo, J.; Sihvola, A. Dielectric polarizability of circular cylinder. *J. Electrostat.* **2005**, *63*, 101–117, doi:10.1016/j.elstat.2004.09.001.

290. Landau, L.D.; Lifshitz, E.M.; Mikhailovich, E. *Electrodynamics of continuous media*; Second Edi.; Pergamon Press, 1984; ISBN 978-0-08-030275-1.

291. Volpe, G.; Petrov, D. Torque detection using brownian fluctuations. *Phys. Rev. Lett.* **2006**, *97*, 1–4, doi:10.1103/PhysRevLett.97.210603.

292. Pecora, R. *Dynamic Light Scattering: Applications of Photon Correlation Spectroscopy*; 2008; ISBN 978-1-4020-4465-6.

293. Mercedes Tirado, M.; López Martínez, C.; García De La Torre, J. Comparison of theories for the translational and rotational diffusion coefficients of rod-like macromolecules. Application to short DNA fragments. *J. Chem. Phys.* **1984**, *81*, 2047–2052, doi:10.1063/1.447827.

294. Doi, M.; Edwards, S.F. Dynamics of rod-like macromolecules in concentrated solution. Part 1. *J. Chem. Soc. Faraday Trans. 2 Mol. Chem. Phys.* **1978**, *74*, 560–570, doi:10.1039/F29787400560.

295. Doi, M.; Edwards, S.F. Dynamics of rod-like macromolecules in concentrated solution. Part 2. *J. Chem. Soc. Faraday Trans. 2 Mol. Chem. Phys.* **1978**, *74*, 560–570, doi:10.1039/F29787400560.

296. Pecora, R. Dynamics of Rodlike Macromolecules in Semidilute Solutions. *J. Polym. Sci. Part C, Polym. Symp.* **1985**, *91*, 83–91, doi:10.1002/polc.5070730113.

297. Fawcett, W. The Electric Field in Crystals: II. The Refractivities of Anatase and Brookite. *Proc. Phys. Soc.* **1963**, *82*, 33–46.

298. O'Donoghue, M. *Gems: Their Sources, Descriptions and Identification*; sixth.; Elsevier, 2006; ISBN 9780750658560.

299. Beleggia, M.; De Graef, M.; Millev, Y.T. The equivalent ellipsoid of a magnetized body. *J. Phys. D. Appl. Phys.* **2006**, *39*, 891–899, doi:10.1088/0022-3727/39/5/001.

300. Tao, P.; Li, Y.; Rungta, A.; Viswanath, A.; Gao, J.; Benicewicz, B.C.; Siegel, R.W.; Schadler, L.S.

TiO2 nanocomposites with high refractive index and transparency. *J. Mater. Chem.* **2011**, *21*, 18623, doi:10.1039/c1jm13093e.

301. Liu, C.; Hajagos, T.J.; Chen, D.; Chen, Y.; Kishpaugh, D.; Pei, Q. Efficient One-Pot Synthesis of Colloidal Zirconium Oxide Nanoparticles for High-Refractive-Index Nanocomposites. *ACS Appl. Mater. Interfaces* **2016**, *8*, 4795–4802, doi:10.1021/acsami.6b00743.

302. Yan, W.; Li, S.; Zhang, Y.; Yao, Q.; Tse, S.D. Effects of dipole moment and temperature on the interaction dynamics of titania nanoparticles during agglomeration. *J. Phys. Chem. C* **2010**, *114*, 10755–10760, doi:10.1021/jp102750k.

303. Zhang, Y.; Li, S.; Yan, W.; Yao, Q.; Tse, S.D. Role of dipole-dipole interaction on enhancing Brownian coagulation of charge-neutral nanoparticles in the free molecular regime. *J. Chem. Phys.* **2011**, *134*, doi:10.1063/1.3555633.

304. Shanbhag, S.; Kotov, N.A. On the origin of a permanent dipole moment in nanocrystals with a cubic crystal lattice: Effects of truncation, stabilizers, and medium for CdS tetrahedral homologues. *J. Phys. Chem. B* **2006**, *110*, 12211–12217, doi:10.1021/jp0611119.

305. Gonzalez, R.; Zallen, R.; Berger, H. Infrared reflectivity and lattice fundamentals in anatases. *Phys. Rev. B - Condens. Matter Mater. Phys.* **1997**, *55*, 7014–7017, doi:10.1103/PhysRevB.55.7014.

306. Shojaee, E.; Abbasnejad, M.; Saeedian, M.; Mohammadizadeh, M.R. First-principles study of lattice dynamics of TiO2 in brookite and cotunnite structures. *Phys. Rev. B* **2011**, *83*, 174302, doi:10.1103/PhysRevB.83.174302.

307. Eremin, A.; Stannarius, R.; Klein, S.; Heuer, J.; Richardson, R.M. Switching of electrically responsive, light-sensitive colloidal suspensions of anisotropic pigment particles. *Adv. Funct. Mater.* **2011**, *21*, 556–564, doi:10.1002/adfm.201001573.

308. Zorn, M.; Tahir, M.N.; Bergmann, B.; Tremel, W.; Grigoriadis, C.; Floudas, G.; Zentel, R. Orientation and dynamics of ZnO nanorod liquid crystals in electric fields. *Macromol. Rapid Commun.* **2010**, *31*, 1101–1107, doi:10.1002/marc.201000049.

309. Heyes, D.M. Translational and rotational diffusion of rod shaped molecules by molecular dynamics simulations. *J. Chem. Phys.* **2019**, *150*, doi:10.1063/1.5092958.

310. De La Cotte, A.; Merzeau, P.; Kim, J.W.; Lahlil, K.; Boilot, J.P.; Gacoin, T.; Grelet, E. Supporting Information: Electric field induced birefringence in non-aqueous dispersions of mineral nanorods. *Soft Matter* **2015**, *11*, 6595–6603, doi:10.1039/c5sm01427a.

311. Yan, X.; Liu, W.; Zhou, Y.; Yuan, D.; Hu, X.; Zhao, W.; Zhou, G. Improvement of electro-optical properties of PSLC devices by silver nanowire doping. *Appl. Sci.* **2019**, *9*, doi:10.3390/app9010145.

312. Yan, X.; Zhou, Y.; Liu, W.; Liu, S.; Hu, X.; Zhao, W.; Zhou, G.; Yuan, D. Effects of silver nanoparticle doping on the electro-optical properties of polymer stabilized liquid crystal devices. *Liq. Cryst.* **2020**, *47*, 1131–1138, doi:10.1080/02678292.2019.1641754.

313. Presnyakov, V. V.; Galstian, T. V. Electrically tunable polymer stabilized liquid-crystal lens. *J. Appl. Phys.* **2005**, *97*, doi:10.1063/1.1896436.

314. Presnyakov, V.; Asatryan, K.; Galstian, T.; Tork, A. Polymer-stabilized liquid crystal for tunable microlens applications. *Opt. Express* **2002**, *10*, 865–870, doi:10.1364/OE.10.000865.

315. van der Wee, E.B. Quantitative 3D real-space studies of arrested colloidal structures and processes, Utrecht University, 2019.

316. Hosseini, S.N.; Chen, X.; Baesjou, P.J.; Imhof, A.; van Blaaderen, A. Synthesis and Characterization of Anatase TiO2 Nanorods: Insights from Nanorods' Formation and Self-Assembly. *Appl. Sci.* **2022**, *12*, 1614, doi:10.3390/app12031614.

317. Miyazawa, T.; Itaya, M.; Burdeos, G.C.; Nakagawa, K.; Miyazawa, T. A critical review of the use of surfactant-coated nanoparticles in nanomedicine and food nanotechnology. *Int. J. Nanomedicine* **2021**, *16*, 3937–3999, doi:10.2147/IJN.S298606.

318. Verschueren, A.R.M.; Stofmeel, L.W.G.; Baesjou, P.J.; van Delden, M.H.W.M.; Lenssen, K.-M.H.; Mueller, M.; Oversluizen, G.; van Glabbeek, J.J.; Osenga, J.T.M.; Schuurbiers, R.M. Optical performance of in-plane electrophoretic color e-paper. *J. Soc. Inf. Disp.* **2010**, *18*, 1–7, doi:10.1889/JSID18.1.1.

319. Dugyala, V.R.; Daware, S. V.; Basavaraj, M.G. Shape anisotropic colloids: Synthesis, packing behavior, evaporation driven assembly, and their application in emulsion stabilization. *Soft Matter* **2013**, *9*, 6711–6725, doi:10.1039/c3sm50404b.

320. Sang, L.; Zhao, Y.; Burda, C. TiO 2 Nanoparticles as Functional Building Blocks. *Chem. Rev.* **2014**, 140520065639008, doi:10.1021/cr400629p.

321. Noel, A.; Mirbel, D.; Cloutet, E.; Fleury, G.; Schatz, C.; Navarro, C.; Hadziioannou, G.; CyrilBrochon Tridodecylamine, an efficient charge control agent in non-polar media for electrophoretic inks application. *Appl. Surf. Sci.* **2018**, *428*, 870–876, doi:10.1016/j.apsusc.2017.09.171.

322. Tadros, T. *Encyclopedia of Colloid and Interface Science*; 2013; ISBN 9783642206658.

323. Tadros, T. Electrostatic And Steric Stabilization Of Colloidal Dispersions. In *Electrical Phenomena at Interfaces and Biointerfaces: Fundamentals and Applications in Nano-, Bio-, and Environmental Sciences*; Hiroyuki Ohshima, Ed.; John Wiley & Sons, Inc., 2012; pp. 153–172.

324. Ponto, B.S.; Berg, J.C. Nanoparticle charging with mixed reverse micelles in apolar media. *Colloids Surfaces A Physicochem. Eng. Asp.* **2020**, *586*, 124275, doi:10.1016/j.colsurfa.2019.124275.

325. Gacek, M.M.; Berg, J.C. The role of acid – base effects on particle charging in apolar media. *Adv. Colloid Interface Sci.* **2015**, *220*, 108–123, doi:10.1016/j.cis.2015.03.004.

326. Smith, G.N.; Eastoe, J. Controlling colloid charge in nonpolar liquids with surfactants. *Phys. Chem. Chem. Phys.* **2012**, 424–439, doi:10.1039/c2cp42625k.

327. Morrison, I.D. Electrical charges in nonaqueous media. *Colloids Surfaces A Physicochem. Eng. Asp.* **1993**, *71*, 1–37, doi:10.1016/0927-7757(93)80026-B.

328. Mathews, M.B.; Hirschhorn, E. Solubilization and micelle formation in a hydrocarbon medium. *J. Colloid Sci.* **1953**, *8*, 86–96, doi:10.1016/0095-8522(53)90009-9.

329. Eicke, H. Surfactants in nonpolar solvents, Aggregation and Micellization. *Top. Curr. Chem. - Micelles* **1980**, *59*, 85–145, doi:10.1007/BFb0048489.

330. Singleterry, C.R. Micelle Formation and Solubilization in Nonaqueous Solvents. *J. Am. Oil Chem.*

1955, *32*, 446–452.

331. Albers, W.; Overbeek, J.T.G. Stability of emulsions of water in oil. II. Charge as a factor of stabilization against flocculation. *J. Colloid Sci.* **1959**, *14*, 510–518, doi:10.1016/0095-8522(59)90016-9.

332. Russel, W., Saville, D., & Schowalter, W. Polymeric stabilization. In *Colloidal Dispersions*; Cambridge University Press, 1989; pp. 310–328 ISBN 9780511608810.

333. FRIBERG, S.E.; FLAIM, T. Surfactant Association Structures. In *Inorganic Reactions in Organized Media*; American Chemical Society, 1982; pp. 1–17.

334. Clint, J.H. Micelle formation of Ionic Surfactants in Polar Nonaqueous Solvents. *Surfactant Aggreg.* **1992**, 82–129, doi:10.1007/978-94-011-2272-6_5.

335. Verbeeck, A.; Voortmans, G.; Jackets, C.; Schryver, F.C. De Characterization and Stabilization of Inverse Micelles. **1989**, *3*, 766–776.

336. Lyklema, J. Principles of interactions in non-aqueous electrolyte solutions. *Curr. Opin. Colloid Interface Sci.* **2013**, *18*, 116–128, doi:10.1016/j.cocis.2013.02.002.

337. Dukhin, A.S.; Goetz, P.J. How non-ionic "electrically neutral" surfactants enhance electrical conductivity and ion stability in non-polar liquids. *J. Electroanal. Chem.* **2006**, *588*, 44–50, doi:10.1016/j.jelechem.2005.12.001.

338. Dukhin, A.; Parlia, S. Ions, ion pairs and inverse micelles in non-polar media. *Curr. Opin. Colloid Interface Sci.* **2013**, *18*, 93–115, doi:10.1016/j.cocis.2013.02.004.

339. Smith, G.N.; Brown, P.; Rogers, S.E.; Eastoe, J. Evidence for a critical micelle concentration of surfactants in hydrocarbon solvents. *Langmuir* **2013**, *29*, 3252–3258, doi:10.1021/la400117s.

340. Smith, G.N.; Finlayson, S.D.; Rogers, S.E.; Bartlett, P.; Eastoe, J. Electrolyte-induced instability of colloidal dispersions in nonpolar solvents. *J. Phys. Chem. Lett.* **2017**, *8*, 4668–4672, doi:10.1021/acs.jpclett.7b01685.

341. Smith, G.N.; Grillo, I.; Rogers, S.E.; Eastoe, J. Surfactants with colloids: Adsorption or absorption? *J. Colloid Interface Sci.* **2015**, *449*, 205–214, doi:10.1016/j.jcis.2014.12.048.

342. Roberts, G.S.; Sanchez, R.; Kemp, R.; Wood, T.; Bartlett, P. Electrostatic charging of nonpolar colloids by reverse micelles. *Langmuir* **2008**, *24*, 6530–6541, doi:10.1021/la703908n.

343. Finlayson, S.D.; Bartlett, P. Non-additivity of pair interactions in charged colloids. *J. Chem. Phys.* **2016**, *145*, doi:10.1063/1.4959122.

344. Lin, T.; Kodger, T.E.; Weitz, D.A. Transport of charged colloids in a nonpolar solvent. *Soft Matter* **2013**, *9*, 5173, doi:10.1039/c3sm50619c.

345. Hsu, M.F.; Dufresne, E.R.; Weitz, D. a. Charge stabilization in nonpolar solvents. *Langmuir* **2005**, *21*, 4881–4887, doi:10.1021/la046751m.

346. Kanai, T.; Boon, N.; Lu, P.J.; Sloutskin, E.; Schofield, A.B.; Smallenburg, F.; van Roij, R.; Dijkstra, M.; Weitz, D.A. Crystallization and reentrant melting of charged colloids in nonpolar solvents. *Phys. Rev. E - Stat. Nonlinear, Soft Matter Phys.* **2015**, *91*, 1–5, doi:10.1103/PhysRevE.91.030301.

347. Lee, J.; Zhou, Z.L.; Alas, G.; Behrens, S.H. Mechanisms of particle charging by surfactants in nonpolar dispersions. *Langmuir* **2015**, *31*, 11989–11999, doi:10.1021/acs.langmuir.5b02875.

348. Guo, Q.; Lee, J.; Singh, V.; Behrens, S.H. Surfactant mediated charging of polymer particles in a nonpolar liquid. *J. Colloid Interface Sci.* **2013**, *392*, 83–89, doi:10.1016/j.jcis.2012.09.070.

349. Espinosa, C.E.; Guo, Q.; Singh, V.; Behrens, S.H. Particle charging and charge screening in nonpolar dispersions with nonionic surfactants. *Langmuir* **2010**, *26*, 16941–16948, doi:10.1021/la1033965.

350. Lee, J.; Zhou, Z.L.; Behrens, S.H. Interfaces Charged by a Nonionic Surfactant. *J. Phys. Chem. B* **2018**, *122*, 6101–6106, doi:10.1021/acs.jpcb.8b02853.

351. Gacek, M.M.; Berg, J.C. Investigation of surfactant mediated acid-base charging of mineral oxide particles dispersed in apolar systems. *Langmuir* **2012**, *28*, 17841–17845, doi:10.1021/la303943k.

352. Michor, E.L.; Ponto, B.S.; Berg, J.C. Effects of Reverse Micellar Structure on the Particle Charging Capabilities of the Span Surfactant Series. *Langmuir* **2016**, *32*, 10328–10333, doi:10.1021/acs.langmuir.6b02959.

353. FOWKES, F.M.; PUGH, R.J. Steric and Electrostatic Contributions to the Colloidal Properties of Nonaqueous Dispersions. **1984**, 331–354, doi:10.1021/bk-1984-0240.ch021.

354. Kemp, R.; Sanchez, R.; Mutch, K.J.; Bartlett, P. Nanoparticle charge control in nonpolar liquids: Insights from small-angle neutron scattering and microelectrophoresis. *Langmuir* **2010**, *26*, 6967–6976, doi:10.1021/la904207x.

355. Kitahara, A.; Satoh, T.; Kawasaki, S.; Kon-No, K. Specific adsorption of surfactants containing Mn or Co on polymer particles revealed by zeta-potential in cyclohexane. *J. Colloid Interface Sci.* **1982**, *86*, 105–110, doi:10.1016/0021-9797(82)90045-5.

356. Keir, R.I.; Ralston, J.; Thomas, J.C. The electrochemistry of nonaqueous copper phthalocyanine dispersions in the presence of a metal soap surfactant: A simple equilibrium site binding model. *J. Colloid Interface Sci.* **1999**, *211*, 252–263, doi:10.1006/jcis.1998.5951.

357. Lee, J.; Zhou, Z.L.; Behrens, S.H. Charging Mechanism for Polymer Particles in Nonpolar Surfactant Solutions: Influence of Polymer Type and Surface Functionality. *Langmuir* **2016**, *32*, 4827–4836, doi:10.1021/acs.langmuir.6b00583.

358. Van Der Hoeven, P.C.; Lyklema, J. Electrostatic stabilization in non-aqueous media. *Adv. Colloid Interface Sci.* **1992**, *42*, 205–277, doi:10.1016/0001-8686(92)80024-R.

359. Yethiraj, A.; van Blaaderen, A. A colloidal model system with an interaction tunable from hard sphere to soft and dipolar. *Nature* **2003**, *421*, 513–517, doi:10.1038/nature01328.

360. Vissers, T.; Imhof, A.; Carrique, F.; Delgado, Á. V; Blaaderen, A. Van Journal of Colloid and Interface Science Electrophoresis of concentrated colloidal dispersions in low-polar solvents. *J. Colloid Interface Sci.* **2011**, *361*, 443–455, doi:10.1016/j.jcis.2011.04.113.

361. Leunissen, M.E.; Christova, C.G.; Hynninen, A.; Royall, C.P.; Campbell, A.I.; van Roij, R.; Blaaderen, A. van Ionic colloidal crystals of oppositely charged particles. **2005**, *437*, 4–6, doi:10.1038/nature03946.

362. Leunissen, M.E. *Manipulating colloids with charges and electric fields*; 2007; ISBN 9789039344651.

363. Leunissen, M.E.; van Blaaderen, A.; Hollingsworth, A.D.; Sullivan, M.T.; Chaikin, P.M. Electrostatics at the oil-water interface, stability, and order in emulsions and colloids. *Proc. Natl. Acad. Sci. U. S. A.* **2007**, *104*, 2585–2590, doi:10.1073/pnas.0610589104.

364. Vissers, T.; Wysocki, A.; Rex, M.; Hartmut, L.; Royall, C.P.; Imhof, A.; Blaaderen, A. Van Lane formation in driven mixtures of oppositely charged colloids †. **2011**, 2352–2356, doi:10.1039/c0sm01343a.

365. Yethiraj, A. Tunable colloids: Control of colloidal phase transitions with tunable interactions. *Soft Matter* **2007**, *3*, 1099–1115, doi:10.1039/b704251p.

366. Rltzoulls, G.; Papadopoulos, N.; Jannakoudakls, D. Densities , Viscosities , and Dielectric Constants of Acetonitrile +. **1996**, 146–148.

367. Michor, E.L.; Berg, J.C. Temperature Effects on Micelle Formation and Particle Charging with Span Surfactants in Apolar Media. *Langmuir* **2015**, *31*, 9602–9607, doi:10.1021/acs.langmuir.5b02711.

368. Poovarodom, S.; Berg, J.C. Effect of particle and surfactant acid-base properties on charging of colloids in apolar media. *J. Colloid Interface Sci.* **2010**, *346*, 370–377, doi:10.1016/j.jcis.2010.03.012.

369. Guo, Q.; Singh, V.; Behrens, S.H. Electric charging in nonpolar liquids because of nonionizable surfactants. *Langmuir* **2010**, *26*, 3203–3207, doi:10.1021/la903182e.

370. Sigma-Aldrich Span80 product specification Available online: https://www.sigmaaldrich.com/specification-sheets/167/059/S6760-BULK_____SIGMA____.pdf.

371. ASTM International *ASTM D664-18e2: Standard Test Method for Acid Number of Petroleum Products by Potentiometric Titration*; West Conshohocken, PA, 2018; Vol. i;

372. ASTM International *ASTM D2896-03: Standard Test Method for Base Number of Petroleum Products by Potentiometric Perchloric Acid Titration*; West Conshohocken, PA, 2015;

373. Parent, M.E.; Yang, J.; Jeon, Y.; Toney, M.F.; Zhou, Z.L.; Henze, D. Influence of surfactant structure on reverse micelle size and charge for nonpolar electrophoretic inks. *Langmuir* **2011**, *27*, 11845–11851, doi:10.1021/la202660d.

374. Strubbe, F.; Verschueren, A.R.M.; Schlangen, L.J.M.; Beunis, F.; Neyts, K. Generation current of charged micelles in nonaqueous liquids : Measurements and simulations. **2006**, *300*, 396–403, doi:10.1016/j.jcis.2006.03.050.

375. Nakayama, N.; Hayashi, T. Preparation of TiO2 nanoparticles surface-modified by both carboxylic acid and amine: Dispersibility and stabilization in organic solvents. *Colloids Surfaces A Physicochem. Eng. Asp.* **2008**, *317*, 543–550, doi:10.1016/j.colsurfa.2007.11.036.

376. Erdem, B.; Hunsicker, R.A.; Simmons, G.W.; David Sudol, E.; Dimonie, V.L.; El-Aasser, M.S. XPS and FTIR surface characterization of TiO2 particles used in polymer encapsulation. *Langmuir* **2001**, *17*, 2664–2669, doi:10.1021/la0015213.

377. Gacek, M.; Brooks, G.; Berg, J.C. Characterization of Mineral Oxide Charging in Apolar Media. *Langmuir* **2012**, *28*, 3032–3036, doi:10.1021/la204000t.

378. Ponto, B.S.; Berg, J.C. Clay particle charging in apolar media. *Appl. Clay Sci.* **2018**, *161*, 76–81, doi:10.1016/j.clay.2018.04.016.

379. Thomas, J.C.; Crosby, B.J.; Keir, R.I.; Hanton, K.L. Observation of field-dependent electrophoretic mobility with phase analysis light scattering (PALS). *Langmuir* **2002**, *18*, 4243–4247, doi:10.1021/la011758e.

List of publications

- **Seyed Naveed Hosseini**, Albert Grau-Carbonell, Anna G. Nikolaenkova, Xiaobin Xie, Xiaodan Chen, Arnout Imhof, Alfons van Blaaderen, and Patrick J. Baesjou, "*Smectic Liquid Crystalline Titanium Dioxide Nanorods: Reducing Attractions by Optimizing Ligand Density*", **Advanced Functional Materials**, 2020, 30, 2005491, doi: 10.1002/adfm.202005491. (Chapter 2).

- **Seyed Naveed Hosseini**, Xiaodan Chen, Patrick J. Baesjou, Arnout Imhof, and Alfons van Blaaderen, "*Synthesis and Characterization of Anatase TiO_2 Nanorods: Insights from Nanorods'* Formation and Self-Assembly", **Applied Sciences**, 2022, 12, 1614, doi.org/10.3390/app12031614. (Chapter 3).

- "*TiO_2 nanorod liquid crystals in external electric fields*", to be submitted. (Chapter 4)

- "*Charging behavior of TiO_2 nanorods in nonaqueous media*"**,** to be submitted. (Chapter 5)

Other publications by the author:

- Xiaodan Chen, **Seyed Naveed Hosseini**, Marijn A. van Huis, "*Heating-Induced Transformation of Anatase TiO2 Nanorods into Rock-Salt TiO Nanoparticles: Implications for Photocatalytic and Gas-Sensing Applications*", **ACS Applied Nano Materials**, 2022, 5, 1600, doi.org/10.1021/acsanm.1c04346.

- **Seyed Naveed Hosseini,** Hamid Salimi Jazi, Mohammadhossein Fathi, "*Novel electrophoretic deposited nanostructured forsterite coating on 316L stainless steel implants for biocompatibility improvement*", **Materials Letters**, 2015, 143, 16, doi.org/10.1016/j.matlet.2014.12.079.

- Majid Jafari Bahramabadi, Mohammad Hossein Enayati, Mehdi Salehi, Mehran Nahvi, **Seyed Naveed Hosseini**, Chan Gyung Park, "*Influence of Nickel-Coated Nanostructured WC-Co Powders on Microstructural and Tribological Properties of HVOF Coatings*", **Journal of Thermal Spray Technology**, 2014, 23, 1456, doi.org/10.1007/s11666-014-0171-5.

- Mohammad Reza Loghman-Estarki, Mousa Pourbafrany, Reza Shoja Razavi, Hossein Edris, Saeed Reza Bakhshi, Mohammad Erfanmaesh, Hossein Jamali, **Seyed Naveed Hosseini**, Morteza Hajizadeh, "*Preparation of nanostructured YSZ granules by the spray drying method*", **Ceramics International**, 2014, 40, 3721, doi.org/10.1016/j.ceramint.2013.09.050.

Oral and poster presentations

- Okinawa Colloids, The Chemical Society of Japan, November 2019, Japan (oral & poster)
- European Materials Research Society (EMRS), September 2019, Poland (oral & poster)
- International Micro-Nano-Conference, December 2019, the Netherlands (poster)
- 50th anniversary of Institute of Solid State Research, March 2019, Forschungszentrum Jülich, Germany (poster)
- Physics@Veldhoven, January 2019, the Netherlands (poster)
- CHAINS, December 2018, the Netherlands (poster)
- Physics@Veldhoven, January 2018, the Netherlands (poster)

About the author

Naveed Hosseini was born on 25th November, 1988 in Isfahan, Iran. He completed high school in 2008 with a major in physics and mathematics and started his Bachelor's degree in Industrial Metallurgical Engineering in Shahinshahr, Isfahan. He graduated with honors as a top student in 2012 and worked for 9 months as a research assistant in the spray drying unit for two research projects. These projects were collaborations between Isfahan University of Technology (IUT) and industries and resulted in two publications for him in the field of nanostructured thermal spray coatings. In the same year, he was awarded to join a Master's program in the Materials Engineering department with a major in *Materials Selection & Characterization methods* at IUT with the entrance exam exemption. In 2015, he graduated with an M.Sc. degree in Materials Engineering. During his Master's, he worked on a research project under the joint supervision of Prof. Mohammadhossein Fathi and Dr. Hamid Salimi Jazi in the Biomaterials Research Group in IUT and the resultant thesis was entitled "Effects of Surface Treatments and Nanostructured Forsterite Coatings on the Corrosion Behavior of Stainless Steel Substrates". After this step, he worked as a part-time research assistant at the Steel Institute in IUT under the supervision of Dr. Maleki. In 2016, he was accepted into a Ph.D. project entitled "*Responsive Colloids for Switchable Optics*" offered by Toegepaste en Technische Wetenschappen in Nederlandse Organisatie voor Wetenschappelijk Onderzoek (NWO-TTW) in Utrecht University. Since 2016, he has worked in the field of nanoparticles synthesis and colloidal liquid crystals for optical applications under the supervision of Prof. Alfons van Blaaderen, Dr. Arnout Imhof, and Dr. Patrick Beasjou and the results of his research have been presented in this thesis, as well as national and international conferences and peer-reviewed scientific journals.

In addition to his research, Naveed enjoys traveling, canoeing, hiking, swimming, watching documentary series, salsa dancing, and playing Setar (a traditional Iranian music instrument).